Electron-induced Dynamics of Small Molecules of Atmospheric and Astrochemical Relevance



David Heathcote

Hertford College

University of Oxford

A thesis submitted in partial fulfilment
for the degree of Doctor of Philosophy in
Physical and Theoretical Chemistry

Michaelmas Term 2020

Table of Contents

List of Tables vi

List of Figures vii

Abstract xii

Acknowledgements xiv

Abbreviations xvi

1 Introduction 1

1.1 Potential energy surfaces 4
1.2 Electron-molecule scattering 8
1.3 Electron ionisation cross-sections 10
1.3.1 Experimental determination of total ionisation cross-sections . 12
1.4 Ion imaging 16
1.4.1 Velocity-map imaging 19
1.4.2 Supersonic expansion 21
1.4.3 Detectors 25
1.4.4 Differences between photoionisation and electron ionisation . . 29
1.5 Summary 32

2 Methods 33

2.1 Theoretical: The binary-encounter-Bethe (BEB) model 33
2.1.1 Calculation of parameters required for the model 35
2.1.2 Heavy atom corrections 35
2.2 Experimental: The electron-molecule crossed beam experiment 37
2.2.1 Experimental set-up 37
2.2.2 Characterisation 40
2.3 Summary 53

3 Image processing **54**
3.1 Centroiding ion hits . . . 55
3.2 Inversion methods . . . 59
3.2.1 Abel integral methods . . . 62
3.2.2 Onion peeling methods . . . 64
3.2.3 Basis function fitting methods . . . 66
3.3 Energy calibration . . . 71
3.4 Covariance analysis . . . 75
3.4.1 Coincidence . . . 77
3.4.2 Covariance maps . . . 85
3.4.3 Extension to ion images . . . 88
3.4.4 Recoil-frame covariance . . . 90
3.4.5 Characterisation of recoil-frame covariance analysis . . . 93
3.5 Inversion of recoil-frame covariance images . . . 105
3.5.1 A new inversion method for electron-molecule scattering experiments . . . 107
3.5.2 Examples: Scattering distributions (velocity-map images) . . . 116
3.5.3 Examples: Recoil-frame covariance maps . . . 120

4 Results: Total electron ionisation cross-sections **125**
4.1 Fitting the cross-sections . . . 129
4.2 Comparison to experimental data . . . 134
4.3 Summary . . . 136

5 Results: Scattering distributions **137**
5.1 Carbon dioxide (CO_2) . . . 138
5.1.1 Partial ionisation cross-sections . . . 139
5.1.2 Scattering distributions resulting from electron ionisation of CO_2 . . . 142
5.1.3 Dissociation of CO_2^{2+} . . . 149
5.1.4 Summary . . . 162
5.2 Nitrous oxide (N_2O) . . . 162
5.2.1 Partial ionisation cross-sections . . . 164
5.2.2 Scattering distributions resulting from electron ionisation of N_2O . . . 165
5.2.3 Covariance analysis of N_2O^{2+} . . . 175
5.2.4 Summary . . . 184
5.3 Carbonyl sulphide (OCS) . . . 184

5.3.1 Partial ionisation cross-sections . . . 186
5.3.2 Scattering distributions resulting from electron ionisation of OCS . . . 188
5.3.3 Covariance analysis of OCS^{2+} . . . 195
5.3.4 Comparison to CO_2 . . . 205
5.3.5 Summary . . . 206
5.4 Sulphur dioxide (SO_2) . . . 206
5.4.1 Partial ionisation cross-sections . . . 208
5.4.2 Scattering distributions resulting from electron ionisation of SO_2 . . . 209
5.4.3 Covariance analysis of $SO_2{}^{2+}$ . . . 216
5.4.4 Summary . . . 224
5.5 Deuterated benzene (C_6D_6) . . . 224
5.5.1 Partial ionisation cross-sections . . . 226
5.5.2 Scattering distributions resulting from electron ionisation of C_6D_6 . . . 229
5.5.3 Dissociation of $C_6D_6{}^{2+}$ . . . 237
5.5.4 Summary . . . 246
5.6 Summary . . . 247

6 Future work **249**
6.1 Experimental development . . . 249
6.1.1 Electron source . . . 249
6.1.2 Ultra-fast scintillator . . . 251
6.1.3 Sliced imaging . . . 253
6.2 Future target systems . . . 256

7 Conclusion **259**

References **262**

A Theoretical determination of total ionisation cross-sections **281**
A.1 The Jain-Khare semi-empirical formalism . . . 281
A.2 The complex scattering potential-ionisation contribution (CSP-ic) method . . . 282
A.3 The Deutsch-Märk formalism . . . 284

B Non-critical derivations **286**
B.1 Beer-Lambert law . . . 286
B.2 Dalitz plots . . . 288

C Scattering distributions and recoil-frame covariance maps recorded for benzene at 75 eV **290**

D Key codes for data analysis **298**

D.1 Imgread 298

D.2 A new inversion method for electron-molecule scattering experiments 314

D.2.1 Basis function generation 314

D.2.2 Inversion code 319

D.3 PyAbel Caller 333

D.4 TOF-TOF covariance 341

List of Tables

1.1 Possible outcomes of inelastic electron scattering 9

3.1 Fitting parameters for basis function scaling 112

4.1 Maximum total ionisation cross-sections and fitting parameters for a range of molecules studied using the BEB model 129

5.1 Comparison of partial ionisation cross-sections of CO_2 at an electron energy of 100 eV 140

List of Figures

1.1 Example of potential energy surfaces for four electronic states of the fictitious molecule AB 6
1.2 Depiction of vertical and adiabatic ionisation potentials 6
1.3 Technical drawing of the beam-gas experiment 14
1.4 Schematic of a dual chevron-mounted microchannel plate assembly . . 25

2.1 Experimental set-up of the electron-molecule crossed beam experiment 37
2.2 Molecular beam temporal profile 41
2.3 Schematic of the solenoid valve used in our experiment 42
2.4 Schematic of the ELS100 electron source 44
2.5 Effect of sweeping the electron beam through the molecular beam . . 45
2.6 Variation of electron current with electron energy 45
2.7 Optimisation of the velocity-map imaging focus 47
2.8 Experiment showing the need to negatively bias the front of the MCPs 49
2.9 Focussing the the PImMS camera 50
2.10 Pulse sequence for the electron-molecule crossed beam experiment . . 51
2.11 Determination of pulse timing for VMI optics 52

3.1 Depiction of the centroiding process 57
3.2 Centroiding with the PImMS camera 58
3.3 Scattering diagram for the crossed electron-molecular beam experiment 60
3.4 Exemplar 3D scattering distribution and 2D projection 62
3.5 Demonstration of the onion peeling method 65
3.6 Example of the velocity basis functions and corresponding projections used in the BASEX inversion method 68
3.7 Depiction of the projections used in the linBASEX inversion method. 69
3.8 Dimensions for the derivation of the energy calibration 71
3.9 Example of a curve used for energy calibration 73
3.10 Experimental setup used in the first coincidence experiment 77
3.11 Coordinate system used to define a three-body concerted decay . . . 80
3.12 Dalitz plot for the dissociation of OCS^{3+} 84

3.13 Possible orientations of an aligned chiral biphenyl molecule 89
3.14 Production of a recoil-frame covariance map 91
3.15 Recoil-frame covariance characterisation - single channel 94
3.16 Recoil-frame covariance characterisation - multiple channels 98
3.17 Simulated three-body dissociation with initial charge separation . . . 101
3.18 Depiction of angular relationship between a pair of covariant fragments 102
3.19 Simulated three-body dissociation with deferred charge separation . . 103
3.20 Justification for an oval feature in covariance maps with deferred charge separation 104
3.21 Examples of the results of covariance analysis plotted in three dimensions for a deferred charge separation process 106
3.22 The coordinate system used for the derivation of the new inversion method 109
3.23 Generation of basis function scaling functions 111
3.24 Comparison of the new inversion method to existing methods for an isotropic case 117
3.25 Comparison of the new inversion method to existing methods for an anisotropic case 119
3.26 Inversion of a covariance image for a two-body dissociation pathway . 120
3.27 Inversion of a covariance image for a three-body dissociation pathway 122

4.1 Total ionisation cross-sections calculated using the BEB model (full energy range example) 126
4.2 Total ionisation cross-sections calculated using the BEB model 127
4.2 (continued) 128
4.3 Comparison of the BEB model with experimental data 135

5.1 Mass spectrum of CO_2 recorded at an electron energy of 100 eV . . . 139
5.2 Partial electron ionisation cross-sections of CO_2 141
5.3 Scattering distributions for the parent ions of CO_2 143
5.4 Scattering distributions of CO^+ generated from CO_2 144
5.5 Scattering distributions of O^+ generated from CO_2 145
5.6 Scattering distributions of C^+ generated from CO_2 147
5.7 TOF-TOF covariance maps of CO_2 recorded at electron energies of 50 eV, 75 eV, and 100 eV 149
5.8 Recoil-frame covariance images for the CO^+/O^+ pair 152
5.9 Momentum distribution of covariant CO^+ and O^+ at 100 eV 153
5.10 Potential energy surface of CO_2^{2+} 154
5.11 Recoil-frame covariance images for the C^+/O^+ pair 156

5.12 Simulation of the C^+ and O^+ dissociation channel of CO_2^{2+} 157
5.13 Recoil-frame covariance images for the O^+/O^+ pair 159
5.14 Kinetic energy distributions of CO_2 obtained by Johnsson *et al.* . . . 161
5.15 Partial ionisation cross-sections for N_2O 164
5.16 Probability of forming each fragment ion of N_2O 165
5.17 Scattering distributions of NO^+ generated from N_2O 166
5.18 Potential energy surfaces for the formation of NO^+ and N_2^+ from N_2O^+ 167
5.19 Scattering distributions of $N_2{}^+$ generated from N_2O 170
5.20 Scattering distributions of N^+ generated from N_2O 171
5.21 Potential energy surfaces for the formation of N^+ and O^+ from N_2O^+ 172
5.22 Scattering distributions of O^+ generated from N_2O 173
5.23 TOF-TOF covariance maps of N_2O recorded at electron energies of 50 eV, 75 eV, and 100 eV 175
5.24 Potential energy surface of N_2O^{2+} 176
5.25 Recoil-frame covariance images for the NO^+/N^+ pair 178
5.26 Recoil-frame covariance images for the N_2^+/O^+ pair 179
5.27 Recoil-frame covariance images for the N^+/O^+ pair 181
5.28 Recoil-frame covariance images for the N^+/N^+ pair 182
5.29 Partial ionisation cross-sections obtained for OCS 186
5.30 Mass spectrum of OCS obtained following electron ionisation at an energy of 100 eV 188
5.31 Scattering distributions of S^+ generated from OCS 189
5.32 Potential energy surface including the first four electronic states of OCS^+ 190
5.33 Scattering distributions of CO^+ generated from OCS 191
5.34 Scattering distributions of CS^+ generated from OCS 192
5.35 Scattering distributions of O^+ generated from OCS 194
5.36 Scattering distributions of C^+ generated from OCS 195
5.37 TOF-TOF covariance maps of OCS recorded at electron energies of 50 eV, 75 eV, and 100 eV 196
5.38 Recoil-frame covariance images for the CO^+/S^+ decay pathway of OCS^{2+} 197
5.39 Recoil-frame covariance images for the CS^+/O^+ decay pathway of OCS^{2+} 198
5.40 Recoil-frame covariance images for the C^+/S^+ pair 201
5.41 Recoil-frame covariance images for the C^+/O^+ pair 202
5.42 Recoil-frame covariance images for the O^+/S^+ pair 203
5.43 Partial ionisation cross-sections obtained for SO_2 208

5.44 Scattering distributions of SO^+ generated from SO_2 . . . 209
5.45 Potential energy surface for SO_2^+ . . . 210
5.46 Scattering distributions of SO^{2+} generated from SO_2 . . . 211
5.47 Scattering distributions of O^+ generated from SO_2 . . . 213
5.48 The unsymmetrised scattering distribution of O^+ at an electron energy of 50 eV . . . 213
5.49 Scattering distributions of S^+ generated from SO_2 . . . 214
5.50 TOF-TOF covariance maps of SO_2 recorded at electron energies of 50 eV, 75 eV, and 100 eV . . . 216
5.51 Recoil-frame covariance images for the SO^+/O^+ pair . . . 218
5.52 Recoil-frame covariance images for the S^+/O_2^+ pair . . . 219
5.53 Recoil-frame covariance images for the S^+/O^+ pair . . . 221
5.54 Recoil-frame covariance images for the O^+/O^+ pair . . . 222
5.55 Partial ionisation cross-sections for electron ionisation of deuterated benzene . . . 227
5.56 Fitting of the PMT trace obtained for benzene at 100 eV to deconvolute the spectrum . . . 228
5.57 Scattering distributions for all fragments of deuterated benzene recorded at 100 eV . . . 230
5.57 (continued) $C_2D_x{}^+$ . . . 231
5.57 (continued) $C_3D_x{}^+$ . . . 232
5.57 (continued) $C_4D_x{}^+$ . . . 233
5.57 (continued) $C_5D_x{}^+$ / $C_6D_x{}^+$ . . . 234
5.58 TOF-TOF covariance map of C_6D_6 recorded at an electron energy of 100 eV . . . 237
5.59 TOF-TOF covariance map of C_6D_6 recorded at an electron energy of 75 eV, showing metastable decay . . . 238
5.60 A plot of all fragments between which covariance is observed for benzene at 100 eV . . . 240
5.61 Recoil-frame covariance maps for two-body dissociation of benzene at 100 eV . . . 241
5.62 Recoil-frame covariance maps for two-body dissociation of benzene into two $C_3D_x{}^+$ fragments at 100 eV . . . 243
5.63 Recoil-frame covariance maps for multi-body dissociation of benzene at 100 eV . . . 244
5.64 Self-covariance map of $CD_x{}^+$ . . . 246

6.1 Comparison between mass spectra recorded with a E404 and P47 scintillator . . . 251
6.2 Example of 3D covariance imaging . . . 253
6.3 Example of the rotations required for three-fold covariance . . . 255
6.4 Two future targets for the crossed electron-molecular beam experiment 256

B.1 Definition of dimensions required for the derivation of the Beer-Lambert law . . . 287

C.1 Scattering distributions for all fragments of deuterated benzene recorded at 75 eV . . . 291
C.1 (continued) $C_2D_x^+$ . . . 292
C.1 (continued) $C_3D_x^+$ . . . 293
C.1 (continued) $C_4D_x^+$ . . . 294
C.1 (continued) $C_5D_x^+$ / $C_6D_x^+$ . . . 295
C.2 Recoil-frame covariance maps for two-body dissociation of benzene at 75 eV . . . 296
C.3 Recoil-frame covariance maps for multi-body dissociation of benzene at 75 eV . . . 297

Abstract

Electron ionisation, and electron scattering in general, is a fundamental physical process. Ubiquitous in the known universe, the interaction of electrons with molecules is thus of great interest.

From experimental and theoretical studies, we can obtain great insight into electron ionisation. We have used the binary-encounter-Bethe model to determine theoretical total ionisation cross-sections, which quantify the ionisation probability for a molecule. We also use an electron-molecule crossed beam experiment to obtain partial ionisation cross-sections, which quantify the probability of forming a specific ion.

The electron-molecule crossed beam experiment utilises the velocity-map imaging technique, which allows the scattering distribution of the product ions to be recorded and the velocity of each ion determined. Study of these data grants us an insight into the molecular dynamics involved, and the potential energy landscape of the molecule under study.

In our experiments, we use a multi-mass imaging sensor to record the scattering distribution of all ions produced following electron ionisation. The use of a multi-mass imaging sensor allows us to utilise covariance analysis techniques, which reveal the correlations between the velocity distributions of different ions. We have recently shown that covariance allows us to much more readily study the dissociation of doubly-charged molecules following electron ionisation than was previously possible

using our experiment. The recoil-frame covariance technique is particularly useful in this context, allowing the momentum of a signal ion to be determined with reference exclusively to a second, covariant, ion.

Scattering distributions are recorded as two-dimensional projections of the three-dimensional distribution, meaning a reconstruction method, or inversion method, is required to 're-inflate' the distribution and obtain the velocity distribution. Recoil-frame covariance analysis cannot occur following inversion, meaning the resulting covariance maps must also be inverted. However, previously available inversion methods cannot validly be used. A new inversion method has been developed to allow the successful inversion of covariance maps.

We have used the above techniques to investigate a number of molecules of both atmospheric and astrochemical relevance, namely carbon dioxide, nitrous oxide, carbonyl sulphide, sulphur dioxide, and benzene. We find that fragmentation following electron ionisation is dominated by dissociation from low-lying electronic states of the molecule, and that a large portion of the energy available, i.e. the kinetic energy of the incident electron, is carried away by the ionising and ejected electrons, rather than being transferred to the molecular framework.

Acknowledgements

AMDG

There are many people to whom I am deeply grateful for their support over the period of my D.Phil. This is by no means an exhaustive list, but here are some of the people and groups I am particularly grateful for. I will begin with one of the few constants of my time in Oxford, namely Hertford College Chapel Choir (and music at Hertford in general). Having a regular schedule of music has been a huge support to me over the past years.

It has been a blessing and a privilege to reside at the Oxford University Catholic Chaplaincy for the past three years. Special thanks must go to the current Chaplains, Fr Matthew Power SJ, Fr Nick King SJ, and Fr Ian Tomlinson SJ, the assistant Chaplains, Becky Short and Alvea Fernandes, and to all of the members of the resident community, of whom there are too many to name here. You were always there to support me, regardless of how my work was going, and being in this community has undoubtedly helped me grow in Faith. I am so grateful that I am able to submit my thesis in the midst of such a community, and it's a fitting way to mark the end of my residence here.

Turning to chemistry, I gratefully acknowledge the support of the members of the mechanical and electronics workshops. There were some weeks when I visited the PTCL basement multiple times a day, and you were always happy to help. Without your assistance, there is no way I'd have any results to present in my thesis. I

should also thank all the other support staff who work tirelessly behind the scenes to ensure the smooth running of the department, without whom the department would quickly grind to a halt.

To all the members of the Vallance group past and present, thank you. You have lit up the basement of the CRL, and made my time in the group thoroughly enjoyable. Particular thanks must go to Dr Jason Lee for all his assistance, including, but by no means limited to, carrying out my initial instruction on how to use the electron-molecule crossed beam experiment, teaching me how to operate a PImMS camera, and introducing me to covariance analysis. To Dr Hansjochen Köckert, who started his D.Phil. at the same time as I joined the group, and with whom I worked on the electron-molecule crossed beam experiment. I learnt a lot from you, and hope you find success in your future endeavours. To Divya Popat, for being there when everyone else had left the group, and coming to me with coding problems. Finally, to Vincent Richardson and James Lomas, both Part II students in the Vallance groups with whom I worked closely. I hope you learnt a lot from the experience; I certainly learnt a lot from each of you. Special thanks to James, with whom I recorded the majority of the data presented in this thesis, for your assistance with the data analysis, and for proofreading my thesis.

To my supervisor, Prof. Claire Vallance, it has been a pleasure working with you for these past years, and look forward to continuing to do so in the coming year. Your never-ending enthusiasm, support and patience has been a blessing to me. You've helped me in so many ways, and are always happy to help, even whilst managing to do a million other things as well. It is fair to say that your guidance has played a major role in my development as a chemist.

Finally, I must thank my family. Their unconditional love and support for me is something which is often taken for granted, but I wish to express my gratitude to them. I hope you enjoy reading about 'teeny particles' and 'Spaceology'!

LDS

Abbreviations

1D	One-dimensional
2D	Two-dimensional
2D NMR	Two-dimensional nuclear magnetic resonance
3D	Three-dimensional
BASEX	Basis set expansion
BEB	Binary-encounter-Bethe
BED	Binary-encounter-dipole
CCD	Charge-coupled device
CMOS	Complementary metal-oxide-semiconductor
COM	Centre of mass
COSY	Correlation spectroscopy
CSP-ic	Complex scattering potential-ionisation contribution
FEL	Free-electron laser
FLASH	Free-Electron Laser in Hamburg
FWHM	Full width at half maximum
GPS	Global Positioning System
HACA	Hydrogen abstraction-acetylene addition
IR	Infra-red
ITO	Indium tin oxide
MALDI	Matrix-assisted laser desorption/ionisation

MCP	Microchannel plate
MET	Multiple-electron transitions
PEPECO	Photoelectron-photoelectron coincidence
PEPICO	Photoelectron-photoion coincidence
PEPIPICO	Photoelectron-photoion-photoion coincidence
PES	Potential energy surface
PImMS	Pixel Imaging Mass Spectrometry
PIPICO	Photoion-photoion coincidence
px	pixels
SMI	Spatial-map imaging
SPAD	Single-pixel avalanche photodiode
uPImMS	Microlens Pixel Imaging Mass Spectrometry
VMI	Velocity-map imaging

1

Introduction



lectron ionisation is a fundamental physical process, in which one or more electrons is ejected from a molecule following interaction with an incident electron. Since Dempster first used electron ionisation at the advent of mass spectrometry,[1] electron ionisation has found a number of applications in analytical techniques. For example, electron ionisation is still widely used in mass spectrometry, where it finds favour due to the fact it can universally ionise molecules, has a relatively high ionisation efficiency, and gives reproducible results.[2]

Of course, electron ionisation plays a role in a number of natural systems. For example, energetic electrons from the Earth's radiation belts can be scattered into the atmosphere by interaction with very low frequency radiation generated by lightning strikes, where the electrons can cause localised ionisation, amongst other processes.[3] These electrons are thought to have an influence on both atmospheric chemistry and climate.[4] Within the atmosphere, the concentration of electrons varies with altitude, but in regions such as the ionosphere, electron concentrations in excess of 10^5 cm^{-3}

are found.[5a] The concentration of electrons in the ionosphere is found to show dependence on the solar flux at a number of altitudes, suggesting photoionisation plays a role in the creation of these electrons.[5] It is inevitable that electrons will scatter off molecules in the atmosphere, so to more accurately model the atmosphere, there is a requirement for high-quality electron-molecule scattering data, including information on dissociation dynamics and product branching ratios. As shall be seen later in this thesis, both are provided by our experiment.

Further afield, electron ionisation is known to play a role in the atmosphere of Venus, with ionising electrons being produced from particle cascades following the interaction of a cosmic ray (high-energy particles emitted by stars, comprising about 84 % protons, 14 % alpha particles, and 2 % electrons, heavier nuclei and more exotic particles)[6] with the atmosphere,[7] and following photoionisation of the atmosphere by sufficiently energetic photons.[8] In interstellar gas clouds (a component of the interstellar medium), cosmic rays are thought to play a major role in the formation of ions, as visible and ultraviolet photons do not penetrate very far into the clouds due to absorption by hydrogen and dust grains.[6] Further electrons are produced following the interaction of cosmic rays with molecules in the gas cloud, and these go on to cause further chemistry. Numerous molecular species have been detected in the interstellar medium; currently, over 200 molecules have been confirmed to exist there,[9–12] and many more molecules are expected to be present. It is clear that the chemistry of the interstellar medium is both rich and varied. It is host to many exotic molecules which would react instantly in the Earth's atmosphere;[6] the existence of these molecules can be attributed to the fact that even in the densest regions of the interstellar medium, which have particle densities of around 10^6 cm^{-3}, pressures are comparable to what would be considered an ultra-high vacuum on Earth.[6]

As would be expected, there are significant variations between the properties of different regions of space. Electrons can be produced through a variety of processes, including the interaction of cosmic rays with molecules as mentioned above, pho-

[a] And references therein.

toionisation, and the interaction of high-energy cosmic rays or photons with dust grains and ices. The latter is known to release as many as 10^4 secondary electrons, with a mean kinetic energy below 20 eV.[13] A study on the interaction of liquid water with high-energy ionising radiation found that the majority of secondary electrons produced have an electron energy below 100 eV[14] which, given the stochastic nature of the ionisation process, should be consistent with the interaction of high-energy ionising radiation with ices. Where the electron energy reaches kinetic equilibrium, such as in HII regions and planetary nebulae, the kinetic energy distribution can be described by a Maxwellian-like distribution, possibly with a tail at high electron energies if higher-energy electrons have recently been injected into the system.[15] Kappa distributions can also be used to describe the kinetic energy distribution of electrons in certain cases, for example in the solar wind, where the relatively low electron densities, coupled with high temperatures and short timescales, mean that thermal equilibrium is not reached.[15,16] Typical electron energies in the solar wind are found to be in the region of several eV to tens of eV.[17] The electron density is highly dependent on the environment, with electron densities spanning the range of 0.001 cm^{-3} up to 1,000 cm^{-3} and higher.[18–25] In HII regions (i.e. where atomic hydrogen is in an ionised state), the electron density can be used as a diagnostic for the pressure and density the ions in that region.[21]

It is clear that it is important to understand the interaction of electrons with molecules to give us a more complete understanding of each of these systems; a number of possible processes in which an electron scatters off a molecule are discussed in section 1.2. Before that, we first introduce a fundamental molecular property which can be used to completely describe the molecular dynamics, namely the potential energy surface.

1.1 Potential energy surfaces

Potential energy surfaces play an important role in understanding the dissociation dynamics of molecular systems. A potential energy surface (PES) describes the potential energy of a molecule in a given electronic state at each point in space, defined by the internal coordinates of the system. For a diatomic molecule, only a single coordinate, the separation between the two atoms, is required to describe the system, and the potential at each separation can be determined to give a potential energy surface. With larger molecules, increasing numbers of coordinates are required to describe the molecule. For a triatomic molecule, the distance between two pairs of atoms, and the angle between the three atoms is required to describe the molecular framework, for a total of three coordinates. For a tetratomic molecule, the distance between three pairs of atoms, the angle between two sets of three atoms, and the dihedral angle between the four atoms is required to describe the molecular framework, for a total of six coordinates. After this, every extra atom added to the molecule increases the number of coordinates required to fully describe the molecule by three.

It is difficult to visualise multi-dimensional potential energy surfaces; they are often simplified by fixing the coordinates of all but one or two coordinates, so that the potential energy surface can be plotted in a two- or three-dimensional form. We will see examples of this later; for example, in section 5.3 we will see potential energy surfaces for carbonyl sulphide (OCS), in which the bond angle and one of the bond lengths has been fixed, and either the CO or CS bond length is changed.

Before we discuss potential energy surfaces in more detail, we will first remind ourselves of the relationship between force and potential. For a diatomic, where a single coordinate is required to describe the relative positions of the two atoms, the potential energy at a separation $\boldsymbol{r}$ is given by $V(\boldsymbol{r})$. The force $\boldsymbol{F}(\boldsymbol{r})$ is then given

by the negative gradient of the potential, i.e.

$$\boldsymbol{F}(\boldsymbol{r}) = -\frac{\mathrm{d}V(\boldsymbol{r})}{\mathrm{d}\boldsymbol{r}} \tag{1.1}$$

For larger molecules where a greater number of coordinates are required to describe the relative positions of the atoms, we need to use partial derivatives. Given a set of n coordinates $\boldsymbol{r}_1, \boldsymbol{r}_2, \ldots, \boldsymbol{r}_n$, with potential given by V, the force $\boldsymbol{F}$ is given by

$$\boldsymbol{F}\left(\boldsymbol{r}_1, \boldsymbol{r}_2, \ldots, \boldsymbol{r}_n\right) = -\left(\frac{\delta V}{\delta \boldsymbol{r}_1}\frac{\delta V}{\delta \boldsymbol{r}_2}\ldots\frac{\delta V}{\delta \boldsymbol{r}_n}\right) = -\nabla V \tag{1.2}$$

where ∇ is the del operator. Thus, the gradient of the potential energy surface describes the forces acting on the atoms in the molecule at any given geometry and, when used in conjunction with the current position and momenta of the atoms, allows us to determine the subsequent motion of the atoms. It follow that if two molecules are produced in an identical state, they will experience the same forces, and will exhibit identical dynamics. Therefore, if we obtain accurate potential energy surfaces, they can be used to completely describe the observed dynamics.[26]

An example of potential energy surfaces for four electronic states of the fictitious molecule AB are shown in figure 1.1. As this is a diatomic, we can completely describe the positions of A and B using a single coordinate, and hence determining the potential energy at each AB separation allows us to construct a potential energy surface. We can see four potential energy surfaces, corresponding to the four electronic states of the AB molecule. Both the lowest-energy state, shown in green, and second-lowest energy state, shown in blue, are bound states. Provided the total energy available does not exceed the barrier height, these states will remain as molecular AB. The bound states also contain vibrational and rotational states; a state's internal energy is defined as the total of the vibrational and rotational energy. The two higher-energy states, shown in orange and black, are repulsive states. AB molecules prepared in these two states will dissociate to their constituent atoms.

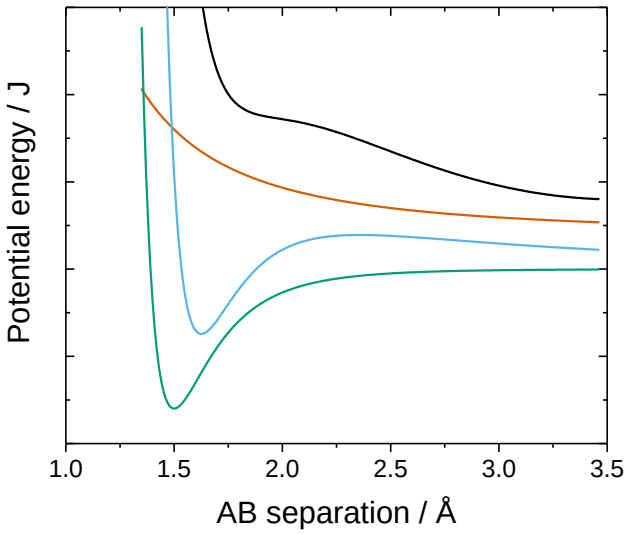


Figure 1.1 Example of potential energy surfaces for four electronic states of the fictitious molecule AB. Green: a bound electronic state, blue: a bound electronic state with a barrier in the exit channel, orange: a repulsive electronic state, black: a repulsive electronic state with a small barrier in the exit channel.

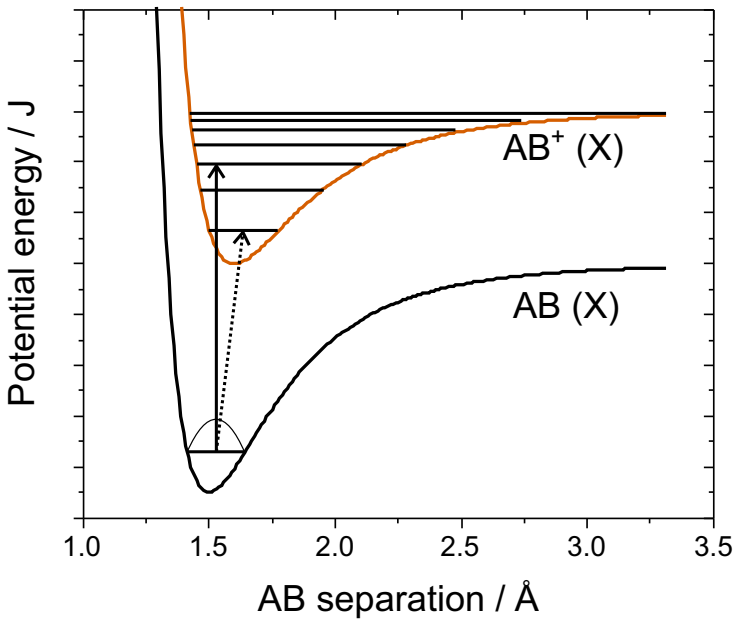


Figure 1.2 Depiction of vertical and adiabatic ionisation potentials from the ground neutral state to the ground cationic state for the fictitious molecule AB. The solid line shows the vertical ionisation potential for a transition to the second vibrational level of AB^+, and the dotted line the adiabatic ionisation potential.

Ionisation occurs via the ejection of an electron from the neutral molecule. There are a number of possible mechanisms by which this can occur. Figure 1.2 shows two ionisation potentials. The dotted line shows the adiabatic ionisation potential, which gives the minimum energy required to ionise a molecule from the initial state, i.e. from the initial state to the ground rovibrational level of the final ionic state. However, the geometry of the excited state is frequently different from that of the initial state, requiring a geometry change to undergo this transition. As will be discussed below, electron ionisation is thought to occur on an ultrafast timescale, much faster than nuclear motions, and is therefore considered to be taking place at a fixed geometry, i.e. it is a vertical transition on the potential energy surface. The solid line in figure 1.2 shows an example of a vertical transition.

Multiple vertical transitions are available, with the probability P of each transition determined by the transition dipole moment

$$P = |\langle \Psi_f | \hat{\mu} \mid \Psi_i \rangle|^2 \tag{1.3}$$

where Ψ_i and Ψ_f are the wavefunctions of the initial and final states, and $\hat{\mu}$ is the dipole operator. With the assumption of no nuclear motion, we can use the Born-Oppenheimer approximation to separate the wavefunction of the molecule into a wavefunction for the nuclei and a wavefunction for the electrons.[27,28] Using the Born-Oppenheimer approximation, equation 1.3 can thus be rewritten as

$$P = |\langle \Psi_{f,\mathrm{elec}} | \hat{\mu} | \Psi_{i,\mathrm{elec}} \rangle \langle \Psi_{f,\mathrm{vib}} | \Psi_{i,\mathrm{vib}} \rangle|^2 \tag{1.4}$$

where $\Psi_{i,\mathrm{elec}}$ and $\Psi_{f,\mathrm{elec}}$ are the initial and final states of the electronic part of the wavefunction, and $\Psi_{i,\mathrm{vib}}$ and $\Psi_{f,\mathrm{vib}}$ are the initial and final states of the vibrational part of the wavefunction. The second term, known as the Franck-Condon factor, indicates that the transition probability is dependent on the overlap between the vibrational wavefunctions of the initial and final state.[28,29]

There are a few other types of ionisation which can occur. If a highly excited state of the neutral is produced, at an energy above the adiabatic ionisation potential, it is possible for the molecule to spontaneously emit an electron, resulting in ionisation. This process is known as autoionisation.[30] Multiple ionisation can occur via Auger decay, in which an inner electron is initially ionised. A second electron fills the resulting hole, with the excess energy being transferred to a third electron, which is then ejected from the molecule.[31–33] Multiple ionisation can also occur via a shake-off mechanism, in which a departing electron interacts with electrons remaining on the molecule, with the interaction transferring sufficient energy to allow one or more electrons to subsequently be ejected from the molecule. If a further electron is not emitted, but the energy transfer results in an electronic state where one or more of the remaining electrons is promoted to a higher-lying molecular orbital, the process is known as a shake-up mechanism.[33]

Now that we have established that potential energy surfaces play an integral role in molecular dynamics, and have established the mechanisms by which ionisation may occur, we can now discuss the various ways in which electrons interact with a molecule.

1.2 Electron-molecule scattering

When an electron scatters off a molecule, the electron can either scatter elastically or inelastically. Here, elastic scattering is defined as a scattering event in which the incident electron's kinetic energy is unchanged, but its propagation direction changes, and inelastic scattering is defined as a scattering event where energy is transferred from the incident electron to the molecule, or vice versa. We will only consider inelastic scattering processes further, as here we are only interested in cases where the molecule has changed state.

Table 1.1 lists a number of processes which can occur as a result of inelastic electron scattering, which will now be discussed in turn. Excitation includes promo-

Process	Mechanism
Excitation	$AB + e^- \rightarrow AB^* + e^-$
Neutral fragmentation	$AB + e^- \rightarrow AB^* + e^- \rightarrow A + B + e^-$
Dissociative attachment	$AB + e^- \rightarrow \left[AB^-\right]^* \rightarrow A^- + B$
Ion pair formation	$AB + e^- \rightarrow AB^* + e^- \rightarrow A^+ + B^- + e^-$
Electron attachment	$AB + e^- \rightarrow AB^-$
Ionisation	$AB + e^- \rightarrow AB^{n+} + (n+1)\,e^-$
Dissociative ionisation	$AB + e^- \rightarrow \left[AB^+\right]^* + 2e^- \rightarrow A^+ + B + 2e^-$
Dissociative ionisation	$AB + e^- \rightarrow \left[AB^{2+}\right]^* + 3e^- \rightarrow A^+ + B^+ + 3e^-$

Table 1.1 A list of possible outcomes of inelastic electron scattering. Note that it is possible to form more than two fragments following electron scattering.

tion of the molecule into an excited rovibrational state and/or an excited electronic state, in which the molecule remains neutral and does not fragment. Note that this definition also allows for the possibility of molecular rearrangement. Neutral fragmentation is an extension of the excitation process, in which the excited molecule dissociates into two or more neutral fragments. If the molecule dissociates to form both a positively and negatively charged ion, the process is known as ion pair formation. Ion pair formation is thought to be a relatively minor channel for the formation of ions compared with dissociative ionisation.[34] For example, a study into ion pair formation in O_2 suggests that it accounts for approximately one hundredth of the total O^+ formation at 34 eV, decreasing at higher electron energies.[34,35] Dissociative attachment, or dissociative electron attachment, occurs predominantly via interaction with low-energy electrons (< 15 eV), via resonance with anionic states of the molecule.[36–39] Electron attachment is a very similar process, and predominantly occurs via interaction with thermal electrons, as there is no body to carry away the excess energy. The anions produced are inherently unstable, requiring stabilisation either by emission of radiation, or a collision with a third body.[38]

The main sources of ions, and hence the main processes considered in this thesis, are ionisation and dissociative ionisation, collectively electron ionisation. Both non-dissociative ionisation and dissociative ionisation involve the ejection of one or more electrons from the neutral molecule, and is classed simply as "ionisation" if the ion

remains intact, and "dissociative ionisation" if the ion dissociates.

We also need to consider the timescale of the interaction between the incident electron and the molecule. It takes an electron with a kinetic energy of 50 eV around 50 as (5×10^{-17} s) to travel 2 Å, which is on the order of the length of a molecular bond. Given that the timescales are typically on the order of hundreds of femtoseconds (10^{-13} s) for vibrational motion, and hundreds of picoseconds (10^{-10} s) for rotational motion,[40] we can see that the electron interacts with the molecule on a significantly faster timescale than nuclear motion, and thus the majority of electronic transitions occur at the geometry of the initial state, i.e. the Born-Oppenheimer approximation holds, and the transition on the potential energy surface can be treated as vertical.

Having established the possible outcomes of electron scattering we now introduce scattering cross-sections, a way of quantifying the outcome of the scattering process.

1.3 Electron ionisation cross-sections

The scattering of electrons by a molecule can be quantified using a number of cross-sections. Cross-sections are the single molecule version of a rate constant, and give the probability with which a certain scattering process occurs, in units of area. Whilst not a perfect literal representation of a cross-section, a cross-section can be considered as the area in which the incident electron must strike the molecule for a certain scattering process to occur. When comparing scattering cross-sections for different processes, their relative magnitudes give the relative probability of a given process occurring in comparison with another. The total cross-section gives the cross-section for all scattering, irrespective of the type. The total cross-section consists of a contribution from both elastic and inelastic scattering, described by their respective cross-sections. The inelastic cross-section includes contributions from a significant number of processes, including rotational, vibrational and electronic excitation, and ionisation. The latter of these is of particular relevance to this work,

and will be the main focus of the remainder of this section.

Two cross-sections are used to describe ionisation. The total ionisation cross-section reflects the probability with which a molecule is ionised, and partial ionisation cross-sections reflect the probability of forming a specific ion fragment. It follows that the sum of the partial ionisation cross-sections must equal the total ionisation cross-section for a given ionisation energy, and hence partial ionisation cross-sections can be obtained from measurements of the branching ratios for formation of different ions (relative partial ionisation cross-sections) by normalising to dedicated total ionisation cross-sections. A distinction should also be made between counting cross-sections, where each ion is counted, and gross cross-sections, where the total charge is measured, i.e. for doubly-charged ions, a counting cross-section will carry the same weight as a singly-charged ion, but in a gross cross-section will carry double the weight, and should be taken into consideration when normalising partial ionisation cross-sections. Both total and partial ionisation cross-sections are a function of the energy of the ionising radiation, thus measurements must be carried out at a range of energies to more completely understand the system under study.

There exist a number of theoretical methods for predicting total ionisation cross-sections. Due to the complexity of the system, these methods are typically semi-empirical or semi-classical. The majority of methods are based in some part on the additivity concept of Otvos and Stevenson,[41] who postulated that the total cross-section can be determined by adding together contributions from each molecular orbital, which can be determined separately. Frequently used methods include the Jain-Khare semi-empirical formalism,[42,43] the complex spherical potential-ionisation contribution (CSP-ic) method,[44,45] the Deutsch-Märk formalism,[46–48] and the binary-encounter-Bethe (BEB) model.[49,50] The BEB model is discussed in section 2.1, whilst the other methods are briefly reviewed in appendix A.

1.3.1 Experimental determination of total ionisation cross-sections

The first experiments to determine total ionisation cross-sections were carried out by Hughes and Klein.[51] In their experiment, electrons emitted by a filament held at a potential slightly above ground are accelerated towards an electrode containing small holes, held at a potential V_0. They then travel towards a second, grounded electrode through a retarding field. The electrons come to rest shortly before reaching the grounded electrode, and are then accelerated back towards the first electrode. The electrons striking this electrode may generate secondary electrons, but the authors believed the error from this to be quite small. The number of electrons E passing into the experiment was determined for a variety of V_0, then the ion current P was determined at a range of V_0. The fraction of collisions resulting in the formation of ions at energy V_0, $f(V_0')$, is then determined using the following expression

$$f(V_0') = f(V_0 - \nu) = \frac{1}{2\alpha p D} \frac{d\,(V_0 P/E)}{dV_0} \tag{1.5}$$

where ν accounts for the non-uniform potential, α gives the number of collisions made by an electron in 1 cm at 1 mm pressure, p is the gas pressure, and D is the distance between the two electrodes.

Smith and Tate were the first to introduce a magnetic field to define the electron beam, a key step in obtaining accurate total ionisation cross-sections.[52] In their experiment,[52,53] a filament emits electrons, which then pass through a set of electrodes. The presence of a magnetic field mean that these slits do not define the geometry of the beam, and no secondary electrons are emitted as a result of electrons striking the electrodes. The filament and first electrode were held at negative the electron energy under study. The electron beam then passes through a field-free region, before passing through another set of electrodes and striking a plate covered in soot, at which point the electron current is measured. Any ions produced in

the field-free region are detected using a second plate; an electric field between two plates running parallel to the beam axis acts to draw out any positive ions. The efficiency of ionisation, ϵ, is then given by

$$\epsilon = \frac{I_+}{I_-}\left[\frac{(T_1T_2)^{0.5}}{273lp}\right] \tag{1.6}$$

where I_+ and I_- are the measured ion and electron current respectively, T_1 and T_2 are the temperatures of the pressure gauge and the apparatus, l is the length of the ion collector, and p is the pressure of the apparatus in mm of mercury. The widely accepted cross-sections measured by Rapp, Golden and co-workers are measured using a very similar set-up,[54–56] and also forms the basis for the majority of current apparatus.

The beam-gas experiment

In our laboratory, a beam-gas experiment is used to determine total ionisation cross-sections experimentally. Whilst no experiments were carried out using this instrument in this work, results from this experiment are used to normalise the partial ionisation cross-sections obtained as part of this thesis.

A schematic of the instrument is shown in figure 1.3. Briefly, sample gas is introduced into the ionisation cell through a needle valve and the cell pressure and temperature measured using an MKS baratron model 690A capacitance manometer and thermistor, respectively. Electrons are emitted by a resistively-heated rhenium filament, and are focused by an Einzel lens (L1 - 3). The electrons then pass through a field-free region; any sample molecules ionised in this region are detected by a negatively-biased ion collector surrounding the field-free region (copper-coloured region in figure 1.3). All remaining electrons pass through L4 and L5, and are collected by a positively-biased Faraday cup (blue region in figure 1.3). The ion and electron currents are measured using a Keithley model 6487 and a Keithley model 486 picoammeter, respectively. As the sample molecules are not confined to the field-free

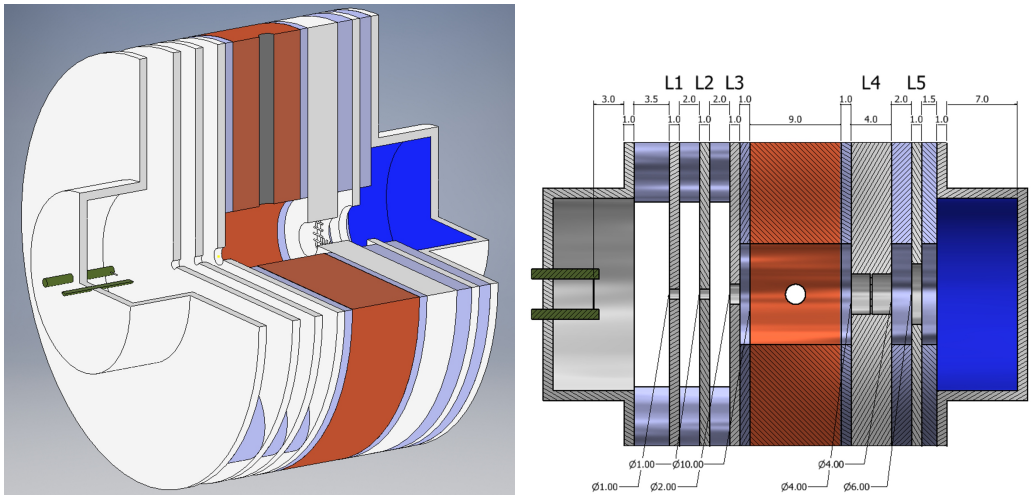


Figure 1.3 The schematic of the beam-gas experiment. The left image shows a three-quarter section view of the experiment, and the right image the cross-section, with the lens elements referred to in the text labelled. In the figure, insulating components are coloured lavender and metallic components are coloured silver, with the exception of the ion and electron collectors, which are coloured copper and blue, respectively.

region, ionisation can occur anywhere along the electron beam path, but ions formed outside this region are not detected.

To determine the cross-sections using these experiments, the Beer-Lambert law, derived in appendix B.1, is used. The Beer-Lambert law for an electron passing through a sample gas is given by

$$\frac{I}{I_0} = e^{-n\sigma_{\mathrm{TOT}}(E)l} \tag{1.7}$$

where I_0 and I are the electron flux, or current, before and after the absorbing medium, n is the number density of the sample gas, $\sigma_{\mathrm{TOT}}(E)$ is the total electron ionisation cross-section at an electron energy E, and l is the path length of the electron beam through the sample gas.

Assuming that ionisation is the only process that scatters electrons out of the primary beam, the transmitted intensity is simply $I = I_0 - I_+$, where I_+ is the measured ion current. Provided that the sample pressure is sufficiently low, it is reasonable to assume that the transmitted electron current, I_-, is approximately the same as the initial electron current, i.e. relatively few electrons collide with

the sample gas. With this approximation in place, the Beer-Lambert law can be rewritten in the following way

$$\frac{I_- - I_+}{I_-} = e^{-n\sigma_{\mathrm{TOT}}(E)l} \tag{1.8}$$

$$1 - \frac{I_+}{I_-} = e^{-n\sigma_{\mathrm{TOT}}(E)l} \tag{1.9}$$

$$\tag{1.10}$$

Using the Taylor expansion $e^x = 1 + x + \ldots$, and provided x is sufficiently small such that higher-order terms in the expansion can be neglected, equation 1.9 becomes

$$1 - \frac{I_+}{I_-} = 1 - n\sigma_{\mathrm{TOT}}(E)l \tag{1.11}$$

$$\frac{I_+}{I_-} = n\sigma_{\mathrm{TOT}}(E)l \tag{1.12}$$

$$\tag{1.13}$$

If it is assumed that the sample behaves as an ideal gas, then it follows that

$$n = \frac{N}{V} = \frac{P}{k_{\mathrm{B}}T} \tag{1.14}$$

where P and T are the pressure and temperature of the gas, respectively, V is the volume of the sample, N is the number of molecules in the sample, and k_{B} is the Boltzmann constant. Combining equations 1.12 and 1.14 together results in the following expression

$$\frac{I_+}{I_-} = \frac{P\sigma_{\mathrm{TOT}}(E)l}{k_B T} \tag{1.15}$$

There is one related experiment which warrants consideration within the wider context of this thesis. Lozier, with guidance from Tate and Bleakney,[57] used a similar experiment to that used by Smith, discussed above, but inserted a circular cylinder in which a series of slots had been cut into the interaction region. This resulted in

only ions produced travelling almost perpendicular to the electron beam direction being detected. By varying the potential between the cylinder and the ion detector, the velocity of the ions produced could also be probed. This data is important in understanding the molecular dynamics induced by electron scattering, and is one of the parameters that we obtain through the experiments carried out as part of this thesis.

Other than ionisation cross-sections, it is important that we understand the scattering dynamics, i.e. the velocity and angular distribution of the ions generated during scattering. Ion imaging, or more specifically the velocity-map imaging technique, is routinely used to obtain these distributions. Both ion imaging and velocity-map imaging are now reviewed, and a number of related experimental aspects are also introduced.

1.4 Ion imaging

Ion imaging has emerged as one of the key experimental techniques for assessing the inner workings of small molecules. It allows the full ion scattering distribution generated by incident ionising radiation, i.e. both the kinetic energy of and the angle at which the ions are produced, to be measured in a single experiment.

Early experiments concerning the dissociation of molecules were carried out using photofragment translational spectrometry.[58,59] In these experiments, a molecular beam is crossed at right angles with laser radiation, and the atoms which recoil perpendicular to the plane defined by the two beams are then detected using a quadrupole mass spectrometer. These experiments allow the translational energy of the molecules under study to be determined from the delay between the laser pulse and detection. The laser polarisation can also be changed in the laboratory frame to gain information on the direction of the transition dipole moment of the molecule under study.

Doppler spectroscopy was the next major development towards ion imaging,

allowing both the energy levels and angular distributions of scattered particles to be determined. The experiment exploits the Doppler shift experienced by a moving particle; the Doppler shift is defined as the difference between absorption frequency of the moving particle and the particle at rest. The absorption frequency is given by the following equation

$$\nu = \left(\frac{c + v_r}{c + v_s}\right) \nu_0 \tag{1.16}$$

where ν is the absorption frequency of the molecule, ν_0 is the absorption frequency of the molecule at rest, c is the speed of light, and v_s and v_r are the velocities of the source and receiver, respectively. The laser is the source in this case and, as this is stationary, equation 1.16 can be rewritten as

$$\nu = \left(1 + \frac{v_r}{c}\right) \nu_0 \tag{1.17}$$

Before discussing the use of this technique, it should be noted that at the time it was standard practice for ions to be detected using a translatable detector, which could be moved to allow detection of the velocity distribution at different scattering angles. The first experiment using Doppler spectroscopy was a variant on laser-induced fluorescence detection.[60] At each angle, a Doppler profile of a scattering distribution can be measured by scanning the excitation light through the Doppler profile of absorption; absorption of light is much more efficient when the energy of the photon matches the spacing between two energy levels, meaning that the Doppler profile contains information on the velocity of the molecular fragments within the scattering distribution. After Doppler profiles are measured at all required angles, a Fourier transform can then be applied to yield a three-dimensional velocity distribution.[61]

The inspiration behind the ion imaging technique came from the work of Hall *et al.*[62] In their work on the photolysis of CD_3I, a pump and probe laser are used to excite the molecule and ionise any resulting CD_3 molecular fragments, respectively. After some delay time in which the ionised fragments recoiled with the velocity

imparted by the dissociation, the ions were extracted by applying a potential to the grid electrodes of a time-of-flight mass spectrometer, with the arrival time of a given ion being determined by its position and velocity at that time. This results in a one-dimensional spectrum as a function of arrival time, with ions travelling towards the detector arriving at an earlier time, and those travelling away from the detector arriving at a later time.

After discussion following a talk given by Houston at a Faraday Discussion,[63] Chandler and Houston developed the first ion imaging experiment.[64] The experiment is largely the same as that carried out by Hall *et al.*, discussed above; CH_3I is excited by a pump laser and any resulting CH_3 molecular fragments are subsequently ionised by a probe laser. The ions are accelerated by a repeller plate, an electrostatic lens, to which a positive potential is applied, through a grounded mesh towards a position-sensitive detector assembly consisting of microchannel plates coupled to a phosphor screen. Detectors will be discussed in detail in section 1.4.3, but for the time being, it is sufficient to say that this detector assembly converts the incident ions into photons, which can then be imaged by a camera. The camera records the two-dimensional projection of the three-dimensional scattering distribution, as captured from the two-dimensional phosphor screen. Provided there exists an axis of cylindrical symmetry, the three-dimensional scattering distribution can be reconstructed from this projection, as will be discussed in section 3.2.

Whilst this technique offered a method to determine both the velocity and angular dependence of a scattering distribution, there were still a number of limitations that needed to be overcome. Firstly, a single ion might cause a number of pixels to light up. Work carried out by Chang *et al.* introduced a method to find the pixel which most accurately describes the pixel which was struck by the ion;[65] the technique is now known as centroiding and is discussed in section 3.1. Secondly, there may be cases where there is no axis of cylindrical symmetry, such that the vast majority of the inversion methods used to reconstruct a three-dimensional scat-

tering distribution from the recorded image are no longer valid. Finally, the images recorded using this method can show blurring due to the non-point source geometry, and the grid electrodes lead to transmission reduction and severe trajectory deflections.[66] This final issue can be overcome by using the velocity-map imaging (VMI) technique.

1.4.1 Velocity-map imaging

Velocity-map imaging, developed by Eppink and Parker,[66] utilises a three plate electrostatic lens with 'open' electrodes, i.e. there is no grid present in the electrodes. The three component electrodes, or plates, are known as the repeller, extractor and ground electrodes. A small hole is drilled in the centre of the repeller electrode to allow the sample to enter the interaction region between the repeller and extractor electrodes, and larger holes are made in the centre of the extractor and ground electrodes to accommodate the expanding scattering distribution. The key advantages of this method over the initial ion imaging experiments are that there is no mesh to perturb the ions produced in the experiment, and that, within a certain volume between the repeller and extractor plates of the electrostatic lens, all ions of the same velocity and mass-to-charge ratio are mapped to the same position on the detector, with the velocity being proportional to the radius from the centre of the ion image. The precision of this technique, and the amount of information available from a single experiment, make this an incredibly powerful analysis tool.

Eppink and Parker also introduced the concept of spatial-map imaging (SMI) in their paper introducing VMI.[66] In SMI, the location at which an ion is produced determines where it is detected on the detector. It is a useful tool in establishing overlap between the various molecular and ionising beams used in scattering experiments. This is of particular use in pump-probe experiments, where it can be used to overlap the foci of the two laser beams in the plane of the detector, for example. The method can also be applied in conjunction with matrix-assisted laser

desorption/ionisation (MALDI) to allow the determination of the composition of a solid sample in a single experiment. MALDI utilises a matrix molecule which absorbs at the wavelength of the oblating laser, and the energy absorbed is then transferred to the sample.[67] The sample is prepared by making a solution of the desired matrix, coating the sample and allowing the matrix to crystallise. The surface is oblated by a laser, then, using spatial-map imaging, the mass spectrum for each region of the sample which maps onto a single pixel of the detector can be determined. Combined with multi-mass imaging sensors such as the Pixel Imaging Mass Spectrometry sensor discussed in section 1.4.3, this allows the spatial determination of the components within a sample in a single experiment.[68–70] This has potential applications in medical fields, where it could be used to identify biomarkers which may be indicative of some other parameter of interest.

The only feature of the ion imaging experiment yet to be discussed is the possibility of imaging the entire three-dimensional scattering distribution in a single experiment where there is no axis of cylindrical symmetry. Gebhardt *et al.* developed a variation of VMI which allows the arrival time of the scattering distribution for each mass to be stretched out, rather than being 'crushed' onto the detector at a single time.[71] They utilise an electrostatic lens consisting of a set of five electrodes, a repeller, an extractor grid, and a further three electrodes which make up an Einzel lens used to velocity-map the ions. Pulsing the repeller and extractor electrodes after a short delay relative to the ion formation time causes the spread in arrival times of the scattering distribution; by taking images at various arrival times, slices through the scattering distribution can be obtained, allowing the three-dimensional scattering distribution to be measured directly. This technique is known as sliced imaging.

Further improvements to the sliced imaging technique were introduced by Townsend *et al.*[72] They also use a five-electrode electrostatic lens, but do not require the potentials on the electrodes to be pulsed, and no grids are required. They show

that the time spread of the ion arrival time is determined by the potential difference between the repeller and the first of the subsequent plates. Whilst a decreased potential between the plates of a conventional VMI lens, obtained by reducing the repeller potential and adjusting the extractor potential to regain velocity-mapping conditions, could achieve the same effect, there are problems with doing so: due to the decreased velocity of the ions along the flight tube, the scattering distributions may no longer fit on the detector, and the ions may not have enough kinetic energy to activate the microchannel plates. The ions may also be deflected to a greater extent due to the increased flight time, meaning the ions spend more time in any stray fields. By introducing an extra pair of electrodes after the conventional repeller and extractor plates however, a higher repeller potential can be used and the potential difference in the interaction region can be reduced, with the first of the new electrodes adjusting the magnification of the resulting ion image and the final electrode restoring VMI conditions.

It is worth pointing out one of the limitations of this technique. If in the process under study ions with similar mass-to-charge ratios are produced, there is the possibility that the two expanded scattering distributions may overlap. This limits the extent to which the scattering distribution can be expanded in time, requiring the use of ultra-fast detectors to allow sliced imaging to be used successfully on these systems.

An important part of any experiment to probe the dissociation dynamics of a molecule is that the molecule is prepared in as well-defined a state as possible. To do this a supersonic expansion is typically used, which converts the vast majority of the molecule's rotational and vibrational energy into translational energy.

1.4.2 Supersonic expansion

To produce a molecular beam, gas is expanded from a higher pressure source region into a lower pressure region through an orifice. Such an expansion can be described

as effusive or supersonic, depending on the speed of the molecular beam relative to the local speed of sound. Precisely which expansion occurs is dictated by the Knudsen number, K_n, given by

$$K_n = \frac{\lambda_0}{D} \tag{1.18}$$

where λ_0 is the mean free path of the gas in the source, and D is the orifice diameter. Anderson and Fenn[73] derive a theoretical expression for the terminal Mach number, M_T, based on two parameters

$$M_T = 2.05\epsilon^{0.4} K_n^{-0.4} \tag{1.19}$$

where ϵ is the collision effectiveness, given by

$$\frac{\mathrm{d}\langle c\rangle}{\mathrm{d}z} = -\epsilon\langle c\rangle \tag{1.20}$$

where $\langle c\rangle$ is the mean random velocity of the gas, and z is the number of collisions. Thus, the collision effectiveness gives an indication on how effectively the collisions in the beam cool the gas, transferring the random velocity into directed velocity along the molecular beam axis. Anderson and Fenn calculate an experimental expression for the terminal Mach number of argon

$$M_T = 1.17 K_n^{-0.4} \tag{1.21}$$

giving a collision effectiveness of around 0.25. Whilst we do not use argon in our experiments, it is reasonable to expect the value of ϵ for the expansions used in our experiments to be of a similar order of magnitude. This means, to a first approximation, that provided the mean free path of the gas is less than the diameter of the nozzle, the gas will undergo a supersonic expansion.

As the gas passes through the nozzle, the molecules undergo a significant number of collisions. These collisions serve to convert almost all rotational and vibrational

energy into translational energy in the beam propagation direction. Molecules travelling towards the nozzle exit are much more likely to leave the nozzle than those travelling in any other direction, resulting in a molecular beam. The beam has a laminar flow, and the molecules within the beam are internally cold and have a narrow range of kinetic energies, corresponding to the top end of the Boltzmann distribution of velocities of the gas in its initial state.

The thermodynamics of supersonic expansion are well described by Christen *et al.*,[74] and are summarised here. The conditions used for the derivation are that the gas is initially in thermodynamic equilibrium, no energy is exchanged between the effusing gas and its environment, i.e. it is an adiabatic process, and that the final state of the beam is considered when particle-particle collisions have ceased, and a steady state has been reached. The total energy of the system can be found by summing the internal molecular energy, U, the work, given by pressure, P multiplied by volume, V, and the kinetic energy, $\frac{m<v>^2}{2}$, where m is the mass of the molecule and $< v >$ is the mean velocity of the molecules. By conservation of energy, E, it follows that:

$$< E > = U_0 + P_0V_0 + \frac{m < v_0 >^2}{2} \tag{1.22}$$

$$= U_1 + P_1V_1 + \frac{m < v_1 >^2}{2} \tag{1.23}$$

where a subscript of zero corresponds to the initial state in the reservoir, and a subscript of one to the final state in the molecular beam. As the enthalpy, H, can be written as $U + PV$, and assuming that any flow within the gas reservoir can be neglected, i.e. $< v_0 > \approx 0$, the two expressions for $< E >$ can be rearranged to give

$$\langle v_1 \rangle = \left(\frac{2\,(H_0 - H_1)}{m} \right)^{\frac{1}{2}} \tag{1.24}$$

This is a general equation for the final velocity of the molecular beam, but by making the assumption that the sample is an ideal gas, an expression for the final velocity

can be obtained which does not require the change of enthalpy to be found.

The isobaric molar heat capacity, C_P, is defined as

$$C_p = \left(\frac{\partial H}{\partial T}\right)_P \tag{1.25}$$

Assuming that C_p is independent of temperature, it follows that

$$H_0 - H_1 = C_p\left(T_0 - T_1\right) \tag{1.26}$$

Substituting this expression into equation 1.24 gives

$$\langle v_1 \rangle = \left(\frac{2C_p\left(T_0 - T_1\right)}{m}\right)^{\frac{1}{2}} \tag{1.27}$$

The approximations about C_p are questionable, but this can be alleviated to some degree by noting that $C_p = C_v + R$, where C_v is the molar heat capacity at constant volume, and R is the gas constant. This can be rewritten in the form

$$C_p = \frac{\gamma}{\gamma - 1}R \tag{1.28}$$

where $\gamma = \frac{C_p}{C_v}$. The variations in the two heat capacities cancel each other out to some extent, making this a better definition of heat capacity in this context. Further assuming the final temperature of the beam is negligible, it follows from equations 1.27 and 1.28 that

$$\langle v_1 \rangle = \left(\frac{2RT_0\gamma}{m\left(\gamma - 1\right)}\right)^{\frac{1}{2}} \tag{1.29}$$

Christen *et al.* argue that there exist dependable equations of state to allow the molar enthalpies to be computed, allowing the general expression given by equation 1.24 to be used to calculate the terminal velocity. In this work, we only require an approximate knowledge of the terminal velocity of the molecular beam, so use the expression given in equation 1.29, which is more readily calculated.

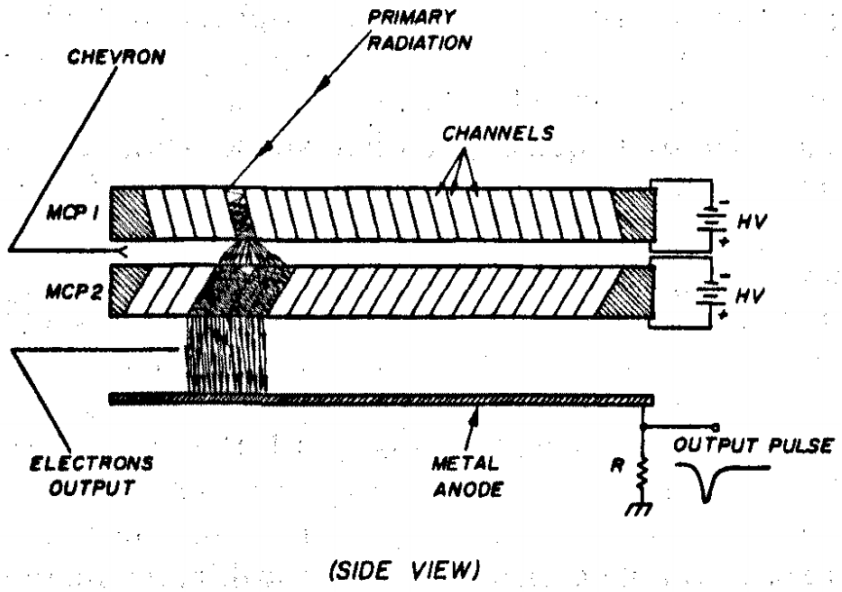


Figure 1.4 Schematic of a dual chevron-mounted microchannel plate assembly, coupled to a metal anode. Radiation enters one of the channels from the top, resulting in a cascade of electrons through the two MCPs. The electron cascade is then detected by a metal anode (or excites a scintillator, as is the case in our experiments). Reproduced from [75], with the permission of Elsevier under license 4917570749610.

After ions are produced in an experiment, a detector is required so that the data can be recorded, stored and subsequently analysed. Detectors used routinely in ion imaging will now be discussed.

1.4.3 Detectors

Any detector used in ion imaging is required to convert the ions produced in the experiment, which have been accelerated towards the detector by the ion optics, into a measurable signal. The vast majority of detectors begin by amplifying the signal using microchannel plates (MCPs). A schematic of an MCP is shown in figure 1.4. An MCP consists of a number of microchannels, typically made of resistively-coated glass, which have been fused together. When the wall of one of these microchannels is struck by an incident ion, a number of electrons are emitted. These are accelerated down the channel, striking the walls and emitting further electrons. These electrons can go on to release further electrons, leading to an electron cascade being emitted

from the other side of the MCP. To increase the gain, two or more MCPs can be stacked in a chevron arrangement; a typical dual chevron-mounted MCP assembly, such as that used in the experiments carried out as part of this thesis, has a gain of approximately 10^6 to 10^7. The open-area ratio of an MCP is defined as the percentage of the active area of the MCP which consists of the open ends of the microchannels, is typically of the order of 50 %, and this is most likely the main limiting factor of the detection efficiency in our experiment. Further details on MCPs can be found from multiple sources; see [75] and [76] and references therein, for example.

Now an electron cascade has been emitted from the MCPs, some way of detecting these electrons is required. There are two classes of detectors that can be used for this purpose: an anode, or a scintillator. Multiple anodes have been used over the years (see [77–83], for example), but are not discussed further in this thesis; whilst it is possible to record multiple ion hits simultaneously using anodes, it is much easier to use a scintillator in this case. Scintillators are substances which, when bombarded with charged particles of sufficiently high energy, emit photons which can then be imaged using a suitable camera. Many materials exhibit this property, but for use in ion imaging, there are a number of desirable properties. The scintillator must have a sufficiently fast decay time such that the photon flux reaches zero by the time ions of the next mass-to-charge ratio arrive. Ideally, it should decay on a timescale faster than that of the experiment, to give a clear indication of the arrival time of the ions, and allow subsequent ion hits in the same location to be clearly seen. Also, the scintillator must have sufficient photon output such that the signal can be detected. The scintillator must be stable enough for it to be used repeatedly over a long period of time, and must not flake off from the detector, which could short circuit the MCPs. Finally, the scintillator must emit photons of a wavelength compatible with the sensor used to image them.

The most commonly used scintillators in the field are P47 (Y_2SiO_5:Ce) and

P43 (Gd_2O_2S:Tb) phosphors. These have decay lifetimes of 70 ns and > 1 ms, respectively.[84] It would be beneficial to use a scintillator with a faster time resolution than this, such that the scintillator response time is not the limiting factor in the time resolution of an experiment, but the brightness of the scintillator must not suffer as a result of the faster response. Winter *et al.* have demonstrated a set of scintillators which fits these requirements,[84] a series of Exalite laser dyes having both a shorter decay lifetime (~ 4 ns) than P47, and emitting a larger number of photons. This offers a significant improvement over the existing scintillators in common use.

It is also possible to detect ions directly using a scintillator and single-photon avalanche photodiode (SPAD), removing the requirement for MCPs. Wilman *et al.* demonstrated this technique using a LYSO ($Lu_1.8Y_0.2SiO_5$(Ce)) scintillator coupled to a Hamamatsu multi-pixel photon counting sensor.[85] This technology is still in its infancy, but promises to offer some very desirable properties. Unlike with MCPs, a scintillator can operate outside an ultra-high vacuum, expanding the range of experiments that can be carried out. The detector will be more robust and, in conjunction with the use of ultra-fast phosphors, may allow for experiments to be carried out at a higher time resolution than achieved using a conventional detector.

If the detector converts the ion signal into an electrical signal, this can be read into a computer, digitised, and stored for further analysis, but if the signal is converted into a photon signal a camera is required to record the data. We now turn our attention to the different cameras available for use in recording ion images.

Cameras

There are two main types of sensor used in imaging: charge-coupled device (CCD) sensors, and complementary metal-oxide-semiconductor (CMOS) sensors. These sensors are effectively identical to those found in readily-available commercial cameras, although specialised cameras may have modified functionality. A discussion of the differences between the two sensor types is beyond the scope of this thesis,

but both have a photosensitive region which generates a charge, which can then be detected and saved to memory.

The most commonly used cameras in ion imaging are intensified charge-coupled device (CCD) cameras. An intensifier consists of a photocathode, which converts the incoming light into an electrical signal, followed by an MCP and scintillator assembly. In an ion imaging experiment, the shutter of the camera is opened over a relatively wide period with respect to the timescale of the experiment, and the intensifier is then pulsed on at the arrival time of the ion of interest. An image can then be recorded for each ion appearing in the mass spectrum in a series of separate experiments.

Whilst it is possible to record ion images for all ions in this fashion, the process quickly becomes incredibly time-consuming as the molecular complexity increases. This was the key motivation for the development of multi-mass imaging sensors, such as the Pixel Imaging Mass Spectrometry (PImMS) sensor,[86–88] and Timepix.[89–91] For use in ion imaging, both sensors can run in a mode in which the arrival time t of ions at the detector is measured, along with the x and y co-ordinates of the activated pixel. Recording only x, y and t co-ordinates significantly reduces the amount of data that needs to be recorded when compared to recording complete images; usually, only a small fraction of the detector detects signal in a given experimental cycle. The increased data efficiency then allows the sensor to operate at a faster rate. Both sensors are able to detect multiple ion hits in the same location within a single acquisition cycle, although the mechanism by which this is achieved is slightly different in each case. The PImMS sensor has four memory registers per pixel, and thus can detect four ion hits to the same pixel in every acquisition cycle. The data is then read out between acquisition cycles. Timepix 3, the third generation of the Timepix family of sensors, continuously reads out from all pixels, but has a dead-time of 475 ns per pixel.

The sensor used in the experiments carried out in this thesis is the microlensed

PImMS 2 sensor (uPIMmS 2). The architecture required in each pixel of a PImMS sensor reduces the photosensitive region of each pixel relative to a conventional sensor, reducing the light-collecting capabilities of the sensor. To counteract this loss in active area, microlenses are placed above the sensor, to focus light from a wider area of the pixel onto the photosensitive region of the sensor. This reduces the potentials required across the MCPs and scintillator, increasing the lifetime of these elements and helping to reduce the chance of accidental damage. The sensor itself consists of an array of 324x324 pixels.

1.4.4 Differences between photoionisation and electron ionisation

The vast majority of VMI experiments do not use electron sources to ionise the molecule under study, rather using laser light to ionise the molecule, which begs the question of how the two ionisation methods differ, both generally and in the context of this experiment. Whilst the general principles of the two types of experiment are very similar, there are some fairly major differences in both the experimental design and the chemistry occurring.

Starting with the physical differences between the experiments, the most obvious difference is the presence of an electron beam rather than a laser beam. Like a laser, the electron beam must be focussed and steered into the interaction region. Rather than using optics, this must be carried out using electric fields, and the size of the focal region is limited by space-charge repulsion between the electrons. This requirement adds extra complication to the experiment; electrons are very susceptible to deflection by any stray electric fields, so care must be taken to keep these to an absolute minimum. Of course, the ion optics, typically held at a couple of kilovolts, must be grounded when using an electron beam to ionise the molecule, whereas with a laser the potentials can be held at the desired voltage throughout the acquisition cycle. This adds an extra complication to the electron ionisation

experiment, requiring the appropriate timing at which to pulse the ion optics to be found, and potentially introducing a small uncertainty in the precise potentials used to accelerate the ions produced. Another point to consider is the extra length of time the ionised molecule can evolve for before being extracted by the ion optics in the electron ionisation experiment.

In terms of the chemistry, there are fewer restrictions imposed in the case of electron ionisation compared with photoionisation, making it significantly more difficult to analyse the results of VMI experiments using electrons as the ionisation source. In an electron scattering process leading to ionisation, a single electron travels towards a molecule with known energy, and one or more electrons is ejected from the molecule. The precise mechanism by which the ionisation process occurs is largely energy-dependent, but the scattering event leads to the incident electron and the scattered electron(s) taking some proportion of the kinetic energy away. Measuring the energy of these electrons poses a significant experimental challenge, which we have yet to overcome. Thus, whilst we know the initial energy of the incident electron, we do not know how much of the energy is transferred to the molecule. In the case of a photoionisation experiment, if a photon is absorbed by a molecule, the entirety of the photon energy is transferred. This makes it significantly easier to gain a complete understanding of the energy division between, say, internal energy and kinetic energy of the ionisation products.

To further complicate matters, there are very few selection rules in the case of electron ionisation. This means that there are very few limitations on the final state in which the molecule can find itself in. Contrast this to photoionisation, in which the transition must occur with a laser polarisation defined by the electric dipole moment operator, to a final state with appropriate symmetry. The photoionisation

selection rules are given by[92]

$$\Gamma_{\text{rve}}(ion) \bigotimes \Gamma_{\text{rve}}(neutral) \supset \Gamma^{*} \text{ for } l \text{ even} \tag{1.30}$$

$$\Gamma_{\text{rve}}(ion) \bigotimes \Gamma_{\text{rve}}(neutral) \supset \Gamma^{(s)} \text{ for } l \text{ odd} \tag{1.31}$$

where $\Gamma_{\text{rve}}(ion/neutral)$ is the irreducible representation of the rovibronic wavefunction of the ion and neutral, with an rve subscript representing the rotational, vibrational and electronic state described, $\Gamma^{(s)}$ is the totally symmetric representation of the molecular symmetry group, Γ^{*} is the antisymmetric representation of the molecular symmetry group, l is the orbital angular momentum quantum number of the orbital the electron is ejected from, and $\bigotimes$ and $\supset$ represent the direct product and superset operators, respectively. Further, the total angular momentum must be conserved, i.e.

$$\Delta J = J^{+} - J = l + \frac{3}{2}, l + \frac{1}{2}, l - \frac{1}{2}, l - \frac{3}{2} \tag{1.32}$$

where J and J^{+} are the total angular momenta of the neutral and ion, respectively. Note that these selection rules can also be extended to an n-photon transition, which is also described in [92].

Despite the fact that there is a greater pool of final states available in the case of electron ionisation, the work carried out as part of photoionisation experiments is still very much relevant to our work. For example, potential energy surfaces generated for use in photoionisation studies are equally valid when considering electron ionisation, allowing us to propose potential dissociation pathways. It is also useful to consider the similarities and differences in the results obtained from the two ionisation methods.

A possible avenue that could be explored is the use of a laser to excite a molecule into some excited state, a 'pump' step, followed by electron scattering to ionise, or 'probe', the resulting state. This method would allow us to study the effect of the initial state of the molecule on the products of electron ionisation. In any case, it

is evident that there is much to be gained from both electron and photoionisation experiments.

1.5 Summary

In this chapter, the concepts upon which the rest of this thesis will be based have been introduced. We will now introduce the experimental and theoretical methods used to acquire the results presented in this thesis.

2

Methods



n this chapter, we will describe the theoretical and experimental methods used as part of this thesis. We will first introduce the binary-encounter-Bethe (BEB) model, a theoretical model which can be used to calculate the total ionisation cross-sections of molecules based on orbital binding energies and kinetic energies obtained through electronic structure calculations. Following that, we will introduce the elctron-molecule crossed beam experiment, which is used to obtain both the scattering distributions and partial ionisation cross-sections of all ions produced following electron scattering of a molecule of interest.

2.1 Theoretical: The binary-encounter-Bethe (BEB) model

The binary-encounter-Bethe (BEB) model was developed by Kim, Rudd and Hwang,[49,50] and is a simplified version of the binary-encounter-dipole (BED) model

developed by the same authors. The models combine modified Mott theory,[93,94] used to describe incident electrons of low energy, with Bethe cross-section theory[95], used to describe high-energy incident electrons, with a switching function controlling the relative weighting of the two models. The BEB model is further simplified by using a calculated value for the differential dipole oscillator strength, as discussed in [49]. The full derivation of both the BED and BEB models can be found in [49]; the BEB cross section is given by

$$\sigma_{\mathrm{BEB}} = \sum_{\text{orbital } i}^{n} \left(\frac{S_i}{t_i + (u_i + 1)} \right) \left[\frac{\ln t_i}{2} \left(1 - \frac{1}{t_i^2} \right) + \left(1 - \frac{1}{t_i} - \frac{\ln t_i}{t_i + 1} \right) \right] \tag{2.1}$$

with

$$t_i = \frac{T}{B_i} \quad u_i = \frac{U_i}{B_i} \quad S_i = 4\pi a_0^2 N_i \left(\frac{R_\infty}{B_i} \right)^2 \tag{2.2}$$

where T is the kinetic energy of the incident electron, B_i and U_i are the binding energy and average kinetic energy of the orbital from which the ionised electron is removed, N_i is the orbital occupation number of said orbital, a_0 is the Bohr radius, and R_∞ is the Rydberg constant. There is also a requirement that T must be greater than B_i for a given molecular orbital in order for its contribution to the cross-section to be non-zero. The benefits of this model are that the cross-section can be calculated based on just two calculated parameters, B_i and U_i, for each molecular orbital, which can be calculated using computational software.

A number of other theoretical methods for determining total ionisation cross-sections have also been developed, a number of which are discussed in appendix A.

We have previously used the BEB model to calculate theoretical total ionisation cross-sections for a large number of molecules,[96,97] and others have shown that the cross-sections obtained using this method reproduce experimentally determined data with reasonable accuracy for a wide range of molecules,[50,98–100] i.e. the maximum cross-section typically falls within around 10 % of the experimentally determined

values,[99,100] which is comparable to the variation between different experiments, and the cross-sections calculated at each incident electron energy match the experimental data to a similar degree. It should also be noted that the model typically overestimates the cross-sections for fluorocarbons by around 40%.[99]

2.1.1 Calculation of parameters required for the model

Bull *et al.* performed a comprehensive benchmarking study on the calculation of the binding energy and average orbital kinetic energy for each orbital.[99] As these are the only inputs to the model, the result is sensitive to the quality of the input. Of course, there are drawbacks in terms of computational time with higher level computational methods, so a balance must be struck between the accuracy of the parameters and the time taken to complete the calculation. In the optimised method, the molecular geometry is first optimised using either restricted or unrestricted Hartree-Fock theories,[101–104] dependent on whether the molecule has unpaired electrons or not. The optimised geometries are used as the starting point to calculate the required parameters. This step uses partial third-order (P3) electron propagator theory[105] to account for electron correlation in the molecule, which is not completely accounted for by the Hartree-Fock method. The ratio of the binding energy obtained using electron propagator theory and Hartree-Fock theory is also used to scale the average kinetic energy values obtained in the calculation, to ensure the virial theorem is satisfied. All calculations are carried out using the aug-cc-pVTZ set of basis functions.[106–108]

2.1.2 Heavy atom corrections

This model runs into difficulties with molecules containing 'heavy' atoms, here defined as having a principal quantum number $n \geq 3$, significantly underestimating the ionisation cross-section when compared with experimental results. The presence of nodes in the radial wavefunction of the valence orbitals lead to a rel-

atively high average kinetic energy for the orbitals, as the kinetic energy is much higher in regions near the core of the orbital. However, the electron is much more likely to be ionised when near the outer edge of the orbital, where its kinetic energy will be significantly lower. Thus, some correction is required to account for this discrepancy.

A couple of corrections have been proposed in the literature. The first, introduced by Hwang *et al.*,[50] attempts to correct the orbital kinetic energy obtained by dividing the average kinetic energy of the molecular orbital by the principal quantum number of the dominant atomic orbital contributing to the molecular orbital, provided the principal quantum number is three or higher. The precise threshold at which this correction should be applied is not very well defined at present, and our efforts to determine what this level should be did not lead to satisfactory results.

The second correction, developed by Huo and Kim,[109] uses relativistic effective core potentials to replace the core electrons, removing the need to calculate their wavefunctions explicitly. This means that the calculated wavefunctions of the valence electrons are no longer required to be orthogonal to the core orbital wavefunctions in the calculation, resulting in there being no radial nodes in the valence orbital wavefunctions, and hence significantly lower average orbital kinetic energies for the valence electrons. The parameters for the excluded core electrons can then be determined by a second 'all electron' calculation.

We believe that further work is required before the BEB model can be reliably applied to molecules containing heavy atoms. Once a greater body of experimental data is available, we plan to carry out a more comprehensive evaluation of both correction methods.

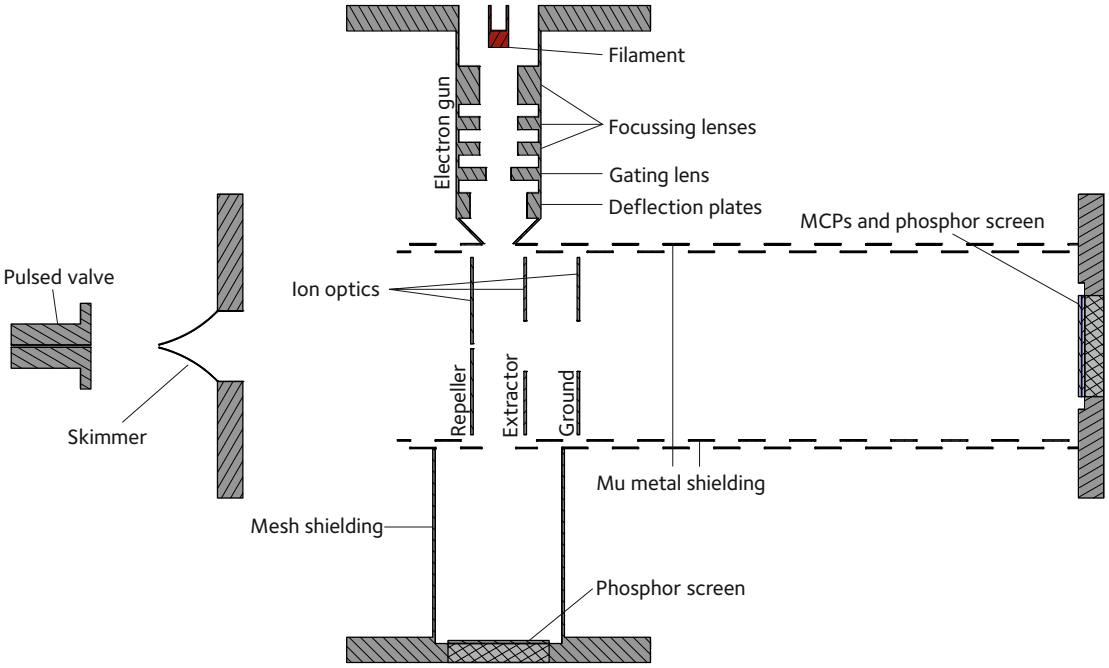


Figure 2.1 The experimental set-up of the electron-molecule crossed beam experiment.

2.2 Experimental: The electron-molecule crossed beam experiment

The experimental results recorded as part of this work were obtained using an electron-molecule crossed beam experiment. In this scattering experiment, a molecular beam is prepared via a supersonic expansion, before being intersected by an electron beam propagating in a direction perpendicular to the molecular beam. From the resulting scattering distribution, any ions produced are extracted and detected. Here, we first give a detailed description of the experimental apparatus. We then outline the experiments needed to characterise the experiment and ensure proper operation, before briefly discussing the differences with photoionisation experiments.

2.2.1 Experimental set-up

Figure 2.1 shows the experimental set-up for this experiment. The experiment consists of two differentially pumped vacuum chambers, which will be referred to as

the source and scattering chamber. The source chamber operates at a base pressure of $\sim 2 \times 10^{-7}$ mbar, which is achieved by using a turbomolecular pump (Pfeiffer Vacuum HiPace 700) backed by a rotary vane pump, and the scattering chamber operates at a base pressure of $\sim 3 \times 10^{-7}$ mbar, which is achieved by using a turbomolecular pump (Pfeiffer Vacuum HiPace 1800) backed by a rotary vane pump. A gas reservoir (not shown) feeds the pulsed solenoid valve, and can be evacuated by a further rotary vane pump. The electron source (PSP Vacuum Technology ELS 100) consists of a lanthanum hexaboride (LaB_6) filament, along with a number of electrostatic lenses used to focus and steer the beam, as described in section 2.2.2. The electron energy produced by the electron source can be varied in 1 eV steps, and has a full width at half maximum (FWHM) of ~ 0.25 eV.[110] The velocity-mapping ion optics consist of three electrostatic lenses: a repeller plate, an extractor plate, and a ground plate, in the same configuration developed by Eppink and Parker for velocity-map imaging experiments. The electron source, interaction region and flight tube are surrounded by grounded mu-metal, which acts to exclude stray magnetic fields from within its bounds due to its high magnetic susceptibility.[111,112] A P47 phosphor screen is also installed in the flange opposite to the electron source, which can be used for calibration of the electron source.

The first step of an experimental cycle is the preparation of a molecular beam. In the case of gaseous samples, the gas is prepared in a gas reservoir either neat or as a mix with helium, which acts as a carrier gas. We typically prepare gas samples at a stagnation pressure of approximately 2 bar. In the case of liquid samples, the liquid is placed in a bubbler and undergoes a series of freeze-pump-thaw cycles to remove atmospheric gases. Helium is then bubbled through the liquid sample, which results in the helium being seeded with the sample. Precise details of stagnation pressures will be given in the results section for each molecule. Once the gas is prepared, it undergoes a supersonic expansion, described in section 1.4.2, through a pulsed solenoid valve (Hannifin-Parker Series 9 general valve) into the vacuum chamber.

The molecular beam passes through a skimmer, which acts to deflect the less efficiently cooled molecules near the edge of the expansion, which could fall below the local speed of sound and cause turbulence, away from the beam, resulting in a collimated molecular beam with a narrow velocity distribution. The molecular beam is then intersected in the interaction region by an electron beam generated via thermionic emission from the LaB_6 filament, propagating in a direction perpendicular to the molecular beam. Particles from the two beams scatter, and result in a number of ions being produced.

After the electron beam has passed through the experiment, the ion optics are rapidly pulsed to VMI conditions using a pair of fast transistor switches (Behlke model HTS-101), with a factory-specified rise time of 8 ns. This accelerates the ions down the flight tube towards the detector. As noted previously, the flight time of the ions is dependent on their mass-to-charge ratio, and the two-dimensional projection of the three-dimensional scattering distributions for ions of each mass-to-charge ratio strike the detector in turn. The detector, consisting of a dual chevron-mounted MCP and P47 scintillator, converts the ion signal into a photon signal which is then imaged by a uPImMS 2 sensor and the data recorded on a desktop computer, completing the experimental cycle. A photomultiplier tube also detects light from the phosphor, and is connected to an oscilloscope (Tektronics 3044B), which can be used both when setting up the experiment and to record the signal intensity as a function of arrival time with a better time resolution than the PImMS camera. The various components of the experiment are triggered by a pulse generator (BNC model 575), as described in section 2.2.2, and these pulses can be mirrored on the oscilloscope to aid in experimental set-up if required.

When carrying out experiments, we first record an image under conditions where the electron and molecular beam scatter off each other, then we record a background image where the electron beam passes through the interaction region before the molecular beam. Sets of 50,000 acquisition cycles, or 'frames', are acquired at once,

and multiple sets of 50,000 frames are recorded to improve the signal-to-noise ratio of the data. For each molecule discussed in this thesis, the number of frames recorded at each electron energy will be stated in the appropriate section. The repetition rate of the experiment was set to 20 Hz for all measurements carried out as part of this work.

Now that the experimental set-up of the crossed electron-molecular beam experiment has been established, we must characterise various experimental parameters, to ensure that the experiment is operating correctly, and that the various adjustable parameters are set at appropriate levels.

2.2.2 Characterisation

In this section, we work systematically through the various aspects of the experiment, highlighting all characterisation steps that are required to successfully operate the experiment. A short justification as to why the characterisation is required will be provided in each case, and the frequency with which the characterisation must be repeated will also be indicated.

Molecular beam

The molecular beam is the the first component of the experiment that must be characterised. The molecular beam should be a collimated beam with a narrow spatial width, should be internally cold, and have a length similar to that of the current pulse used to open the pulsed valve. Optimisation of the molecular beam is carried out by observing the integrated signal from the phosphor screen, measured by a PMT and displayed on an oscilloscope. Signal is observed when the electron beam and molecular beam overlap. The electron beam is much shorter (by around three orders of magnitude) than the molecular beam pulse, meaning that we only ionise a small part of the molecular beam. By scanning the delay between the electron beam and molecular beam, the temporal profile of the molecular beam can

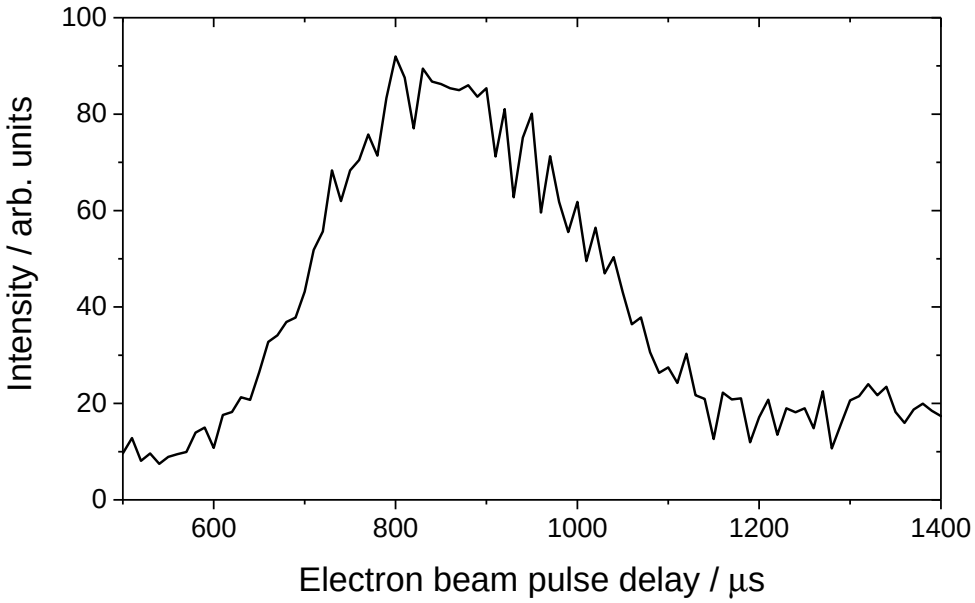


Figure 2.2 Temporal profile of the molecular beam. The profile was obtained by varying the delay of the electron beam with respect to the molecular beam, and recording the signal from the phosphor screen using a PMT at each delay stage. The total signal of the parent ion (in this case O_2^+) was then integrated and plotted against the delay to obtain the molecular beam temporal profile.

be probed. A typical molecular beam profile can be seen in figure 2.2. We can see that the beam has a well-defined temporal distribution, with a beam length comparable to the value of 200 μs chosen for the experiment.

It is important that the molecular beam is running under conditions where it undergoes a supersonic expansion, leading to efficient cooling of the sample molecule and a well-defined beam. If the amount of gas coming through the valve is too great, the molecular beam begins to exhibit an effusive tail; excess gas which does not pass through the skimmer is not extracted from the source chamber at a fast enough rate, and the skimmer then acts as an effusive source. The higher concentration of gas in the source chamber also reduces the mean free path of the molecules, meaning that the molecules in the molecular beam are less likely to pass through the source chamber without collision, further compounding the problem. The beam profile in figure 2.2 shows no evidence of an effusive tail, which tells us we have a supersonic molecular beam, with no effusive component.

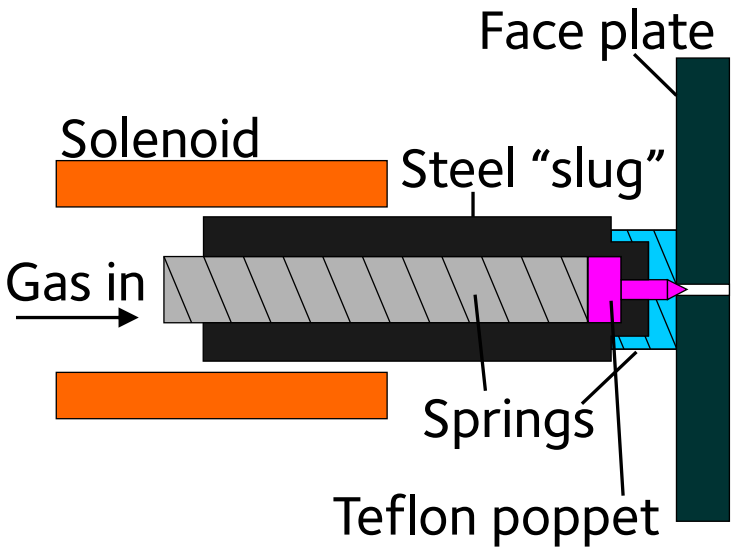


Figure 2.3 Schematic of the key components of the solenoid valve used in our experiment. The solenoid (orange) is an electromagnet, which becomes magnetised when current is passed through it, and pulls back the steel “slug” (black). This allows gas to flow through the orifice in the face plate. When the current is turned off, the spring (grey) pushes the poppet (pink) back against the face plate, sealing the orifice.

There are a few parameters that can be changed to adjust the molecular beam. The first is the molecular beam pulse length itself. This should be minimised to reduce the total amount of gas entering the experiment, and to reduce the consumption of sample gas, whilst still maintaining the integrity of the molecular beam; if the pulse is too fast, the solenoid valve does not open properly, leading to degradation of the molecular beam. We have found the optimal molecular beam length to be around 200 μs, and this value is used for all experiments carried out in this work.

The remaining adjustments concern the pulsed valve itself, so it is worth understanding the basic principle by which a solenoid valve operates. Figure 2.3 shows the main components of the valve. Initially, the spring coloured grey holds a Teflon poppet against the orifice, sealing the valve. When a current is applied across the solenoid, it pulls back on the steel “slug” in which the poppet is housed, allowing gas to flow through the orifice. When the current applied across the solenoid is removed, the grey spring acts to return the slug and poppet to their initial position, sealing the orifice. A second spring (shown in blue) reduces the impact of the slug

and poppet with the face plate.

By changing the current applied through the solenoid, the force applied to open the valve can be adjusted. The current should be high enough that the valve opens properly, but not so high that when the voltage is removed, the restoring force is large enough to cause the valve to bounce open after closing, which would cause further beam pulses. If the voltage is too high, the wear on the poppet is also increased, meaning that it must be replaced much more frequently.

Finally, we can change how tightly the face plate is screwed on to the pulsed valve. It is important that this is correct, as if it is too tight, the valve cannot open properly, and if it is too loose then the springs within the valve are unable to close the orifice, and the valve will leak. In many experiments using solenoid valves, the valve tension must be optimised before placing the valve in the vacuum chamber, by checking for deflection of a piece of tissue placed in front of the valve orifice when a pulse of gas is emitted from the valve. In our experiment, we can adjust the valve tension by rotating a tube connected to the body of the pulsed valve whilst the valve is installed on the vacuum chamber. This allows us to make minor adjustments to this parameter to ensure optimal conditions for each sample gas and backing pressure.

The molecular beam pulse is checked and optimised at the start of each experiment.

Electron beam

The requirements of the electron beam are that it is well focussed in the interaction region, has a narrow energy distribution, has a known current, and overlaps with the molecular beam both spatially and temporally. Characterisation experiments are required in each of these cases. The schematic of the electron source is shown in figure 2.4 for reference.

The simplest to characterise is the overlap of the molecular and electron beams.

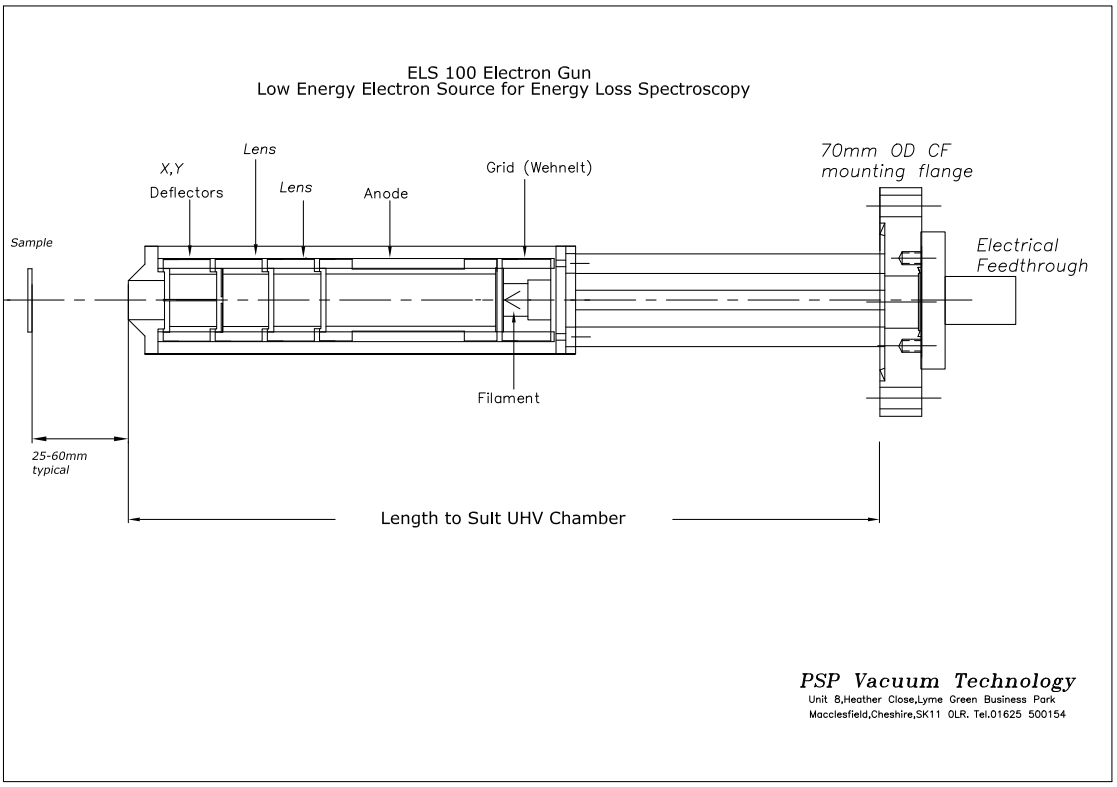


Figure 2.4 Schematic of the ELS100 electron source. Reproduced with permission from [113].

As the direction of the molecular beam is defined by the geometry of the experiment, the electron beam must be steered by electrostatic optics to make the two beams overlap. This is done by using the x deflection and y deflection dials on the electron source power supply. The two deflection parameters adjust potentials applied to two pairs of plates, with each pair of plates located either side of the centre of the electron source along the relevant axis. Within each pair, the two plates have equal but opposite potentials applied to them, which deflects the electron beam. In our experiments, we set the x deflection, which deflects the beam along the molecular beam axis, such that both plates are grounded. This means that the electron and molecular beams should interact at approximately the centre of the ion

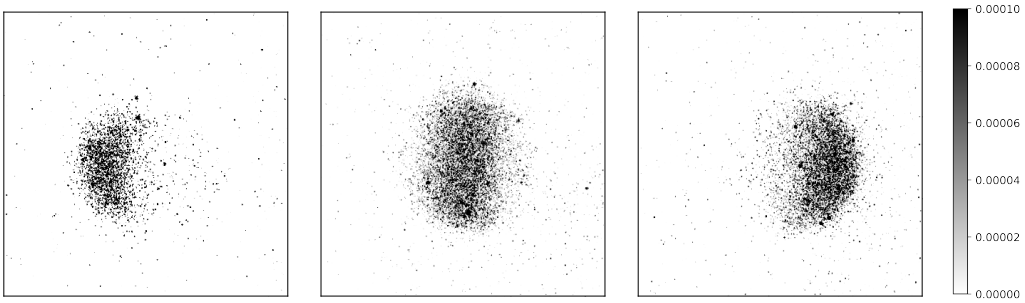


Figure 2.5 Images recorded using spatial-map imaging for three different y deflection values, showing the electron beam move through the molecular beam. The image measures 400 px by 400 px.

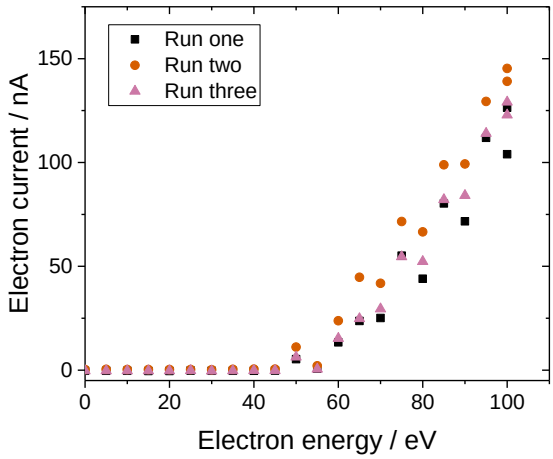


Figure 2.6 Variation of electron current with electron energy for the electron source. The results from three repeats are shown. The data was recorded by first sweeping down in steps of 10 V, then sweeping back up in steps of 10 eV, offset by 5 eV from the downward sweep.

optics. We then sweep the electron beam through the molecular beam by adjusting the y deflection, which deflects the electron beam perpendicular to the molecular beam axis, and find the y deflection which gives us the maximum signal. Figure 2.5 shows a series of images recorded using a CCD camera under spatial-map imaging conditions at various y deflections. The y deflection is checked and adjusted if necessary at the start of each experiment.

It is useful to know the current of the electron beam at each electron energy used in our experiments. To measure this, a copper plate coated in colloidal graphite was installed in a detector opposite to the electron source. A current amplifier (FEMTO

DLPCA-200) was then used to measure the electron current at a range of different electron energies. Unfortunately, the electron source had to be run with a continuous beam rather than the pulsed beam used in normal operation for these measurements in order to obtain a measurable signal, but the beam current during the electron beam pulses should be similar to that during continuous operation. Figure 2.6 shows the results of this characterisation experiment. We see that the electron current falls off rapidly with decreasing electron energy. As the total ionisation cross-section of most molecules also falls off below around 70 eV, it is relatively challenging to record high-quality ion images at lower electron energies.

The ion lenses which dictate the focus of the electron beam must be adjusted to ensure the electron beam is properly focussed in the interaction region. The electron beam focus is a function of three ion lenses: the Wehnelt, the anode, and the focus. The Wehnelt limits the area from which electrons are emitted from the surface of the lanthanum hexaboride crystal, and confines the emitted electrons to pass through a hole in the lens. The focus and anode then act to either focus or collimate the beam. As we cannot easily measure the focus of the beam in the interaction region, we define our focus by visually inspecting the beam shape produced by the electron beam, run in continuous mode, incident on the phosphor screen used previously. The lens potentials are adjusted until the beam spot is at its brightest, is round in shape, and is of a similar size to the exit orifice of the electron source. This means that as many electrons are successfully being emitted as possible, and the beam is at worst collimated and at best focused in the vicinity of the interaction region.

To pulse the electron beam, we apply a potential to an electrostatic lens within the electron source, specifically the lens directly before the x and y deflectors (see figure 2.4). To pulse the electron beam, the lens is initially held at a potential 40 V above the kinetic energy of the electrons. The electrons are repelled by this lens and, as the potential barrier exceeds the electron energy, the electrons cannot exit the electron source. The lens is then pulsed to ground potential, which allows the

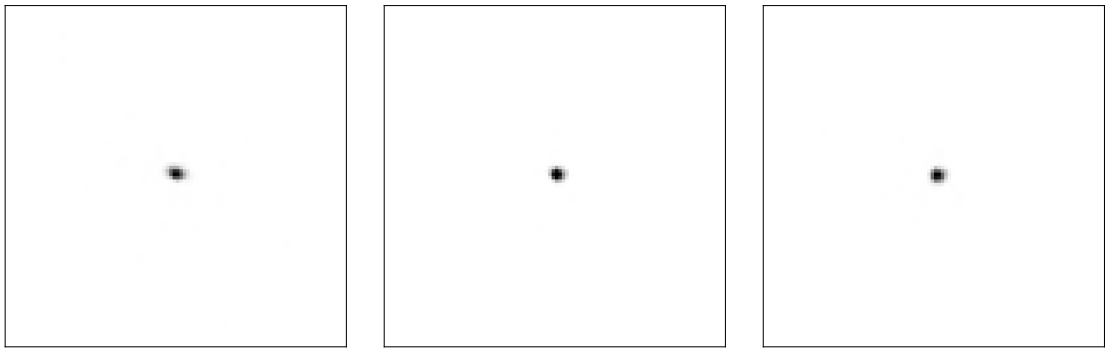


Figure 2.7 Optimisation of the velocity-map imaging focus using the CO_2^+ parent ion. Data are recorded for around 1,000 acquisition cycles at a range of extractor potentials. The central figure shows the VMI focus using the optimised extractor potential (in this case 1.615 kV), and the figures to the left and right show the VMI focus with the extractor potential 25 V below and above this value, respectively. The image measures 101 px by 101 px.

electrons to pass through, before being restored to the initial value after the desired electron beam pulse length.

It is important that the electron beam pulse length is of the appropriate length. There is a minimum length at which the electron pulse is stable, which can be found by studying the electron beam temporal profile, measured using a phosphor screen and PMT. In our experiments, we have found this minimum to be around 180 ns. The upper limit of the pulse length is determined by the time before which the ions produced at the start of the beam are no longer properly velocity-mapped, i.e. they have travelled too far from the interaction region. For the range of electron pulse lengths used in this thesis, 180 ns to 1 μs, we have found that there is little difference in the scattering distributions obtained. We typically adjust the electron beam pulse length to strike a balance between having a short pulse to reduce the spread in the creation time of the scattering products, whilst giving us sufficiently high signal-to-noise ratio that the data recorded is of a usable quality for analysis.

Ion optics

Once the electron beam has passed through the interaction region, the resulting ions are extracted and velocity-mapped onto the detector by the ion optics. The potentials on the ion optics must therefore be set to the appropriate potentials to achieve velocity-mapping conditions. To find these potentials, the potential on the repeller plate is fixed. The electron and molecular beams are overlapped so signal can be seen, and the extractor potential is then varied until the parent ion signal appears as a small spot on the detector. The parent ion appears as a small spot in velocity-map imaging because the loss of an electron during the ionisation process imparts almost no momentum to the parent. Thus, the parent ion image simply reflects the (narrow) transverse velocity distribution of the molecular beam. Figure 2.7 shows an example of the optimisation of the VMI focus.

Detector potentials

It is important that the potentials on the detector are set correctly in these experiments. If the potentials are too low no signal will be observed, but if the potentials are too high there is a real risk of damaging the detector. As noted previously, the detectors used in this experiment consist of two chevron-mounted MCPs and a P47 scintillator. We can apply potentials to the front and back of the MCP stack, and to the scintillator, and the higher the potential across a component, the brighter the signal. The potential across the MCPs and phosphor are adjusted until the size of the pixel clusters recorded with the camera are appropriate for centroiding (discussed in section 3.1) by striking a balance between the number of electrons being emitted from the back of the MCP, and the energy at which the electrons are accelerated towards the phosphor.

In most cases, the front of the MCPs would be grounded, as this means that the flight tube is a field-free region. In our experiment however, we observe a large background peak at short times with the front MCP grounded. Figure 2.8 shows

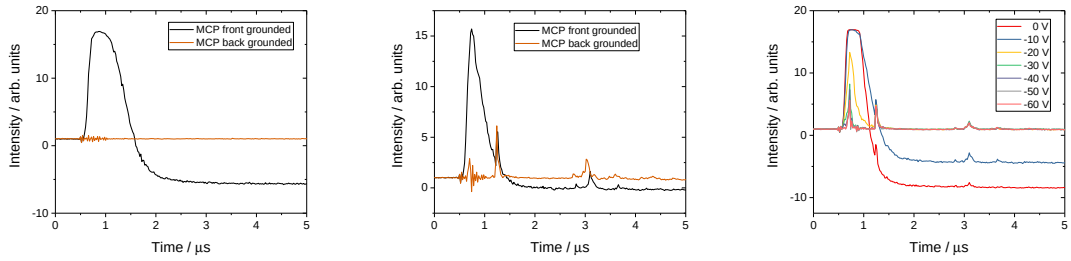


Figure 2.8 Characterisation experiment showing the need to negatively bias the front of the MCPs, using the background gas present in the experimental chamber (predominantly water). In all cases, the potential between the front and back of the MCP stack is maintained at 1.75 kV. (a) shows the mass spectrum recorded using a PMT to capture the total signal from the scintillator when the ion optics were turned off, (b) shows the mass spectrum recorded when the ion optics were turned on, and (c) shows the mass spectrum recorded with the ion optics on, but varying the potential applied to the front of the MCP stack.

the results of the diagnostic experiments we used to identify the source of this peak. The potential difference across the MCPs was maintained at 1.75 kV in all cases, to maintain the same MCP gain in all measurements. The molecular beam is turned off, so any signal is from background gas in the experimental chamber, which is predominantly water. Figure 2.8(a) shows, in the absence of ion optics, the difference between having either the front of the MCPs grounded, or held at a potential of -1.75 kV. We see that there is a large peak when the MCP front is grounded, with the signal level falling below zero following the peak. When the front of the MCP is instead held at the negative potential, we see no peak. Figure 2.8(b) shows the same experiment, but with the ion optics pulsed as in a typical experiment. We see very similar results to those seen in figure 2.8(a). The large peak observed with the front of the MCPs grounded is narrower when the ion optics are pulsed. Figure 2.8(c) shows the effect of varying the potential applied to the front of the MCPs, and we see that the large peak rapidly decreases in intensity with an increasing negative bias on the front of the MCPs. Given that the background peak disappears when even a small charge is applied to the front of the MCPs, and that the peak appears at

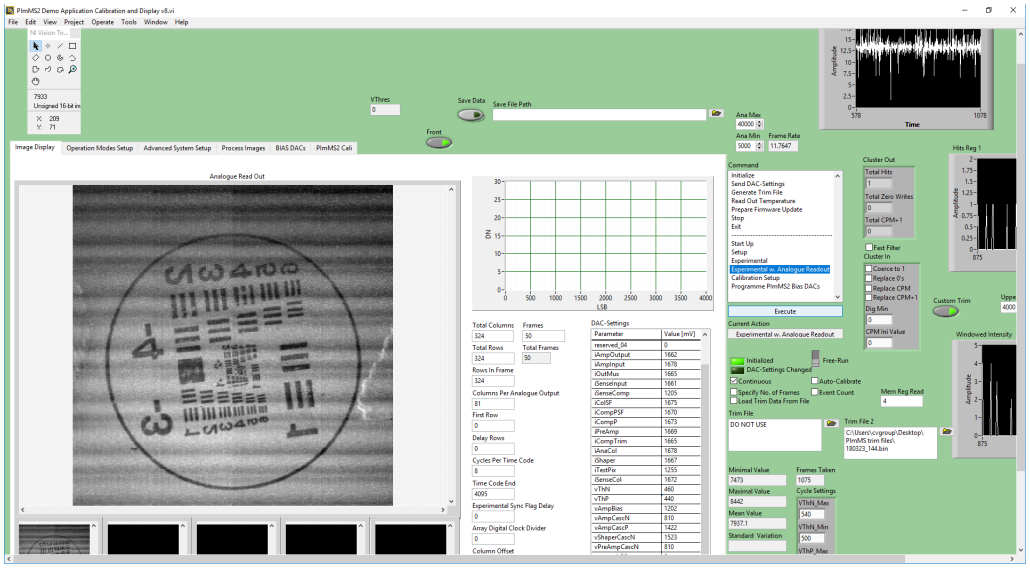


Figure 2.9 An example of the PImMS camera running with analogue readout, focussed using a 1951 USAF resolution test chart.

around t_0 in the time-of-flight spectrum (found from previous experiments where the peak was present, not shown), we conclude that the source of this peak is electrons. The exact source of the electrons is unknown, but one potential source could be from the scattering of the electron beam off molecules present in the experimental chamber. Whilst this signal is fairly diffuse, it is nonetheless an intense signal once integrated over the entire detector, leading to saturation of the PMT used to check the ion signal at even relatively low detector potentials. To help preserve both the PMT and detector, we therefore apply a small negative bias of -50 V, and adjust the other potentials accordingly; this does not affect the operation of the detector, as this is dictated by the potential difference between the components, rather than the absolute potentials. The effect of the small bias potential on the velocity-mapping is not significant.

Camera focussing

The camera must be focussed on the plane of the phosphor screen in order to detect the signal. As both the CCD and PImMS camera use typical camera lenses, this is carried out in exactly the same way as with any other manually-focussed camera.

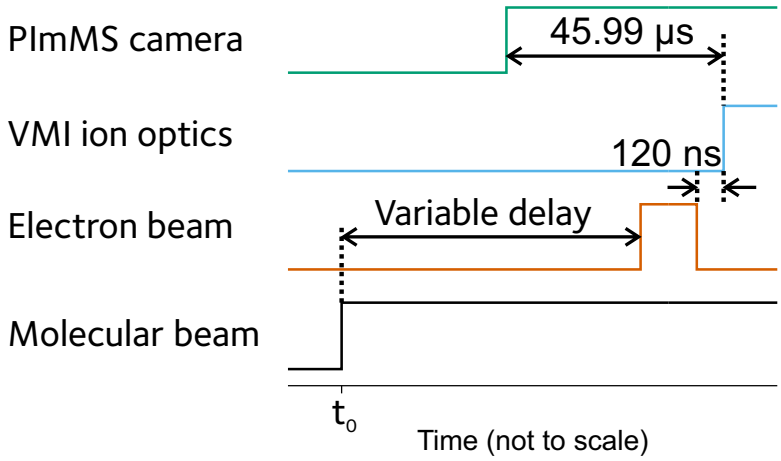


Figure 2.10 The pulse sequence for the electron-molecule crossed beam experiment when using the PImMS camera. Note that the time scale is non-linear and not to scale.

The focal point is dependent on the type of detector being used. If a fibre-coupled detector is being used, the camera can be focussed on the back of the phosphor feedthrough by using, for example, a 1951 USAF resolution test chart. Otherwise, the camera must be focussed on the back of the phosphor through a glass substrate, where the camera is focussed on a shadow cast on the phosphor. A typical focussing test image for the PImMS camera is shown in figure 2.9.

Pulse timings

Last, but by no means least, the timings at which the various parts of the experiment are triggered must be set. This is absolutely imperative to the successful running of this experiment and, if incorrectly set, will at best result in no data being acquired, and at worst cause damage to sensitive equipment on the experiment. The full series of pulses when using the PImMS camera is shown in figure 2.10, and is described below.

The pulse sent to the molecular beam source marks the start of our experimental cycle. The electron beam delay is set relative to the molecular beam pulse, using a characterisation method already discussed. By measuring a molecular beam profile, for example the one shown in figure 2.2, it is possible to find the appropriate delay

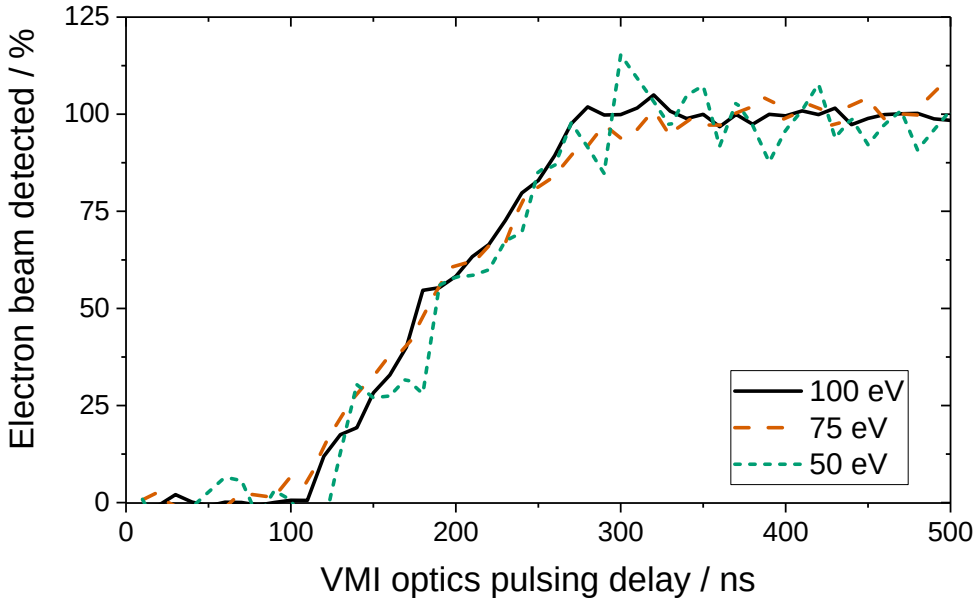


Figure 2.11 Results of an experiment to determine the appropriate delay between the electron beam pulse and VMI optics pulse. A PMT was used to measure the signal produced by the electron beam incident on a phosphor screen whilst varying the delay between the electron beam pulse and the VMI optics pulse. The PMT signal was then integrated and plotted against delay. A baseline subtraction was then applied, and the plot then scaled such that the plot reflected the percentage of the electron beam passing through the experiment. The process was carried out at three electron energies.

at which the electron beam should be triggered. The timing is chosen such that the electron beam triggers at the front edge of the peak, as this gives maximum signal, whilst ionising molecules which are likely to have been efficiently cooled; the faster molecules arriving at the start of the beam have typically undergone efficient cooling, with the vast majority of their internal energy being converted to translational energy. The timing for this pulse is dependent on the identity of the sample gas, but is typically of the order of 750 μs. When recording background images, the electron beam passes through the interaction region before the molecular beam, for which we typically use a delay on the order of 50 μs.

The ion optics are used to extract the ions created by the electron beam's passage but, as has been noted previously, it is important that the electron beam has passed through the interaction region before the potentials on the ion optics are ramped

from ground to their operating potentials. To ensure the timing for this pulse is correct, we use a PMT to measure the total photon flux from the phosphor screen opposite the electron beam source, varying the timing until the photon flux remains at a constant value. The results of this experiment are shown in figure 2.11, which shows that, at all electron energies, it takes a little under 300 ns for an electron beam of length 180 ns to clear the interaction region. In our experiments, we have set the ion optics to pulse 120 ns after the end of the electron beam pulse, i.e. with a 300 ns delay after the start of the electron beam pulse for a 180 ns beam.

Finally, the camera must be triggered. In the case of the CCD camera, the trigger is sent concurrently with the electron beam pulse. The precise timing of this pulse is not important, as this just serves to open the shutter, but only intensified signal can be recorded. The intensifier is triggered at the arrival time of the ion of interest, displaced by a few tens of nanoseconds to account for electronic delays. The precise delay can be found by observing the resulting ion image as the timing of the intensifier is swept across an ion arrival time. In the case of the PImMS camera, the trigger timing is again relatively unimportant, provided the ions arrive when the sensor is active. In our experiments, the PImMS sensor is triggered at -45.99 μs relative to the trigger sent to the ion optics.

2.3 Summary

In this chapter we have introduced both an experiment and a theoretical method that can be used to give significant understanding on the electron ionisation of a molecule. The experimental setup and characterisation of the crossed electron-molecule beam experiment has been discussed in detail. The velocity-map images recorded in this experiment need further processing before they can be used to draw any meaningful conclusions from the data, however. In the next chapter, a comprehensive discussion of the various techniques used to process the recorded ion images to extract useful data is given.

3

Image processing



nce we have recorded ion images, we need to process the images to allow us to extract as much information as possible from the data. The data is first centroided, as will be discussed in section 3.1, which identifies the location at which the ion strikes the detector. When recording with a CCD camera, this can be carried out on-the-fly, however, with the PImMS sensor this is carried out after the data have been recorded, before the PImMS data is separated into individual images. A background subtraction is then applied, giving us an image of the 2D projection of the 3D scattering distribution for each ion.

At this point, we need to reinflate the projection of the scattering distribution so that we can extract information on the energetics of the various dissociation processes occurring. This can be achieved using image inversion methods, discussed in section 3.2, to find the central slice of the 3D scattering distribution, which fully describes the scattering distribution and from which the radial distribution can be found; the radius of an ion image is proportional to the square root of the kinetic energy of the ion. To work out the proportionality constant between the pixel units

in which we record our data and kinetic energy units, we need to apply an energy calibration; this is discussed in section 3.3.

We can also use the covariance analysis discussed in section 3.4 to analyse our data. Covariance analysis provides correlations between two partner fragments and, if the formation of the two fragments are correlated, such as is the case for the dissociation of a dication into two cation fragments, so are the kinetic energies of the two fragments produced. The analysis requires data to be recorded separately for each experimental cycle, which is precisely how the PImMS camera records data. We use the centroided PImMS data for this analysis, as any further statistical processing, such as a background subtraction, would require the data from all the frames to be summed.

In this section, each of these techniques will be described in turn.

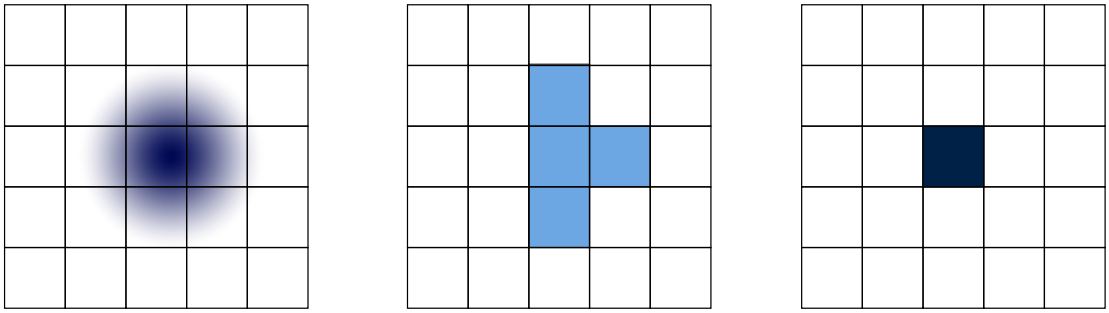
3.1 Centroiding ion hits

Centroiding, a technique initially developed by Chang *et al.*,[65] is used to find the precise position at which an ion hits the detector. Typically, our detectors are run at potentials such that each incident ion causes multiple adjacent pixels in the camera to record signal. We, however, want each ion hit to be represented by a single count, rather than a variable count based on the size of the cluster, which could lead to bias in the ion count for different masses and regions of the detector, due to mass discrimination effects and differing sensitivity across the detector. To establish where an ion has hit, we find all clusters of pixels with a size greater than one; this is done because any noise, such as the dark noise of the camera, will generally only be detected on a single pixel, thus we can remove a significant amount of the noise from the images in this way. Whilst a small amount of signal will also be removed, the improvement in image quality is worth the relatively small loss of signal; taking a typical cluster size distribution recorded in one of our experiments and shown in figure 3.1(b), the single pixel cluster count was 189,708, significantly higher than the

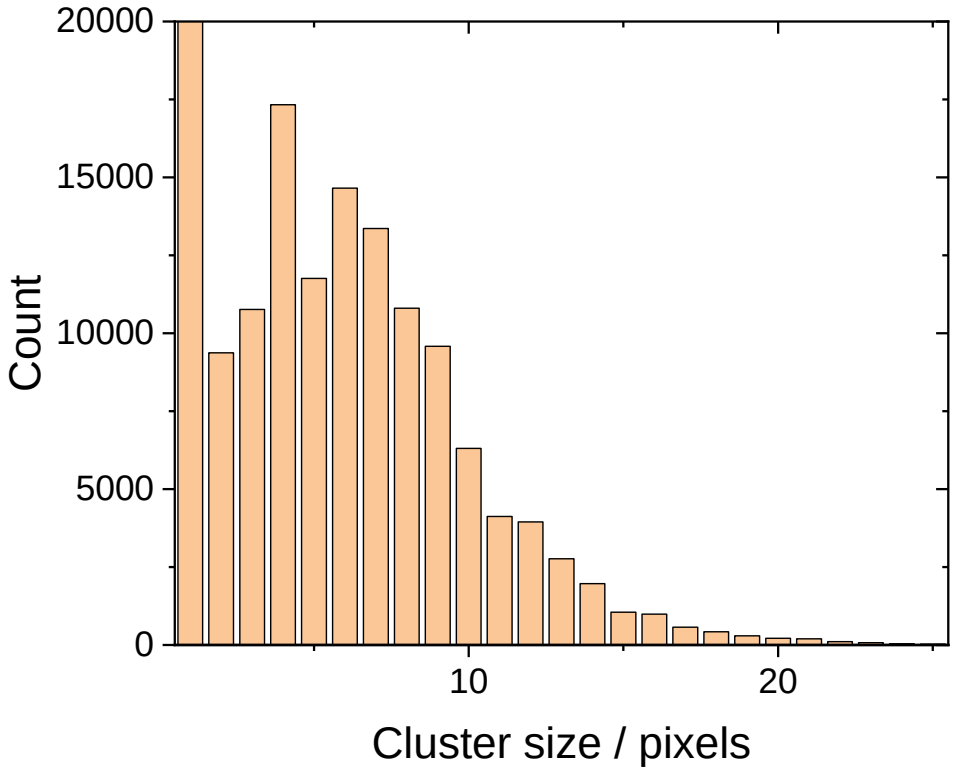
count for larger clusters. Once the clusters have been found, we then find the centre of mass of the cluster, and assign the ion hit to the closest pixel to that point. An example of this process is shown in figure 3.1(a).

When using the PImMS camera, there is a further complication. As we have now added a time dimension, it is possible that the signal from one ion may appear in multiple time bins. An ion hit will give maximum photon flux at the scintillator position corresponding to the centre of the MCP channel the ion strikes, with decreasing intensity with distance from this point. The photon flux will increase for a certain amount of time, before decaying away (see figure 3.2). The PImMS sensor only registers a hit once a certain threshold is reached, and it is evident that different pixels will reach this threshold at different times; see figure 3.2 for a visual representation. As such, we need to allow for a time spread in the centroiding algorithm. The time spread should be large enough that all appropriate pixels are included in the cluster, but not so big that unrelated signal is included in the centroiding process. The simplest way of finding the appropriate time spread is to check the signal in different time bins and see how long it takes before signal corresponding to a single ion hit is no longer observed. The centroided ion hit is assigned an arrival time corresponding to the time at which the first pixel within the cluster detected signal. For the PImMS data files recorded in this work, a time spread of six was typically used, and time centroiding was applied using code written by Dr Jason Lee.

It is important to check that the centroiding procedure does not introduce artefacts into the overall image, which may be the case in experiments with high levels of signal. High signal levels can lead to clusters from individual ion hits overlapping, meaning that it is no longer possible to distinguish the two hits. The manifestation of this problem can be seen in multiple ways: when studying the cluster size distribution, one might see a second feature in the cluster size distribution, from where two clusters overlap; there may be a qualitative difference in the images themselves,



(a)



(b)

Figure 3.1 A depiction of the centroiding process. a) shows how the centroiding process works, with the left image showing the light impinging on the detector, the central image showing the pixels which register hits, and the right image the result of the centroiding algorithm, b) shows a typical cluster size distribution (the count for a cluster size of one has been cut off, actual value 189,708).

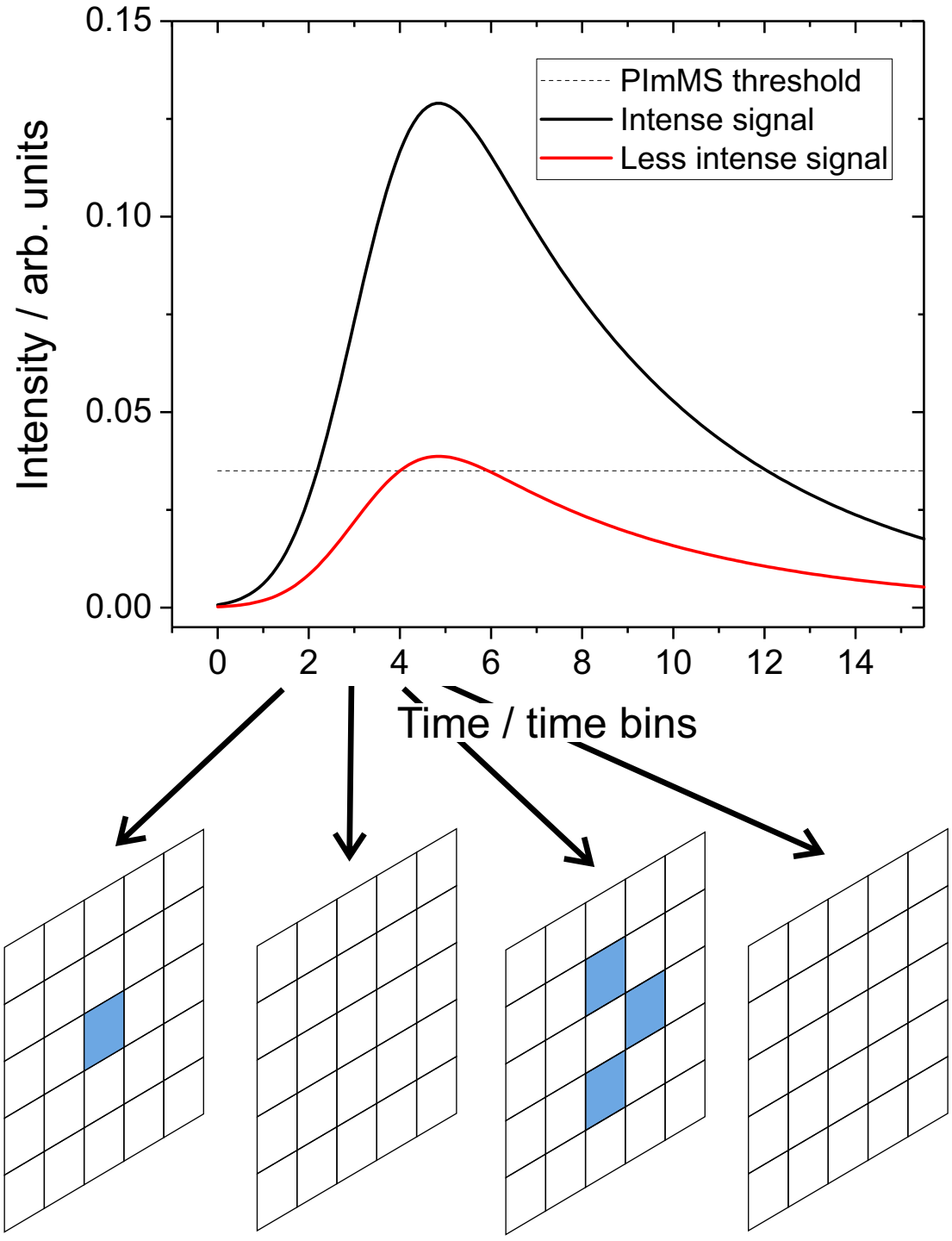


Figure 3.2 A simplified example of centroiding with the PImMS camera. Using the example shown in figure 3.1(a), due to the differences in intensity for each pixel, different pixels trigger at different times, after the photon flux for the pixel exceeds their signal threshold value; centroiding must therefore occur in space as well as time. Summing all the times gives the central image of figure 3.1(a). In this case, a time spread of three would be appropriate, and this would give the same result as the right image of figure 3.1(a) in the second time bin.

for example the centre of some feature becoming a dot, surrounded by no signal; the radial distribution may change after the centroiding process. In the electron scattering experiments presented in this thesis the signal level is relatively low, so there has been no evidence of any centroiding issues of this type.

Once the data has been centroided, it can be subjected to further processing. We will now discuss the reinflating of the full three-dimensional scattering distribution from the measured two-dimensional projection using inversion methods.

3.2 Inversion methods

As has been previously established, in our VMI experiments the scattering distribution is crushed along the TOF axis, so that all ions of a given mass arrive at the detector almost simultaneously, i.e. we record the 2D projection of the 3D scattering distribution. Whilst is is possible to qualitatively interpret the 2D projection, a quantitative analysis requires us to consider the 3D scattering distribution. To recover the 3D scattering distribution, we use one of a number of inversion methods.

Inversion methods analogous to those used here find use in a range of different fields in which the measured data constitute a projection of a higher-dimensional distribution. For example, in plasma diagnostics, inversion methods are used to reconstruct the radial information from experiments carried out using optical emission spectroscopy;[114–116] in astrochemistry, inversion methods can be used to study cometary atmospheres[117] and in conjunction with radio astronomy to unpick the structures of objects;[118,119] in atmospheric chemistry, inversion methods can be used to probe the composition of the atmosphere, using low Earth orbit satellites to receive radio signals from Global Positioning System (GPS) satellites.[120–123] Of course, the methods are also used extensively in the electron and ion imaging communities to reconstruct scattering distributions after being crushed during the VMI experiment.

The vast majority of inversion methods used in VMI experiments rely upon the presence of an axis of cylindrical symmetry in the scattering distribution to allow

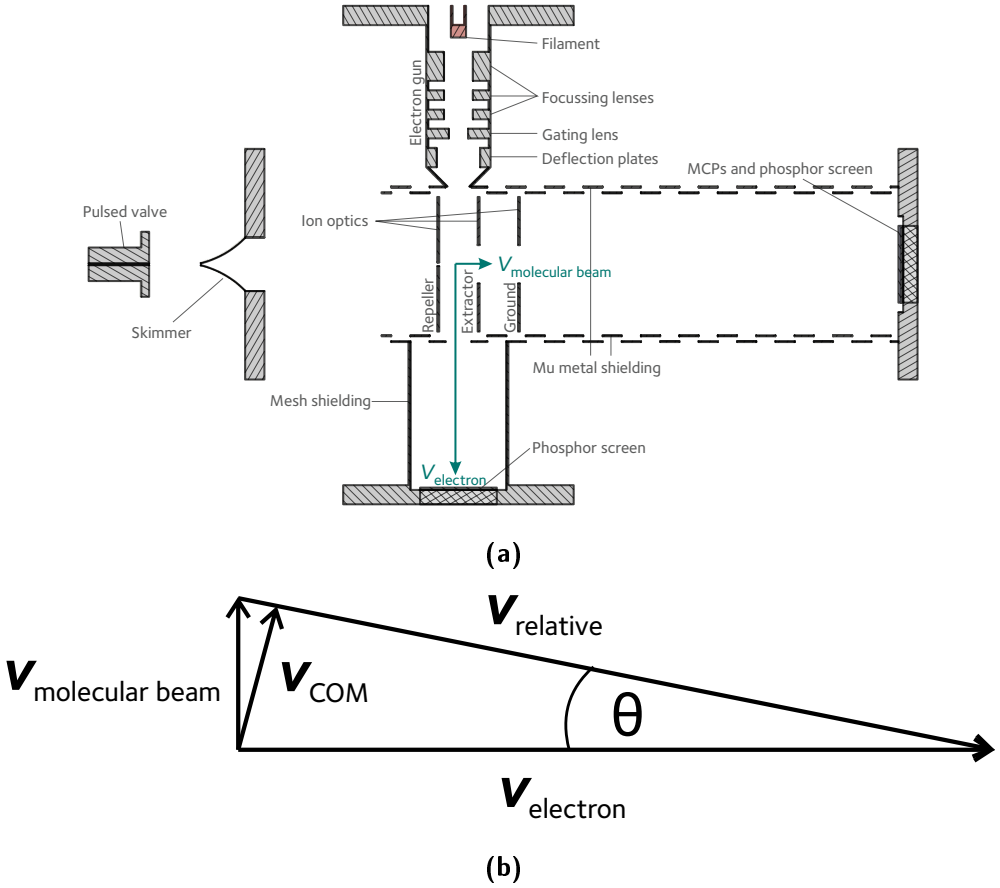


Figure 3.3 A scattering diagram for the electron-molecule crossed beam experiment described in section 2.2. a) shows the the velocity vectors of the electron and molecular beams within the experimental apparatus, and b) shows the scattering diagram with the velocity of the centre of mass and the relative velocity vector defined. Note that the diagrams are not to scale.

the inversion to be carried out. In a photolysis experiment, this axis of symmetry is defined by the polarisation vector of the laser; this is taken into account when defining the experimental geometry. In the electron scattering experiment introduced in section 2.2, the axis of cylindrical symmetry is given by the relative velocity vector, $\boldsymbol{v}_{\mathrm{rel}}$, between the molecular and electron beams; in the centre of mass (COM) frame, the collision between the two particles occurs head-on along the vector of $\boldsymbol{v}_{\mathrm{rel}}$ and, as there is no reason why scattering should occur in a specific direction within any cone about $\boldsymbol{v}_{\mathrm{rel}}$ for a randomly oriented molecule, $\boldsymbol{v}_{\mathrm{rel}}$ must be an axis of cylindrical symmetry.

The scattering diagram for an electron-molecule collision is shown in figure 3.3.

The velocity of the electron beam can be determined from the kinetic energy of the electron beam using the classical equation for kinetic energy (or the relativistic equivalent for sufficiently high-energy electrons). The molecular beam velocity can be calculated using the expression for molecular beam velocity given previously, in equation 1.29. For the case of dioxygen scattering with a 70 eV electron, the velocities of the molecular beam and electron beam are approximately 705 m s^{-1} and 4.96×10^6 m s^{-1}, respectively. From these velocities, the angle θ can be found; in this case $\theta = 0.01°$. This means that the axis of cylindrical symmetry, which corresponds to the direction of $\boldsymbol{v}_{\text{rel}}$, lies almost exactly along the electron propagation vector. When we record the 2D projection of the scattering distribution at the detector, it is therefore a valid assumption to use the electron propagation direction as the axis of cylindrical symmetry for the subsequent analysis. The velocity of the centre of mass can also be found, but is relatively unimportant here, just leading to a translation of the centre of the scattering distribution from the centre of the detector.

Whilst the scattering distribution has an axis of cylindrical symmetry, there is no requirement for the scattering distribution to be isotropic. Scattering distributions $P(r, \theta)$ from VMI experiments are typically described by the following equation at each radius

$$P(r, \theta) = I(r) \left[1 + \sum_{n>0} \beta_n(r) P_n(cos(\theta)) \right] \tag{3.1}$$

where $I(r)$ is the intensity of the image at radius r, $P_n(x)$ is the n^{th} Legendre polynomial, β_n is the n^{th} beta parameter, and θ is the angle from the axis of cylindrical symmetry. The number of n terms included in the expansion depends on the experiment. In our electron scattering experiments, we have found that only the β_0 term contributes, i.e. the images are isotropic, and equation 3.1 just becomes $I(r)$. In experiments involving photons, the number and identity of the non-zero β terms is dependent on both the number and polarisation of the photons used to ionise the molecule.[124–126] In this work we are focusing on electron scattering experiments, so unless otherwise stated, all images are considered to be isotropic.

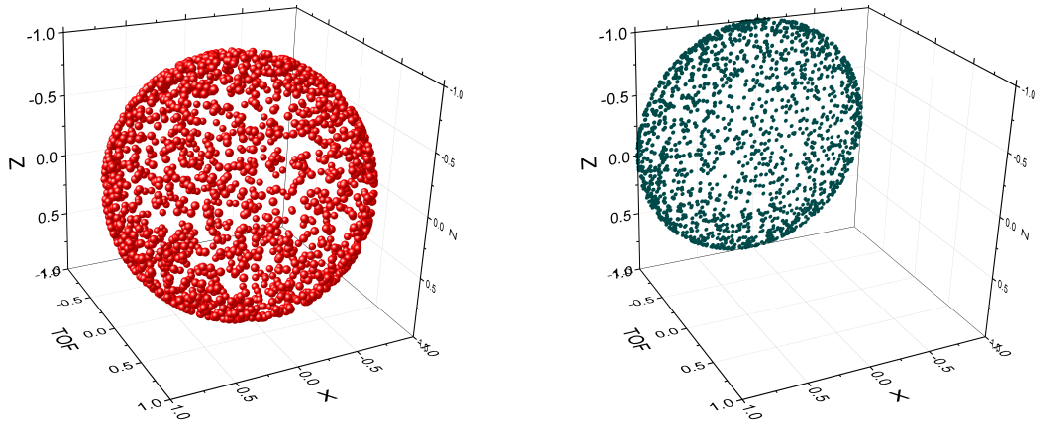


Figure 3.4 An example of a 3D scattering distribution with cylindrical symmetry (left) and its 2D projection (right).

Inversion methods can largely be assigned to one of three groups, based on the method used to invert the image; we now define and discuss each of these groups in turn.

3.2.1 Abel integral methods

The earliest method used for inversion of 2D projections was developed by Niels Henrik Abel,[127] and is the basis of a number of inversion methods. A sound derivation is provided by Eppink *et al.*,[128] which is summarised here. Consider a 3D distribution with an axis of cylindrical symmetry, such as that shown in figure 3.4. This distribution can be described by some function $i(x, y, z)$, where the TOF axis is defined to lie along the y axis, and the z axis is the axis of cylindrical symmetry. What we actually record is the projection of this, also shown in figure 3.4, which we shall call $p(x, z)$. If we consider only a single row of this projection, i.e. where $z = z_0$, it follows that:

$$f(x) = 2 \int_0^\infty s(x, y)\ dy \tag{3.2}$$

where $s(x, y) = i(x, y; z_0)$. The integral is technically from minus infinity to infinity, but as the image has cylindrical symmetry this can be replaced with two times the integral from zero to infinity. The presence of an axis of cylindrical symmetry allows us to replace $s(x, y)$ with $s(r)$, where $r^2 = x^2 + y^2$, and, after applying the

appropriate Jacobian for the transform in coordinate system, it follows that:

$$f(x) = 2\int_x^\infty \frac{s(r)r}{(r^2 - x^2)^{\frac{1}{2}}}\, dr \tag{3.3}$$

This is the forward Abel transform. By applying the Fourier transform convolution theorem, we can obtain the inverse transform, which is given by:

$$s(r) = \frac{1}{\pi}\int_r^\infty \frac{\frac{df(x)}{dx}}{(x^2 - r^2)^{\frac{1}{2}}}\, dx \tag{3.4}$$

By solving the Abel integral given in equation 3.4, it is possible to recover the original 3D distribution from the recorded 2D projection.

Whilst this method does invert images successfully, there are some issues. The inversion is highly sensitive to noise, and the singularity when $r \to x$ makes finding an analytical solution more challenging, and can introduce noise into the resulting distribution. This is particularly apparent when $x \to 0$, as the size of the denominator in equation 3.4 rapidly increases within the integral, amplifying any noise in the central region. This centreline noise is frequently seen when using Cartesian methods, and can make it difficult to interpret the inverted image. A number of methods have been developed to help solve the Abel integral, one of which is briefly discussed below.

Hansen-Law

The Hansen-Law method, developed by Hansen and Law, utilises a recursive algorithm for carrying out Abel inversion,[129] which is summarised here. They noted that the Abel transforms are linear, space-variant operators, for which efficient computational methods developed for use with space-invariant systems cannot be used. However, under an appropriate coordinate transform, the Abel transforms do become space-invariant, or convolutional. This would require the image data to be placed on a non-uniform grid however, which would counteract the benefits of the

coordinate transform. To avoid this problem, they first carry out the coordinate transform, then model the Abel transform using a set of linear differential equations of the state-variable type, before applying the reverse coordinate transform to yield a set of space-variant state equations equivalent to the Abel integral. Inversion is carried out starting from the outer edge of each row of the image, propagating recursively towards the centre, and offers a significant increase in computational speed over numerical integration.

Their algorithm also includes a Kalman filter,[130] which is applied at the point of inversion and acts to reduce noise from the data. When stepping in from the outer edge, the Kalman filter uses the information from previous data points to make a prediction of the next point. This is then compared with the measured data and the two combined, resulting in a filtered estimate of the inverted distribution. A further smoothing step is then carried out using the estimates from the Kalman filtering step, sweeping back in the opposite direction to the initial inversion. This is done due to the fact that there is initially only a small amount of prior knowledge to estimate the next point in the Kalman filter, meaning that without a second pass, the filtering is less efficient near the outside of the image.

This method provides a robust and computationally efficient method for carrying out an Abel inversion.

3.2.2 Onion peeling methods

Onion peeling methods work, as the name implies, in a very similar way to peeling an onion.[131] If we take the 2D projection of a cylindrically symmetric scattering distribution, in this case the exemplar image shown in figure 3.5(a), and propagate from the outer edge until we find some signal, we will eventually reach the signal at the outer edge of the image. This signal, which can only come from ions produced with velocities with no component out of the image plane (i.e. their kinetic energy is perpendicular to the time-of-flight axis in our experiments), must be part of the

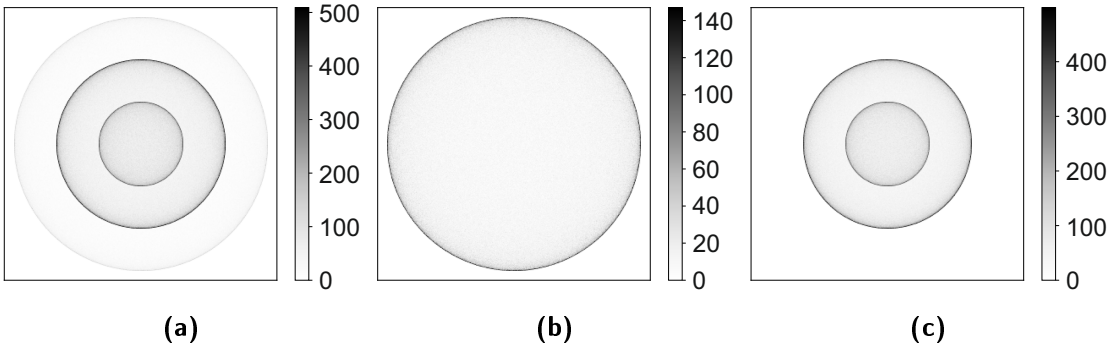


Figure 3.5 A demonstration of how the onion peeling method proceeds. (a) shows the original ion image. Propagating from the outer edge of the image, when signal is found, the contribution from this signal to the centre of the image is calculated, shown in (b). This is subtracted from image (a) to give image (c), and the process continues.

central slice which describes the 3D scattering distribution. However, any signal at lower radius than this outer signal is convoluted with the contributions from the projections of the outer layer of signal.

Fortunately, we know that the scattering distribution contains an axis of cylindrical symmetry, so we can calculate the contribution to the rest of the image from the signal at the outer edge, as shown in figure 3.5(b). This can then be subtracted from the original image to give an image with the outer layer peeled off, shown in figure 3.5(c). By repeating this process until the centre of the image is reached, the entire central slice can be reconstructed from the measured image.

There exist both Cartesian[132,133] and polar[134,135] implementations of onion peeling. The Cartesian method takes each row of the image in turn, propagating from the outer edge of the image for each row. The reconstruction uses the 1D projection of a circle to calculate the contribution of the outer edge of the signal to the points at lower radius, which is then subtracted from the original image. The polar method converts the Cartesian image into polar coordinates then, rather than propagating from the outer edge of each row, the algorithm propagates from the maximum radius of the image inwards. Once a ring of signal is found, the algorithm fits the function $1+\sum_n \beta_n P_n(cos(\theta))$, where $P_n(x)$ is the n^{th} Legendre polynomial, and θ is the angle

with respect to the axis of cylindrical symmetry, which describes the anisotropy of the image. The parameters from the fit are then used to reconstruct the sphere corresponding to the outer ring, and this is subtracted from the original image.

As the basis functions used to generate the function to subtract can be generated in advance and read into memory when running the algorithm, these methods are fast and robust. Artefacts can be introduced when using polar onion peeling if the circular image has been significantly distorted but, as far as we are aware, this is not an issue in our experiments.

3.2.3 Basis function fitting methods

Basis function fitting methods utilise basis functions with a known inverse function to fit the data, typically using linear regression. The 2D projection of a 3D scattering distribution, $I(v_p)$, can be described by a set of weighted basis functions according to the following equation

$$I(v_p) = \sum_{i}^{\text{all } i} w_i \rho(v_p)_i \tag{3.5}$$

where v_p is the velocity in the 2D projection, w_i is the weight of the i^{th} basis function $\rho(v_p)_i$, which has a known inverse function with velocity i. Linear regression adjusts the weights such that the basis functions describe the projection of the scattering distribution. This is done by minimising an appropriate fitting function; in the case of least squares linear regression, this function is given by:

$$\sum_{x=0}^{\max\ v_p} \left(I_x - \sum_{i}^{\text{all } i} w_i \rho_{i,x} \right)^2 \tag{3.6}$$

where the subscripted x denotes the value of v_p for the current iteration of the sum. By multiplying the weights by the known inverse function of $\rho(v_p)_i$, the inverted image and radial distribution can be obtained.

When carrying out linear regression, regularisation can also be applied. Regularisation is typically used to prevent overfitting of the data with the basis functions.

This typically manifests as a ringing signal, where subsequent weights alternate between positive and negative signal. Perhaps the most common regularisation method used is Tikhonov, or ridge, regularisation.[136–139] Tikhonov regularisation penalises large weights by adding a term, $\alpha \sum_i^{\text{all } i} w_i^2$, where α is a user-defined penalty weighting factor, to the minimisation function given in equation 3.6, i.e. the function to minimise becomes:

$$\sum_{r=0}^{\max\ v_p} \left(I_r - \sum_i^{\text{all } i} w_i \rho_{i,r} \right)^2 + \alpha \sum_i^{\text{all } i} w_i^2 \tag{3.7}$$

By applying an appropriate α we can, in cases where the radial distribution has been over-fitted, remove the vast majority of ringing.

These methods are fast, as the basis functions and their inverse functions are calculated in advance and stored for future use, and the basis functions can be adjusted to give a better fit; for example, if the features in an image are broad, the width of the basis function radius might be increased to better fit the data. A number of inversion methods use basis function fitting, a few of which are discussed below.

Basis Set Expansion (BASEX)

Developed by Dribinski *et al.*, Basis Set Expansion, or BASEX,[140] is probably the most well-known inversion method to fall in this family. The method uses functions of the form:

$$\chi_k(r) = \left(\frac{e}{k^2}\right)^{k^2} \left(\frac{r}{\sigma}\right)^{2k^2} e^{-\left(\frac{r}{\sigma}\right)^2} \tag{3.8}$$

$$\approx e^{-2\left(\frac{r}{\sigma - k}\right)^2} \tag{3.9}$$

where $\chi_k(r)$ is the k^{th} inverse function at radius r, and σ is the standard deviation of the function. The inverse functions are practically indistinguishable from Gaussians, but can be analytically integrated, which allows the basis functions, $\rho_k(r)$ used to

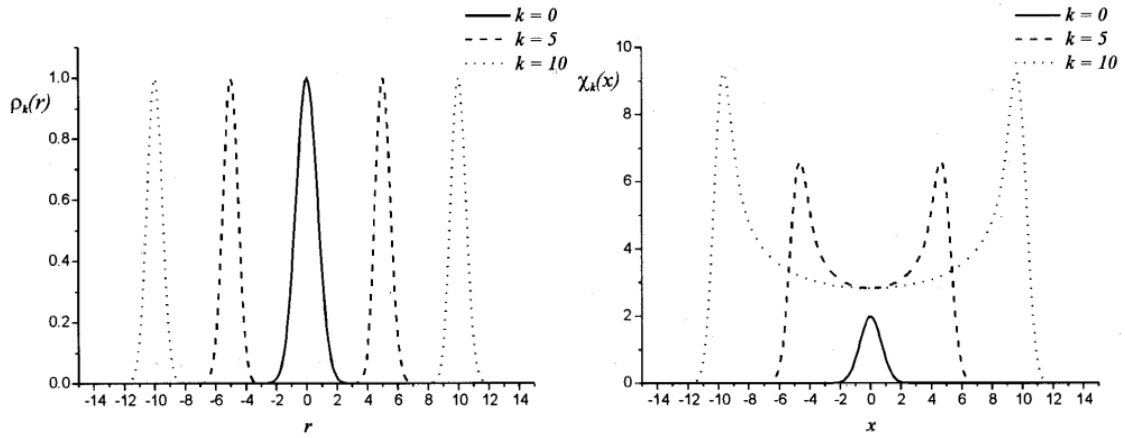


Figure 3.6 Example of the velocity basis functions (left) and corresponding projections onto the image plane (right) used in the BASEX inversion method for basis functions with $\sigma = 1$, where k is the central point of the basis function. Reproduced from [140], with the permission of AIP Publishing under license 4917570384241.

fit the data to be found using the forward Abel transform; the basis functions used for the fitting are given by:

$$\rho_k(r) = 2\sigma\chi_k(x)\left[1 + \sum_{l=1}^{k^2}\left(\frac{x}{\sigma}\right)^{-2l} \times \prod_{m=1}^{l}\frac{(k^2+1-m)\left(m-\frac{1}{2}\right)}{m}\right] \tag{3.10}$$

Figure 3.6 shows the form of both functions.

BASEX is a Cartesian inversion method, i.e. it takes each row of the image in turn, and fits the basis functions to the data from the row. A polar version has also been developed, and will now be briefly discussed.

pBASEX

pBASEX, developed by Garcia *et al.*, is based on the BASEX algorithm, with the main modification being the choice of coordinate system.[141] In pBASEX the set of functions given by:

$$\chi_k(r,\theta) = \sum_{l=0}^{l=l_{\max}} c_{kl} e^{-\frac{(r-r_k)^2}{\sigma}} P_l(cos(\theta)) \tag{3.11}$$

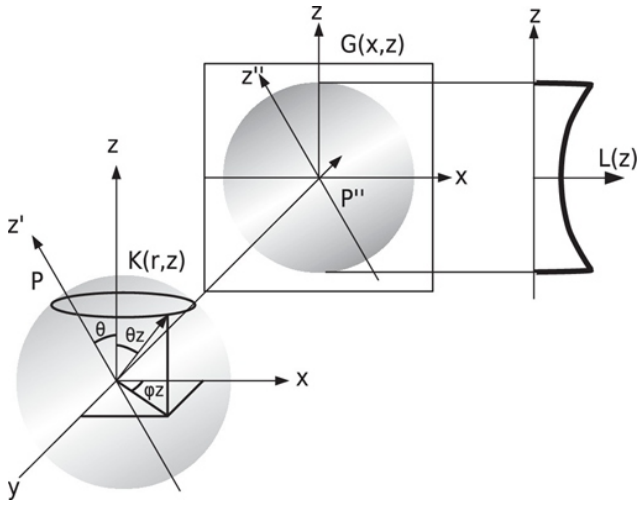


Figure 3.7 Depiction of the projections used in the linBASEX inversion method. The bottom-left co-ordinate system shows the original 3D scattering distribution. The central co-ordinate system shows the 2D projection of the 3D distribution. One potential 1D projection of the 2D distribution is shown on the right. The axis of cylindrical symmetry is labelled $z^{|}$ in the 3D distribution and $z^{||}$ in the 2D distribution. Reproduced from [142], with the permission of AIP Publishing under license 4917570234091.

where c_{kl} is the k^{th} weighting coefficient for the l^{th} Legendre polynomial, θ is the angle with respect to the axis of cylindrical symmetry, $P_l(x)$ is the l^{th} Legendre polynomial, and r_k is the maximum radius of the k^{th} basis function, are used as the inverse functions; the basis functions can be found by applying the forward Abel transform to these functions, in exactly the same way as with BASEX.

lin-BASEX

The lin-BASEX[142] method takes the measured image and projects it along an axis, giving a one-dimensional (1D) function, and a fit is then carried out on this 1D projection. The 1D projection of a uniform shell is a step function, and the 1D projection of an anisotropic shell perpendicular to the axis of cylindrical symmetry (i.e. the case where $z = z^{||}$ in figure 3.7) can be found by using a sum of Legendre polynomials, $\sum_l P_l(\frac{z}{r_k})$, where l is the order of the Legendre polynomial, z is the coordinate of the 1D projection and r_k is the radius of the shell, to modify the step function. By taking projections at multiple different angles, which requires

a further Legendre polynomial to account for the symmetry axis no longer lying perpendicular to the projection axis, it is possible to find both the anisotropy and the radial distribution of the original 3D scattering distribution.

Fourier moment analysis

The Fourier moment analysis technique developed by Bass *et al.* is slightly different from the inversion methods discussed previously, in that it does not require the probed three-dimensional distribution to possess cylindrical symmetry.[143] This method is based on the analysis of the Fourier moments of the scattering distribution recorded using a number of different laser polarisations. It is mathematically quite complex, but in the case of a pump-probe experiment using linearly polarised light, for example, various combinations of the Fourier moments, found by carrying out an integral over the angular coordinate of the image, acquired for different experimental geometries are found, and are fitted using basis functions based on the two-dimensional projection of spherical harmonics. The fitting parameters give the associated bipolar moments,[144] which describe the dynamics of the system.

A new inversion method for electron-molecule scattering experiments

We have recently been developing a new inversion method, and have shown that it works well with isotropic images such as those obtained from the electron-molecule scattering experiments presented in this thesis. The method draws on ideas considered in the lin-BASEX method, which uses both the concept of fitting a 1D distribution, and modifying the basis function from an isotropic system to deal with an anisotropic system. The main motivation for the development of this technique was to allow us to invert recoil-frame covariance images, discussed in section 3.4.4. In the process of carrying out the covariance analysis, the axis of cylindrical symmetry required for the majority of the inversion methods described here is removed, meaning that these methods cannot be used to invert a covariance image. Whilst it

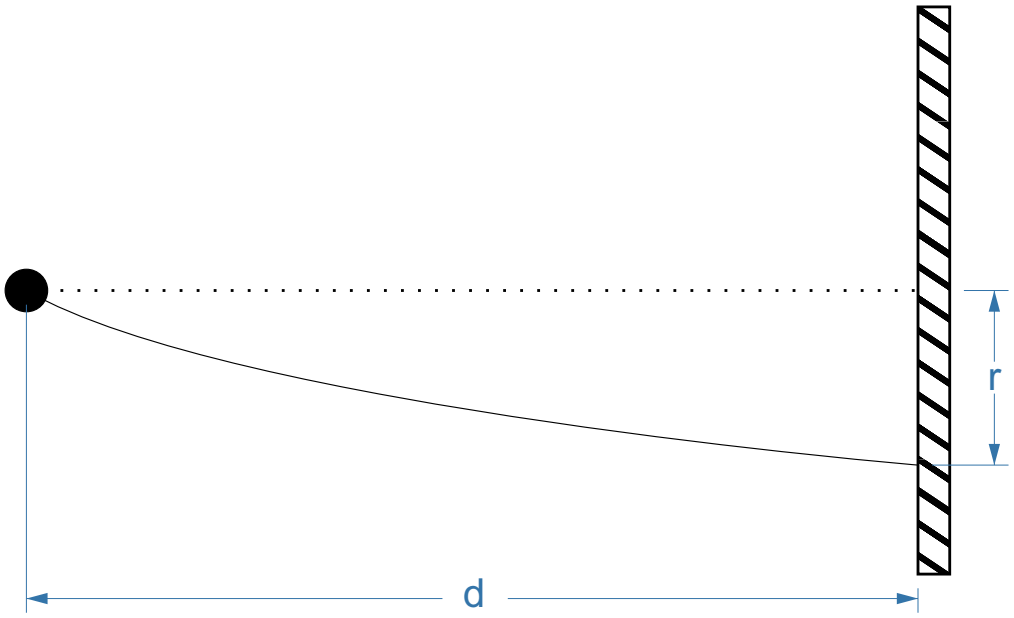


Figure 3.8 The dimensions used in the derivation of the energy calibration discussed in the text. d is the distance from the interaction region to the detector, and r is the radius from the image centre at which the particle strikes the detector.

is completely valid for the inversion method to be used on scattering distributions with an axis of cylindrical symmetry, it makes more sense to discuss this inversion method once covariance analysis has been discussed. As such, this inversion method will be discussed in detail in section 3.5.

3.3 Energy calibration

All images recorded by a camera are recorded by an array of pixels. This is all very well for qualitative analysis, but if we want to understand the dynamics of the processes occurring more fully, we need some way to convert our radial distribution from pixels to quantifiable units. The next section discusses how this conversion is carried out.

As has been previously stated, the radius of a velocity-map image is proportional to the square root of the corresponding kinetic energy. This can be shown in the following way:

Consider the diagram shown in figure 3.8. A particle of charge q is accelerated

by the ion optics (not shown) through a potential V. The electric field imparts a kinetic energy on a charged particle along the time-of-flight (TOF) axis, $E_{k\parallel}$, given by

$$E_{k\parallel} = qV \tag{3.12}$$

Kinetic energy can also be given by $E_k = \frac{1}{2}m\boldsymbol{v}^2$, where m is the mass of the particle and $\boldsymbol{v}$ is the velocity of the particle, given by $\boldsymbol{v} = \frac{\boldsymbol{s}}{t}$, where $\boldsymbol{s}$ is the displacement and t is the time-of-flight. The kinetic energy resulting from the velocity component along the TOF axis is equal to the expression given in equation 3.12, so it follows

$$qV = \frac{1}{2}m\left(\frac{\boldsymbol{d}}{t}\right)^2 \tag{3.13}$$

where $\boldsymbol{d}$ is the distance between the particle's starting position and the detector, as defined in figure 3.8. This incidentally gives the mass calibration required to convert the mass spectrum from time to mass units, as V and $\boldsymbol{d}$ are fixed, so $t = k\left(\frac{m}{q}\right)^{\frac{1}{2}}$, where $k = \left(\frac{\boldsymbol{d}^2}{2V}\right)^{\frac{1}{2}}$. By knowing the arrival time and masses of two particles, it is possible to find k either graphically, or by solving simultaneous equations.

Continuing the derivation, we can find the kinetic energy of the particle resulting from the velocity of the particle perpendicular to the TOF axis, which is given by

$$E_{k\perp} = \frac{1}{2}m\boldsymbol{v}_\perp^2 \tag{3.14}$$

$$= \frac{m\boldsymbol{r}^2}{2t^2} \tag{3.15}$$

where $\boldsymbol{r}$ is the radius, as defined in figure 3.8, and $\boldsymbol{v}_\perp$ is the velocity of the particle perpendicular to the TOF axis. The time-of-flight, t, also appears in equation 3.13; substituting this into equation 3.15 gives

$$E_{k\perp} = \frac{V}{\boldsymbol{d}^2}qr^2 \tag{3.16}$$

$$= cq\boldsymbol{r}^2 \tag{3.17}$$

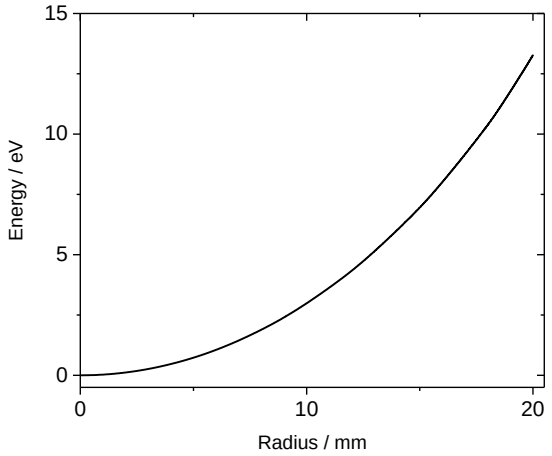


Figure 3.9 An example of a curve used for carrying out an energy calibration on the radius of the ion images.

So we see that the square root of the kinetic energy is proportional to the radius. Note that it is also possible to carry out the same process for a conversion from radius to velocity and momentum units, in which case the calibration would also have a mass dependence. We know the size of the detector in millimetres, and can find the dimensions of the detector in pixel units by recording an image, so we can find a factor to convert a number of pixels into millimetres. All that remains is to find the scaling factor c used to convert from radius to kinetic energy units.

There are a few ways that the scaling factor can be found. The first is by finding the proportionality constant k for the mass calibration, then using the fact that $c = \frac{1}{4k^2}$ to find c. The second is to run a calibration experiment, in which a simple molecule for which the dissociation dynamics are well understood is dissociated and the ion images recorded under the same experimental conditions that will be used in subsequent experiments. As the energy of the ions produced in the dissociation are already known, they can be used to calibrate the pixel to energy conversion. A typical calibration experiment might use the photodissociation of a diatomic molecule at a well-defined wavelength. Since the photon energy is known, if the bond dissociation energy and the final electronic states of the two atomic products are also known, the velocities of the two atoms can then be calculated. The third method is

to simulate the ion trajectories using software such as SIMION.[145] SIMION simulates the electric fields generated by the ion optics, and uses the resulting potential surfaces to calculate the trajectory taken by a charged particle formed at any point in the field, in this case the centre of the interaction region. By giving a number of different particles a range of initial energies and seeing where they strike the detector, a calibration can be found. SIMION simulations are used to calibrate the radial distributions in this thesis; ion images produced from electron scattering typically have fairly broad features, and as mentioned previously, a slight negative potential is applied to the front of the MCP to help reduce electron noise at the detector. As SIMION calculates the potential experienced by the charged particle at all points, it gives a more accurate representation than the derivation given above. A typical calibration curve is shown in figure 3.9.

There is one final aspect of the change in variables that needs to be considered here. When carrying out the unit conversion either from time t to mass over charge m/z, in the case of the mass calibration, or pixels r to energy units E in the case of the velocity calibration, it is necessary to apply a Jacobian to the intensity scale, to correct for the non-linear spacing of points in the new units. Taking the example of the energy calibration, the area under the curve of radius against intensity is proportional to the number of ions appearing at that radius. This should remain unchanged when the units are converted to kinetic energy, i.e.

$$\int f\left(E_{k\perp}\right)\, dE_{k\perp} = \int g(r)\, dr \tag{3.18}$$

where $f\left(E_{k\perp}\right)$ is the intensity as a function of $(E_{k\perp})$ (i.e. the kinetic energy distribution), and $g(r)$ is the intensity as a function of r (i.e. the radial distribution). By differentiating equation 3.17 with respect to r, we find

$$\frac{dE_{k\perp}}{dr} = 2cqr \tag{3.19}$$

substituting this result into equation 3.18 gives

$$f\left(E_{k\perp}\right) = \frac{f(r)}{2cqr} \tag{3.20}$$

$$= \frac{f(r)}{(4cqE)^{\frac{1}{2}}} \tag{3.21}$$

This results in an expression that tells us how the intensity from the radial distribution must be adjusted when converting from pixel units to kinetic energy units.

Now that it has been established how to find the energy of the ions studied in our experiments, we now turn our attention to covariance analysis techniques, which can be used to help disentangle the dissociation of multiply charged ions in our experiments.

3.4 Covariance analysis

Covariance analysis is a standard statistical technique which can be used to reveal correlations between two variables. The two variables can have any number of dimensions, with the resulting covariance matrix having a number of dimensions equal to the sum of the number of dimensions of the two variables. For example, if we were looking at covariance between the rolls of two dice, each variable would take a single value, which in this case is considered as a zero-dimensional variable. When we calculate the covariance of this system, a single value of covariance will result. If we instead took two sets of 100 dice and instead defined our variable as the frequency distribution of each number, which would give a one-dimensional (1D) variable, we would obtain a two-dimensional (2D) covariance matrix as a result. Covariance analysis finds use in a wide variety of fields. For example, in finance, it can be used to look for correlations between various assets; in meteorology, it can be used within the generation of weather forecasts;[146] in biological sciences, it can be used to analyse biological pathways.[147] This is by no means the limit of the use of covariance within each field, and is certainly a non-exhaustive list of all

the disciplines which utilise covariance analysis, but it does demonstrate that the approach finds widespread usage across a range of disciplines.

Mathematically, covariance can be described by the following equation:

$$\mathrm{Cov}\left(\mathbf{X},\mathbf{Y}\right) = \left\langle \left(\mathbf{X} - \left\langle \mathbf{X} \right\rangle\right)\left(\mathbf{Y} - \left\langle \mathbf{Y} \right\rangle\right)\right\rangle \tag{3.22}$$

$$= \left\langle \mathbf{XY} \right\rangle - \left\langle \mathbf{X} \right\rangle \left\langle \mathbf{Y} \right\rangle \tag{3.23}$$

where $\mathbf{X}$ and $\mathbf{Y}$ are variables, and $<\ldots>$ indicates the expectation value, or mean, of the contained expression. To explain the equation, say we have a set of data from an experiment in which we have taken n readings of the variables $\mathbf{X}$ and $\mathbf{Y}$, and we wish to find the covariance between the two variables. For the i^{th} reading of $\mathbf{X}$ and $\mathbf{Y}$, we subtract the respective means from each reading, then multiply these two data points together to obtain the product of the displacement from the mean of the two values. We can see that if the two values are either both larger or both smaller than their respective means this will give a positive value, and if one value is bigger and the other smaller we will obtain a negative value. We then carry out this calculation for each of the n readings and take the mean of this value. Note that Bessel's correction, i.e. dividing by $n-1$ instead of n when finding the standard deviation of a sample to give a non-biased estimate of the standard deviation, is also applicable here.

Since covariance mapping techniques were first used in the spectroscopy and dynamics community,[148] the use of covariance as an analytical technique has expanded considerably. In this section, we will briefly review coincidence analysis, the predecessor of covariance analysis in the field of ion imaging, and discuss the advantages and disadvantages of coincidence in comparison with covariance. We will then move on to discuss the use of covariance maps and recoil-frame covariance, and the inversion of recoil-frame covariance images. Later in the thesis, covariance analysis will play an important role in studying the fragmentation of multiply charged parent ions.

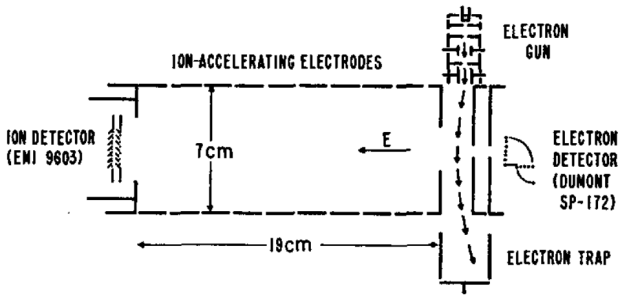


Figure 3.10 The experimental setup used in the first coincidence experiment. Reproduced from [149], with the permission of AIP Publishing under license 4917561472491.

3.4.1 Coincidence

Coincidence measurements preceded covariance analysis in the field of ion imaging. The two techniques are used for similar purposes, but each have their own niche, as will be discussed later in this section. When employed in the context of a photodissociation study, coincidence measurements work in much the same way as covariance analysis, but rely on the experiment having a low count rate, such that fewer than one molecule dissociates each acquisition cycle. This means that, by measuring the resulting individual electrons and/or ions produced, it is possible to unambiguously assign them to a given event. By building up statistics on the correlations observed from a large number of events, it is possible to gain an understanding of the dissociation dynamics of the molecule under study.

The first documented use of coincidence techniques in relation to time-of-flight mass spectrometry was in 1965 by McCulloh *et al.*[149] In their experiment, shown in figure 3.10, sample molecules are bombarded with a 1 keV electron beam within the interaction region, which is held within an electric field of strength 150 V cm^{-1}. Any ions formed, and their complementary ejected electrons, are then accelerated in opposite directions towards their respective detectors. If an electron is detected, the system is triggered to wait for an ion, or ions, at the other detector. If an ion is not detected within the experimental cycle, the electron count is also discarded to remove false coincidences. The resulting data are then used in the coincidence analysis. In

the case of single ionisation, one electron and one ion are detected, and in the case of double ionisation, an electron signal will be measured from the two ejected electrons, and either one or two ion signals detected, depending on whether the parent ion fragments before reaching the detector. Provided the count rate per frame is low enough, such that on average fewer than one molecule is ionised per acquisition cycle, this allows each dissociation pathway to be unambiguously identified. Higher count rates lead to the presence of false coincidences, i.e. signal from unrelated processes occurring in the same frame. Whilst drifts in the supply voltages employed in this early experiment limited acquisition times to around five minutes, making it difficult to obtain sufficient counts when measuring coincidence from the dissociation of doubly charged parent ions, more recent coincidence experiments have overcome this problem.

This method was quickly applied to photolysis experiments by Brehm *et al.*[150] They carried out a study on the unimolecular decay kinetics of methane after irradiation by monochromatic light at a wavelength of 58.4 nm from a Helium discharge lamp. By measuring the arrival of the electrons and ions in coincidence, they were able to unambiguously identify the dissociation pathways. They termed this analysis photoelecton-photoion coincidence (PEPICO). As with electron ionisation, these methods can also be applied to cases of multiple ionisation, using the photoion-photoion coincidence (PIPICO),[151] photoelectron-photoion-photoion coincidence (PEPIPICO),[152] and photoelectron-photoelectron coincidence (PEPECO)[153,154] techniques. Focussing on electron-ion-ion coincidence measurements, the arrival time of each ion is measured; this can be plotted as a scatter graph. Coincidences appear as diagonal features in this scatter graph, or coincidence map, and the gradient of each feature is indicative of the dissociation mechanism which forms the detected ions. Eland and co-workers give a detailed analysis of different slopes in [152] and [155], which we will now discuss.

If we consider a time-of-flight experiment, each ion has a flight time, $t_{0;x}$, when

produced with rest velocity (defined as the velocity of the molecular beam), where x is the identity of the ion. However, if the ion gains momentum along the TOF axis during the process in which it is formed, this makes a small difference to the arrival time of the ion. The time-of-flight, t_x can then be defined using the following equation

$$t_x = t_{0,x} + k\boldsymbol{p}_x cos(\theta) \tag{3.24}$$

where k is the a constant inversely proportional to the drawout field strength, $\boldsymbol{p}_x$ is the momentum of ion x, and θ is the angle between the TOF axis and the momentum vector. We can also define a time deviation term, δt_x, which is defined as

$$\delta t_x = t_x - t_{0,x} \tag{3.25}$$

We can therefore see that there is a direct relationship between the time deviation and the momentum along the TOF axis. The gradient of the coincidence map gives the ratio between the δt terms for each of two ions, so for ions A^+ and B^+, the gradient of the coincidence map would give the value of $\frac{\delta t_A}{\delta t_B}$. As the values of δt are proportional to the momentum along the TOF axis, we can thus determine what the gradient of the coincidence map should be for a given process. For example, in a two-body dissociation, the two ions are produced with equal and opposite momenta, due to conservation of momentum, which means that the gradient of the signal in the coincidence map would be -1.

For a three-body dissociation of a doubly-charged ion, more effort is required to determine the expected gradient. There are three potential pathways by which a three-body dissociation of a doubly-charged ion can occur. The first is a concerted pathway, in which the three bodies are created instantaneously, in much the same way as for a two-body dissociation. The second is an initial charge separation process, in which the two charges separate in the first step via Coulomb explosion, and one of the charged species goes on to further fragment into a charged and

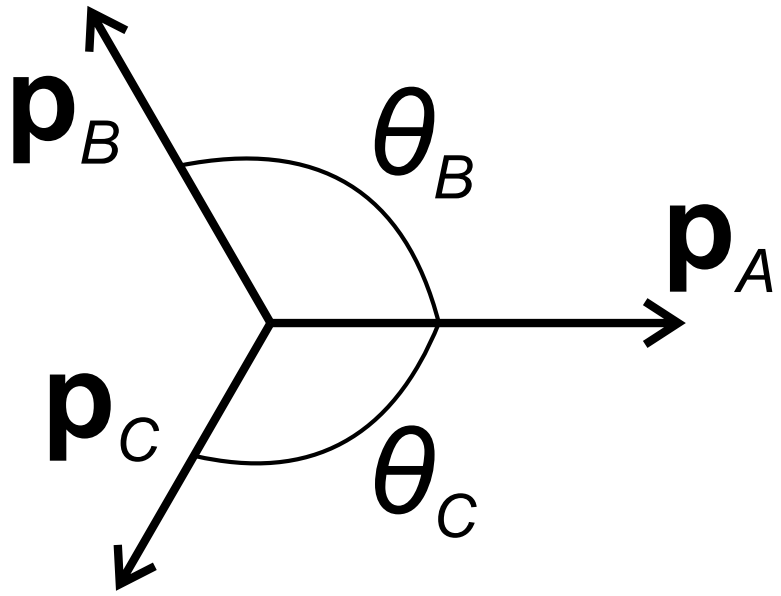


Figure 3.11 The coordinate system used to define a three-body concerted decay, as discussed in the text. The momentum of the three ions A, B, and C must be conserved.

neutral species. The third is a deferred charge separation process, in which the parent ion dissociates into a charged and neutral species, and the charged species then dissociates via Coulomb explosion to produce two ions. Starting with the case of a concerted dissociation, $ABC^{2+} \rightarrow A^+ + B^+ + C$, due to conservation of momentum, the following three statements must be true

$$\boldsymbol{p}_A + \boldsymbol{p}_B + \boldsymbol{p}_C = 0 \tag{3.26}$$

$$|\boldsymbol{p}_A| + |\boldsymbol{p}_B| cos(\theta_B) + |\boldsymbol{p}_C| cos(\theta_C) = 0 \tag{3.27}$$

$$|\boldsymbol{p}_B| sin(\theta_B) + |\boldsymbol{p}_C| sin(\theta_C) = 0 \tag{3.28}$$

$$\tag{3.29}$$

where $\boldsymbol{p}_x$ is the momentum of fragment x, and θ_x is the angle with respect to ion A^+. Note that the coordinate system has been defined such that ion A^+ lies along the x axis, and the other two fragments have zero z component, as shown in figure 3.11.

Due to Coulombic repulsion, the two ions should never be travelling in the same direction. From this, it should be evident that these conditions limit the gradient of the coincidence map to be less than zero, however, we can consider a number of cases for which the gradient can be determined, and hence reduce this range. For example, if we consider a process in which the neutral spectator atom is left with a mean velocity of zero, the momenta of the two ionic fragments will be equal and opposite, leading to a gradient of -1. If we take an extreme in which the neutral fragment obstructs one of the ions until it has left the region of Coulombic repulsion, i.e. it effectively dissociates via an initial charge separation pathway, the gradient will be given by $-\frac{m_{\mathrm{B}}}{m_{\mathrm{BC}}}$, where m_x is the mass of fragment x, as discussed below. Other concerted dissociation pathways should result in intermediate gradients between these two extremes.

For other three-body dissociation pathways, the dissociation takes part in two steps. Thus, it makes sense to define the magnitude of the momentum gained by the two fragments in each step, $\boldsymbol{p}_1$ and $\boldsymbol{p}_2$. For the initial charge separation case, we can define the dissociation pathway as follows

$$\mathrm{ABC}^{2+} \rightarrow \mathrm{A}^{+} + \mathrm{BC}^{+} \rightarrow \mathrm{A}^{+} + \mathrm{B}^{+} + \mathrm{C} \tag{3.30}$$

Ions A^{+} and BC^{+} are created with momentum of magnitude $|\boldsymbol{p}_1|$. However, the BC^{+} ion then undergoes a subsequent fragmentation, which partitions the momentum from the first dissociation into the two fragments. This ratio can be found trivially by evaluating $\frac{\boldsymbol{p}_B}{\boldsymbol{p}_{BC}}$ and $\frac{\boldsymbol{p}_C}{\boldsymbol{p}_{BC}}$ for the two fragments. The three fragments thus have momenta given by

$$\boldsymbol{p}_A = \boldsymbol{p}_1 \tag{3.31}$$

$$\boldsymbol{p}_B = -\boldsymbol{p}_1 \left(\frac{m_B}{m_{BC}} \right) + \boldsymbol{p}_2 \tag{3.32}$$

$$\boldsymbol{p}_C = -\boldsymbol{p}_1 \left(\frac{m_C}{m_{BC}} \right) - \boldsymbol{p}_2 \tag{3.33}$$

Note that this does assume that the BC^+ ion dissociates at a sufficiently large separation from A^+ that there is no appreciable Coulomb repulsion between the two ions. If the BC^+ ion has time to rotate, the mean value of the momentum imparted by the second dissociation step along the direction of $\boldsymbol{p}_1$ is zero. This leads to a gradient in the coincidence map of $-\frac{m_{\mathrm{B}}}{m_{\mathrm{BC}}}$. We can also consider the case where $\boldsymbol{p}_2$ lies along the same vector as $\boldsymbol{p}_1$: where the two vectors point in the same direction, i.e. for the case described in equation 3.32, the gradient is given by

$$\frac{\boldsymbol{p}_B}{\boldsymbol{p}_A} = -\frac{m_{\mathrm{B}}}{m_{\mathrm{BC}}} + \frac{\boldsymbol{p}_2}{\boldsymbol{p}_1} \tag{3.34}$$

In a similar way, when $\boldsymbol{p}_2$ points in the opposite direction to $\boldsymbol{p}_1$, the gradient is given by

$$\frac{\boldsymbol{p}_B}{\boldsymbol{p}_A} = -\frac{m_{\mathrm{B}}}{m_{\mathrm{BC}}} - \frac{\boldsymbol{p}_2}{\boldsymbol{p}_1} \tag{3.35}$$

If the BC^+ ion fragment rotates to a degree before dissociating, the gradient will take an intermediate value between these two extremes.

For a deferred charge separation, we can define the dissociation pathway as follows

$$\mathrm{ABC}^{2+} \rightarrow \mathrm{AB}^{2+} + \mathrm{C} \rightarrow \mathrm{A}^+ + \mathrm{B}^+ + \mathrm{C} \tag{3.36}$$

We can derive the momenta of the three fragments in much the same way as for the initial charge separation case; the momenta have values

$$\boldsymbol{p}_A = \boldsymbol{p}_1 \left(\frac{m_A}{m_{AB}} \right) + \boldsymbol{p}_2 \tag{3.37}$$

$$\boldsymbol{p}_B = \boldsymbol{p}_1 \left(\frac{m_B}{m_{AB}} \right) - \boldsymbol{p}_2 \tag{3.38}$$

$$\boldsymbol{p}_C = -\boldsymbol{p}_1 \tag{3.39}$$

$$\tag{3.40}$$

If the AB^{2+} fragment has sufficient time to rotate before dissociation, the mean value

of $\boldsymbol{p}_1$ will be zero. This is equivalent to adding extra thermal motion to a two-body dissociation, and results in a gradient of -1. Due to the first dissociation step, this process can be distinguished from, say, a concerted dissociation with a stationary neutral spectator by the width of the covariance signal; the first dissociation step should result in a significantly greater broadening than thermal motion. If both $\boldsymbol{p}_1$ and $\boldsymbol{p}_2$ lie along the same vector, the gradient is then given by

$$\frac{\boldsymbol{p}_B}{\boldsymbol{p}_A} = \frac{\boldsymbol{p}_1\left(\frac{m_B}{m_{AB}}\right) - \boldsymbol{p}_2}{\boldsymbol{p}_1\left(\frac{m_A}{m_{AB}}\right) + \boldsymbol{p}_2} \tag{3.41}$$

$$= -1 + \frac{m_{AB}\boldsymbol{p}_1}{m_A\boldsymbol{p}_1 + m_{AB}\boldsymbol{p}_2} \tag{3.42}$$

Again, the gradient can take intermediate values between the two limiting cases, dependent on the geometry of the process. We can see that there is a lot of information that we can obtain from the analysis of a coincidence map, beyond the identity of pairs of ions formed in the same process.

Coincidence analysis can also be used to study fragmentation into a greater number of ions. By using Dalitz plots,[156] it is possible to describe a three-body decay using a 2D scatter plot, as the twelve-dimensional problem (the decay is described by three four-momenta) can be reduced to just two degrees of freedom, as shown in appendix B.2. The technique has been used in a variety of coincidence experiments in the field of particle physics and ion imaging (see [157–166] for example). In a recent example, Ramadhan *et al.*[167] detect three ions produced via the X-ray-induced Coulomb explosion of carbonyl sulphide (OCS), detected using a capacitively coupled film anode detector, which allows the 3D momenta of the ions to be determined. As the experiment was carried out under coincidence conditions, the authors were both able to distinguish the dissociation channels, and to use this information to find the total kinetic energy release for the possible two-body and three-body dissociation pathways from the doubly-charged parent at different excitation energies. They then considered the dissociation of triply-charged OCS using

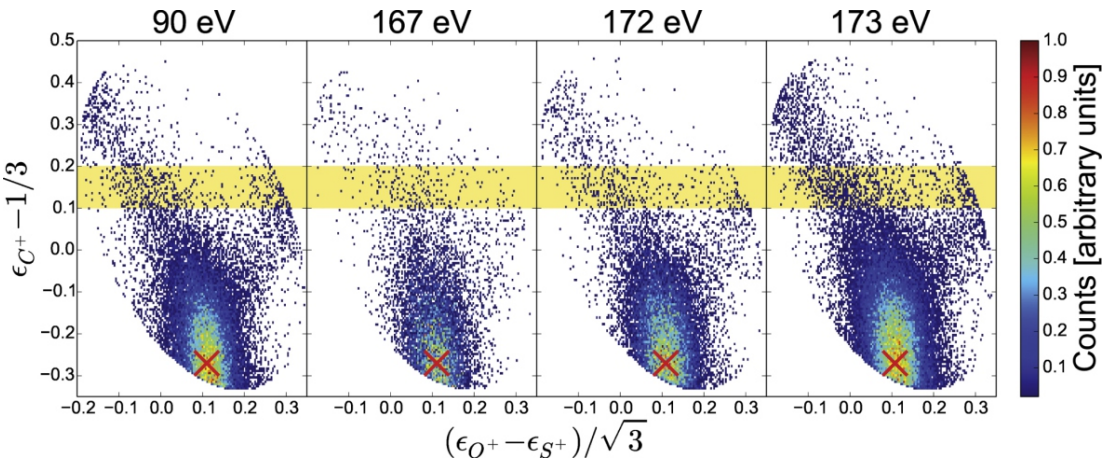


Figure 3.12 Dalitz plot for the dissociation of OCS^{3+} after ionisation by photons of four different wavelengths. The oval shape of the plot arises due to the need to conserve momentum. The intensity in each plot has been normalised such that the maximum is one. The yellow band is used to define an area for further analysis in [167]. Reproduced with permission from [167], © IOP Publishing. All rights reserved. Permission conveyed through Copyright Clearance Centre, Inc., license ID 1066215-2.

a Dalitz plot, as shown in figure 3.12. Different dissociation pathways appear in different regions of the Dalitz plot; in the case of $OCS^{3+} \rightarrow O^+ + C^+ + S^+$, regions of the Dalitz plot indicate the presence of a concerted dissociation mechanism from the ground-state geometry (the region indicated by the red cross in figure 3.12), as well as two sequential dissociation mechanisms (the diagonal features in figure 3.12), which correspond to initial loss of S^+ (top-left to bottom-right) and O^+ (top-right to bottom-left), with the amount of rotation before the second dissociation process determining the location within the feature on the Dalitz plot.

It is clear that coincidence techniques are extremely powerful tools for unpicking the inner workings of molecular dissociation, but they do have limitations. Whilst the technique allows all ions produced to be unambiguously assigned to a given fragmentation channel, this comes with a requirement of a very low count rate per frame to avoid false coincidence. In experiments using high-power lasers or having a relatively low repetition rate, this makes the use of coincidence techniques impractical. It was to overcome these limitation that the first experiment using the

covariance technique[148] was devised.

3.4.2 Covariance maps

Covariance maps are depictions of covariance matrices in graphical form, typically in the form of heat maps or contour plots. To give an example which should be familiar to many chemists, two-dimensional nuclear magnetic resonance (2D NMR) techniques such as correlation spectroscopy (COSY) use covariance maps to show coupling between the nuclear spins of two different atoms. These couplings appear as positive peaks on the off-diagonal of the covariance map. In the field of reaction dynamics, covariance maps are used to display covariance between different signals. In the vast majority of cases to date, the signal used has been the product time-of-flight spectrum, as was initially demonstrated by Frasinski *et al.*[148] Frasinski has also written an excellent review article on this topic recently ([168]), which is recommend to the interested reader.

When studying covariance between time-of-flight signals, it is common for autocovariance maps to be used. In an autocovariance map, covariance is found between a variable and its transpose, i.e. it is described by the following expression:

$$\mathrm{Cov}\left(\mathbf{X}\mathbf{X}^{\intercal}\right) = \left\langle \mathbf{X}\mathbf{X}^{\intercal} \right\rangle - \left\langle \mathbf{X} \right\rangle \left\langle \mathbf{X}^{\intercal} \right\rangle \tag{3.43}$$

This serves to demonstrate covariance between different regions of a function; for example, in a TOF-TOF covariance map (an autocovariance map of a time-of-flight spectum with itself), covariance can be seen between two regions of a time-of-flight spectrum when the two relevant ions are generated in the same process. The diagonal elements in this case correspond to the variance of the signal at that point, given by $\left\langle \mathbf{X}^2 \right\rangle - \left\langle \mathbf{X} \right\rangle \left\langle \mathbf{X} \right\rangle$. As with the coincidence experiments discussed above, the gradient of the TOF-TOF covariance map can be used to gain an insight into the dissociation mechanism of multiply-charged parent ions, which can be used to help elucidate the dissociation mechanism associated with the particular product channel under study.

Partial covariance mapping

TOF-TOF covariance assumes that there is no fluctuation in experimental parameters which could cause correlation between ions independently of the dynamics of the system under study. Realistically, however, this will not be the case for the majority of instruments; in a photolysis experiment for example, variations in the laser intensity cause all ions to be correlated, as the signal level for all ions is proportional to the laser power. Fortunately, statistical methods are available that are able to estimate the *true* covariance map, also known as the partial covariance map, from the measured covariance map and some measured variable experimental parameter[169,170]. The method works by generating a covariance matrix corresponding to the fluctuation, and subtracting this from the previously obtained covariance matrix. A mathematical derivation can be found in [170]; the resulting equation is

$$\mathrm{pCov}\left(\mathbf{X},\mathbf{Y};P\right)=\mathrm{Cov}\left(\mathbf{X},\mathbf{Y}\right)-\frac{\mathrm{Cov}\left(\mathbf{X},P\right)\mathrm{Cov}\left(P,\mathbf{Y}\right)}{\mathrm{Cov}\left(P,P\right)} \tag{3.44}$$

where $\mathrm{pCov}\left(\mathbf{X},\mathbf{Y};P\right)$ is the partial covariance matrix, independent of the fluctuating experimental parameter, P, and $\mathrm{Cov}\left(\mathbf{X},\mathbf{Y}\right)$ is the covariance between X and Y as defined previously. Note that as P has a single value on each acquisition cycle, $\mathrm{Cov}\left(\mathbf{X},P\right)$ will be a vector, and $\mathrm{Cov}\left(P,P\right)$ will be a single value, the variance of P. Partial covariance mapping is not limited to a single fluctuating parameter; Zhaunerchyk *et al.* have also derived equations to allow this analysis to be carried out when there are multiple fluctuating parameters.[171]

Partial covariance is particularly useful when analysing data from an experiment in which there is significant variation in an experimental parameter. For example, when using high-energy lasers, such as free-electron lasers, the pulse energy can vary shot-to-shot power by an order of magnitude or more, in which case there is significant benefit in using this technique. In our experiment, we have not implemented a way of measuring experimental fluctuations of either the electron beam or the

gas density in the interaction region at present, but believe we may be able to use a function of the total signal intensity recorded in each acquisition cycle, which should be a function of any fluctuating parameter. We plan to explore this method in more detail in the near future, once we have implemented code to allow partial covariance analysis to be carried out.

Triple covariance

So far we have only considered covariance between two bodies but, as with coincidence experiments, it is also possible to study three-body dissociation events. For this, the expression for covariance given in equation 3.22 can be modified to include a third term, i.e.

$$\mathrm{Cov}\left(\mathbf{XYZ}\right) = \left\langle \left(\mathbf{X} - \left\langle \mathbf{X} \right\rangle\right)\left(\mathbf{Y} - \left\langle \mathbf{Y} \right\rangle\right)\left(\mathbf{Z} - \left\langle \mathbf{Z} \right\rangle\right) \right\rangle \tag{3.45}$$

$$= \left\langle \mathbf{XYZ} \right\rangle - \left\langle \mathbf{XY} \right\rangle \left\langle \mathbf{Z} \right\rangle - \left\langle \mathbf{XZ} \right\rangle \left\langle \mathbf{Y} \right\rangle - \left\langle \mathbf{YZ} \right\rangle \left\langle \mathbf{X} \right\rangle + 2 \left\langle \mathbf{X} \right\rangle \left\langle \mathbf{Y} \right\rangle \left\langle \mathbf{Z} \right\rangle \tag{3.46}$$

where $\mathbf{Z}$, like $\mathbf{X}$ and $\mathbf{Y}$, is some function or variable, typically the time-of-flight spectrum in the field of reaction dynamics. The technique was first applied in this context by Frasinski *et al.*,[172] who studied the dissociation of N_2O prepared in a multiply-charged state by multiphoton ionisation. The authors explain that the three-dimensional covariance map has one autocorrelation line, and three autocorrelation planes, and that each feature will have sextuple repetition in the covariance map, as there is symmetry in each of the autocorrelation planes. Zhaunerchyk *et al.* have also derived a general expression to describe partial covariance in three dimensions[171].

It is also worth noting that, whilst covariance analysis is a powerful technique, it does suffer from signal-to-noise issues.[172] With a detection efficiency of 50%, only 12.5% of the time will all three ionic fragments be detected, and this number rapidly falls off with decreasing detection efficiency. However, once one ion has been detec-

ted, there is a 25% chance of detecting the other two. Coupled with the relatively low frequency of three-body dissociation events forming three charged fragments in our experiments, we have yet to successfully utilise this technique, but hope to be able to in the future.

Now that we have established what can be achieved by considering covariance between time-of-flight spectra, we turn our attention to ion imaging. As we are using a sensor with multi-mass imaging capabilities, it follows that it should also be possible to find covariance between images recorded at different arrival times, i.e. for ions with different mass-to-charge ratios, as signal is recorded for both arrival times within the same acquisition cycle, which is a requirement for both coincidence and covariance techniques to be used. This is indeed the case; we now discuss the covariance technique in relation to ion images.

3.4.3 Extension to ion images

Covariance mapping was used by Hansen *et al.* to extract angular correlation information from 2D ion images.[173] In their experiment, in which they studied laser-induced torsion of the axially chiral biphenyl molecule 3,5-difluoro-3′,5′-dibromo-4′-cyanobiphenyl, the molecules first passed through an electrostatic deflector which deflected the molecules according to their effective dipole moment, before being adiabatically aligned by an elliptically polarised infra-red (IR) laser. A second IR laser was used to induce torsional motion in the molecule, then a third IR laser was used to probe the structure by inducing coulomb explosion via strong-field ionisation. Ion images of F^+ and Br^+ were recorded using a CCD camera; for the covariance analysis, the x and y coordinates of all ion hits of the ion of interest were recorded on a shot by shot basis.

As noted previously, the molecules are aligned, but this does not define the orientation of the molecule, it just defines the axis to which the dipole moment is confined. As shown in figure 3.13, if the principal axis of symmetry lies in the

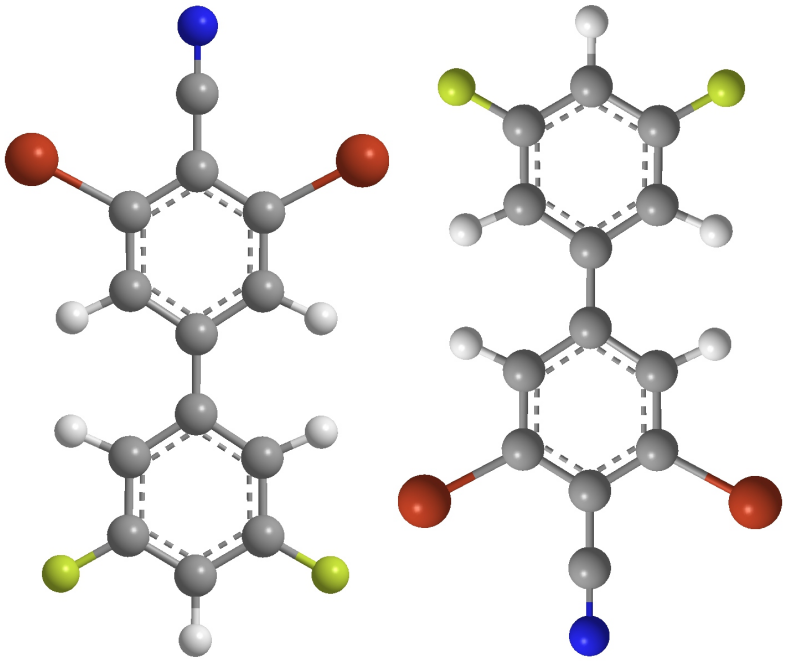


Figure 3.13 The two possible orientations of an aligned chiral biphenyl molecule. Note that there is still free rotation of the molecular entity about the vertical axis.

vertical direction, i.e. either the fluorine atoms are both on the upper phenyl ring and the bromine atoms on the lower phenyl ring or vice versa; the summed ion images will show contributions from both orientations. However, by calculating an autocovariance map of the angular distribution of their ion images in the same way as the TOF-TOF covariance maps discussed above, the contributions from the two different orientations could be disentangled. Covariance was seen between pairs of angles corresponding to both ions up or both ions down, but not between angles on the top and bottom.

In a collaboration with members of the Pixel Imaging Mass Spectrometry (PImMS) consortium,[174–176] this work was further developed to exploit the unique capabilities of the PImMS sensor, resulting in the advent of the recoil-frame covariance technique.

3.4.4 Recoil-frame covariance

Recoil-frame covariance is a recently-developed analysis technique which allows us to create an image depicting the velocity vectors of an ion of interest with respect to a second reference ion, where the two ions have originated from the same molecule. The technique requires that ion images are recorded for both ions of interest on each experimental cycle, so is reliant on the use of a multi-mass imaging sensor such as the PImMS sensor[88] to record the data.

Figure 3.14 shows the steps used to produce a recoil-frame covariance map, in this case the dissociation of XY^{2+} to give X^+ and Y^+. Firstly, we acquire n experimental cycles of data using the PImMS camera. A reference ion and an ion of interest are then chosen; in this case Y^+ is chosen as the reference ion. The mean ion image for each ion is then determined, i.e. we sum the ion hits across all experimental cycles, and divide by the number of experimental cycles to give mean ion images, as shown in figure 3.14(b). Note that the mean ion image has been represented schematically in the form of rings for clarity; in reality, all representations of ion images are confined to a pixel grid. We then take the ion hits for the i^{th} experimental cycle of the dataset (figure 3.14(c)) and define a reference direction, in this case to the right. The ion images for the experimental cycle are then rotated as shown in figure 3.14(d), so that in each case one of the reference ions lies along the reference direction. The ion images of the ion of interest at each orientation are then summed; this is repeated for each experimental cycle of the dataset to give the $\langle \mathbf{YX} \rangle$ term, shown on the left of figure 3.14(e). This gives us the true covariance, plus the false covariance from all ions which were not generated from the same molecule as the reference ion. Then, using the mean ion images rather than the ion image for each experimental cycle, the same process is repeated to give the $\langle \mathbf{Y} \rangle \langle \mathbf{X} \rangle$ term, giving us the false covariance; this is then subtracted from the $\langle \mathbf{YX} \rangle$ image to give the recoil-frame covariance map.

In this example case, we can see that the X^+ and Y^+ ions recoil in a straight line.

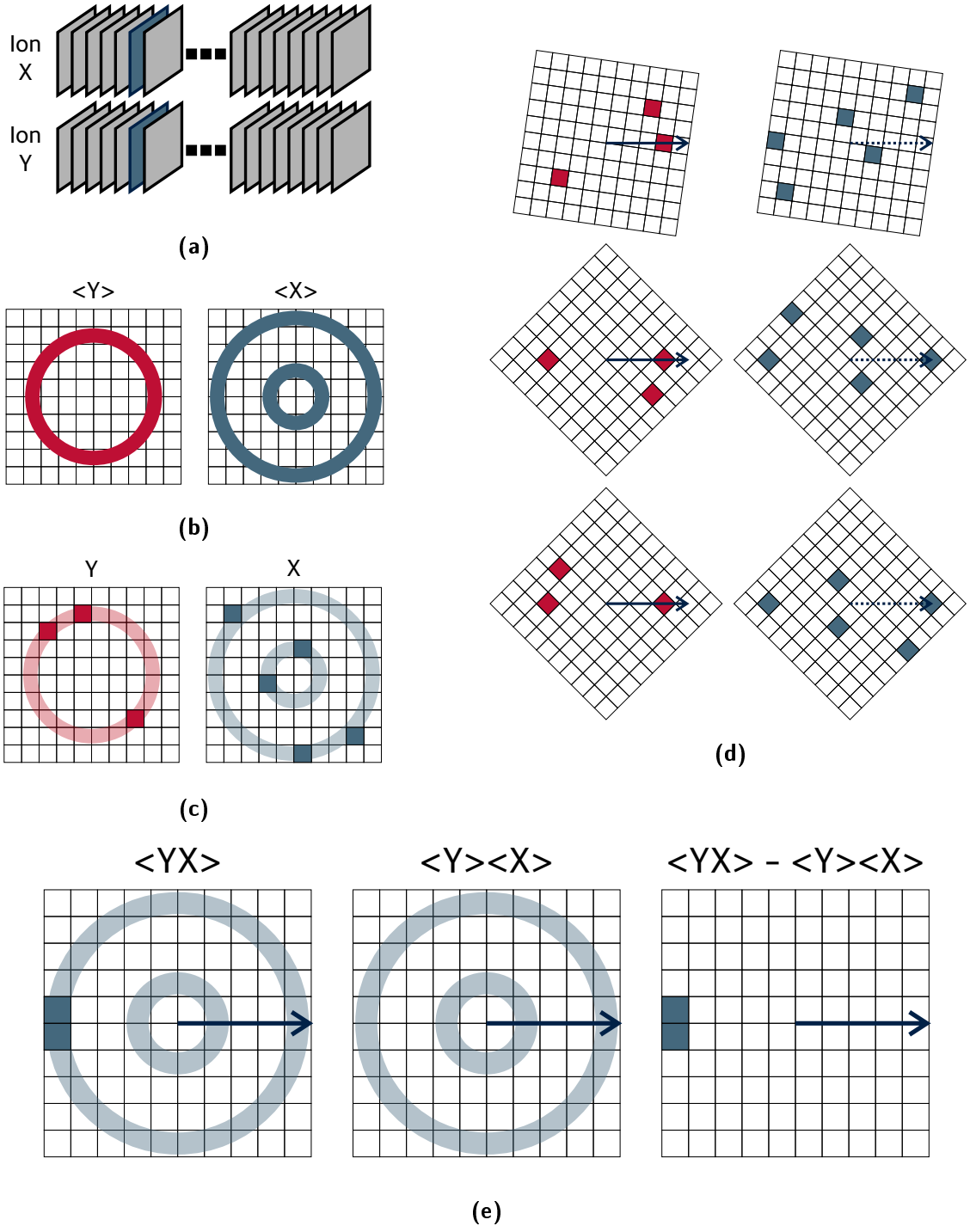


Figure 3.14 An example of the process used to create a covariance map, in this case for the process $XY^{2+} \rightarrow X^{+} + Y^{+}$ with Y^{+} being defined as the reference ion. n experimental cycles are recorded (a) and the mean ion images calculated (b). For each experimental cycle (c, with (b) superimposed), the two images from the experimental cycle are rotated into all orientations where the reference ion, Y^{+}, lies along a chosen reference direction (d). The rotated ion images of X^{+} are then summed, and this process repeated for all experimental cycles to give $\langle \mathbf{YX} \rangle$. (d) is repeated for the mean ion images (b) to give $\langle \mathbf{Y} \rangle \langle \mathbf{X} \rangle$, which is then subtracted from $\langle \mathbf{YX} \rangle$ to give the recoil-frame covariance map (e).

This is true of all two-body dissociations, as momentum must of course be conserved. We only see covariance between ions produced from the same parent molecule, so we can also conclude that the outer ring in the ion image of X^+ corresponds to the charge separation process, whereas the inner ring corresponds to a different process which does not produce Y^+. By running the analysis in reverse (i.e. choosing ion X^+ as the reference ion), it is possible to compare the momenta of the fragments, which in some cases can give further insight into the dissociation process. As will be seen later in this work, recoil-frame covariance is capable of pulling out even relatively minor channels from the data. Evidently, recoil-frame covariance has the potential to be a powerful technique, further extending the application of the velocity-map imaging technique. One final point to note is that the full covariance matrix in the case of two ion images would have four dimensions, and the recoil-frame covariance image could in principle be projected out of this. By using the method described above, however, only two dimensions are required, greatly reducing the computational requirements of the calculation.

A number of the useful features of covariance can be demonstrated using simulated data. The advantage of using simulated data for this purpose is that we know precisely what input we have provided, so we can interpret the results in the light of this knowledge. In the following section, we will first establish consistency between TOF-TOF and recoil-frame covariance calculations, then explore what the recoil-frame covariance maps look like in various situations. We will also use the simulations to establish the meaning of negative covariance in the context of recoil-frame covariance. There has been much discussion of the meaning of negative covariance in the literature; a definitive statement on the matter appears in Frasinski's covariance review,[168] where he argues that there is no negative covariance between fragments produced in competing pathways; the two dissociations are statistically independent. He also argues that negative covariance may appear as a result of experimental fluctuations. However, the meaning of negative covariance in

recoil-frame covariance maps is less well understood.

3.4.5 Characterisation of recoil-frame covariance analysis

Initially, a very simple simulation is used, in this case for a two-body dissociation, $AB^{2+} \rightarrow A^+ + B^+$, with the assumption that all ions are detected. Ions A^+ and B^+ are given a velocity in a random direction with a magnitude of 100 image pixels[a] (100 px) and 80 px, respectively. One molecule dissociates in each acquisition cycle, and a total of 100,000 acquisition cycles are simulated. This means that we expect to see one covariance event in each acquisition cycle, and no false covariance. Simulated data is used so that we know exactly what process we are studying, allowing us to more easily interpret the results we obtain. The plotted images for the simulations all have dimensions of 324 px by 324 px, to match the dimensions of the PImMS sensor.

The first thing to check is that the analysis codes used to carry out recoil-frame and TOF-TOF covariance analysis are consistent with one another. The total intensity of the recoil-frame covariance image for an ion pair should be equal to the total intensity of the corresponding off-diagonal element in the TOF-TOF covariance map (the equivalent to taking the TOF-TOF covariance between the two time ranges used in the recoil-frame covariance calculation). The two sums should be equal, as the number of each ion in each acquisition cycle is the same in both cases. This is indeed the case. We have also manually calculated the expected results for a simple case, and found that the results match those of the analysis codes, which gives us confidence that there are no errors in either the recoil-frame or TOF-TOF covariance analysis codes.

Once we have convinced ourselves that the code we are using is valid, we can begin to determine how the recoil-frame covariance images should be interpreted.

[a]Whilst pixels are not strictly a unit of velocity, remember that the radius is proportional to the velocity, hence this is not an unreasonable step. Working in pixel units also makes the simulations easier to understand.

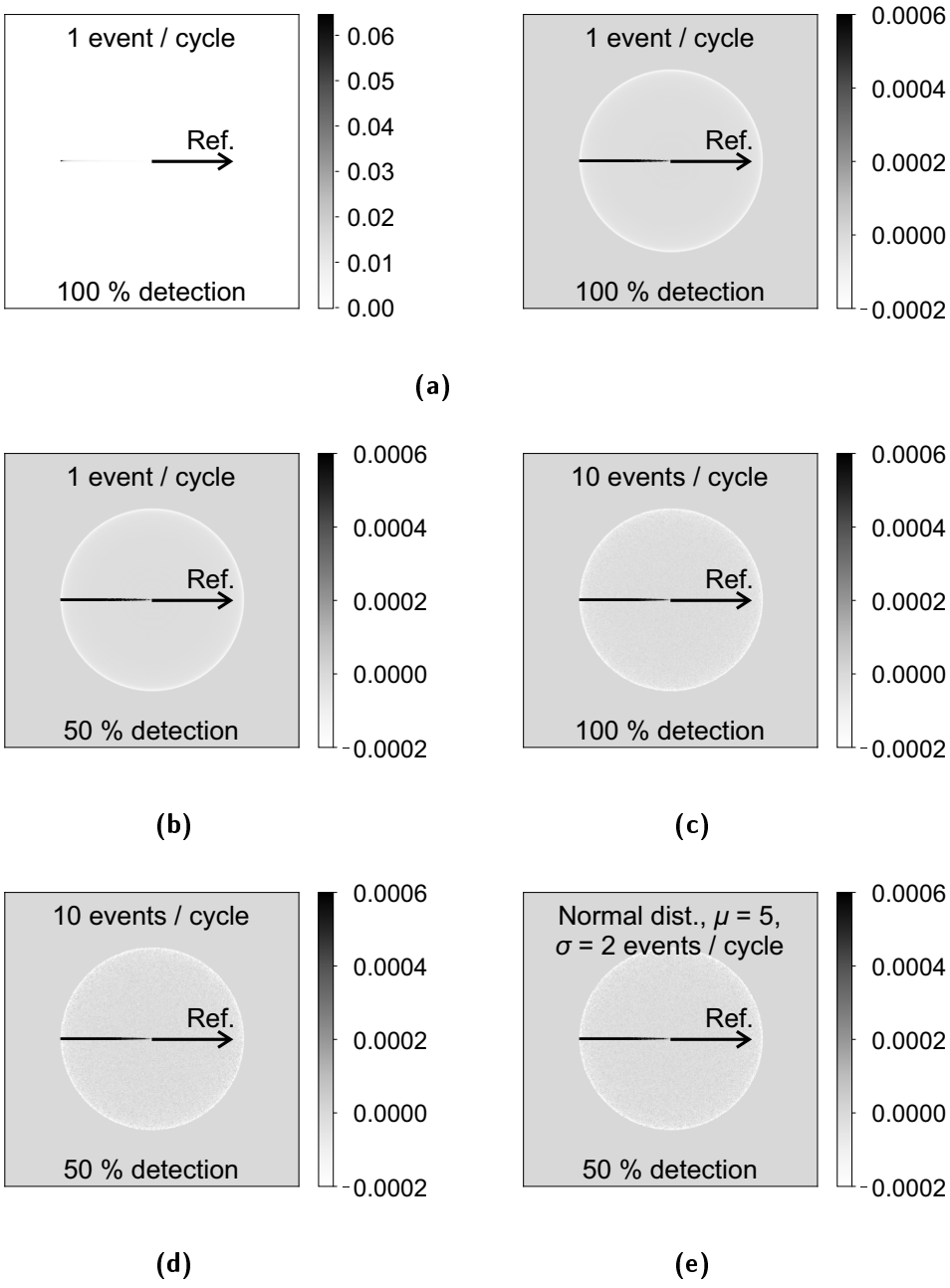


Figure 3.15 Recoil-frame covariance maps obtained for simulated data, for the dissociation $AB^{2+} \rightarrow A^{+} + B^{+}$. a) shows results for one dissociation event per experimental cycle with 100% detection efficiency (left: full-range colour scale, right: fixed colour scale, with maximum intensity approximately 100 times less than the maximum intensity in the image, used for the remaining subfigures), b) is the same as a), but with 50% detection efficiency, c) is the same as a), but with ten dissociation events per experimental cycle, d) shows results for ten dissociation events per frame with 50% detection efficiency, and e) shows results for a variable number of dissociation events per experimental cycle (mean five, standard deviation two) with 50% detection efficiency.

For the covariance analysis in this section, ion B^+ is used as the reference ion, and ion A^+ is the signal ion. For display purposes, the recoil-frame covariance images have been normalised such that all positive intensity sums to one. The reasoning behind this will be discussed later in this section, but it does allow the images to be displayed on a consistent colour scale, making the results easier to interpret. Using the simulated data described above results in the recoil-frame covariance image shown in figure 3.15(a). We see that there is a very clear positive covariance in the opposite direction to the reference direction, and negative covariance at all other points accessible by the signal ion. Note that, instead of seeing a sharp feature at a radius of 100 (the radius at which A^+ appears), we see a tail extending to the centre of the image. This is due to the fact that the recoil-frame covariance method rotates vectors of all covariant A^+ ions to lie relative to the corresponding B^+ ion, which does not change the intrinsic radial distribution of the scattering distribution. Consider, for example, a molecule dissociating in a direction perpendicular to the plane of the detector. The two ions are created in the same process, so will be covariant, but will strike the same position on the detector. At the other extreme, if the molecule dissociates in the plane of the detector, the ions produced will strike the detector at a radius corresponding to their velocities. Depending on the orientation of the dissociating molecule, any intermediate velocity projection between these two extremes can be accessed.

The covariance analysis does not change the magnitude of the vector describing the ion hit, just its direction, hence any signal in the recoil-frame covariance image will have the same radial distribution as the scattering distribution of the covariant ions. For a two-body dissociation with an isotropic scattering distribution, for example, the positive covariance will have the same distribution as the 2D projection of a sphere. This is the idea on which the inversion method we have developed, which will be discussed in detail in section 3.5.

We see that any changes made to the simulation, for example decreasing the

detection efficiency to 50%, increasing the number of events to ten per experimental cycle, or effecting both changes simultaneously, shown in figures 3.15(b), 3.15(d), and 3.15(d), respectively, leads to no real change in the normalised covariance image. This is to be expected, as the process under study is exactly the same. If the recoil-frame covariance images are not normalised, changing to a 50% detection efficiency results in the magnitude of the covariance decreases by a factor of four, as only in one in four cases are both the reference and signal ion for a given dissociation event detected in a single acquisition. Increasing the number of molecules dissociating by a factor of ten similarly increases the magnitude by a factor of ten, as ten times more covariant events are observed on each acquisition cycle.

We can also vary the number of molecules dissociating on each acquisition cycle; figure 3.15(e) shows the resulting recoil-frame covariance images from a simulation in which the number of molecules dissociating in each experimental cycle is given by a normal distribution with a mean of five and standard deviation of two, with a 50% detection efficiency. Again, the normalised covariance image is almost identical to those discussed previously, and the non-normalised intensity scaled relative to the case with a single event per acquisition cycle by a factor of five. The resulting covariance images are all consistent with each other, and we interpret the images in the following way: the covariance maps essentially reveal how the signal varies with respect to the mean. In the case of a two-body dissociation occurring with no dependence on orientation, the mean appears as the projection of a spherical shell onto the detector. Once the data from each cycle have been rotated such that the reference ion lies along the reference direction, we are more likely to find the partner ion directly opposite the reference ion than anywhere else. This leads to a greater number of ions than the mean appearing opposite the reference direction, leading to positive covariance, whilst in all the other directions there are fewer ions found than in the mean image, leading to negative covariance. This allows us to determine the dynamics of the two ions with respect to one another. We also use this to justify

the normalisation we have applied to the images; the positive covariance gives us the relative velocity distribution of the two ions, and this can be thought of as a probability distribution. The negative covariance can also be considered in a similar way, giving the probability an ion will not land with a particular relative velocity in comparison to that expected from the mean image.

Of course, for a polyatomic molecule it is unlikely that there will only be a single dissociation channel, so we can add other channels as well. Figure 3.16 shows the recoil-frame covariance image obtained for a system in which the following three dissociation channels are available:

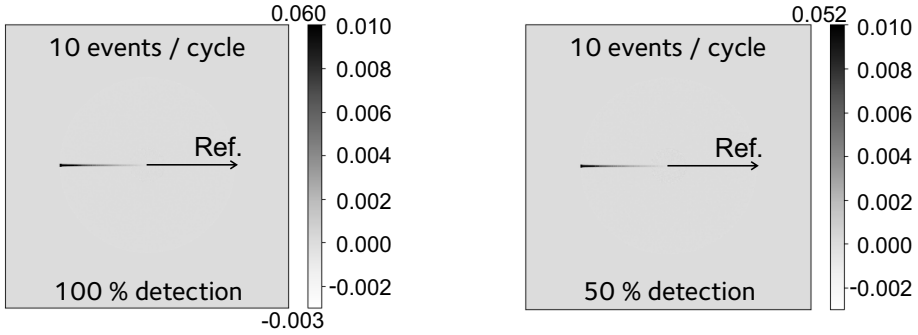
$$AB^+ \rightarrow A^+ + B \tag{3.47}$$

$$AB^+ \rightarrow A + B^+ \tag{3.48}$$

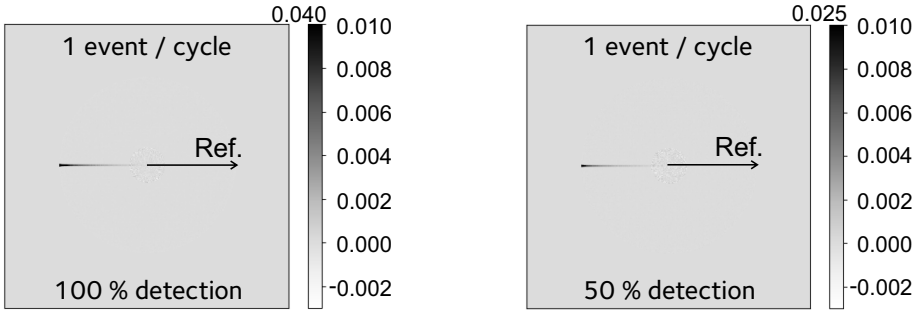
$$AB^{2+} \rightarrow A^+ + B^+ \tag{3.49}$$

where channels 3.47 and 3.48 occur with a frequency of five and ten events per acquisition cycle, respectively, and channel 3.49 occurs at either 0.1, one, or ten events per acquisition cycle. For the 0.1 case, a random number is generated for each acquisition cycle, and if it is less than 0.1, a molecule dissociates. Ion A^+ produced via channel 3.47 appears at a radius of 20 px, ion B^+ produced via channel 3.48 appears at a radius of 40 px, and channel 3.49 is unchanged from the previous simulation. The B^+ ion is again used as the reference ion for the covariance analysis. In all cases, we see that the signal in the area of the recoil-frame covariance image corresponding to the non-covariant channels go to zero. This makes complete sense, as there is no correlation between the two ions, and hence there should be no difference between the contribution to the two terms of the covariance expression; there is, on average, no deviation from the mean. We also see that, as the number of covariant frames per experimental cycle decreases, the signal from the covariance becomes much weaker with respect to the statistical noise arising from the false covariance subtraction.

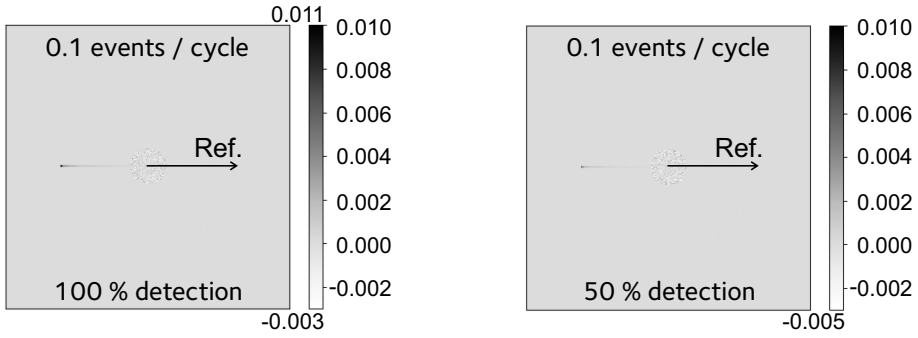
We can conclude that recoil-frame covariance images give us information purely



(a)



(b)



(c)

Figure 3.16 Recoil-frame covariance maps obtained for simulated data, for the dissociation consisting of channels 3.47 to 3.49, at a frequency of ten, five, and either ten (a), one (b) or 0.1 (c) events per experimental cycle, respectively. Left and right figures are for 100% and 50% detection efficiency, respectively. If the maximum or minimum intensity of the image is outside the bounds of the colour scale, the value is given above or below the colour bar, respectively.

on covariant channels, and the positive and negative covariance seen in the image then describes the dynamics of the dissociation within the covariant channel. As far as we are concerned, this is entirely consistent with Frasinski's arguments on TOF-TOF covariance maps, that competing channels are independent of one another, resulting in zero covariance for those channels.

So far we have only discussed two-body dissociation. Whilst this mechanism is often a dominant pathway in the dissociation of doubly-charged ions, it is by no means the only pathway available, and becomes less and less important as the initial charge of the molecule increases. We will now consider three-body dissociation pathways, which are frequently observed in our data.

Three-body dissociation

As we have previously established, there are three potential pathways by which a three-body dissociation of a doubly-charged ion can occur: a concerted dissociation in which the three fragments are generated in a single step; an initial charge separation process, where the ion undergoes Coulomb explosion into two fragments in an initial dissociation step, followed by the loss of a neutral fragment from one of the ions; and a deferred charge separation process, where a doubly charged ion loses a neutral fragment, before undergoing a subsequent Coulomb explosion. We have already established that we are able to distinguish between these processes by using the gradient of a TOF-TOF covariance map; now we will determine the extent to which we can distinguish the three pathways through their recoil-frame covariance images, to further support the assignments.

The dynamics observed for a concerted dissociation mechanism vary, and are determined by the structure of the dissociating molecule. The two detected ions are no longer constrained by conservation of momentum to lie on the same vector. As we take a 2D projection of the scattering distribution, in the covariance image we will see a shell at a radius dictated by the velocity with which the ion is produced,

provided the two ions are produced with well-defined velocity. The angle at which the two ions travel away from each other can be determined from the angle which describes the arc made by the 2D projection of the shell. If the covariance analysis is carried out using each of two covariant fragments as a reference, it is then possible to determine the momentum of the neutral fragment in this manner.

To probe the differences between the two two-step processes, we employ a further set of simulations. For the initial charge separation process

$$ABC^{2+} \rightarrow A^{+} + BC^{+} \rightarrow A^{+} + B^{+} + C \tag{3.50}$$

ion A^{+} is given a velocity of 80 px, and ion BC^{+} a velocity of 100 px in the first step, and the dissociation can occur with any orientation. In the second step, B^{+} is given a velocity of 30 px, and the dissociation can again occur with any orientation. For the deferred charge separation processes

$$ABC^{2+} \rightarrow AB^{2+} + C \rightarrow A^{+} + B^{+} + C \tag{3.51}$$

ion AB^{2+} is given a velocity of 30 px in the first step, and the dissociation can occur with any orientation. In the second step, A^{+} is given a velocity of 80 px, B^{+} is given a velocity of 100 px, and the dissociation can again occur with any orientation. Both simulations were carried out in 3D space, and a 2D projection was taken once both dissociation steps had been accounted for. The simulations were carried out over 100,000 experimental cycles, and five ABC^{2+} molecules were made to dissociate in each frame. The neutral C fragment would not be detected in an experiment, so it is not included in the simulation.

Figure 3.17(a) shows the scattering distribution for the two ions generated via an initial charge separation dissociation pathway. We can see that A^{+} has a well-defined velocity, but B^{+} has a much less well-defined velocity distribution, due to the extra dissociation step leading to its production. Figure 3.17(b) shows the recoil-frame

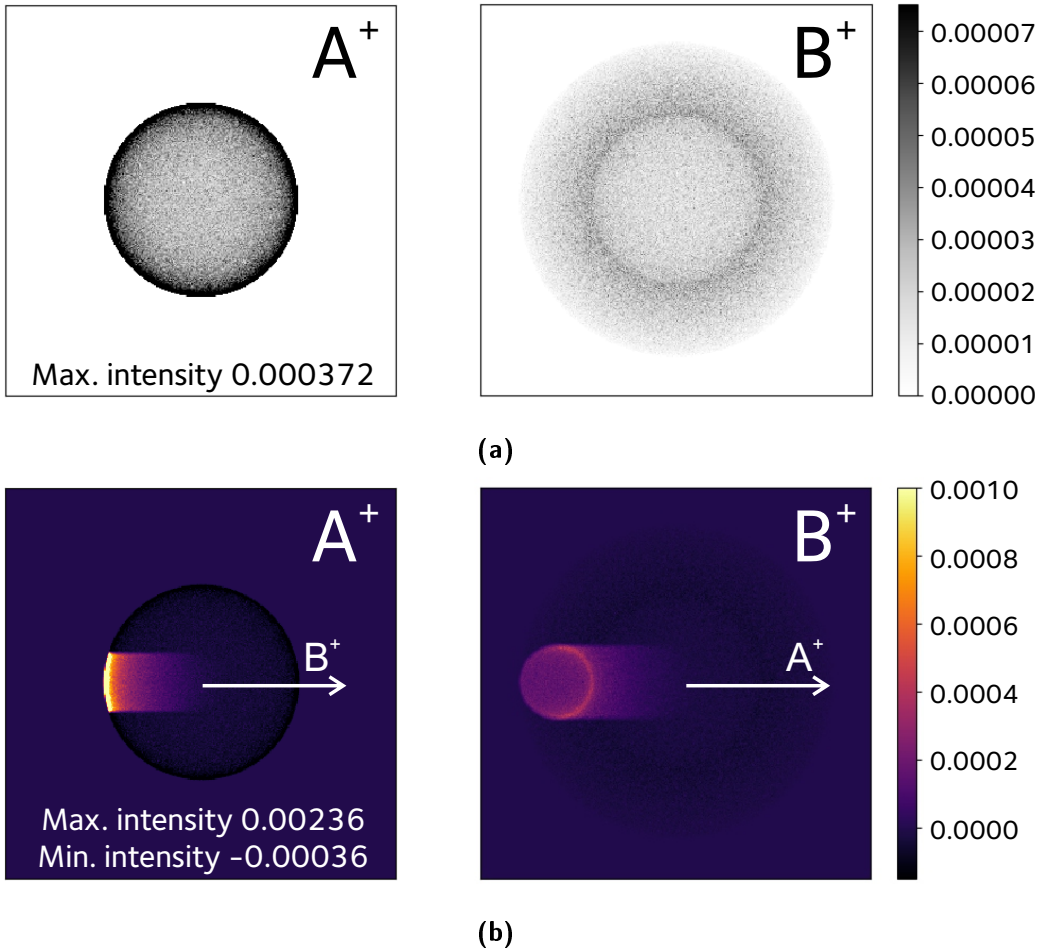


Figure 3.17 Results for the simulation of a three-body dissociation with initial charge separation for the simulated data discussed in the text. a) shows the scattering distribution for each ion, and b) shows the recoil-frame covariance image for each ion with respect to the other. Where an image is saturated on the colour scale, this is noted on the image.

covariance images for each ion with reference to the other. We can immediately notice that some of the properties discussed previously, namely the distribution of positive and negative covariance, and the presence of a 'tail' resulting from taking a 2D projection of the scattering distribution, are present. The covariance image for B^+ with reference to A^+ (right of figure 3.17(b)) shows a sphere of 30 px radius centred on a point 100 px opposite to the reference direction. This is no surprise, as the reference ion undergoes no further fragmentation, and thus only the fragmentation of the BC^+ ion changes the covariance image. The covariance image for A^+ with reference to B^+ (left of figure 3.17(b)) appears as a shell with a maximum

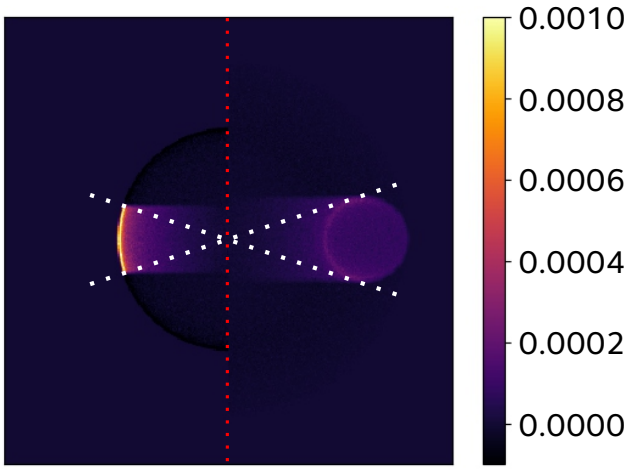


Figure 3.18 A depiction of the angular relationship between a pair of covariant fragments. The left hand side of the two images in figure 3.17(b) have been taken and combined into a single image. The centre of the image has been marked by a dotted red line, and the maximum angle at which signal is observed with respect to horizontal has been marked with dotted white lines.

radius dictated by the energy imparted to the ion in the charge separation step. The fact that a shell is observed, rather than a point, is due to the subsequent dissociation of the co-fragment, which means that the two ions are no longer confined to lie on the initial dissociation vector. This can be seen clearly in figure 3.18. In this figure, the left hand side of the two covariance images from figure 3.17(b) have been plotted in the same image, with one of the covariance images flipped along the vertical axis. The white dotted lines show the maximum radial extent of the two covariance images with respect to the horizontal, and it can be seen that they cross at the centre of the image, marked by the red dotted line. Incidentally, if an ion A^+ and B^+ are detected in the same experimental cycle, the two must lie on a vector passing through the centre of the image in this plot.

Figure 3.19(a) shows the scattering distribution for the two ions generated via a deferred charge separation dissociation pathway. Both scattering distributions have a similar appearance, and are also similar to that observed for ion B^+ in the initial charge separation case. This should come as no surprise, given that in all three cases the scattering distribution is effectively blurred out by 30 px with

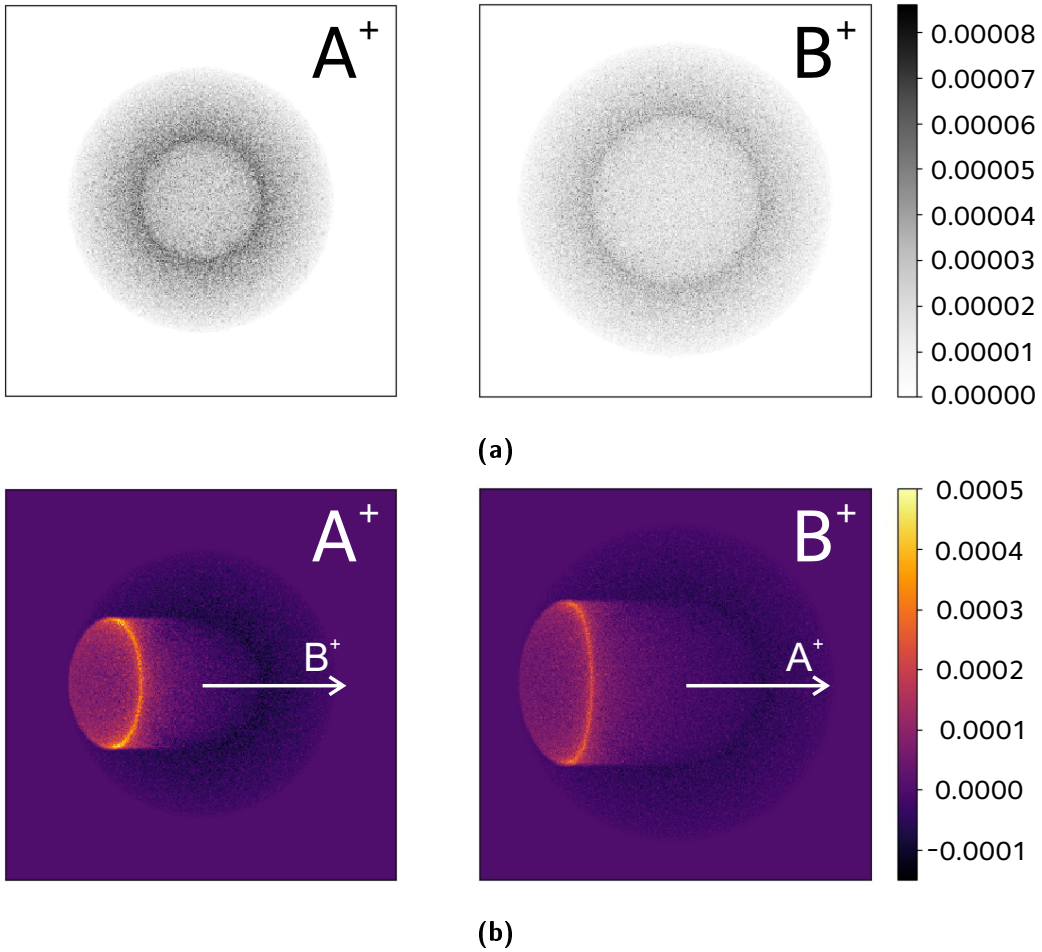


Figure 3.19 Results for the simulation of a three-body dissociation with deferred charge separation for the simulated data discussed in the text. a) shows the scattering distribution for each ion, and b) shows the recoil-frame covariance image for each ion with respect to the other.

respect to a two-body dissociation by the loss of a neutral fragment. Turning to the covariance images, shown in figure 3.19(b), we see quite a different result than that obtained from the initial charge separation case. In this case, we see an oval-shaped distribution in both cases. We can justify this by considering the two potential vector diagrams shown in figure 3.20. In the top case, both dissociation steps occur along the same vector, which will result in signal being along the x axis of the covariance image, with the magnitude of the spread dictated by the velocity imparted on the doubly-charged ion in the first dissociation step, in this case 30 px. If the first dissociation step occurs perpendicular to the Coulomb explosion axis, as shown in

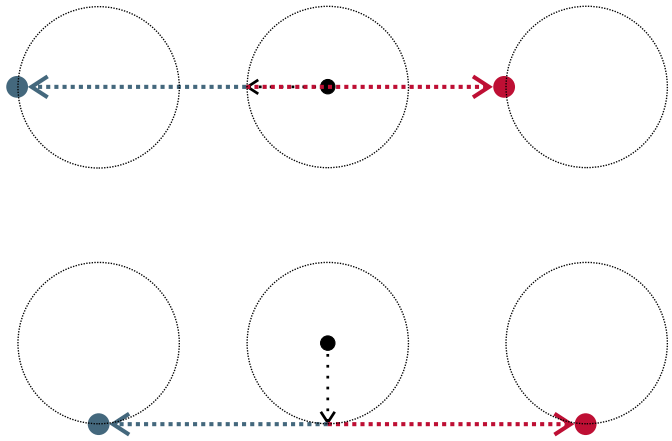


Figure 3.20 Two vector diagrams describing a deferred charge separation process in the plane of the image. The black dot shows the centre of the image, the black dotted arrow the doubly-charged ion's velocity from the first dissociation step, and the coloured dotted arrows the velocity vectors of the two ions from the Coulomb explosion step. The dotted circles have a radius equal to the velocity imparted by the first dissociation step, and are centred on the centre of the image, and the positions the two ions would reach if the Coulomb explosion occurred from the centre of the image.

the lower example in figure 3.20, we see that a rotation is required to make, say, the red ion lie along the reference direction, and this rotation will mean that the covariance image will appear as an oval, rather than a sphere.

These simulations show that, in principle at least, it should be possible to distinguish between the three potential pathways based on the recoil-frame covariance images. In practice, it is slightly more tricky than this, as the velocities imparted on the fragment by each dissociation step are generally not explicitly known, and also usually span a distribution. This may make it harder to distinguish the features, particularly if the loss of a neutral does not change the velocity of the ion fragment by a very significant degree. Nonetheless, this should give us more confidence in the assignment of a mechanism to a given dissociation channel. Finally, at present, we have only considered an isotropic case. We see no reason why the results should differ for an isotropic and anisotropic case, but intend to run simulations for an anisotropic case in future.

3.5 Inversion of recoil-frame covariance images

As previously discussed, existing inversion methods are unable to invert covariance images, as the covariance analysis removes the axis of cylindrical symmetry from the image. We are also unable to invert the images prior to carrying out covariance analysis: the covariance analysis is carried out separately on the data from each acquisition cycle, and the results are then summed to give the overall covariance image. In order to perform an Abel inversion, the data from many acquisition cycles must be summed prior to the inversion, since the inversion algorithms tend to be very sensitive to noise. Therefore, we cannot perform the covariance analysis on the inverted images, since we have already averaged the data over all acquisition cycles. Thus, the covariance image for, say, the products of a two-body dissociation will not appear as a single point but, as we have seen in our simulations above, as a point of maximum intensity at some radius, with a decay in intensity towards lower radii. If we could somehow manage to remove this tail, and determine both the radial and angular distribution of the covariance image, this would allow us to make a much more quantitative analysis of the data.

It is worth first understanding exactly what we obtain following covariance analysis. To gain an insight into this, we can use simulations in three-dimensional space, allowing us to effectively carry out the covariance analysis in three-dimensional space. We will use a deferred charge separation process for this purpose, more precisely the data set used in figure 3.19, where ion A^+ is the reference ion, and B^+ is the signal ion. Note that we have made a change such that only a single molecule dissociates in each acquisition cycle, and have not carried out a subtraction of false covariance. As we are using simulated data, we know the exact coordinates of both ions in 3D space.

To begin with, we will pretend we are carrying out the rotation of ion A^+ to the reference direction (the x axis) as if we had taken a 2D projection, i.e. we will rotate

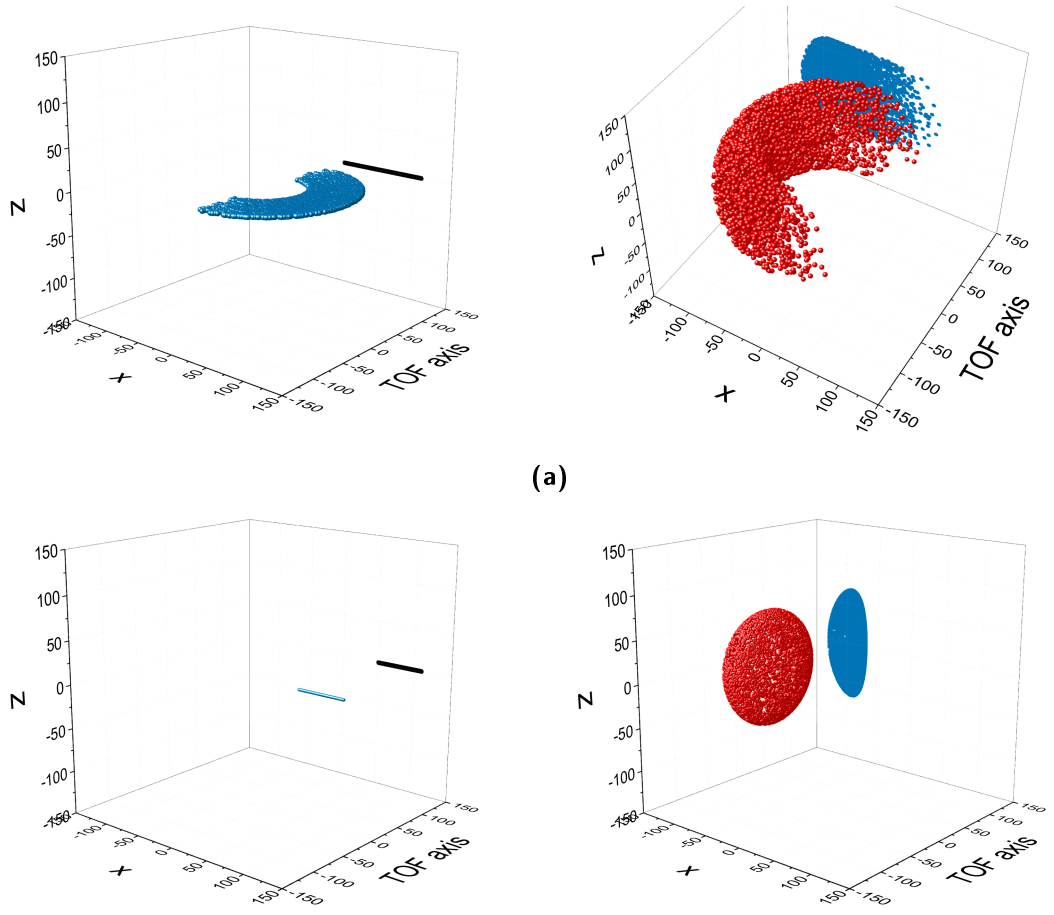


Figure 3.21 Examples of the results of covariance analysis plotted in three dimensions for the deferred charge separation process shown in figure 3.19. Left images depict the reference ion, and right images the signal ion. The projection in the xz plane is shown behind each distribution. (a) shows what the distribution of the covariance image looks like in three dimensions, i.e. we have carried out the rotations based on the x and z coordinates, but have retained the coordinate along the TOF axis. Note that the xz projection here is the equivalent to the results obtained in figure 3.19. (b) shows the distribution of the covariance image if the third dimension is considered, and the x axis is used as the reference direction.

the ions about the TOF axis (the y axis) until the component of the reference ion in the z axis is zero. Figure 3.21(a) shows the position of the reference ions (left), and the signal ions (right) after this rotation. If we instead set the reference direction to lie along the x axis, we obtain the results seen in figure 3.21(b). Therefore, what we obtain from using recoil-frame covariance on a 2D projection of the scattering distribution is the projection of the solid of rotation of the distribution seen in figure 3.21(b) about the z axis, from an angle $\phi = \frac{\pi}{2}$ to $\frac{3\pi}{2}$, where ϕ is the angle from the x axis in the xy plane. The "inverted image" which should be obtained following inversion of the covariance image corresponds to the distribution shown on the right of figure 3.21(b) (or in two dimensions, the central slice of the distribution). Our aim is to obtain the kinetic energy associated with this distribution in the same way as is routinely achieved for velocity-map images.

We now present our initial efforts to attempt to obtain kinetic energy distributions from covariance images.

3.5.1 A new inversion method for electron-molecule scattering experiments

Back in section 3.2.3, we noted that we have recently been developing a new inversion method. We established that the main motivation for the development of the technique was to allow us to invert recoil-frame covariance images as, in the process of carrying out the covariance analysis, the axis of cylindrical symmetry required for the majority of the inversion methods is removed, meaning that they are no longer able to invert the image successfully. Now that we have a better understanding of covariance analysis, we are in a position to discuss the new inversion method in detail; the theory of the inversion method and its implementation is described below.

Isotropic case

We will first consider the case where ionisation probability is independent of molecular orientation. This results in an isotropic scattering distribution, which we can model using the first spherical harmonic:

$$C_{00}\left(\theta_T, \phi_T\right) = \frac{1}{\sqrt{4\pi}} \tag{3.52}$$

where θ_T is the angle of the velocity vector $\boldsymbol{v}$ with reference to the time-of-flight axis and ϕ_T is the angle of vector $\boldsymbol{v}$ with respect to x in the xy plane (see figure 3.22). We can integrate the spherical harmonic along the time-of-flight (TOF) axis as follows:

$$\int_{-\infty}^{\infty} C_{00}\left(\theta_T, \phi_T\right)\ d\boldsymbol{v}_{\mathrm{TOF}} = \int_{0}^{\infty} \frac{2}{\sqrt{4\pi}}\ d\boldsymbol{v}_{\mathrm{TOF}} \tag{3.53}$$

where $\boldsymbol{v}_{\mathrm{TOF}}$ is the velocity along the TOF axis. We know that $\boldsymbol{v}_{\mathrm{TOF}} = \left(\boldsymbol{v}^2 - \boldsymbol{v}_p^2\right)^{\frac{1}{2}}$, where $\boldsymbol{v}_p$ is the projection of the true velocity, $\boldsymbol{v}$, into the image plane. By differentiating $\boldsymbol{v}_{\mathrm{TOF}}$ with respect to $\boldsymbol{v}$, we can find a Jacobian to modify equation 3.53, giving us the following expression:

$$\int_{0}^{\infty} \frac{2}{\sqrt{4\pi}}\ d\boldsymbol{v}_{\mathrm{TOF}} = \int_{\boldsymbol{v}_p}^{\infty} \frac{1}{\sqrt{4\pi}} \left(\frac{\boldsymbol{v}^2}{\boldsymbol{v}^2 - \boldsymbol{v}_p^2}\right)^{\frac{1}{2}}\ d\boldsymbol{v} \tag{3.54}$$

Now let us assume we are modelling a shell of radius $\boldsymbol{v}_0$. We can modify equation 3.54 by applying a delta function, $\delta(\boldsymbol{v} - \boldsymbol{v}_0)$:

$$\int_{\boldsymbol{v}_p}^{\infty} \frac{1}{\sqrt{4\pi}} \left(\frac{\boldsymbol{v}^2}{\boldsymbol{v}^2 - \boldsymbol{v}_p^2}\right)^{\frac{1}{2}} \delta(\boldsymbol{v} - \boldsymbol{v}_0)\ d\boldsymbol{v} = \frac{1}{\sqrt{4\pi}} \left(\frac{\boldsymbol{v}_0^2}{\boldsymbol{v}_0^2 - \boldsymbol{v}_p^2}\right)^{\frac{1}{2}} \tag{3.55}$$

Equation 3.55 gives us the expression for the two-dimensional projection of a three-dimensional spherical distribution onto a plane, which we could use to fit a typical scattering distribution. However, we are considering the case of a covariance image, so we integrate this function over the angular coordinate to give the radial

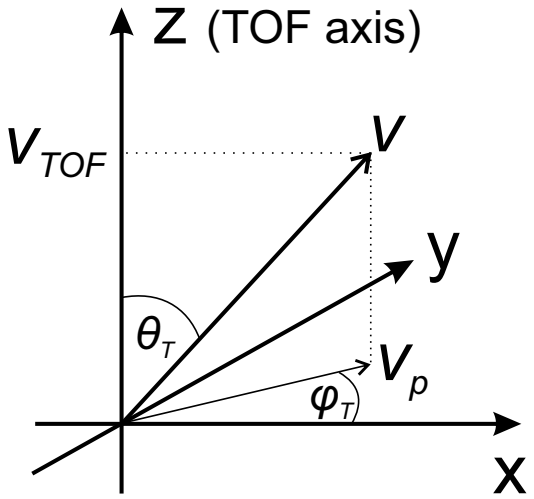


Figure 3.22 The coordinate system used for the derivation of the new inversion method. All terms are defined in the text.

distribution, $f(\boldsymbol{v}_p)$:

$$f(\boldsymbol{v}_p) = \int_0^{2\pi} \frac{1}{\sqrt{4\pi}} \left(\frac{\boldsymbol{v}_0^2}{\boldsymbol{v}_0^2 - \boldsymbol{v}_p^2} \right)^{\frac{1}{2}} \boldsymbol{v}_p \; d\phi_T \tag{3.56}$$

$$= \sqrt{\pi} \left(\frac{\boldsymbol{v}_0^2}{\boldsymbol{v}_0^2 - \boldsymbol{v}_p^2} \right)^{\frac{1}{2}} \boldsymbol{v}_p \tag{3.57}$$

Note that we have applied the Jacobian, $\boldsymbol{v}_p$ for conversion between Cartesian and polar coordinate systems.

We must now extend the single recoil velocity case to a more general case; in most instances, each fragment ion will be formed with a range of recoil velocities. To this end, we now define a series of basis functions of the form described by the real part of equation 3.57. We define our normalised basis functions, $\rho\left(\boldsymbol{v}_p\right)_i$, as follows:

$$\rho\left(\boldsymbol{v}_p\right)_i = \frac{\left(\frac{\boldsymbol{v}_i^2}{\boldsymbol{v}_i^2 - \boldsymbol{v}_p^2} \right)^{\frac{1}{2}} \boldsymbol{v}_p}{\int_0^{\infty} \left(\frac{\boldsymbol{v}_i^2}{\boldsymbol{v}_i^2 - \boldsymbol{v}_p^2} \right)^{\frac{1}{2}} \boldsymbol{v}_p \; d\boldsymbol{v}_p} \tag{3.58}$$

We need to fit our basis functions to the radial distribution by adjusting the weight,

w_i, of each basis function such that the following expression is true:

$$I\left(\boldsymbol{v}_p\right) = w_{\text{baseline}} + \sum_{i}^{\text{all } i} w_i \rho\left(\boldsymbol{v}_p\right)_i \tag{3.59}$$

where $I\left(\boldsymbol{v}_p\right)$ is the radial distribution of the image. The fit is carried out using least squares linear regression, and from the weights we are then able to reconstruct the inverted image, as will be discussed below. As we are fitting the radial distribution rather than directly fitting the image itself, we can invert both a typical scattering distribution and a covariance image, despite the fact that the covariance analysis removes the axis of cylindrical symmetry.

Anisotropic case

We now consider cases where the scattering distribution is no longer isotropic, for example in a laser photolysis experiment. In these cases, the anisotropy of the scattering distribution at a given radius can be modelled using the following equation:

$$P(r,\theta) = I(r)\left[1 + \sum_{n>0} \beta_n(r) P_n(cos(\theta))\right] \tag{3.60}$$

where $I(r)$ is the signal intensity at radius r, $\beta_n(r)$ is the n^{th} beta parameter at radius r which is adjusted to fit the data, $P_n(x)$ is the n^{th} Legendre polynomial, and θ is the angle with respect to the scattering distribution's axis of cylindrical symmetry. We hypothesised that there exists some function which can modify the basis functions given in equation 3.58 to allow us to also invert anisotropic distributions.

Consider the two-dimensional projection of a shell with anisotropy parameters given by β_n, which has a radial distribution $f\left(\frac{r}{r_{\text{max}}}; \beta_n\right)$, where r is the radius and r_{max} is the radius of the shell. We can find this radial distribution analytically via a simulation for any set of beta parameters. We can find the ratio of these radial distributions with respect to the radial distribution of the uniform shell discussed

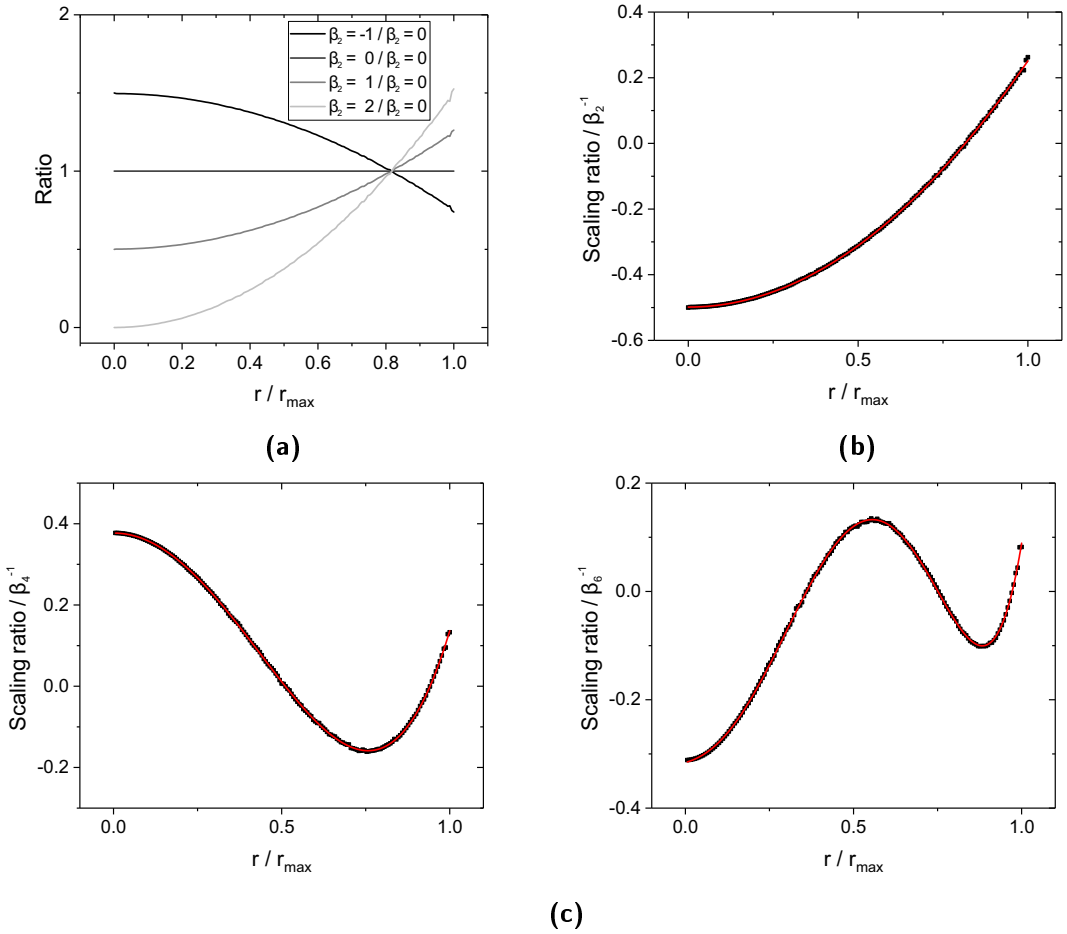


Figure 3.23 Generation of basis function scaling functions. (a) shows the ratio between radial distributions of anisotropic shells with different β_2 values with respect to an isotropic shell, (b) shows the rate of change of (a) with respect to β_2, and (c) shows the result of the same process with β_4 (left) and β_6 (right). A polynomial fit has been carried out on the curves in (b) and (c), shown in red; fitting parameters are given in table 3.1.

previously using the following equation:

$$\frac{f\left(\frac{r}{r_{\max}};\beta_n\right)}{f\left(\frac{r}{r_{\max}};0\right)} \tag{3.61}$$

To simplify the problem, we will only modify one beta parameter at a time, setting all other beta parameters to zero. Figure 3.23(a) shows the result of evaluating equation 3.61 with varying β_2. What is striking here is that, for a given $\frac{r}{r_{\max}}$, the

k	$a_k(\beta_2)$	$a_k(\beta_4)$	$a_k(\beta_6)$
0	-0.49854 ± 0.00042	0.37695 ± 0.00067	-0.31589 ± 0.00103
1	-0.00152 ± 0.00196	0.00613 ± 0.00917	0.18097 ± 0.02038
2	0.75146 ± 0.00190	-1.90669 ± 0.03690	1.40602 ± 0.12465
3		0.06854 ± 0.05504	7.72015 ± 0.31316
4		1.59166 ± 0.02715	-22.17286 ± 0.34281
5			13.27069 ± 0.13565

Table 3.1 Fitting parameters from the polynomial fit shown in figures 3.23(b) and 3.23(c). The polynomial can be recreated by evaluating $\sum_{k=0}^{k_{\max}} a_k(\beta_n) \left(\frac{r}{r_{\max}}\right)^k$.

change with respect to β_2 is constant. Thus, by evaluating the following:

$$\frac{d\left(\frac{f\left(\frac{r}{r_{\max}};\,\beta_n\right)}{f\left(\frac{r}{r_{\max}};\,0\right)}\right)}{d\beta_n} \tag{3.62}$$

we obtain a scaling function, shown in figure 3.23(b). We can repeat the same process with other β_n; figure 3.23(c) shows the resulting scaling function for β_4 and β_6. We can fit the scaling functions using polynomials; fitting parameters are given in table 3.1.

Everything is now in place to derive a scaling function, $s\,(r)$, for the original basis functions. The scaling function is given by:

$$s\,(r) = 1 + \sum_{n>2} \beta_n \sum_{k=0}^{k_{\max}} a_k(\beta_n) \left(\frac{r}{r_{\max}}\right)^k \tag{3.63}$$

where $a_k(\beta_n)$ is the fitting parameter for the k^{th} power of $\frac{r}{r_{\max}}$ for β_n, given in table 3.1. Where r exceeds $r_{\max}$, the value of $s(r)$ takes a value of zero. The basis functions given by equation 3.58 are then multiplied by this scaling factor to give modified basis functions, which can then be used for linear regression in exactly the same way as described previously. Note that r and $r_{\max}$ in equation 3.63 correspond to $\boldsymbol{v}_p$ and i in equation 3.58.

We note that at present there is a significant limitation for the anisotropic case. As will be shown below, we are able to successfully invert anisotropic velocity-map

images, but this requires that the beta parameters are known prior to the inversion. Since another inversion method is required to obtain the beta parameters, it is clear that further work is required before this method will be used to invert anisotropic scattering distributions.

Now that the theory behind the inversion method has been introduced, we will now discuss the implementation of this inversion method, developed as part of the current work.

Implementation

In our implementation, rather than directly using the expression described in equation 3.57 as our basis set, we instead use an analytical basis function, generated by simulating points on a shell, projecting these onto a 2D plane and finding the radial distribution of this function using the angular integration function of the PyAbel package,[177] with the appropriate Jacobian for conversion from Cartesian to polar coordinates applied. The reason for using an analytical function rather than equation 3.57 is due to the singularity when $\boldsymbol{v}_p = \boldsymbol{v}_i$. Basis sets are generated up to some maximum radius with a step in radius defined by the user. The radius of each shell is defined as a Gaussian with standard deviation σ, which is also defined by the user. We define an inner region, which is used for all basis sets, in which the step between basis functions is 0.5 pixel units (px), up to a radius of 5 px, with σ twenty times smaller than the radius of the given basis function. This allows any sharp features near the centre of the image to be properly fitted. A switching function is used to transition between the pre-defined inner region and the user-defined outer region. To prevent a large jump in the step between basis functions, for cases where the step between the radius of basis function is defined to be greater than 1 px, an extra basis function is added between the inner and outer region. For example, if a step of 2 px was required, a basis function would be defined at a radius of 0.5 px to five in steps of 0.5 px, followed by basis functions with radius 6 px, 7 px, 9 px,

11 px, et cetera. If σ exceeds 0.25 px, i.e. the fixed value of σ at a radius of 5 px, a transition between this fixed value and the user-defined σ is also introduced, to prevent overly wide basis functions in the central region of the image. σ is increased from 0.25 px by an increment of 0.1 px times the sum of the user-defined sigma and step size for each subsequent basis function. For example, if a σ of 2 px and step of 2 px was required, σ would have a value of

Basis function radius / px	σ / px
...	
4.5	0.225
5.0	0.250
6.0	0.650
7.0	1.050
9.0	1.450
11.0	1.850
13.0	2.000
...	

for each basis function radius. All basis functions are normalised such that their integral is equal to one. As basis set generation is a fairly slow step, the basis set is saved after it has been generated, for future use.

When carrying out the fitting shown in equation 3.59, we apply ridge regularisation, discussed previously in section 3.2.3. Ridge regularisation penalises large weights by adding a term, $\alpha \sum_i^{\text{all } i} w_i^2$, where α is a user-defined penalty weighting factor, to the minimisation carried out in linear regression. By applying an appropriate α we can, in cases where the radial distribution has been over-fitted, remove the vast majority of ringing.

To adjust the basis functions for anisotropic systems, values of β_n must first be

obtained from the original scattering distribution using some other method. Once we have obtained β_n, we use equation 3.63 to generate a scaling function, which is applied to the basis functions previously generated. Where $\sigma > 0$, the scaling functions for the outer basis functions are first convoluted with a Gaussian with the same standard deviation as that used when generating the basis functions.

To obtain the inverted radial distribution, we multiply the weights, w_i, by the known inverses, $\phi(\boldsymbol{v})_i$ of the basis functions, $\rho(\boldsymbol{v}_p)_i$, where $\boldsymbol{v}$ is the velocity in 3D space, as previously defined (see figure 3.22 and associated text). The sum of the known inverses is non-uniform, so a correction is applied to account for this. Overall, the radial distribution, $f(\boldsymbol{v})$, is described by the following equation

$$f(\boldsymbol{v}) = \frac{\sum_i^{\text{all i}} w_i \phi(\boldsymbol{v})_i}{\sum_i^{\text{all i}} \phi(\boldsymbol{v})_i} \tag{3.64}$$

To reconstruct the central slice of the scattering distribution, i.e. the inverted image, we use equation 3.60, reproduced below

$$P(r,\theta) = I(r)\left[1 + \sum_{n>0} \beta_n(r) P_n(cos(\theta))\right] \tag{3.65}$$

where $P(r,\theta)$ is the probability distribution at radius r and angle θ, and all other terms are as previously defined. The values of $I(r)$ are given by $f(\boldsymbol{v})$, obtained using equation 3.64. Note that r is equivalent to $\boldsymbol{v}$ here. To generate the image, a total number of 'hits' is chosen, typically 100,000 or more, which is equivalent to multiplying equation 3.65 by the chosen number of hits. For each value of $\boldsymbol{v}$ a number of hits is assigned, according to the probability density described by $f(\boldsymbol{v})$. The points are then distributed at radius r with anisotropy described by the term in square brackets in equation 3.65.

Due to the fact that the reconstruction uses polar co-ordinates, but maps onto a Cartesian grid, it is necessary to blur r, rather than using a single value for each discrete point in the distribution $f(\boldsymbol{v})$. At present, a Gaussian blur is used, with

the user-defined σ value being used to define the standard deviation of the Gaussian blur. In future the blur may have a fixed standard deviation, but given that σ is typically set to either one, two, or three for the scattering distributions presented here, the change in the reconstructed images following this change would be small. Once we have carried out this process at each radius, we have reconstructed the central slice, and we then need only divide by the total number of hits to convert the image back into a probability distribution. The code for our implementation of the inversion method can be found in appendix D.2.

We will now demonstrate that this method can be successfully used to invert images from systems which undergo both isotropic and anisotropic dissociation. This will be followed by a discussion on the use of the inversion method with recoil-frame covariance images, found in section 3.5.3.

3.5.2 Examples: Scattering distributions (velocity-map images)

To demonstrate that the inversion method is successful for an isotropic case, we will use the example of the O^+ fragment scattering distribution produced when an electron scatters off a molecule of CO_2 at an energy of 100 eV. The results of this are shown in figure 3.24; note that the ion images are normalised such that the total intensity of the image is equal to unity, and the radial distribution is normalised to unit area under the curve. In this case, both the step between and standard deviation of the basis functions are equal to one pixel, and the regularisation parameter is set to 0.0025. We can see that the fit to the radial distribution of the scattering distribution achieved using the basis set generated using these parameters, shown in figure 3.24(b), is excellent. The resulting radial distribution of the inverted image is shown in figure 3.24(c), and compared to the radial distribution obtained using both the Hansen-Law and BASEX inversion methods. Again, excellent agreement is seen between the three methods. This has also been shown to be the case with

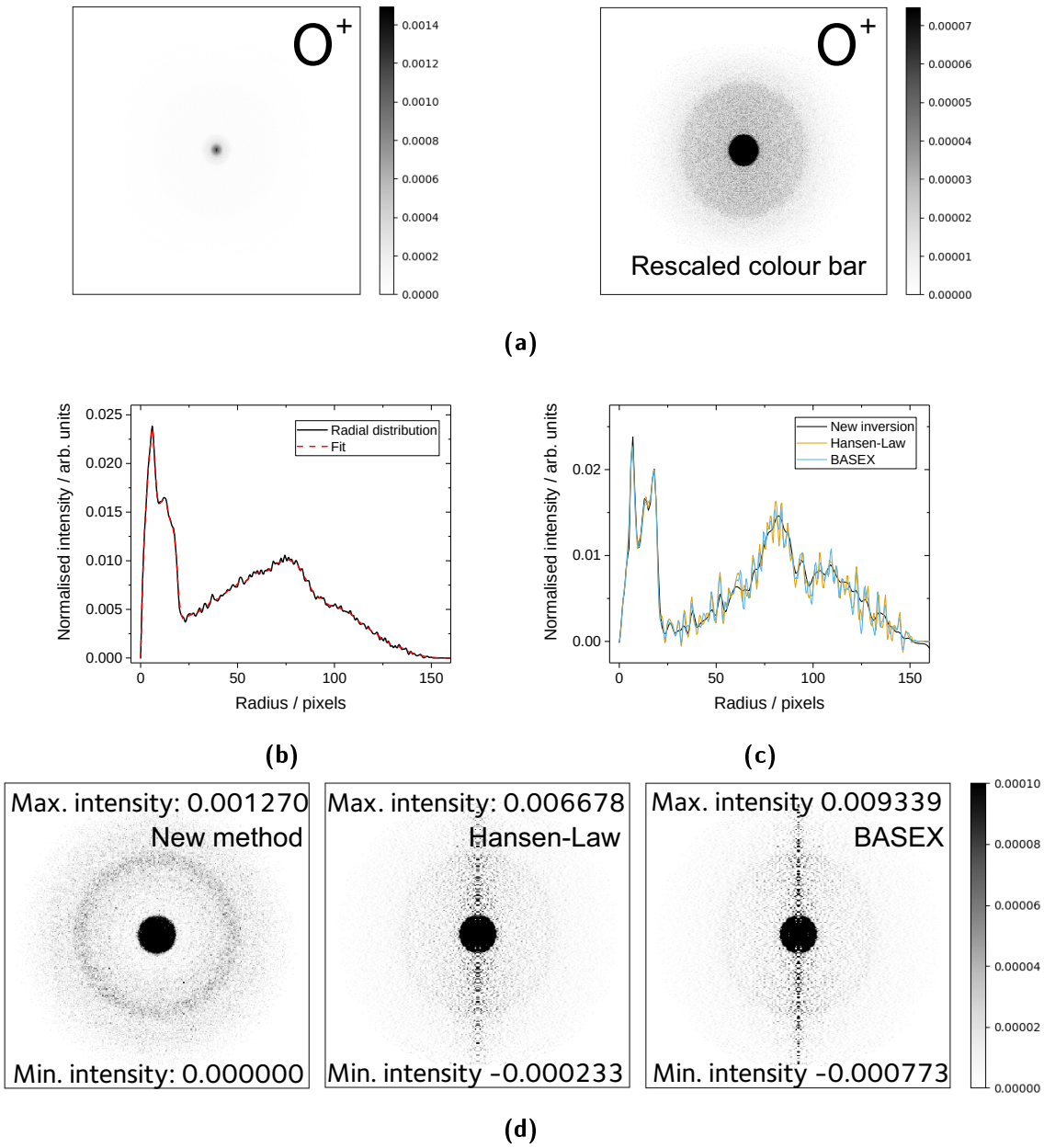


Figure 3.24 A comparison of the new inversion method to established methods for an isotropic case. The data used is the O^+ scattering distribution resulting from the bombardment of CO_2 with 100 eV electrons. a) shows the scattering distribution with two different upper limits on the colour scale (the maximum on the colour bar is left: the maximum pixel intensity in the image, and right: half the maximum pixel intensity in the image). b) shows the radial distribution of the scattering distribution, and the fit achieved by the new inversion method. c) shows the radial distribution of the inverted image obtained using the new inversion, Hansen-Law, and BASEX, and d) shows the associated inverted images. Note that certain areas are saturated on the colour scale.

a number of other isotropic scattering distributions not shown here, which gives us confidence that the new inversion method is successfully recovering the central slice of the scattering distribution.

There is some variation in the inverted images shown in figure 3.24(d), particularly in the maximum and minimum intensity observed in the image. A possible reason for the variation is the centre-line noise generated through the inversion using both the Hansen-Law and BASEX algorithms; both show oscillation between positive and negative signal near the centre. As our method reconstructs the inverted image based on the radial distribution, rather than the other two methods which use the inverted image to determine the radial distribution, our inversion does not suffer from noise to the same degree, but is highly dependent on the quality of the radial distribution obtained from the inversion.

To test the method with an anisotropic case, a simulation was used to probe dissociation channels with a variety of beta parameters. In the simulation, a scattering distribution consisting of four different dissociation channels was defined. The dissociation channel had the following parameters

$$\{[2, 50, (2, 0)], [6, 90, (-1, 0)], [10, 70, (0, 2)], [4, 60, (1.2, 1.2)]\} \tag{3.66}$$

in the format $[i, r, (\beta_2, \beta_4)]$, where i is the frequency of dissociation via the channel in each experimental cycle, r is the radius in pixels which the ion travels, and β_2 and β_4 are the beta parameters used to define the anisotropy of the dissociation channel. The simulation is run for 20,000 experimental cycles. The resulting scattering distribution is shown in figure 3.25(a).

Due to the fact that the features in the simulated scattering distribution are much sharper than those seen with the experimental data used in the isotropic test case above, a different basis set is required for the inversion method here. In this case, the step between and standard deviation of the basis functions are both equal to half a pixel, and the regularisation parameter is set to 0.0005. We again see that

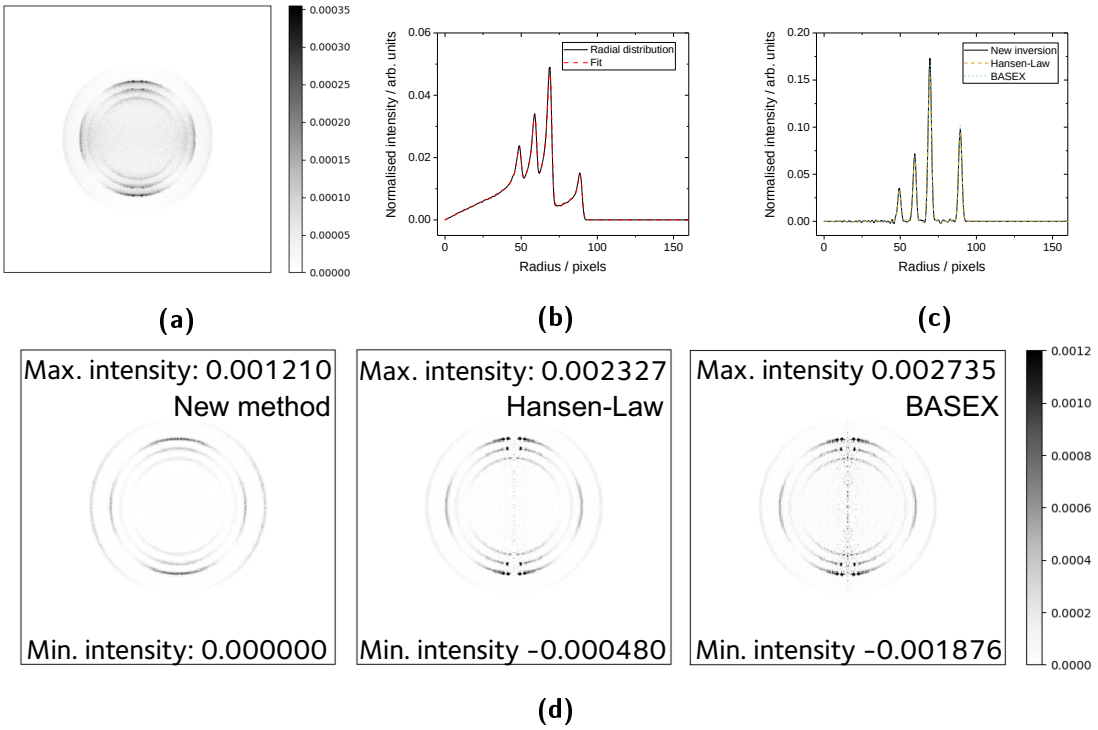


Figure 3.25 A comparison of the new inversion method to established methods for an anisotropic case. The data used is the simulated scattering distribution discussed in the text. a) shows the scattering distribution, b) shows the radial distribution of the scattering distribution, and the fit achieved by the new inversion method, c) shows the radial distribution of the inverted image obtained using the new inversion, Hansen-Law, and BASEX, and d) shows the associated inverted images. Note that certain areas are saturated on the colour scale.

the fit to the radial distribution of the scattering distribution, shown in figure 3.25(b) is excellent, and that the new inversion method gives consistent results with both Hansen-Law and BASEX, as shown in figures 3.25(c) and 3.25(d). The method has also been shown to work well using experimental data obtained through photolysis experiments, but these data have not been included here.

Whilst the inversion method can successfully invert anisotropic images, the requirement to use another inversion method to determine the beta parameters for the inversion is the main shortfall of this method at present. It may be the case that the beta parameter can be determined directly from the radial distribution, but this would almost certainly lead to the model having too much flexibility, and result in a low-quality inversion. Whilst this does not affect the inversion of the isotropic

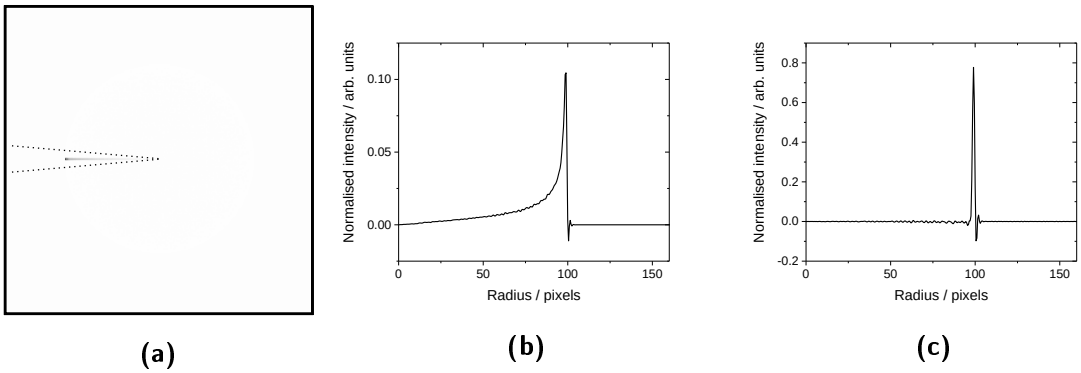


Figure 3.26 An example of the inversion of a covariance image resulting from a two-body dissociation pathway. a) shows an example of a covariance image for a two-body dissociation process, with an arc of $\frac{\pi}{18}$ rad depicted by black dotted lines, b) shows the radial distribution of the arc in a), and c) shows the result of using our new inversion method on the radial distribution in b).

scattering distributions measured as part of this thesis, it is an area that requires further development.

3.5.3 Examples: Recoil-frame covariance maps

We will now attempt to determine the radial distribution of the covariance image using our new inversion method. An example of a recoil-frame covariance image obtained from a two-body dissociation, in which ion A^+ has a velocity of 100 px, ion B^+ a velocity of 80 px, and B^+ is the reference ion, is shown in figure 3.26(a). If we take the radial distribution of the area contained within the white dotted lines (an arc of angle $\frac{\pi}{18}$ rad), shown in figure 3.26(b), we see that this is remarkably similar to the radial distribution of the 2D projection of a sphere. This makes sense if one considers the process used to produce the images. In the determination of the $\langle \mathbf{XY} \rangle$ term, the ion vectors are rotated, but their magnitude remains the same. Hence, it follows that the radial distribution of this term must be the same as that of the scattering distribution, albeit with a greater portion of the signal concentrated in a direction opposite to the reference direction. The second term, $\langle \mathbf{X} \rangle \langle \mathbf{Y} \rangle$, will similarly have the same radial distribution as the scattering distribution which, in the case of an isotropic distribution, will not vary with angle. The two terms have

approximately equal magnitudes, which means that the radial distribution of the entire covariance image cannot be used, but by taking an arc from the covariance image, we can determine the radial distribution of the covariant channel, and hence determine the velocity of the ion. Figure 3.26(c) shows the result of using our inversion method on the radial distribution shown in figure 3.26(b). We can clearly see that in this case, ion A^+ is produced with a velocity of 100 px, which matches exactly with the simulation parameters.

In the case of three-body dissociation, the situation is slightly less straightforward. If the molecule dissociates via an initial or deferred charge separation pathway, the positive region of signal within the covariance image is no longer described by an arc, as can be seen clearly in figures 3.17(b) and 3.19(b). For the following discussion, we will only consider one of the deferred charge separation covariance images, reproduced in figure 3.27(a), but the same arguments can be applied in each case.

Before attempting to invert the covariance image, it is worth determining what the result of the process should be if the inversion is successful. To do this, we return to the simulations; we will use the same simulations employed to discuss three-body dissociation in section 3.4.5, i.e. based on a Coulomb explosion that results in one ion having a velocity of 80 px and the other 100 px, a neutral loss resulting in the ion fragment gaining a velocity of 30 px, and both dissociation steps assumed to be isotropic. We have already seen that, if we carry out a rotation in three dimensions and define the x axis as the reference direction, we obtain the covariance images shown in figure 3.21(b). The radial distribution of this distribution is therefore the result we are aiming for. We do not have any code which is able to obtain a radial distribution from a three-dimensional distribution at present, but fortunately the x axis is an axis of cylindrical symmetry. Therefore, we have inverted the image using the Hansen-Law method; the resulting image is shown in figure 3.27(b), and the corresponding radial distribution in figure 3.27(d).

Now that we know the expected result, we can attempt to invert the covariance

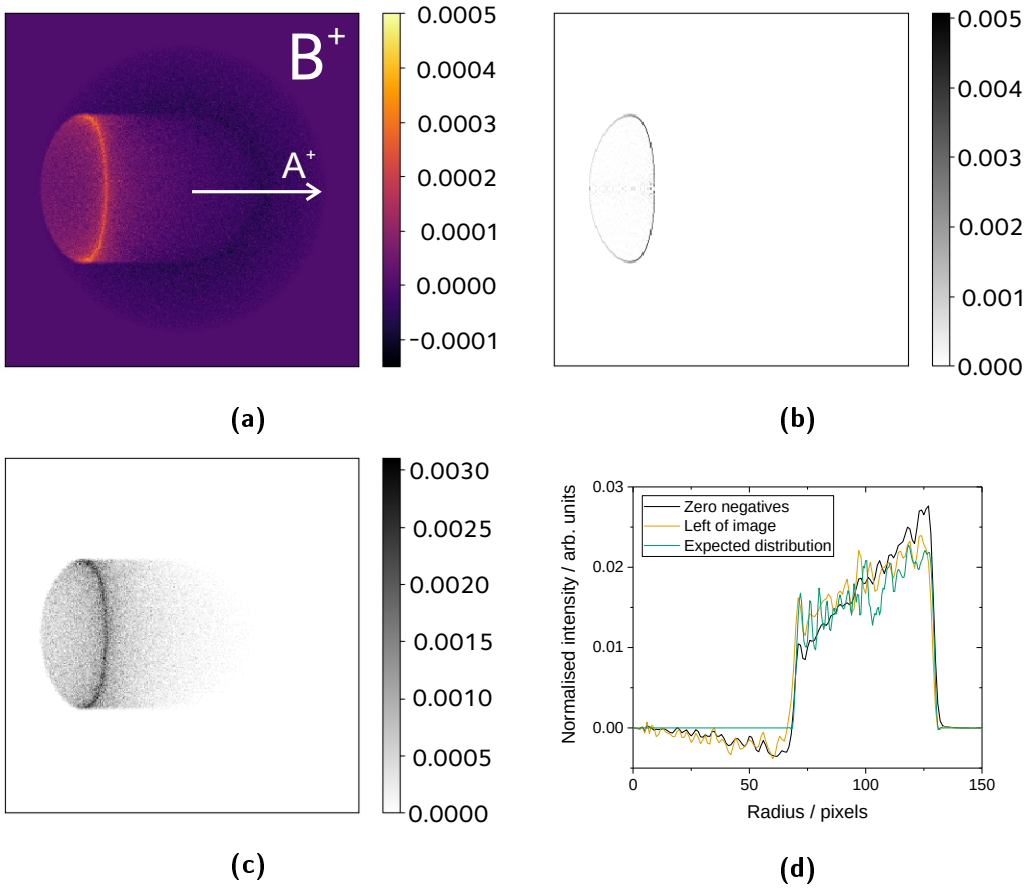


Figure 3.27 An example of the inversion of a covariance image resulting from a three-body deferred charge separation process. a) shows the covariance image, obtained through simulation of a deferred charge separation pathway, to be inverted, b) shows the results of a simulation of the scattering distribution used to generate the covariance image where the reference ion has been rotated to lie along the x axis, and the resulting distribution inverted using the Hansen-Law method to give the expected result of the inversion, c) shows the $\langle \mathbf{XY} \rangle$ term of the covariance analysis where only one molecule is allowed to dissociate a frame, and d) shows the radial distribution of the expected result given in b), along with the result of using our new inversion on the covariance image in a), either with negative values zeroed, or just using the left-hand side of the image.

images. One might predict that by zeroing any negative values in the covariance image we will successfully recover the radial distribution of the process. However, whilst this method accurately determines the limits within which signal is observed, the signal level is underestimated at low radii, and an overestimated at high radii, as can be seen in figure 3.27(d). The reason for this is that as the radius increases, the proportion of negative covariance increases. The negative covariance has a radial distribution approximately matching that of the original scattering distribution, as it is produced from the subtraction of the $\langle \mathbf{X} \rangle \langle \mathbf{Y} \rangle$ term, and hence has no angular dependence. This means that, when the negative covariance is zeroed, the intensity at lower radii will be underestimated, and at higher radii overestimated, as observed in the radial distribution.

From this reasoning, it follows that a potential solution is to take some arc from the covariance image, and obtain the radial distribution to invert from this arc. We already know that the $\langle \mathbf{X} \rangle \langle \mathbf{Y} \rangle$ term from the covariance analysis is isotropic, so we need to determine the spatial distribution of the $\langle \mathbf{XY} \rangle$ term. This can be found by using a simulation in which only one molecule dissociates on each experimental cycle, which means there will be no false covariance; the $\langle \mathbf{XY} \rangle$ term for this simulation is shown in figure 3.27(c). We see that the vast majority of intensity is on the left-hand side of the image, and that the signal on the right-hand side all appears at lower radii than that of the main feature. So if we find the radial distribution of just the left-hand side of the image, we expect that it will be accurate in our region of interest, but will underestimate the true radial distribution at lower radii. This is exactly what we observe, and is shown in figure 3.27(d).

Whilst this method does manage to accurately determine the radial distribution of the covariant channel here, some caution must be taken. If, say, the positive covariance on the right-hand side of the image extended to a greater radius, this may begin to adversely affect the radial distribution in the region of interest. This can be circumvented to some degree by taking the radial distribution of a greater arc

than π rad, although the larger the arc, the noisier the radial distribution becomes as the radial distribution tends to zero. We believe that the size of the arc should therefore be chosen to maximise signal-to-noise, whilst maintaining the integrity of the radial distribution in the region of interest.

Whilst not strictly required for the distributions seen in this thesis, we have also shown that this method can successfully invert a two-body covariance image for an anisotropic distribution, provided the appropriate beta parameters are found beforehand. Further work is required to determine whether this method can be used for more complex processes.

We have made good progress in the development of an inversion method capable of inverting both velocity-map images and covariance images by fitting the radial distribution of the image with a set of basis functions, but it is clear that further work is still required. We are able to successfully invert isotropic scattering distributions, such as those discussed in this thesis, and have shown we can also invert covariance images obtained from isotropic scattering distributions, provided the radial distribution of an appropriate segment of the image is considered. We plan to find a more robust method to determine the size of the segment that should be used which does not require the user to make a judgement on the appropriate segment size, but the method itself has been shown to perform well. Significant efforts are still required to allow the method to be used for anisotropic images. One of the main limitations of the method here is that the beta parameters must be provided for the inversion to function correctly. Ideally, we would like to instead be able to use the inversion method without any prior knowledge, and obtain the beta parameters from the fit. We are also yet to properly explore the use of the inversion method on covariance images obtained from anisotropic scattering distributions. To summarise, we have made an excellent start in our efforts to invert covariance images, but there are a number of challenges that we still need to overcome.

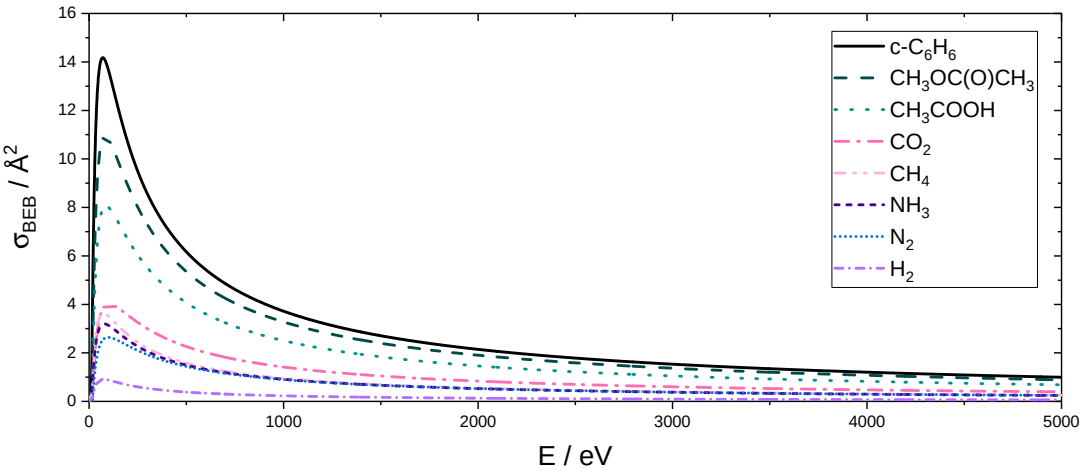
4

Results: Total electron ionisation cross-sections

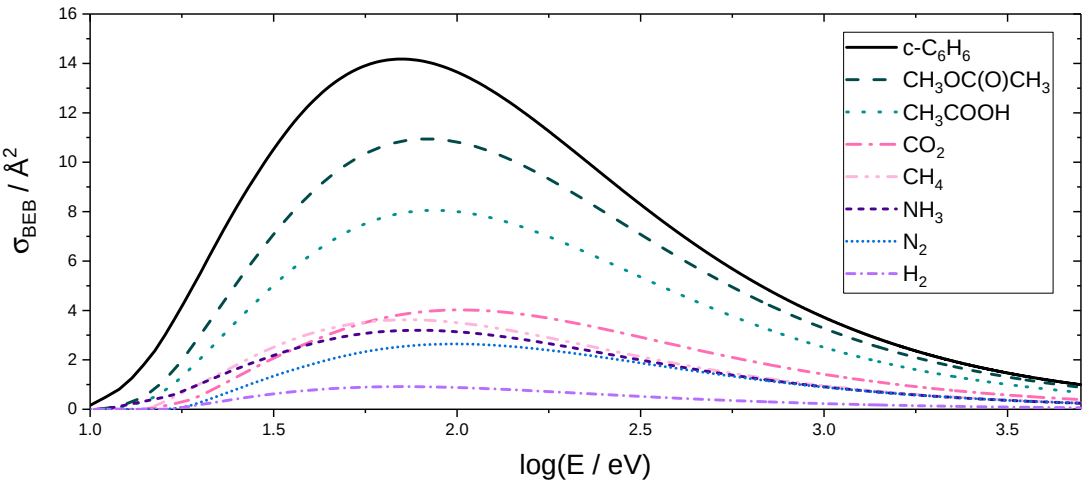


ack in section 2.1, we introduced the binary-encounter-Bethe (BEB) model as a method of calculating total electron ionisation cross-sections. In this chapter, we will present the results we obtain using the BEB method for a variety of molecules, and introduce a fitting function that can be used to parametrise the total ionisation cross-sections we obtain. We have previously published the work presented in this chapter in the Journal of Physics B ([97]).

We have calculated total ionisation cross-sections for a range of neutral molecules found in the interstellar medium, planetary and cometary atmospheres, and circumstellar shells, in an electron range from 0 to 5,000 eV. Figure 4.1 shows the total ionisation cross-sections obtained for a selection of molecules across the full energy range, displayed on both a linear and logarithmic scale. As the peak in the total ionisation cross-section is generally found in the 50-100 eV region, with a smooth



(a)



(b)

Figure 4.1 Total ionisation cross-sections calculated using the BEB model displayed over the entire calculated electron energy range (0-5,000 eV) for a selection of molecules. Displayed on a linear (a) and logarithmic (b) scale. Adapted from [97] © IOP Publishing. All rights reserved. Permission conveyed through Copyright Clearance Centre, Inc., license ID 1065118-1.

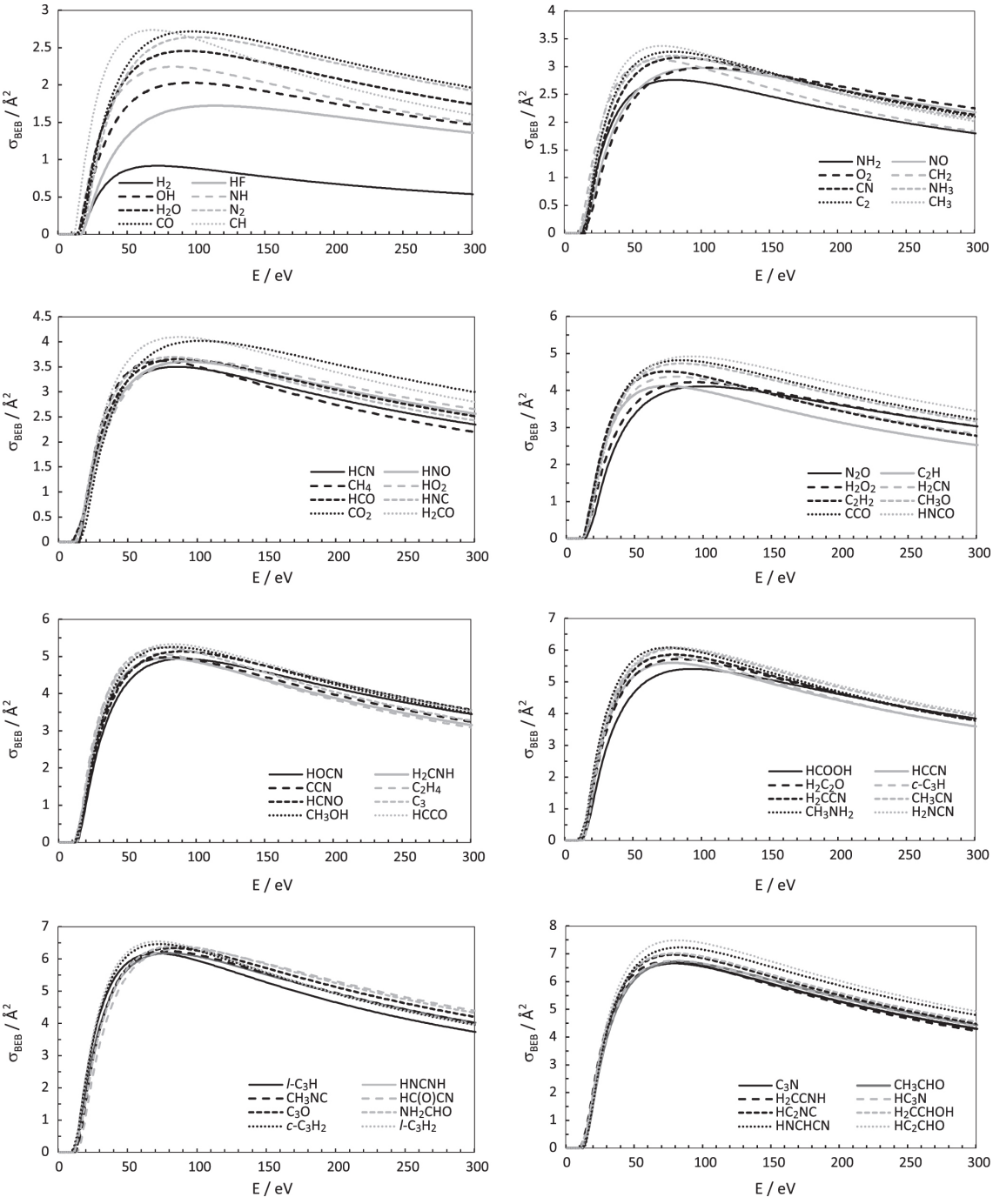


Figure 4.2 Total electron ionisation cross-sections obtained using the BEB model for a range of molecules found in the interstellar medium, containing only first and second row atoms, for the electron energy range 0-300 eV. Cross-sections are plotted in order of increasing maximum cross-section. Reproduced from [97] © IOP Publishing. All rights reserved. Permission conveyed through Copyright Clearance Centre, Inc., license ID 1065118-1.

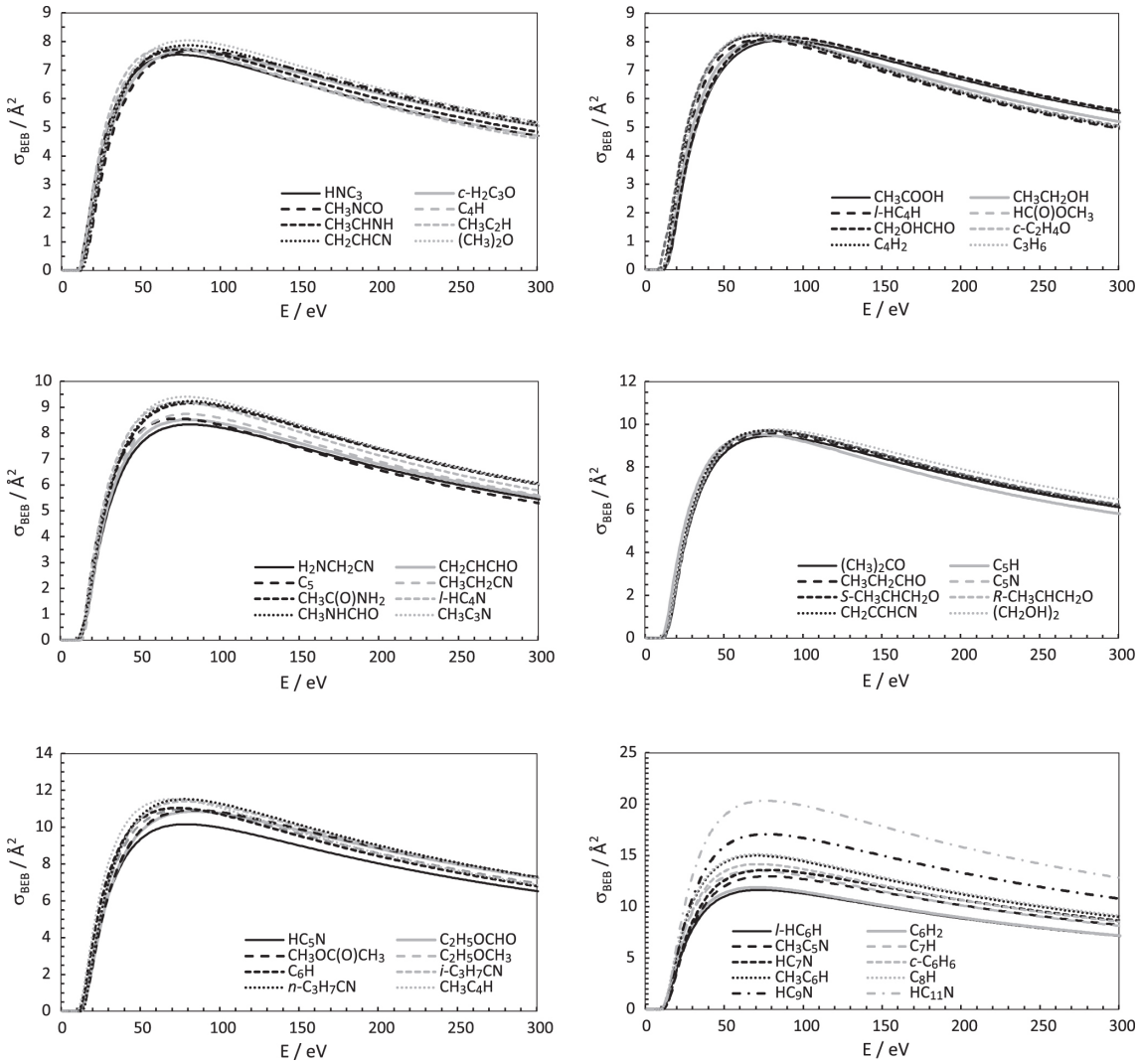


Figure 4.2 (continued)

decay at higher electron energies, we have only plotted the total ionisation cross-sections in the energy range 0-300 eV; the resulting cross-sections are shown in figure 4.2. Numerical data for the total ionisation cross-sections over the electron energy range 0-5,000 eV are available for all molecules considered here, and can be found in the supplementary data of [97] (`http://stacks.iop.org/JPB/51/195203/mmedia`). The complete data set is not reproduced here due to the large amount of data making it impractical. The maximum of the total ionisation cross-section for each molecule, and the electron energy at which it occurs, can be found in table 4.1.

4.1 Fitting the cross-sections

For use in computational models, it is more convenient if we fit the data with an analytical function. In this case, we have fitted each cross-section with an equation widely used in simulations of fusion edge plasmas [178]

$$\sigma(E) = \left(\frac{a_1}{E}\right)\left[1 - \frac{E_t}{E}\right]^{a_2}\left[\log_e\left(\frac{E}{E_t}\right) + a_3 + a_4\left(\frac{E_t}{E}\right)\right] \tag{4.1}$$

where E is the incident electron energy, E_t is the first ionisation energy of the molecule, and a_1, a_2, a_3 and a_4 are fitting parameters. Table 4.1 provides the maximum cross-section and the energy at which it occurs, the calculated value of E_t obtained in the process of determining the parameters required to use the BEB model and used for the fitting process, and the values of a_1, a_2, a_3 and a_4 obtained from the fitting process.

Table 4.1 Maximum total ionisation cross-sections, $\sigma_{\max}$, and the electron energy at which the maximum occurs, $\mathrm{EE}_{\max}$, are provided for the molecules studied in this chapter. Also provided are the calculated first ionisation potential of each molecule, E_t, and the fitting parameters obtained following the fitting of the calculated cross-sections using equation 4.1. Adapted from [97] © IOP Publishing. All rights reserved. Permission conveyed through Copyright Clearance Centre, Inc., license ID 1065118-1.

Molecule	$\sigma_{\max}$ / Å^2	$\mathrm{EE}_{\max}$ / eV	E_t / eV	a_1 / Å^2	a_2	a_3	a_4
H_2	0.92	71	16.40	51.11	1.704	0.494	0.314
HF	1.72	113	16.30	196.08	2.480	-0.639	1.325
OH	2.03	95	12.83	183.78	3.091	-0.517	1.425
NH	2.25	83	13.23	170.96	2.502	-0.288	1.058
H_2O	2.46	92	12.79	212.69	3.005	-0.459	1.344
N_2	2.64	98	15.98	239.02	2.506	-0.263	1.060
CO	2.72	96	14.19	238.29	3.092	-0.276	1.303
CH	2.74	67	10.53	161.09	2.815	-0.135	1.041

Table 4.1 (continued)

Molecule	σ_{max} / Å^2	EE_{max} / eV	E_t / eV	a_1 / Å^2	a_2	a_3	a_4
NH_2	2.76	80	11.76	196.40	2.981	-0.250	1.178
NO	2.98	97	9.52	256.41	5.617	-0.500	2.279
O_2	2.98	103	12.17	288.87	3.886	-0.572	1.707
CH_2	3.12	67	10.18	182.93	2.976	-0.145	1.080
CN	3.16	84	14.06	247.26	2.368	-0.267	1.022
NH_3	3.20	78	10.81	218.95	3.367	-0.237	1.283
C_2	3.27	78	13.30	233.14	2.306	-0.217	0.961
CH_3	3.38	70	9.67	191.79	3.826	0.054	1.270
HCN	3.50	84	14.16	263.1	2.583	-0.112	0.981
HNO	3.61	92	10.27	308.59	4.124	-0.608	1.768
CH_4	3.62	73	14.29	222.98	2.068	0.142	0.639
HO_2	3.63	97	11.61	335.29	3.637	-0.621	1.656
HCO	3.66	86	9.22	284.13	4.781	-0.504	1.972
HNC	3.70	81	12.16	264.47	3.115	-0.161	1.194
CO_2	4.02	102	14.14	384.22	3.044	-0.452	1.355
H_2CO	4.10	86	10.95	317.43	3.743	-0.373	1.528
N_2O	4.11	99	13.39	382.50	3.197	-0.466	1.402
C_2H	4.12	72	11.57	264.76	2.656	-0.174	1.026
H_2O_2	4.23	93	11.45	375.27	3.491	-0.600	1.598
H_2CN	4.39	79	10.95	300.45	3.425	-0.202	1.314
C_2H_2	4.52	73	11.67	287.22	2.749	-0.103	0.985
CH_3O	4.74	83	10.85	347.91	3.733	-0.290	1.495
CCO	4.82	83	11.01	371.58	3.275	-0.460	1.419
HNCO	4.93	90	11.94	409.23	3.339	-0.435	1.428
HOCN	4.94	90	12.56	414.35	2.996	-0.440	1.320

Table 4.1 (continued)

Molecule	σ_{max} / Å^2	EE_{max} / eV	E_t / eV	a_1 / Å^2	a_2	a_3	a_4
H_2CNH	4.96	77	9.60	325.72	4.082	-0.222	1.536
CCN	4.99	80	11.10	354.06	3.330	-0.278	1.349
C_2H_4	5.07	72	10.67	319.38	3.053	-0.188	1.195
HCNO	5.14	88	11.12	423.13	3.491	-0.515	1.508
C_3	5.25	75	12.26	350.43	2.547	-0.173	1.001
CH_3OH	5.26	82	11.09	381.96	3.493	-0.277	1.383
HCCO	5.34	82	10.02	398.32	3.834	-0.455	1.591
HCOOH	5.41	93	11.66	462.42	3.601	-0.477	1.550
HCCN	5.60	78	10.90	385.85	3.312	-0.255	1.309
H_2C_2O	5.72	82	9.83	417.80	4.139	-0.379	1.635
c-C_3H	5.82	73	10.09	371.47	3.435	-0.221	1.310
H_2CCN	5.87	79	10.56	399.97	3.683	-0.203	1.410
CH_3CN	6.05	80	12.86	429.32	2.725	-0.145	1.041
CH_3NH_2	6.09	75	10.63	392.64	3.282	-0.172	1.215
H_2NCN	6.09	81	10.35	439.71	3.602	-0.372	1.426
l-C_3H	6.18	70	9.32	379.47	3.632	-0.257	1.402
HNCNH	6.18	79	10.16	442.99	3.540	-0.411	1.452
CH_3NC	6.25	78	10.96	425.54	3.413	-0.192	1.299
HC(O)CN	6.34	89	12.28	510.73	3.283	-0.338	1.356
C_3O	6.35	81	11.37	479.35	3.070	-0.411	1.312
NH_2CHO	6.41	84	10.61	490.60	3.636	-0.433	1.502
c-C_3H_2	6.47	72	9.32	400.35	3.820	-0.218	1.412
l-C_3H_2	6.55	71	10.63	411.19	2.902	-0.224	1.121
C_3N	6.66	79	11.86	471.36	2.884	-0.254	1.166
CH_3CHO	6.72	82	10.36	476.90	3.956	-0.261	1.553

Table 4.1 (continued)

Molecule	σ_{max} / Å^2	EE_{max} / eV	E_t / eV	a_1 / Å^2	a_2	a_3	a_4
H_2CCNH	6.73	75	9.57	439.77	3.817	-0.280	1.467
HC_3N	6.76	80	12.18	472.50	3.134	-0.107	1.162
HC_2NC	6.97	78	11.68	479.01	3.147	-0.151	1.180
H_2CCHOH	7.03	79	9.61	487.24	4.056	-0.342	1.602
HNCHCN	7.24	82	11.89	532.20	3.123	-0.26	1.240
HC_2CHO	7.49	81	11.10	546.56	3.298	-0.334	1.339
HNC_3	7.54	73	10.13	498.84	3.372	-0.304	1.342
c-H_2C_3O	7.68	81	9.71	550.02	4.102	-0.374	1.643
CH_3NCO	7.69	84	10.96	576.69	3.647	-0.331	1.470
C_4H	7.71	71	10.47	492.76	3.015	-0.262	1.194
CH_3CHNH	7.74	75	10.23	496.18	3.612	-0.154	1.339
CH_3C_2H	7.81	68	9.87	461.67	3.195	-0.173	1.187
CH_2CHCN	7.88	78	11.28	537.10	3.285	-0.168	1.243
$(CH_3)_2O$	8.05	78	10.21	544.51	3.837	-0.217	1.471
CH_3COOH	8.05	87	11.01	626.47	3.755	-0.372	1.550
CH_3CH_2OH	8.07	78	10.86	551.24	3.444	-0.208	1.331
l-HC_4H	8.08	72	10.58	514.79	3.105	-0.206	1.170
$HC(O)OCH_3$	8.15	86	11.29	633.21	3.592	-0.355	1.472
CH_2OHCHO	8.18	86	10.91	636.48	3.709	-0.398	1.529
c-C_2H_4O	8.22	71	7.72	521.46	4.569	-0.487	1.802
C_4H_2	8.23	71	10.12	517.53	3.172	-0.252	1.231
C_3H_6	8.31	71	9.97	496.09	3.596	-0.059	1.268
H_2NCH_2CN	8.33	80	11.89	596.94	2.989	-0.242	1.175
CH_2CHCHO	8.51	80	10.31	595.55	3.740	-0.289	1.464
C_5	8.57	73	11.73	574.68	2.505	-0.279	1.057

Table 4.1 (continued)

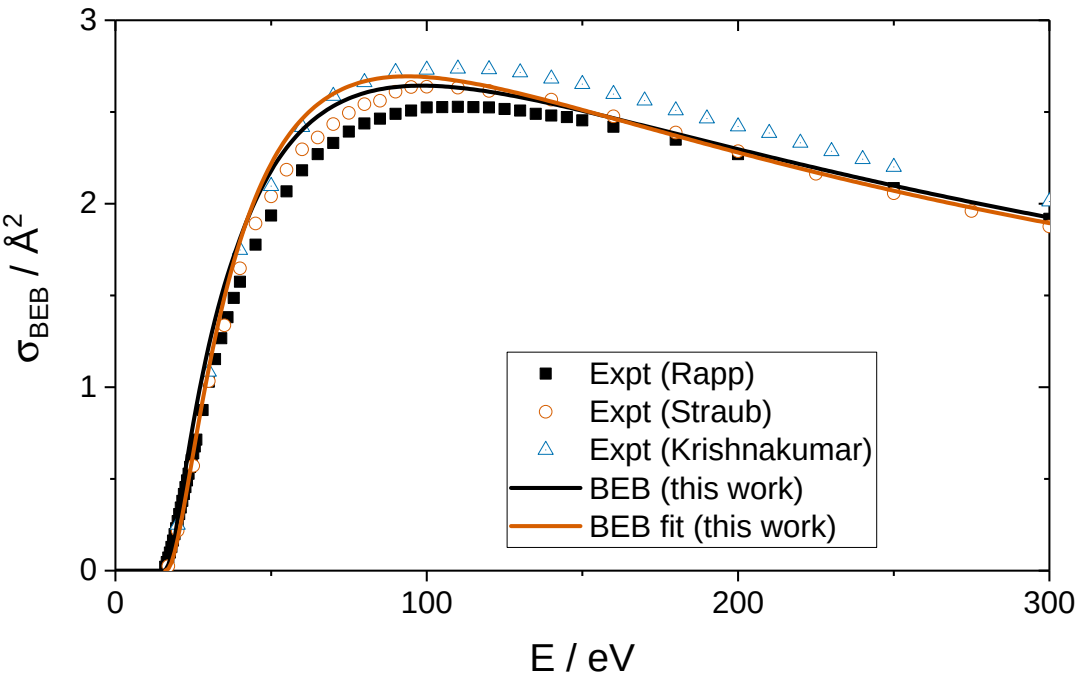
Molecule	σ_{max} / Å^2	EE_{max} / eV	E_t / eV	a_1 / Å^2	a_2	a_3	a_4
CH_3CH_2CN	8.75	78	12.58	596.20	2.769	-0.094	1.024
$CH_3C(O)NH_2$	9.16	81	10.12	653.85	3.869	-0.337	1.535
l-HC_4N	9.20	75	9.98	609.90	3.568	-0.290	1.410
CH_3NHCHO	9.24	80	10.10	655.13	3.879	-0.324	1.529
CH_3C_3N	9.41	78	11.36	644.54	3.172	-0.196	1.220
$(CH_3)_2CO$	9.46	79	9.87	638.31	4.158	-0.209	1.610
C_5H	9.52	71	9.00	593.55	3.916	-0.290	1.522
CH_3CH_2CHO	9.61	79	10.18	645.82	3.926	-0.189	1.504
C_5N	9.67	78	11.33	677.08	3.113	-0.263	1.251
S-CH_3CHCH_2O	9.71	78	10.68	660.87	3.559	-0.204	1.360
R-CH_3CHCH_2O	9.71	78	10.68	660.87	3.559	-0.204	1.359
CH_2CCHCN	9.72	77	10.88	654.17	3.286	-0.214	1.261
$(CH_2OH)_2$	9.77	82	10.85	723.59	3.476	-0.365	1.428
HC_5N	10.16	78	11.17	684.90	3.465	-0.119	1.282
C_2H_5OCHO	10.86	83	11.14	800.41	3.533	-0.293	1.417
$CH_3OC(O)CH_3$	10.94	83	10.70	799.22	3.777	-0.297	1.514
$C_2H_5OCH_3$	10.98	76	10.05	714.16	3.852	-0.163	1.452
C_6H	11.06	72	10.19	710.08	3.244	-0.265	1.272
i-C_3H_7CN	11.41	77	12.33	761.75	2.811	-0.077	1.026
n-C_3H_7CN	11.53	77	12.35	765.06	2.800	-0.065	1.015
CH_3C_4H	11.54	69	9.51	691.43	3.443	-0.211	1.299
l-HC_6H	11.64	72	10.03	739.99	3.328	-0.251	1.276
C_6H_2	11.89	70	9.40	744.05	3.418	-0.329	1.365
CH_3C_5N	12.99	76	10.57	865.96	3.455	-0.211	1.315
C_7H	13.54	69	8.94	835.23	3.698	-0.335	1.468

Table 4.1 (continued)

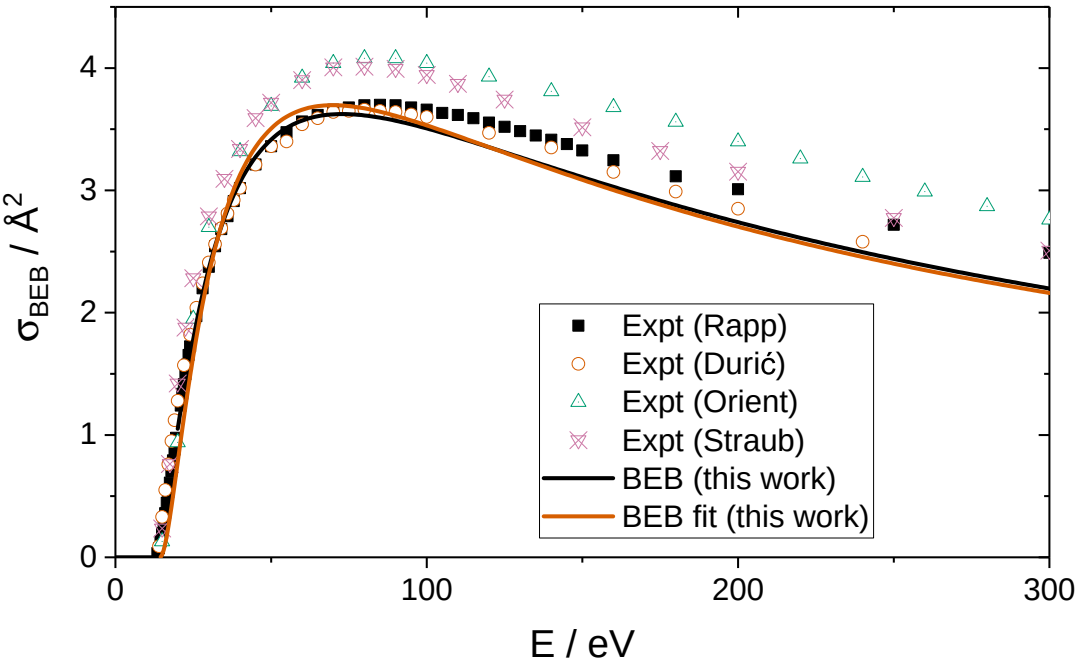
Molecule	σ_{max} / Å^2	EE_{max} / eV	E_t / eV	a_1 / Å^2	a_2	a_3	a_4
HC_7N	13.61	77	10.57	923.26	3.375	-0.268	1.321
c-C_6H_6	14.18	71	9.50	857.47	3.644	-0.178	1.344
CH_3C_6H	15.01	69	9.31	914.32	3.563	-0.257	1.369
C_8H	15.14	70	8.99	942.85	3.670	-0.349	1.471
HC_9N	17.09	76	10.18	1143.49	3.523	-0.278	1.375
$HC_{11}N$	20.35	75	9.91	1357.89	3.621	-0.303	1.416

4.2 Comparison to experimental data

Figure 4.3 compares the total ionisation cross-section we obtain from the BEB model, the fit obtained using equation 4.1, and experimental data from the literature [56, 179–183] for the molecules N_2 and CH_4. We see that, as has previously been noted, there is generally excellent agreement between the experimental and theoretical results. We do note however, that the BEB cross-section typically slightly overestimates the experimental cross-sections at low electron energies, whilst slightly underestimating the cross-section at higher electron energies. We attribute the overestimation at lower electron energies to the fact that the BEB model assumes that any interaction between molecule and electron results in the formation of an ion. However, as discussed back in section 1.2, there are a number of other possible outcomes to such an interaction. At higher electron energies, the discrepancy can be attributed to multiple ionisation. As noted in section 1.3, the experimental cross-sections are recorded as gross cross-sections, i.e. doubly-charged ions carry a weight of two, triply-charged ions carry a weight of three, etc. The BEB model instead provides a counting cross-section, in which all ions have an equal weight.



(a)



(b)

Figure 4.3 Comparison of the total ionisation cross-sections calculated using the BEB model, the fit obtained using equation 4.1, and experimental data from the literature [56, 179–183] for (a) N_2, and (b) CH_4.

4.3 Summary

In this chapter, we have reported total electron ionisation cross-sections calculated using the BEB model for a large number of molecules known to be found in the interstellar medium and circumstellar shells, a number of which are terrestrially unstable. We have also fitted the obtained cross-sections using a widely-used analytical function, and have provided the associated fitting constants.

In the next chapter, we will analyse and interpret data obtained using the electron-molecule crossed beam experiment.

5

Results: Scattering distributions

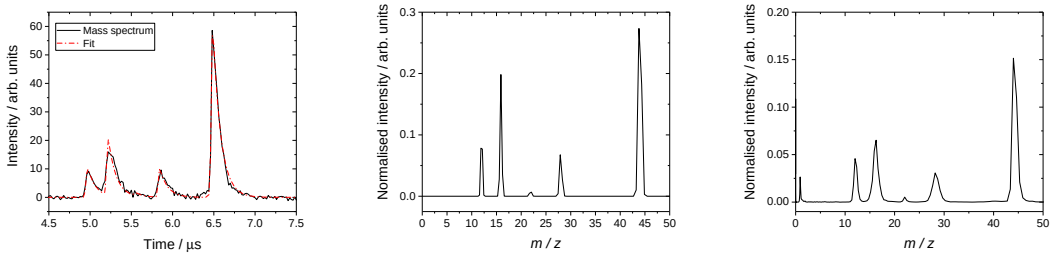
We now turn our attention to experiments carried out using the electron-molecule crossed beam experiment. In the last few years, we have studied a number of molecules using this instrument, five of which will be discussed here. We will first examine the electron-induced dissociation dynamics of carbon dioxide in section 5.1. This will be followed by a similar discussion for nitrous oxide, carbonyl sulphide, and sulphur dioxide, in sections 5.2, 5.3, and 5.4, respectively. Finally, in section 5.5, we will discuss the dissociation dynamics of deuterated benzene, the largest molecule we have studied with our experiment. Note that all scattering distributions and recoil-frame covariance images have dimensions of 324 px by 324 px, with zero kinetic energy corresponding to the centre of the image. Ions at a given radius from the centre of the image have the same kinetic energy; the conversion from pixel units to kinetic energy is discussed in section 3.3.

5.1 Carbon dioxide (CO_2)

Carbon dioxide is well-known to be a major component of the Earth's atmosphere, and has received significant attention in recent years as a contributor to climate change. CO_2 has an absorption band close to the peak of the black body emission spectrum of the Earth, at 4.3 μm, meaning it plays a key role in the infrared radiative transfer in the Earth's atmosphere.[184] Industrially, it finds use in the food industry in areas such as food storage and carbonation of drinks, and in the chemicals industry, where it can be used as a cooling agent or as a reagent in its own right. Further afield, carbon dioxide was first detected in the interstellar medium in 1989,[185] and has been found in a wide number of environments in space.[186] It is known to be a major constituent of interstellar ice,[186,187] which is known to facilitate the formation of complex organic species.[188] The fact that CO_2 is readily available, small, and highly symmetric, makes it an ideal candidate for both theoretical and experimental studies, and it has thus been the subject of numerous investigations over the years.

In the present study, scattering distributions for the products of electron ionisation were first recorded at an electron energy of 100 eV and 50 eV, using an extractor potential of 2 kV, a repeller potential of 1.58 kV and an electron beam pulse duration of 180 ns. Data was then recorded at a later date for an electron energy of 75 eV, using an extractor potential of 1.615 kV, and an electron beam pulse duration of 400 ns (with the timing of the ion optics pulse adjusted accordingly). A total of 800,000, 2,400,000, and 2,100,000 acquisition cycles were recorded at electron energies of 100 eV, 75 eV, and 50 eV, respectively, and an equal number of acquisition cycles of background data was recorded, where the electron beam passes through the interaction region before the arrival of the molecular beam. Signal and background acquisitions were alternated every 50,000 acquisition cycles to reduce the effect of any experimental drift on the background subtraction.

Mass spectra were also recorded using a photomultiplier tube (PMT) to measure



(a) (b) (c)

Figure 5.1 The mass spectrum of CO_2 recorded at an electron energy of 100 eV. a) shows the recorded PMT trace, and the fit of a Gaussian convoluted with an exponential decay, where the Gaussian width and decay lifetime are fixed, b) shows the deconvoluted mass spectrum, and c) shows the mass spectrum obtained by integrating over the x and y co-ordinates of the 100 eV PImMS data file.

the total signal from the phosphor screen at electron energies ranging from 20 eV to 100 eV in 5 eV steps, using an extractor potential of 2.075 kV and a repeller potential of 2.5 kV. We have sufficient signal to present data above an electron energy of 70 eV. Data acquisition was carried out by alternating between recording 1,000 acquisition cycles of signal and background, for a total of 5,000 acquisition cycles of signal, and the background signal subtracted from the signal to give the final mass spectrum.

We will first present the partial ionisation cross-sections of CO_2 and compare these to those found in the literature. Next, we will discuss the dissociation of singly-charged carbon dioxide, and finally the dissociation of doubly-charged carbon dioxide.

5.1.1 Partial ionisation cross-sections

The mass spectrum we obtain using the PMT for an incident electron energy of 100 eV is shown in figure 5.1(a). It is evident that the decay of the P47 scintillator is significant with respect to the timescale of the experiment, thus we need some way of removing this decay from the spectrum. To do this, we fit each peak in the mass spectrum with a Gaussian convoluted with an exponential decay, fixing both the width of the Gaussian and the lifetime of the exponential decay. The resulting fit is

Fragment	PImMS / Å^2	PMT / Å^2	Straub *et al.*[190] / Å^2	King *et al.*[191] / Å^2
C^+	0.374	0.375	0.327	0.312
O^+	0.815	0.709	0.675	0.631
CO^+	0.483	0.354	0.410	0.414
CO_2^+	1.883	2.116	2.370	2.205
CO_2^{2+}	0.035	0.037	0.0028	0.028

Table 5.1 Comparison of partial ionisation cross-sections of CO_2 at an electron energy of 100 eV. Data in the column labelled PMT was recorded using a photomultiplier tube, and that labelled PImMS by integrating over the x and y co-ordinates of the scattering distribution recorded using the PImMS camera. The other two sets of data are taken from the literature. Note that King and Price reported cross-sections relative to those of CO_2^+, so have here adjusted so the sum of the cross-sections is 3.59 Å^2, in the same manner as our data.

shown in figure 5.1(a), and the deconvoluted mass spectrum is shown in figure 5.1(b). From the decay constant, we can estimate the half-life of the P47, which in this case is found to be 65 ns. This is in reasonable agreement with the literature value of 70 ns.[189] The width of the Gaussians, representing the deconvoluted ion signal, were found to be of the order of 10 ns. The width of the Gaussians is determined by the ion optics, which are set up for optimal spatial resolution, rather than optimal time resolution, and the kinetic energy of the ions produced. The pulse length of the electron beam can also play a role, as ions produced early in the beam can move further from the centre of the interaction region with a longer electron beam pulse. We can also obtain a mass spectrum by integrating over the x and y co-ordinates of the PImMS data; the mass spectrum obtained at an electron energy of 100 eV using this method is shown in figure 5.1(c).

Total ionisation cross-sections have been measured experimentally by Rapp and Englander-Golden[56] and Hudson *et al.*[192] to be 3.52 Å^2 and 3.66 Å^2, respectively. As was previously discussed, we use these dedicated measurements to calibrate our partial ionisation cross-sections. Using a mean of these two values to normalise our mass spectra, we obtain the partial ionisation cross-sections listed in table 5.1. We see reasonable agreement with the values reported in the literature in both cases,

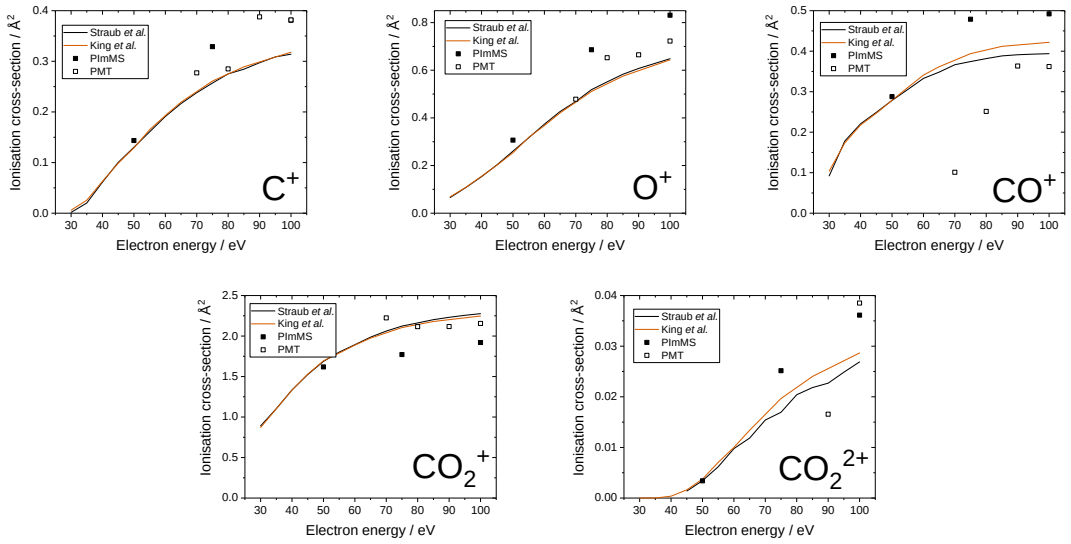


Figure 5.2 Partial electron ionisation cross-sections of CO_2 obtained from a PMT, and by integrating over the x and y co-ordinate of the scattering distribution recorded using the PImMS sensor. Data recorded by Straub *et al.*[190] and King and Price[191] are included for comparison.

with the data recorded using the PMT having slightly better agreement than that recorded with the PImMS camera. It is worth noting that a number of the literature measurements separate out contributions caused by fragmentation of multiply-charged parent ions, which has not been considered here. Our data seem to show a lower cross-section for CO_2^+ formation when determined using the PImMS data. This is most likely due to the fact that if multiple ions hit the same point on the detector at the same time, the PImMS sensor will only detect one ion. As the parent ion is the most common product of electron ionisation of CO_2, and is focussed by the velocity-mapping optics onto a single spot in the centre of the detector, it is possible we have not quantitatively recorded the CO_2^+ ion using the PImMS camera. When the PMT mass spectra were recorded, the VMI optics were defocussed such that the parent ion no longer strikes as well-defined a location, and the scintillator emission is greater if two ions hit the same spot, resulting in this mass spectrum showing better agreement with the literature.

As noted above, we only have sufficient signal-to-noise for our PMT traces above an electron energy of 70 eV. As such, we have determined our partial ionisation

cross-sections using both methods, and will compare the results. Figure 5.2 shows the partial ionisation cross-sections we obtain, along with the data of Straub *et al.*[190] and King and Price.[191] To account for the fact that the data have been normalised to different total ionisation cross-sections, all data has been normalised to the total ionisation cross-sections recorded by Hudson *et al.*.[192] We see that, whilst our data are generally consistent with that reported in the literature, some of the data points show significant deviation from previously reported values.

As discussed above, there is a well-understood issue with the PImMS mass spectra, i.e. the underestimation of the parent cross-section due to multiple ion hits in the same place at the same time. This effect should become less pronounced at lower electron energies, as the electron current, and hence the signal level, rapidly falls off with decreasing electron energy. This is evident in our data; at an electron energy of 50 eV we see excellent agreement with the literature values, whereas at 75 eV and 100 eV we underestimate the cross-section of the parent ion, and consequently overestimate the cross-sections of all other ions. With regard to the mass spectra recorded using the PMT, the opposite is true. The signal-to-noise ratio of the recorded mass spectra decreases significantly with decreasing electron current, hence the fitting becomes less accurate at lower electron energies.

It is evident that the cross-sections recorded for CO_2 in this work will need to be repeated at a later date, either with higher statistics using the PMT, or by defocussing the ion optics before recording mass spectra using the PImMS camera.

5.1.2 Scattering distributions resulting from electron ionisation of CO_2

It should come as no surprise that a large number of studies have focussed on the dissociation of CO_2^+, with various experiments determining appearance potentials and kinetic energy release distributions for both photoionisation[193–200] and electron

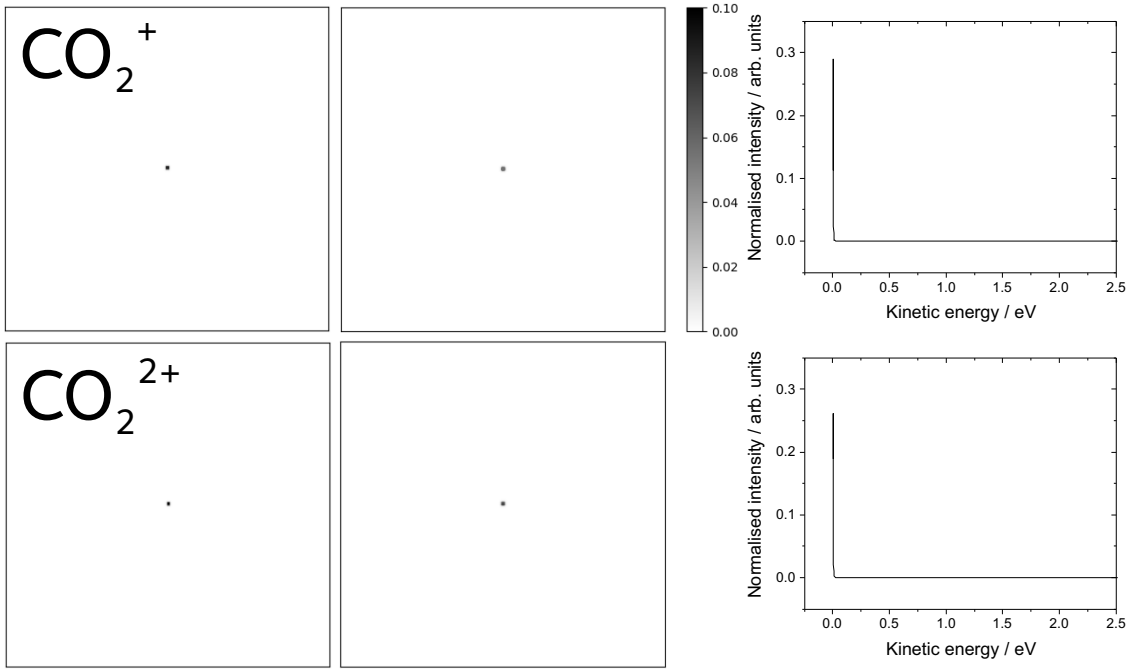


Figure 5.3 The scattering distribution obtained for CO_2^+ and CO_2^{2+} at an electron energy of 100 eV. The columns show the symmetrised image, the inverted image, and the kinetic energy distribution.

ionisation.[34,201–205a] There are three different ionic products that can be formed from the dissociation of CO_2^+: namely C^+, O^+, and CO^+, and all three of these ions are observed in our data. We will now study the scattering distribution of each of these ions in turn, and compare our results with those of other experiments reported in the literature.

Figure 5.3 shows the scattering distribution and associated kinetic energy distribution obtained for CO_2^+ and CO_2^{2+} at an electron energy of 100 eV. We see that ions are formed with very little kinetic energy. As was discussed in section 2.2.2, this is to be expected, given that the formation of CO_2^+ and CO_2^{2+} requires the loss of one or two electrons, respectively. Momentum must be conserved in the loss of the electrons and, as the mass of CO_2 is significantly greater than that of an electron, there is little change in the velocity of the parent ions. The images therefore simply reflect the transverse velocity distribution of the molecules in the molecular beam. For the rest of this thesis the scattering distribution of the parent ions will not be

[a]And also a number of references therein

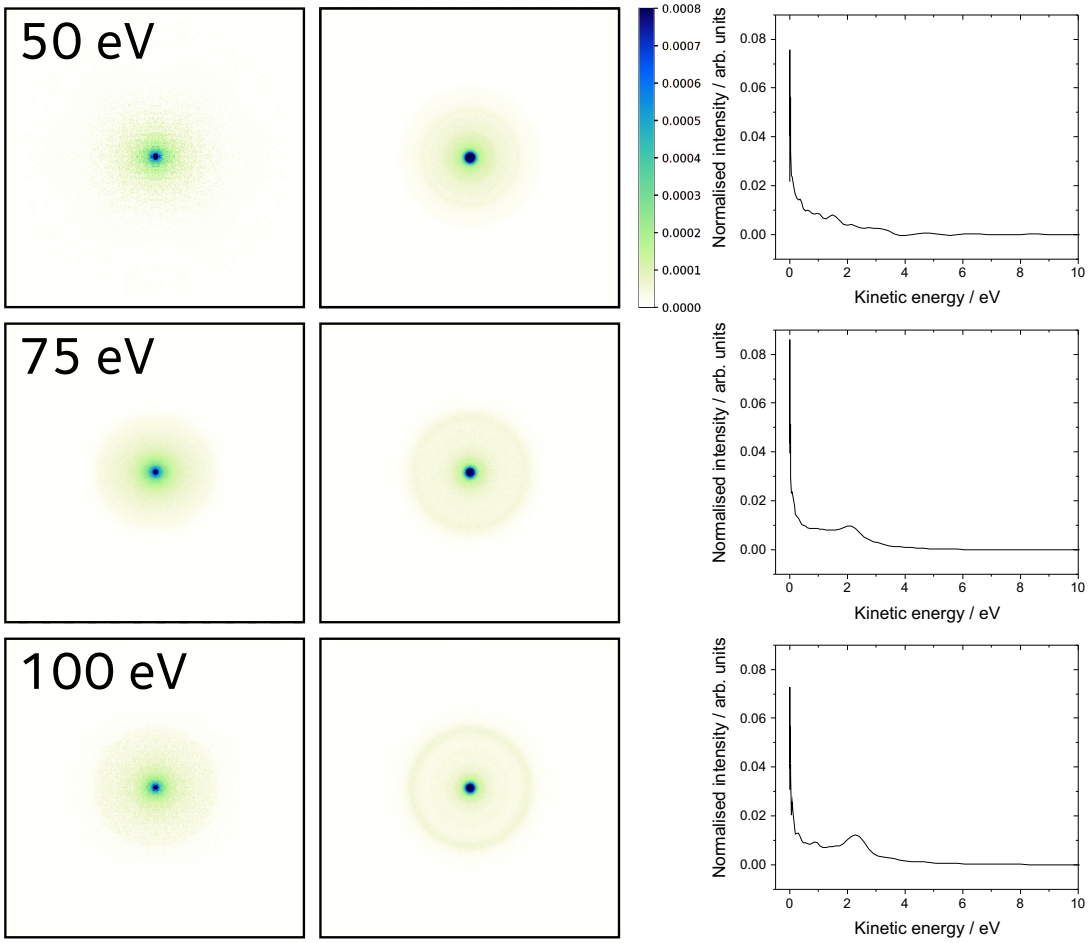


Figure 5.4 The scattering distribution recorded for CO^+ produced from CO_2 after ionisation by electrons of 50 eV, 75 eV, and 100 eV. The columns show the symmetrised image, the inverted image, and the kinetic energy distribution.

shown, but can be assumed to have a very similar form to that shown here.

Figure 5.4 shows the scattering distribution and associated kinetic energy distribution for CO^+ at electron energies of 50 eV, 75 eV, and 100 eV, which are consistent with the kinetic energy release distributions recorded by Lee.[34] We see that the majority of ions are produced with almost no kinetic energy, and that a channel with a kinetic energy of around 2 eV grows in as the electron energy increases. The channel at 2 eV is consistent with the two-body dissociation of CO_2^{2+}, as will be discussed below. The fact that the kinetic energy distribution has a maximum at zero kinetic energy is consistent with a 'statistical' dissociation, where there is time for any energy deposited in the molecule to be redistributed between the available modes

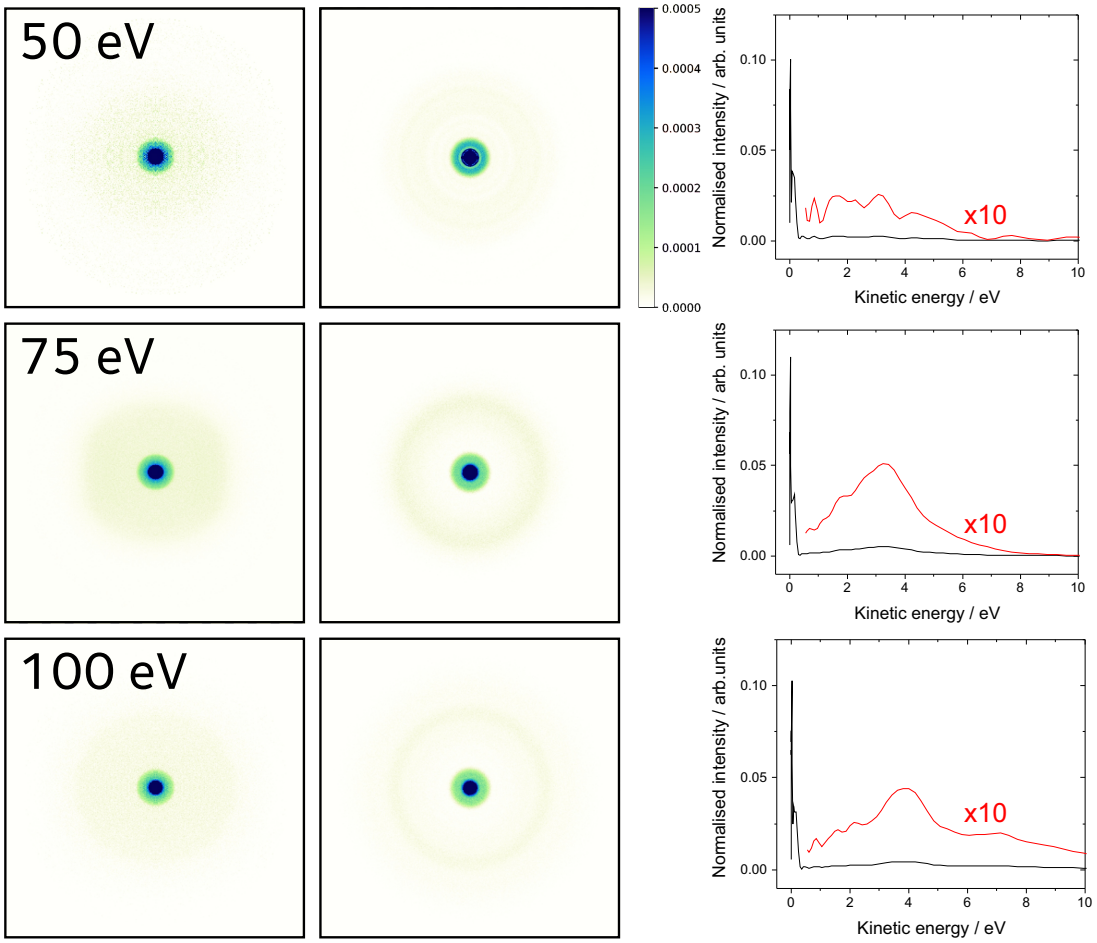


Figure 5.5 The scattering distribution recorded for O^+ produced from CO_2 after ionisation by electrons of 50 eV, 75 eV, and 100 eV. The columns show the symmetrised image, the inverted image, and the kinetic energy distribution.

before the molecule dissociates. We can also note that qualitatively, there is very little change in the kinetic energy distribution with increasing electron energy, other than the increasing prominence of the dissociation of doubly-charged CO_2.

Figure 5.5 shows the scattering distribution and associated kinetic energy distribution for O^+ at electron energies of 50 eV, 75 eV, and 100 eV. These appear to be largely consistent with the distributions recorded by Locht and Davister[204] and Lee,[34] although the peak we observe at around 7 eV for an electron energy of 100 eV is not seen in either of their results. The main feature we observe is a peak at zero kinetic energy, again consistent with a statistical dissociation. We also see the growth of relatively weak features at higher kinetic energies as the electron energy

increases, which are attributed to decay of CO_2^{2+}.

In the literature there has been a significant amount of discussion on dissociation of the $\tilde{C}\ ^2\Sigma_g^+$ state following photoionisation,[193–196,198,199] from which both O^+ and CO^+ can be generated (note that in a photoionisation experiment, specific states can be accessed exclusively). However, as noted by Crowe and McConkey,[202] this process is only responsible for a small fraction of CO^+ and O^+ formation. They come to this conclusion based on the measured appearance potential of the O^+ ion, which is greater than the value expected for dissociation from the $\tilde{C}$ state. The partial ionisation cross-sections for the two ions also show very different behaviour, rather than the two cross-sections following the same trend, but weighted in proportion to the product branching ratio of the $\tilde{C}$ state, as would be expected from dissociation from a single electronic state. In our work, we also observe a higher partial ionisation cross-section for the formation of O^+ than for CO^+ formation, whilst it has been shown that dissociation from the $\tilde{C}$ state gives the opposite result.[193,198] Both Ehrhardt and Kresling[201] and Locht and Davister[204] present five distinct appearance potentials, which is indicative of at least five potential pathways for the formation of O^+; the presence of these extra pathways explains the discrepancy with studies that only access the $\tilde{C}$ state of CO_2^+.

Figure 5.6 shows the scattering distribution and associated kinetic energy distribution for C^+ at electron energies of 50 eV, 75 eV, and 100 eV. We can see that there is very little difference in the kinetic energy distribution over the electron energy range considered in this thesis; in all cases we observe a maximum intensity at a kinetic energy of zero, decaying away to approximately zero for a kinetic energy of 4 eV. The tail extends slightly further at an electron energy of 100 eV due to an increasing contribution from the dissociation of doubly-charged CO_2. The distribution observed is again consistent with a statistical dissociation. Our data are consistent with the kinetic energy distributions presented by Locht and Davister[204] and Lee,[34] but differ slightly from those of Velotta *et al.*, who observed a shoulder

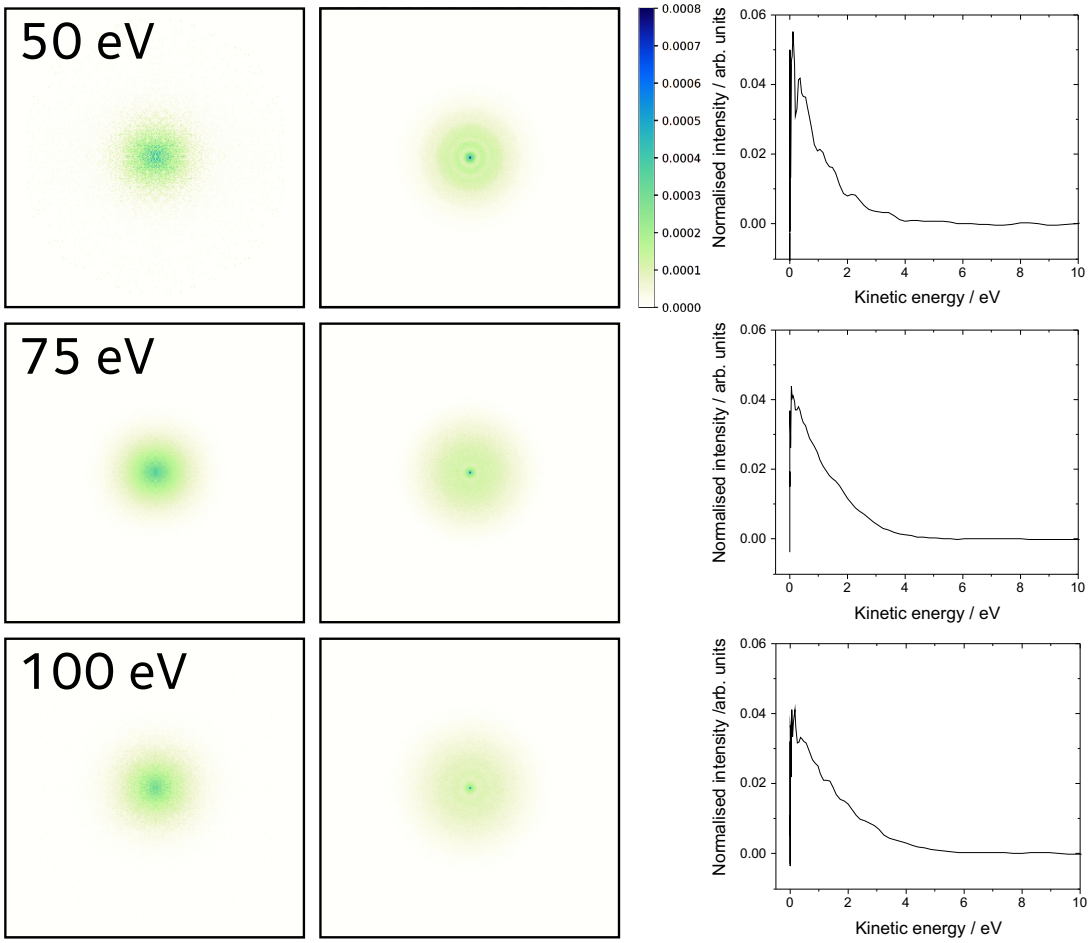


Figure 5.6 The scattering distribution recorded for C^+ produced from CO_2 after ionisation by electrons of 50 eV, 75 eV, and 100 eV. The columns show the symmetrised image, the inverted image, and the kinetic energy distribution.

peak at around 1 eV.[203]

There are two possible sets of products for the formation of C^+ from CO_2^+, as follows

$$CO_2^+ \rightarrow C^+ + 2O \tag{5.1}$$

$$CO_2^+ \rightarrow C^+ + O_2 \tag{5.2}$$

From our results, it is difficult to determine whether there is a preference for one pathway over the other. However, two other studies have found that the latter pathway is the dominant process.[198,204] The dissociation is thought to occur via an electronic state of CO_2^+ with C_{2v} symmetry, with rearrangement to form OOC^+,

which dissociates to give C^+ and O_2.[198] Dissociation can occur from a number of electronic states of CO_2^+ arising from multiple-electron transitions[204] (which can be accessed via a shake-up mechanism, as discussed in section 1.1), with the energetics of the decay process then dictating the kinetic energy distribution observed. The large amount of rearrangement required to produce C^+ is consistent with the statistical dissociation discussed above.

All of the observed ions are found to have a remarkably low kinetic energy when compared with the energy of the incident electron, even after the energy required to ionise the molecule and break the bonds have been accounted for. For the features corresponding to dissociation of the singly-charged parent molecule, there is also very little change in the kinetic energy distribution with increasing electron energy, implying that the dissociation is occurring from the same electronic state(s) in the electron energy range of 50 eV to 100 eV. We believe the most consistent explanation for these observations is that the parent ion is born in a large number of electronic states before relaxing down to a small set of low-lying electronic states, the topology of which dictates the dissociation dynamics.[206] Experiments carried out at lower electron energies would be welcome to determine how close to the threshold of single ionisation these conclusions hold, and to allow us to more readily determine the potential energy surface(s) involved in electron ionisation, but our current electron source does not provide a sufficiently high electron current to allow these measurements to be carried out.

Based on the low kinetic energy of the observed ions, we can also deduce that the two outgoing electrons carry away the majority of the energy of the incident electron. Given that the time taken for the electron to pass through the molecular region is small, on the order of tens of attoseconds for an electron energy of 100 eV, and certainly much faster than the timescale of nuclear motion, very little of the electron energy is transferred to the nuclear framework.[207]

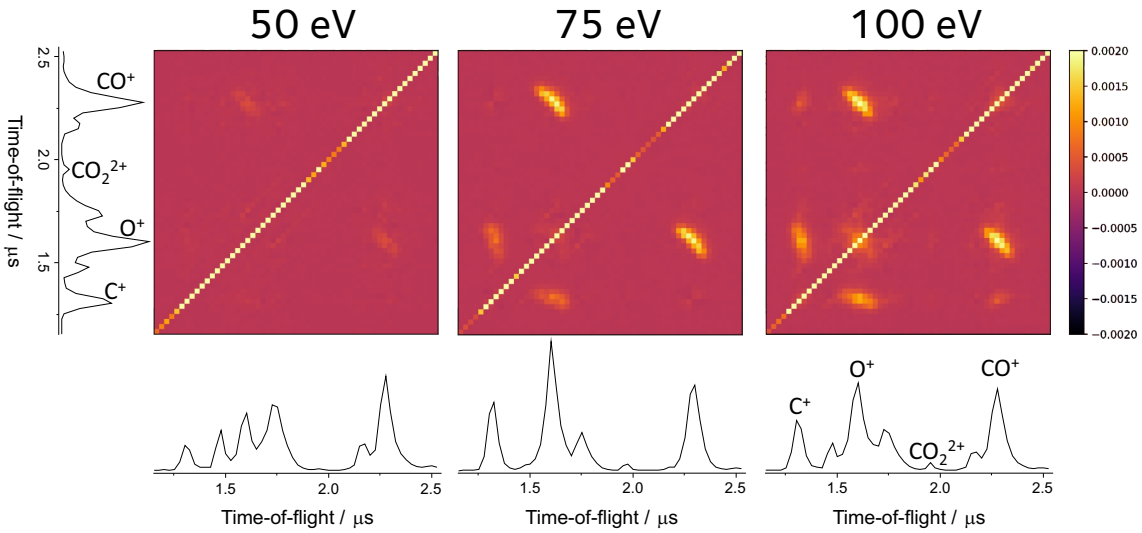


Figure 5.7 TOF-TOF covariance maps of CO_2 recorded at electron energies of 50 eV, 75 eV, and 100 eV. The time-of-flight spectra used for the analysis is shown below the map, with the ions of interest indicated on the 100 eV TOF spectrum. Note that the TOF spectra are not background subtracted (a necessity of covariance analysis), so signal from background ions are also observed in the TOF spectra.

5.1.3 Dissociation of CO_2^{2+}

Whilst less common than single ionisation, double ionisation is known to occur at an appreciable rate in electron scattering, particularly at the upper end of the range of electron energies accessible in this work. According to the cross-sections of Tian and Vidal,[208] double ionisation is around an order of magnitude less likely to occur than single ionisation at an electron energy of 100 eV. A number of studies of the dissociation of CO_2^{2+} have previously been carried out via both photoionisation[209–219] and electron ionisation,[191,208] using techniques such as the PEPIPICO technique and TOF-TOF covariance analysis. A number of works have also derived potential energy surfaces for CO_2^{2+};[213,220] these papers serve as the basis for our discussion of the dissociation of CO_2^{2+}.

According to the the results of Tian and Vidal, there are five pathways via which

CO_2^{2+} can dissociate,[208] as follows

$$CO_2^{2+} \rightarrow CO^+ + O^+ \tag{5.3}$$

$$CO_2^{2+} \rightarrow C^+ + O^+ + O \tag{5.4}$$

$$CO_2^{2+} \rightarrow C + 2O^+ \tag{5.5}$$

$$CO_2^{2+} \rightarrow C^{2+} + 2O \tag{5.6}$$

$$CO_2^{2+} \rightarrow C + O^{2+} + O \tag{5.7}$$

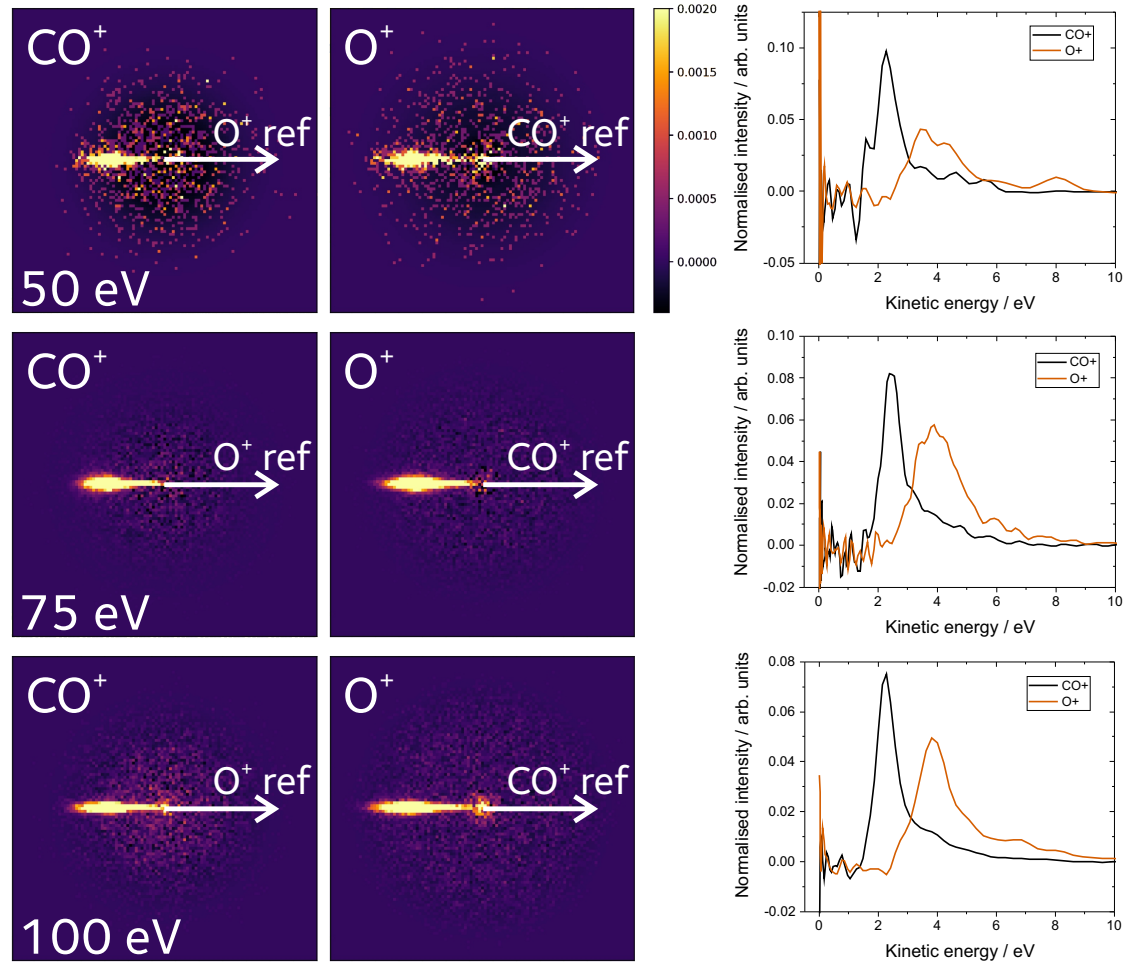
From the TOF spectrum recorded using the PImMS camera, we are able to produce a TOF-TOF covariance map, as was discussed in section 3.4.2. Whilst the PImMS data has a more limited time resolution (25 ns in this case) than the readouts typically used for this purpose, it is sufficient both to determine which channels are available at a given electron energy, and to determine the approximate gradient of the covariance signal in order to help determine the mechanism, as was discussed in section 3.4.1. Figure 5.7 shows the TOF-TOF covariance maps recorded at 50, 75 and 100 eV for CO_2. At an electron energy of 50 eV, we see that the only pathway with an appreciable signal is the two-body dissociation given in pathway 5.3. At an electron energy of 75 eV, we see an increase in the signal from pathway 5.3, clear contribution from pathway 5.4, and a very faint contribution from 5.5, and at an electron energy of 100 eV, all three pathways show an increase in signal. Of course, it is impossible to see pathways 5.6 and 5.7 via this method as they only result in a single charged species, but we see no evidence of C^{2+} or O^{2+} ions in our data. According to the cross-sections of Tian and Vidal,[208] these two processes occur with a much lower frequency than the other three, with cross-sections for the five product channels at an electron energy of 95 eV being 0.120 Å^2, 0.0661 Å^2, 0.0262 Å^2, 8.57 $\times 10^{-4}$ Å^2, and 5.27 $\times 10^{-4}$ Å^2 in the order listed above. We can conclude that the signal-to-noise ratio of our instrument is insufficient to record the weak C^{2+} and O^{2+} signals.

Having established that we see all three of the possible pathways in which covariance can be observed, we now investigate the corresponding recoil-frame covariance images.

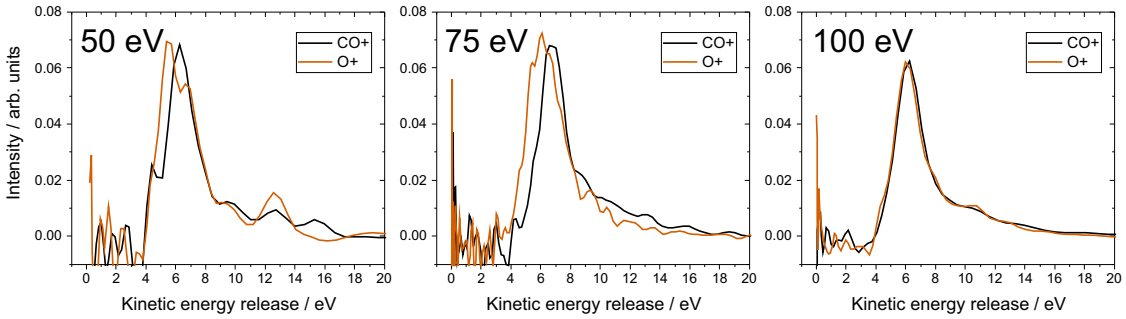
Two-body dissociation

Pathway 5.3, forming CO^+ and O^+, is a two-body dissociation, thus the two ions are expected to have momenta with the same magnitude, but in opposite directions. The recoil-frame covariance images have been plotted in figure 5.8 for incident electron energies of 50, 75, and 100 eV, along with the corresponding energy distribution, obtained by inverting the left-hand side of the image as discussed in section 3.5, then converting from pixel units to kinetic energy units using the calibration discussed in section 3.3. Of course, given that we know the mass and kinetic energy of both ions, it is also possible to determine the momentum distribution of each ion, as is shown in figure 5.9 for an electron energy of 100 eV. We see that, as expected, momentum has been conserved.

In previous work, there has been some disagreement over the kinetic energy release, or releases, observed for this process. Curtis and Eland reported a single dissociation channel with a kinetic energy release of 6 eV, with a full width at half maximum (FWHM) of 3 eV.[209] In contrast to this, Dujardin *et al.* report three distinct channels, centred at 4.5 eV, 6.5 eV, and 9.4 eV.[210] Masuoka *et al.* observe a change in kinetic energy release over the photon energy 40 to 50 eV, from a kinetic energy release centred at 4.4 eV to a kinetic energy release centred at around 6 eV, where it remains up to a photon energy of 100 eV.[212] Similar observations are made by Alagia *et al.*, however the kinetic energy release of the lower energy channel is found to be approximately 3.5 eV.[216] Wu *et al.* ionise CO_2 using strong-field ionisation, and observe a kinetic energy release of approximately 5.2 eV.[217] Long *et al.* report a broad kinetic energy release centred around 5.5 eV.[219] King and Price report two dissociation channels, one with a kinetic energy release of 4.4 eV for



(a)



(b)

Figure 5.8 Recoil-frame covariance images for the formation of CO^+ and O^+ from CO_2^{2+} at three electron energies, along with the associated kinetic energy distributions (a). The label in the kinetic energy distribution corresponds to the signal ion, obtained using the inversion method discussed in section 3.5.1 (as will be the case for all subsequent recoil-frame covariance maps). (b) shows the kinetic energy release, which has been determined from the kinetic energy distribution of each signal ion independently, based on conservation of momentum.

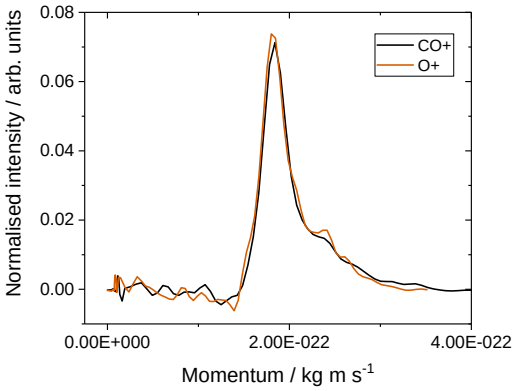


Figure 5.9 Momentum distribution of covariant CO^+ and O^+ recorded at 100 eV. The two momenta match, showing momentum is conserved.

an incident electron energy of 50 eV, increasing to 5 eV for an electron energy of 65 eV, and a second channel with kinetic energy of 7.5 eV above an electron energy of 50 eV.[191] If we consider the kinetic energy distributions obtained in our work, we see that, whilst the signal level increases significantly with increasing electron energy, there is very little difference between the kinetic energy distributions over the electron energy range of 50-100 eV. The main feature is observed to have a kinetic energy release of approximately 6 eV, with a tail extending out to higher kinetic energies. The consistency in the kinetic energy distributions indicates that the potential energy surfaces from which this dissociation occurs are not changing significantly over this energy range. The fact that the tail in the kinetic energy distribution is not smooth is most consistent with decay from a number of electronic states.

Hochlaf *et al.* have calculated potential energy surfaces for the dissociation of CO_2^{2+} along the C-O bond,[220] as shown in figure 5.10. The approximate bond length of neutral CO_2 has also been added to the figure, and the ground state of the dication has been shown to lie 37.34 eV above that of neutral CO_2.[213] Given the fact that electron ionisation is not constrained by the same selection rules as photoionisation, and both the CO_2^{2+} and CO^+ can be internally excited, it is difficult to determine the precise potential energy surface(s) over which the dissociation occurs, but it

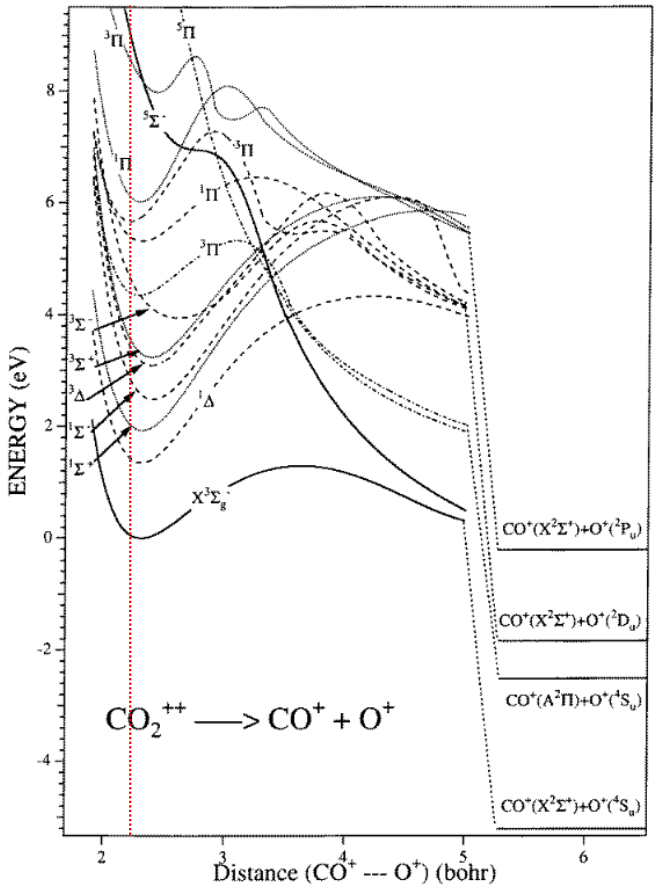


Figure 5.10 Potential energy surface of CO_2^{2+} calculated by the CASSCF approach with $R_{CO} = 2.3$ Bohr, reproduced with permission from [220]. The bond length of neutral CO_2 has also been indicated. © IOP Publishing. All rights reserved. Permission conveyed through Copyright Clearance Centre, Inc., license ID 1066215-3.

seems likely that the dissociation will be dominated by the lower-lying states. One potential pathway for the main dissociation channel could be from an internally excited $\tilde{X}\ ^3\Sigma_g^-$ ground state of the doubly-charged ion, dissociating to the lowest energy states of CO^+ and O^+; the energy separation between the potential barrier of the $\tilde{X}\ ^3\Sigma_g^-$ state and the ground states of the two ionic fragments is approximately 6.5 eV. Tian and Vidal suggest that, as the ionisation cross-sections of both CO_2^{2+} and the $CO_2^{2+} \rightarrow CO^+ + O^+$ dissociation channel peak at approximately the same energy (120 eV), the two pathways may involve similar electronic states.[208]

Three-body dissociation

The covariance images and associated kinetic energy distributions for pathway 5.4, $CO_2^{2+} \rightarrow C^+ + O^+ + O$, are shown in figure 5.11. Whilst it is possible to determine a kinetic energy distribution from the 50 eV scattering distribution, it should be evident from the covariance map that the signal level is not sufficiently high to allow us to determine the distribution with any accuracy, so it has been omitted here. We see a significant change in the kinetic energy distribution on increasing from an electron energy of 75 eV to 100 eV. It is evident that in this energy range, new dissociation pathways become available. There is also a clear difference in the covariance images recorded at the two energies, further confirming the change in dominant dissociation pathway. This does, however, contrast with the results of Masuoka *et al.*, who observed no real change in the kinetic energy release distribution of this channel above an electron energy of 70 eV.[212] The only other study we could find which gave information on the kinetic energy release of this channel was that of King and Price, where they used a Monte-Carlo simulation to determine two components of kinetic energy release at 6.0 eV and 9.5 eV for an electron energy of 60 eV.[191] A potential cause for the discrepancy between our work and that of Masuoka *et al.* could be due to the fact that in our experiments we are using electron ionisation, rather than photoionisation, and may therefore be accessing some state(s) not available via photoionisation.

As discussed previously, a three-body dissociation can proceed via any one of three mechanisms: a concerted dissociation, an initial charge separation, or deferred charge separation. We can establish the mechanism both from the gradient of the TOF-TOF covariance map, and the recoil-frame covariance map. Both Tian and Vidal[208] and King and Price[191] conclude that the dissociation proceeds via an initial charge separation process, and our data corroborates their findings. The expected gradient for the feature is -0.43 $\left(\frac{m_{C^+}}{m_{CO^+}}\right)$, and King and Price observe that the gradient matches this below 65 eV, becoming less negative at higher electron energies

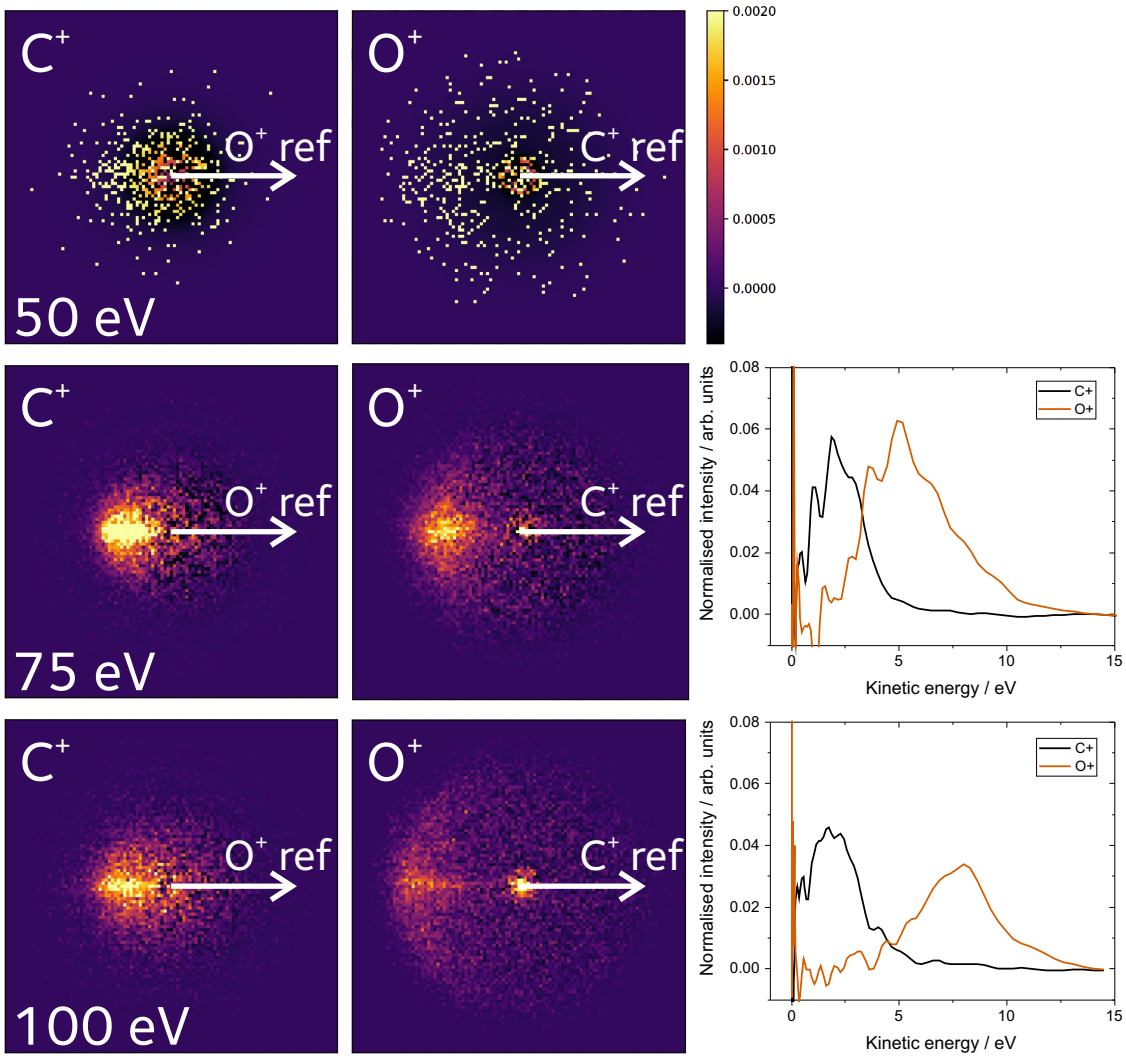


Figure 5.11 Recoil-frame covariance images for the formation of C^+ and O^+ from $CO_2{}^{2+}$ at three electron energies, along with the associated kinetic energy distributions.

(-0.34 at 100 eV, -0.26 at 200 eV). The fact that the gradient changes seems to be consistent with our observed change in kinetic energy distribution, as a change in gradient implies a change in the dissociation mechanism. A gradient of less that -0.43 is consistent with the neutral decay step resulting in the C^+ ion gaining kinetic energy back along the initial direction of travel of the CO^+ ion, on a timescale which allows little time for the CO^+ fragment to rotate before it decays.

We can gain further insight by studying the recoil-frame covariance maps. We see two main features at 100 eV, a well-defined feature opposite to the reference direction readily visible in both maps, and a feature spanning a large range of

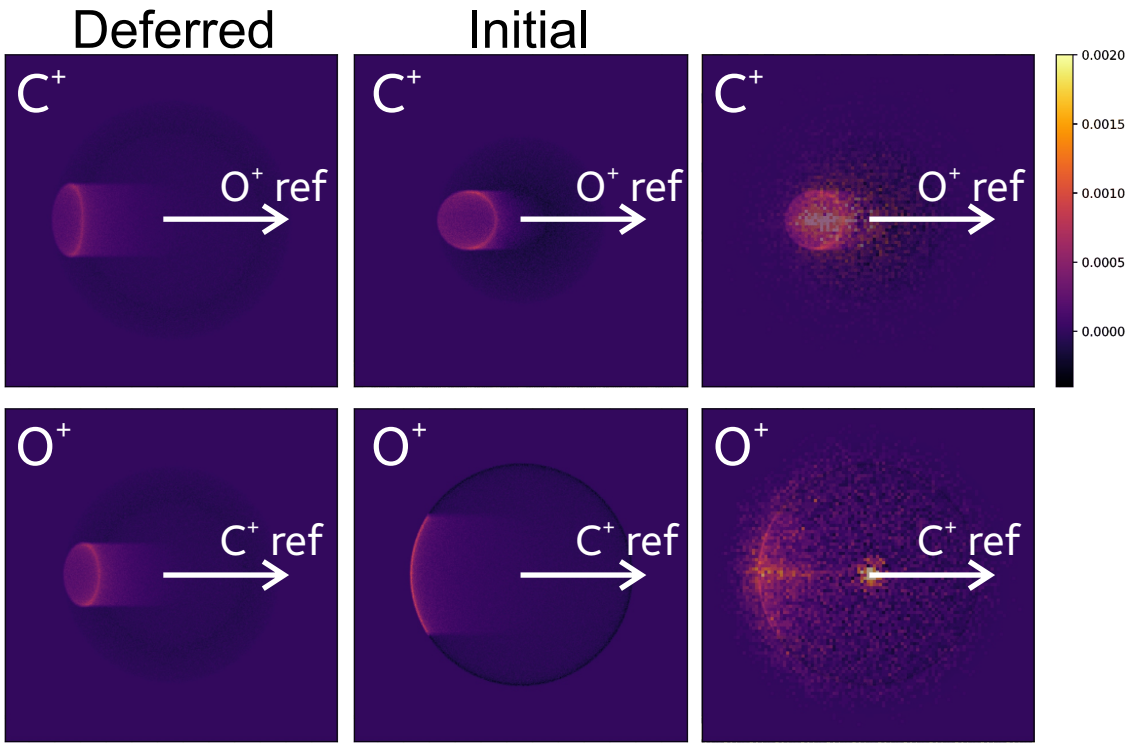


Figure 5.12 Simulation of the covariance images obtained for a deferred charge separation (left) and initial charge separation process (centre) for the dissociation channel $CO_2^{2+} \rightarrow C^+ + O^+ + O$. The right images show the experimental covariance image obtained at an electron energy of 100 eV overlaid with the initial charge separation simulation.

angles at constant radius in the O^+ map, with a corresponding 'blob-like' feature in the C^+ map. The second feature is consistent with an initial charge separation process in which the CO^+ fragment has time to rotate, as can be shown through a Monte-Carlo simulation. In this case, a total of 500,000 molecules are made to fragment over 100,000 acquisition cycles. According to Hsieh and Eland, for a photon energy of 48.8 eV the best fit for the energy release of the two steps of an initial charge separation are Gaussians centred at 5.0 eV and 0.8 eV, with widths of 3.5 eV and 1.0 eV, respectively.[221] However, we note that the peak of the kinetic energy distribution we record at an electron energy of 100 eV, the kinetic energy of the O^+ is greater than the 5 eV kinetic energy release found by Hsieh and Eland. To determine a value for the charge separation step, we have used the modal kinetic energy of the O^+ atom (~8 eV), and from this calculated the approximate kinetic

energy release for the charge separation process, initially assuming a CO^+ partner fragment, of ∼12.5 eV. For the simulations reported here, a kinetic energy release of 12.5 eV is set for the charge separation step, and 1 eV for the neutral loss step. The results of the simulation are shown in figure 5.12, along with the expected results for a deferred charge separation. Despite the relatively non-rigorous choice of energetics for the two dissociation steps, we see that the covariance images obtained from the simulation of initial charge separation match the feature in the experimental image remarkably well, lending weight to our assignment of the mechanism. The central feature could result from either a concerted charge separation in which the neutral O blocks the C^+ ion, an initial charge separation where either no kinetic energy is released in the neutral loss step, or if the dissociation occurs along the velocity vector of the CO^+ ion. Given the gradient of the coincidence spectrum reported by King and Prince, the latter is the most consistent mechanism, and this is what we propose here. For the 75 eV covariance image, the main feature is observed to lie along the reference axis. This feature has a greater angular spread than that observed at 100 eV, and is thus proposed to be the result of an initial charge separation process in which the kinetic energy release in both the charge separation and the neutral loss step is relatively small.

Pathway 5.5, $CO_2^{2+} \rightarrow C + 2O^+$, is widely accepted to proceed via a concerted dissociation. The gradient of all TOF-TOF coincidence and covariance maps have been found to be -1, which is consistent with a concerted dissociation. A gradient of -1 would also be consistent with a deferred charge separation pathway, however it seems unlikely that the molecule would undergo the rearrangement required to produce O_2^{2+}, required for a deferred charge separation pathway. The gradient is inconsistent with an initial charge separation process, for which one would expect a gradient of -0.57.

Figure 5.13 shows the recoil-frame covariance maps, along with the associated kinetic energy distributions. As both the reference and signal ion are the same for

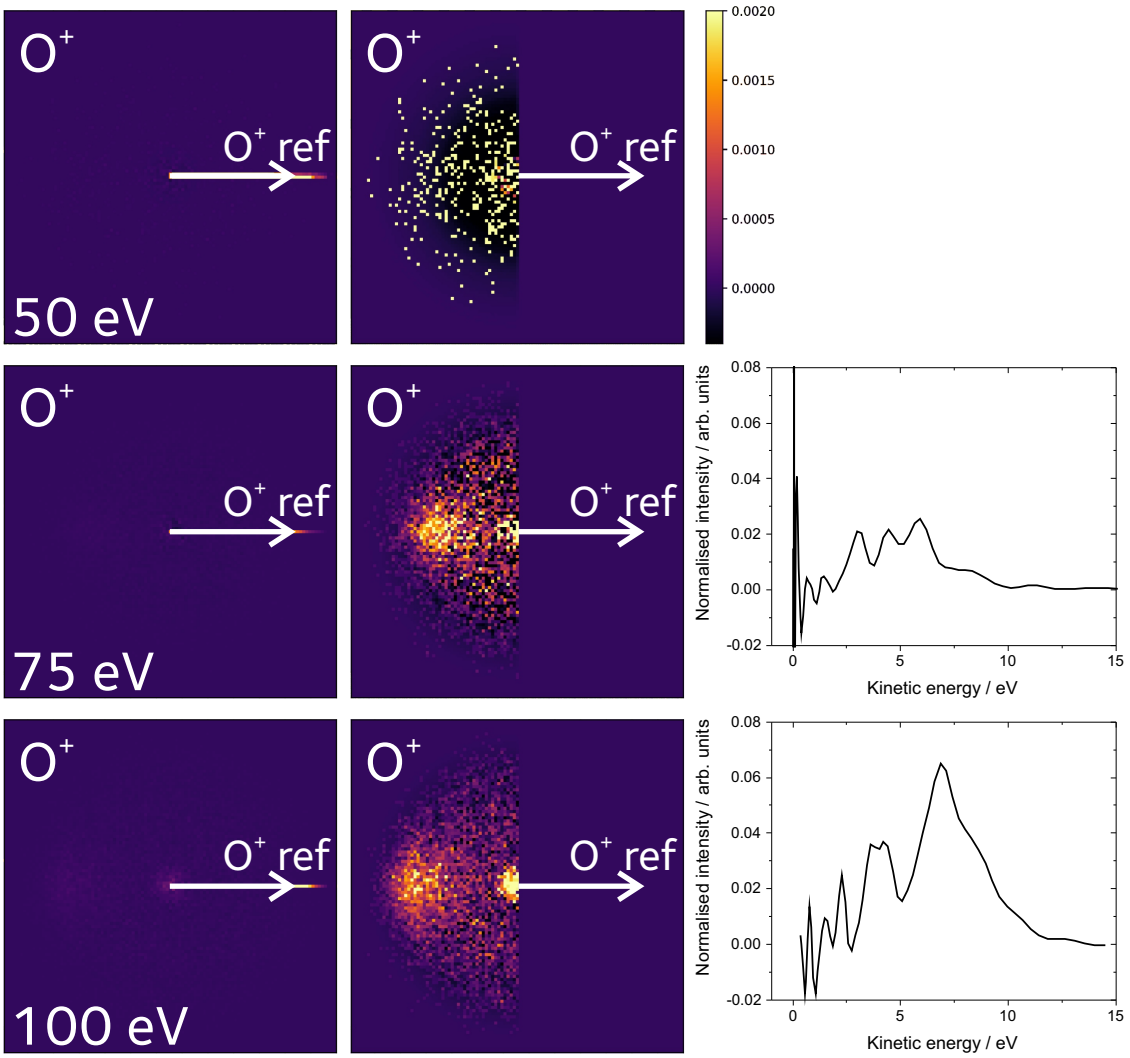


Figure 5.13 Recoil-frame covariance images for the formation of O^+ and O^+ from CO_2^{2+} at three electron energies, along with the associated kinetic energy distributions.

this pathway, we see a strong feature pointing along the reference direction, known as self-covariance; within each frame, it is evident that one of the signal ions must be the same as the reference ion, so will always lie along the reference direction, i.e. every ion is covariant with itself. The left-hand side of the covariance map has also been plotted to show the signal of interest. Note that there is evidently insufficient signal at 50 eV for a meaningful kinetic energy distribution to be obtained. We see no evidence in our data which is inconsistent with a concerted pathway. As with the other three-body dissociation pathway, we see a change in the kinetic energy distribution with increasing kinetic energy. We see two dominant channels in the

100 eV kinetic energy distribution, with peaks at 3.9 eV and 6.8 eV, and see shoulders on the higher-energy peak, indicative of decay from further electronic state(s). Note that, under the assumption the neutral carbon remains approximately stationary, the kinetic energy release will be double the peak value, as two O^+ ions are produced in the dissociation. The peaks below an energy of 2.5 eV are most likely a result of noise in the covariance image; no meaningful signal is observed in the covariance image at the corresponding radius. The dissociation most likely proceeds via a number of repulsive electronic states.

In the 75 eV kinetic energy distribution, peaks are observed at 3 eV, 4.4 eV, 5.9 eV, and 8.3 eV. The signal-to-noise ratio of the covariance map is relatively low, so some care has to be taken in the interpretation of these results. There is evidently a large difference between this kinetic energy distribution and that observed for an incident electron energy of 100 eV. The two lower-energy peaks observed here are most likely consistent with the peak at 3.9 eV in the 100 eV distribution, the peak at 5.9 eV either shifts to higher energy and becomes more intense, or a second channel at an energy of around 7 eV grows in over this energy range. The pathway resulting in a peak at 8.3 eV is responsible for the main shoulder in the 100 eV kinetic energy distribution.

In coincidence experiments in which no information on the position of the ion hits are obtained, it can be difficult to determine the kinetic energy distribution for ions of the same mass-to-charge ratio, due to the dead time between the detection of the first ion and the detector being reset to allow the detection of a second ion. By using velocity-map imaging in conjunction with a multi-mass imaging sensor, there is no such problem, as unless both ions strike the same position on the detector, there is no issue of dead time, and both ions can be successfully detected.

We can also compare our results to those obtained through photoionisation. Johnsson *et al.* have used velocity-map imaging to study photoionisation of CO_2 using a free-electron laser (FEL) set to a wavelength of 45.55 eV;[197] the kinetic

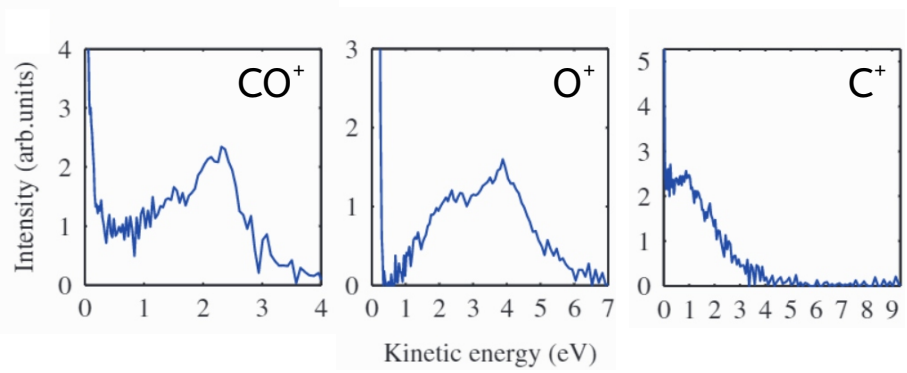


Figure 5.14 Kinetic energy distributions obtained by Johnsson *et al.* upon photoionisation of CO_2 using 45.55 eV photons. Adapted from [197]. © Taylor & Francis. All rights reserved.

energy distributions they obtain are shown in figure 5.14. We see that there is in general good agreement between the positions of the peaks observed by Johnsson *et al.*, and those found in our recoil-frame covariance analysis. This shouldn't be particularly surprising, given that the Coulomb repulsion between the two ionic fragments plays a major role in determining the kinetic energy of the ions formed from the electronic states of doubly-charged ions. For the formation pathway of CO^+ and O^+, they propose two dominant sets of products: formation of CO^+ and O^+ in their electronic ground states, with a kinetic energy release of 6.1 eV (CO^+ 2.2 eV, O^+ 3.9 eV), in agreement with our results, and formation of CO^+ and O^+ in their first-excited and ground electronic states, respectively, with a kinetic energy release of 3.6 eV (CO^+ 1.3 eV, O^+ 2.3 eV). We do not see evidence for the latter pathway in our data, suggesting it is not a major dissociation pathway following electron ionisation.

We also observe intensity at low kinetic energy, which can be attributed to dissociation of ${CO_2}^+$. Johnsson *et al.* measured the kinetic energy of the ejected electrons, allowing them to determine the electronic states involved in the dissociation. They find that the $\tilde{C}$ state can dissociate to form both CO^+ and O^+, with the ion carrying ~ 0 eV and $\sim$ 0-0.5 eV, respectively,[197] kinetic energies consistent with those observed in our experiments. They also identify at least four dissociation pathways

which form C^+ and O_2 from states involving multiple-electron transitions, with the C^+ carrying away energies ranging from 0 eV to 3.6 eV.

5.1.4 Summary

We have reported partial ionisation cross-sections, scattering distributions, and recoil-frame covariance images for the electron ionisation products of carbon dioxide. We have discussed the scattering distributions in the context of previous work reported in the literature, and have demonstrated the use of the covariance analysis technique to obtain new insight into the dissociation of multiply-charged parent ions. It has been observed that the majority of the energy of the incident electron is most likely carried away by the outgoing electrons, rather than being transferred to the molecular framework, and that the dissociation dynamics are dominated by the topology of one or more low-lying electronic states, which are populated prior to dissociation. Further work is required to record high-quality partial ionisation cross-sections, but general agreement has been shown with previously reported values, and methodologies for future experiments have been outlined.

5.2 Nitrous oxide (N_2O)

Nitrous oxide (N_2O) is a linear triatomic molecule, and has found use in a number of industrial applications. It has been used in the medical profession for almost 200 years, finding use in anaesthesia due to its rapid onset and offset of effect, lack of odour, and a number of other desirable properties.[222] It also finds use as a rocket propellant, due to being safe to store at room temperature, but decomposing exothermically at higher temperatures (specifically above 793 K) to produce N_2 and O_2. Thrust can be achieved by emitting these gases, and the O_2 produced can also be combusted with a wide variety of fuels, further increasing the thrust.[223] In atmospheric chemistry, N_2O is known to be a greenhouse gas, with a global warming potential 296 times that of CO_2.[224] In recent years, emissions of N_2O have increased,

predominantly due to agricultural sources.[225] N_2O itself is stable in the troposphere, but undergoes photodissociation in the stratosphere, supplying ozone-depleting NO radicals,[224,226] and is currently the dominant ozone-depleting emission.[227] N_2O has also been found in the interstellar medium. First detected in 1994 by Ziurys *et al.*,[228] it is known to be formed via both neutral-neutral reactions in regions of sufficiently high temperature, for example in certain regions of Sagittarius B2,[229] and in extraterrestrial ices.[230]

In the present study, scattering distributions for the products of electron ionisation were recorded at an electron energies of 50 eV, 75 eV and 100 eV using an extractor potential of 2 kV and a repeller potential of 1.58 kV. The electron beam pulse duration was set to 180 ns at all electron energies, with the timing of the ion optics pulse set accordingly. A total of 750,000, 800,000, and 1,850,000 acquisition cycles were recorded at electron energies of 100 eV, 75 eV, and 50 eV, respectively, and an equal number of acquisition cycles of background data were recorded. Signal and background acquisitions were alternated every 50,000 acquisition cycles to reduce the effect of any experimental drift on the background subtraction.

Mass spectra were recorded using a photomultiplier tube (PMT) directed towards the scintillator at electron energies ranging from 40 eV to 100 eV in 10 eV steps, using an extractor potential of 3.742 kV and a repeller potential of 5 kV. Data acquisition was carried out by first recording 2,500 acquisition cycles of signal followed by 2,500 acquisition cycles of background at each electron energy. The background signal is then subtracted from the signal to give the final mass spectrum. Note that the measurement was carried out using a longer flight tube (397 mm) than that used for the remainder of the experiments carried out in this thesis (197 mm), hence the higher extractor and repeller potentials.

We will first present the partial ionisation cross-sections of N_2O and compare these to those previously reported in the literature. Next, we will discuss the scattering distributions we obtain, and the results of the covariance analysis between

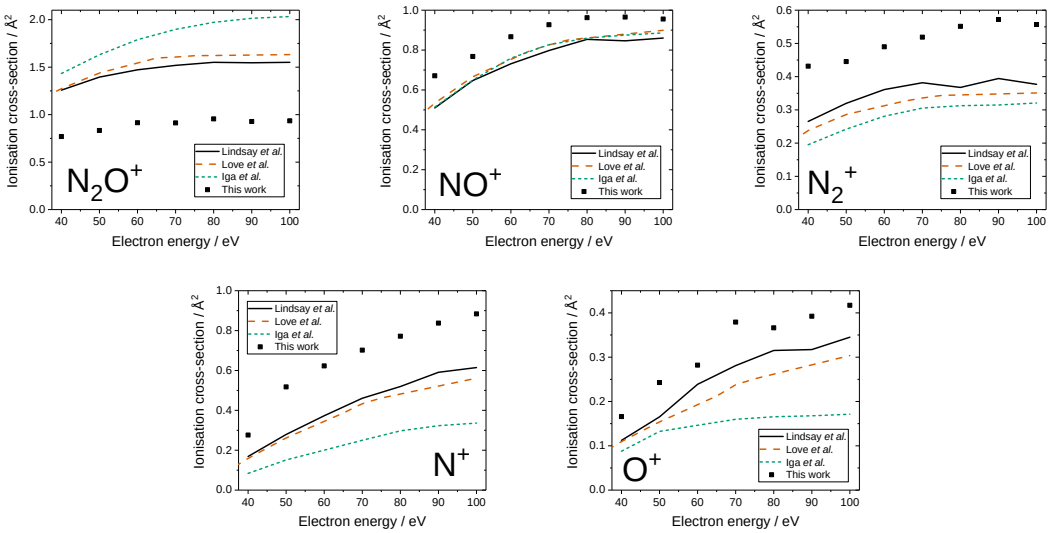


Figure 5.15 Partial ionisation cross-sections obtained for N_2O by fitting mass spectra recorded using a PMT pointing towards the phosphor screen on our experiment, compared to results from the literature [231–233]. All partial ionisation cross-sections have been normalised to the total ionisation cross-sections of Rapp and Englander-Golden.[56]

the detected fragment ions. Finally, we will compare the results we obtain for N_2O with those obtained for CO_2, discussed in the previous section.

5.2.1 Partial ionisation cross-sections

Figure 5.15 shows the partial ionisation cross-sections we obtain for N_2O, obtained after fitting the mass spectra obtained using the PMT with Gaussians convoluted with an exponential decay, as discussed previously. The results are compared to other partial ionisation cross-sections available in the literature [231–233]. The sums of all partial ionisation cross-sections have been normalised to the total ionisation cross-sections of Rapp and Englander-Golden.[56] We see that we significantly underestimate the cross-section of N_2O^+, whilst we overestimate the cross-section of all the fragment ions. The reason for this is that, unfortunately, our mass spectra were recorded under VMI conditions for N_2O which, as discussed previously, leads to a lowering in the parent ion signal relative to the fragment ions. However, if we plot the relative probability of forming a given fragment ion, which avoids the need to consider the parent ion, we see that our results are in good agreement with those

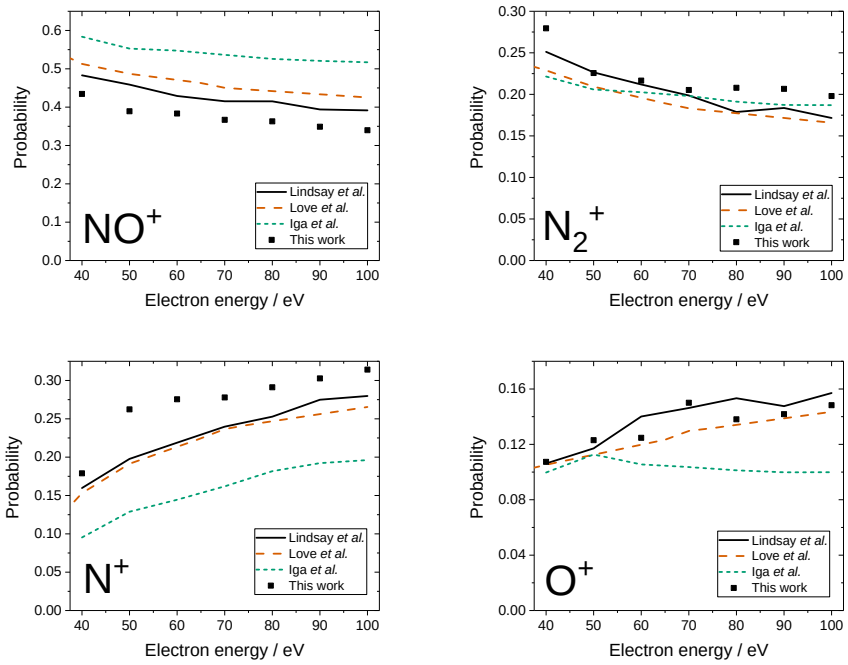


Figure 5.16 Probability of forming each fragment ion of N_2O compared to results from the literature [231–233]. By removing the contribution from N_2O^+, we can more readily assess the accuracy of the remaining partial ionisation cross-sections.

reported in the literature. These data can be found in figure 5.16.

5.2.2 Scattering distributions resulting from electron ionisation of N_2O

The electron ionisation of N_2O has previously been studied by Olivier *et al.*, through an experiment which utilises a retarding potential lens, combined with a quadrupole mass spectrometer.[234,235] Briefly, ions are produced by a Nier-type ion source, which utilises an electron beam of controllable energy to ionise the sample gas, with the ions then being accelerated through a series of slits, as in a conventional mass spectrometer. After passing through the source exit slit, the ions then pass through a retarding lens, and are then accelerated at the entrance slit of a quadrupole mass spectrometer. By varying the potential applied to the retarding lens, ions of different kinetic energies can be allowed into the mass spectrometer; the quadrupole can be used to select ions of a specific mass-to-charge ratio. By varying either the

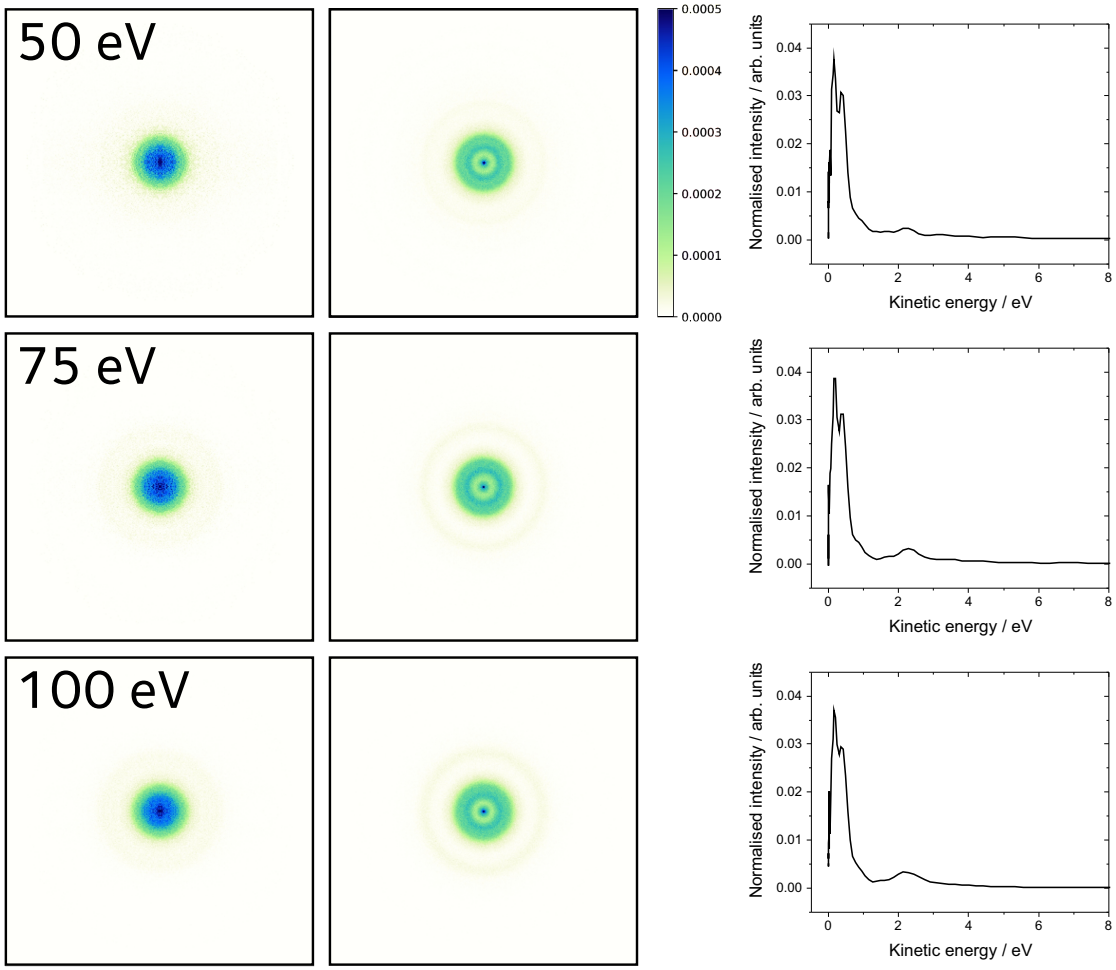


Figure 5.17 The scattering distribution recorded for NO^+ produced from N_2O after ionisation by electrons of 50 eV, 75 eV, and 100 eV. The columns show the symmetrised image, the inverted image, and the kinetic energy distribution.

retarding potential at a fixed electron energy, or by varying the electron energy at a fixed retarding potential, the kinetic energy releases at each electron energy can be determined. A full description of their methods can be found in [236]. A number of photoionisation studies have also focused on N_2O; we will discuss our data in light of these previous experiments.

Figure 5.17 shows the scattering distribution obtained at three electron energies for the NO^+ ion. The scattering distribution consists of a relatively weak central feature, a double peak at low kinetic energy, with maxima at 0.15 eV and 0.35 eV, consistent with an impulsive dissociation on a weakly repulsive potential energy surface, and a feature at a kinetic energy of approximately 2.2 eV, which is attributed

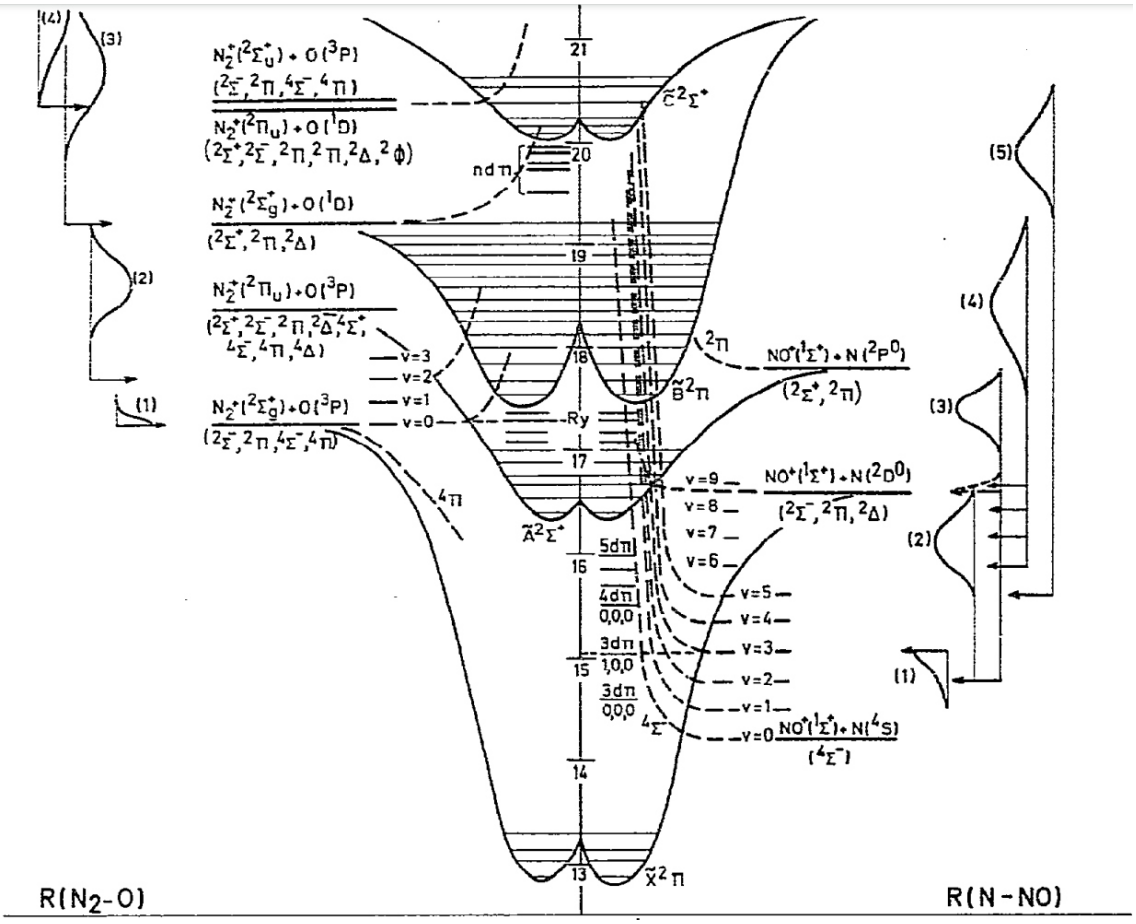


Figure 5.18 Potential energy surfaces for the formation of NO^+ and N_2^+ from N_2O^+. The pathways discussed by Olivier *et al.* are also indicated. Reproduced from [234], with the permission of Elsevier under license 4930370368186.

to the dissociation of N_2O^{2+}. We also observe a shoulder with a kinetic energy of approximately 0.9 eV. This suggests there are multiple pathways for formation of NO^+. We also observe that there is very little difference in the kinetic energy distribution across the range of energies considered, as we previously found to be the case for CO_2.

Olivier *et al.* previously found a total of five dissociation processes with appearance potentials below 30 eV in their experiment, at 15.29 eV, 16.9 eV, 17.6 eV, 19.25 eV. and 27.3 eV.[234] Other than the final process, they attribute each process to predissociation following population transfer to a $^4\Sigma^-$ state of N_2O, from a number of different initial electronic states. They attribute the process with an appearance energy of 15.29 eV to autoionisation of excited N_2O prepared in one of

the Rydberg states corresponding with the $\tilde{A}$ state of N_2O^+, which then dissociates into ground state NO^+ and N with very little kinetic energy release. The second threshold corresponds with the energy of the $\tilde{A}$ state, which is thought to dissociate along the $^4\Sigma^-$ potential energy surface to give products in the ground electronic state, with NO^+ in the $v = 2$ vibrational state. The third threshold corresponds with the energy of the $\tilde{B}$ state, which they again attribute to predissociation to a $^4\Sigma^-$ state, followed by dissociation to vibrationally excited ($v = 6 - 9$) NO^+ in its electronic ground state. The fourth threshold corresponds to formation of ions either via autoionisation of the Rydberg series corresponding to the $\tilde{C}$ state, or the $\tilde{C}$ state itself, which dissociates following predissociation to the $^4\Sigma^-$ state. The final threshold is attributed to double ionisation.

Unfortunately, no kinetic energy distribution for NO^+ is provided by Olivier *et al.* above an electron energy of 18 eV, meaning a direct comparison to our data cannot be made. However, we can determine the approximate energy available for each of the pathways discussed above using the potential energy surface provided by Olivier *et al.*. The dissociation pathways do not necessarily match the energies we see in our data, but there are a number of possible reasons why this might be the case. Firstly, there could be a radiative decay step involved, which would reduce the energy available to partition into internal and kinetic energy. Secondly, there is no mention of the relative importance of each of the pathways; it could be that dissociation is dominated by only a small number of states. Given the lack of change in the kinetic energy distribution from dissociating singly-charged N_2O with increasing electron energy, we believe that at the very least the latter statement is true. Whether this is due to direct formation of the ion in these state(s), or the ion relaxing from some highly-excited state down to these state(s) is not entirely clear, but as we noted previously, dissociation seems to be dominated by a small number of low-lying electronic states of the parent ion; the constancy of the kinetic energy distribution across the energy range 50 eV to 100 eV appears to be true across all

the fragment ions studied in this work.

A number of photoionisation studies have also been carried out concerning the production of NO^+ from N_2O^+. It has been found that the $\tilde{A}$ state can dissociate via transition first to a state of $^4\Pi$ symmetry, which couples to a state of $^4\Sigma^-$ symmetry from which the ion can dissociate, as discussed above.[237–239] Dissociation has also been found to occur via vibronic coupling to the $\tilde{X}$ state, followed by adiabatic dissociation to give electronically excited N and NO^+ in its electronic ground state,[238,239] and can also occur via transition first to a state of $^4\Pi$ symmetry, followed by a second transition to a state of either $^2\Sigma^-$ or $^2\Delta$ symmetry, which can then dissociate to give electronically excited N and NO^+ in its electronic ground state.[239] Lebech *et al.* find that dissociation from the $\tilde{B}$ state predominantly gives NO^+ and N in their electronic ground state, with NO^+ in vibrational state $v = 0 - 6$,[240] and the ions being produced with a mean kinetic energy of approximately 0.15 eV across the photon energy range 18.45 eV to 21.2 eV, in agreement with one of the peaks we observe in our data. It is also clear from their data that the departing electron carries away the excess energy introduced by increasing the photon energy, rather than the NO^+ ion; transition to the $\tilde{B}$ state is still observed after the $\tilde{C}$ state is accessible. Lebech *et al.* also find that, in contrast to the findings of Olivier *et al.* discussed above, NO^+ formed from the $\tilde{C}$ state is predominantly formed in its electronic ground state, but with atomic N in its third-lowest electronic state (a state with ^2P symmetry), and appears with a mean kinetic energy of approximately 0.45 eV.[241] They also find that a small proportion of dissociation is consistent with formation of N in its second-lowest electronic state (^2D), a finding corroborated by Tang *et al.*.[242] Tang *et al.* propose that dissociation occurs via coupling to the $\tilde{B}$ state of N_2O^+, which can adiabatically dissociate to give N in its ^2P electronic state, and NO^+ in its electronic ground state, with the second pathway being accessed following predissociation to a state of either $^2\Sigma^-$ or $^2\Delta$ symmetry.[242]

Figure 5.19 shows the scattering distribution obtained at three electron energies

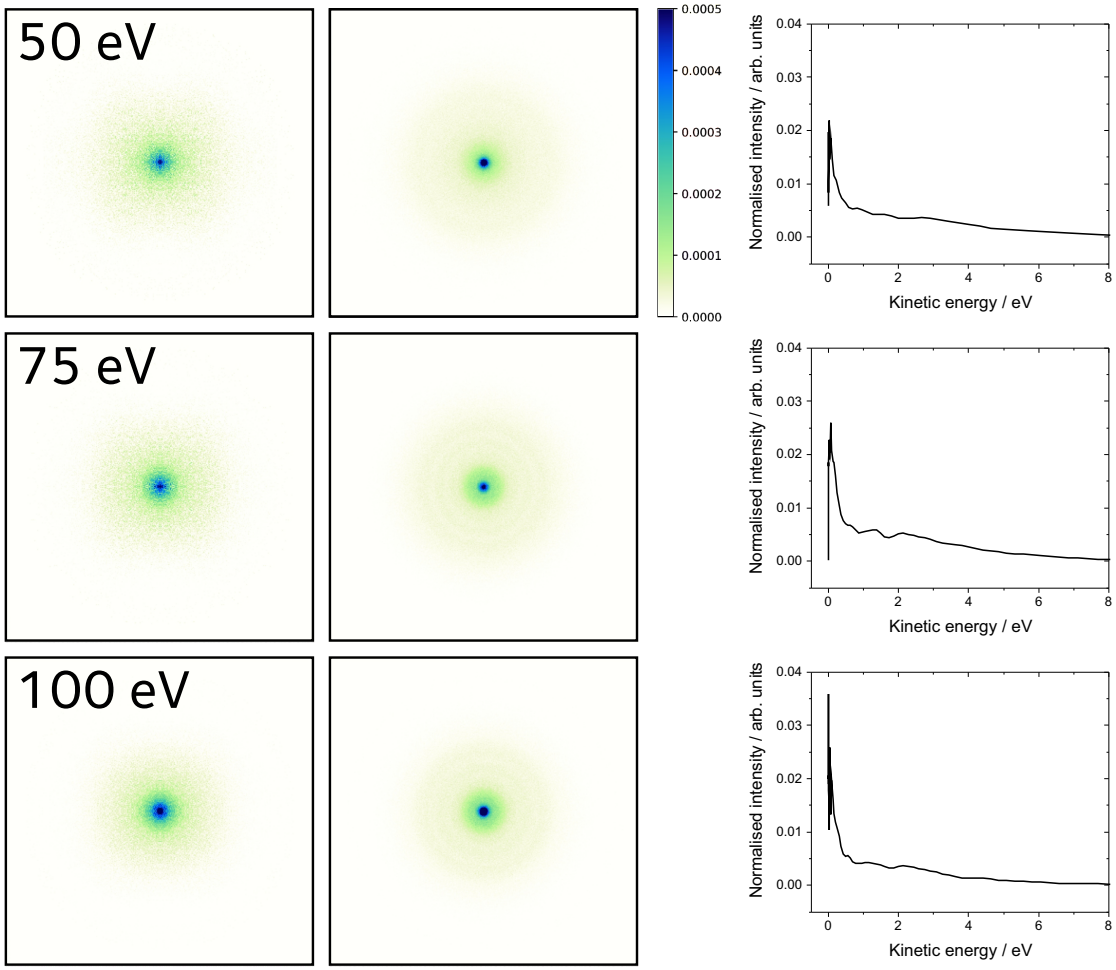


Figure 5.19 The scattering distribution recorded for $N_2{}^+$ produced from N_2O after ionisation by electrons of 50 eV, 75 eV, and 100 eV. The columns show the symmetrised image, the inverted image, and the kinetic energy distribution.

for the $N_2{}^+$ ion. We see that the signal is concentrated at low kinetic energies, with a long tail extending out to around 8 eV. The distribution is most consistent with a statistical dissociation process. Olivier *et al.* also find the same result, reporting a smooth peak in their kinetic energy distribution at thermal energy, broadening towards higher energy with increasing electron energy.[234] A number of states are involved in the dissociation process, including predissociation of the $\tilde{A}$, $\tilde{B}$, and $\tilde{C}$ states of N_2O^+, and autoionisation of states of N_2O^+, followed by dissociation to give $N_2{}^+ + O$, usually (but not always) in their electronic ground state.[234]

In their photodissociation experiment, Lebech *et al.* find that dissociation of the $\tilde{B}$ state results in the production of $N_2{}^+$ with little kinetic energy release. They find

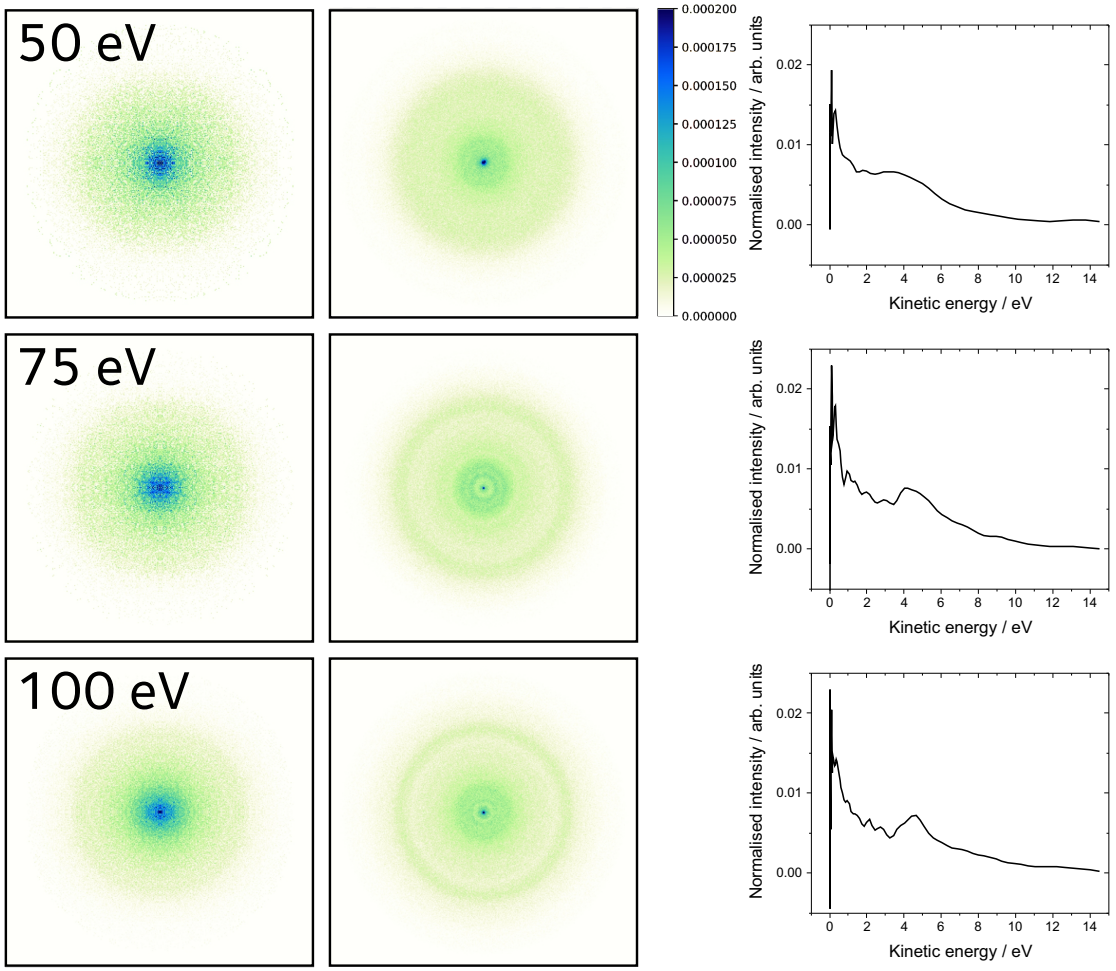


Figure 5.20 The scattering distribution recorded for N^+ produced from N_2O after ionisation by electrons of 50 eV, 75 eV, and 100 eV. The columns show the symmetrised image, the inverted image, and the kinetic energy distribution.

that the $\tilde{B}$ state can dissociate to give ground-state products, with dissociations to produce either product in their first electronic state also potentially contributing.[240] From the $\tilde{C}$ state, they find that dissociation predominantly results in formation of ground-state N_2^+, along with O atoms in their first excited (^{1}D) state.[241]

Figure 5.20 shows the scattering distribution obtained at three electron energies for the N^+ ion. We observe a central feature consisting of a number of closely-spaced but distinct peaks, with a long tail extending out to high kinetic energies. We also see a feature which appears at an energy slightly above 4 eV, which grows stronger with increasing electron energy, and is attributed to the dissociation of doubly-charged N_2O.

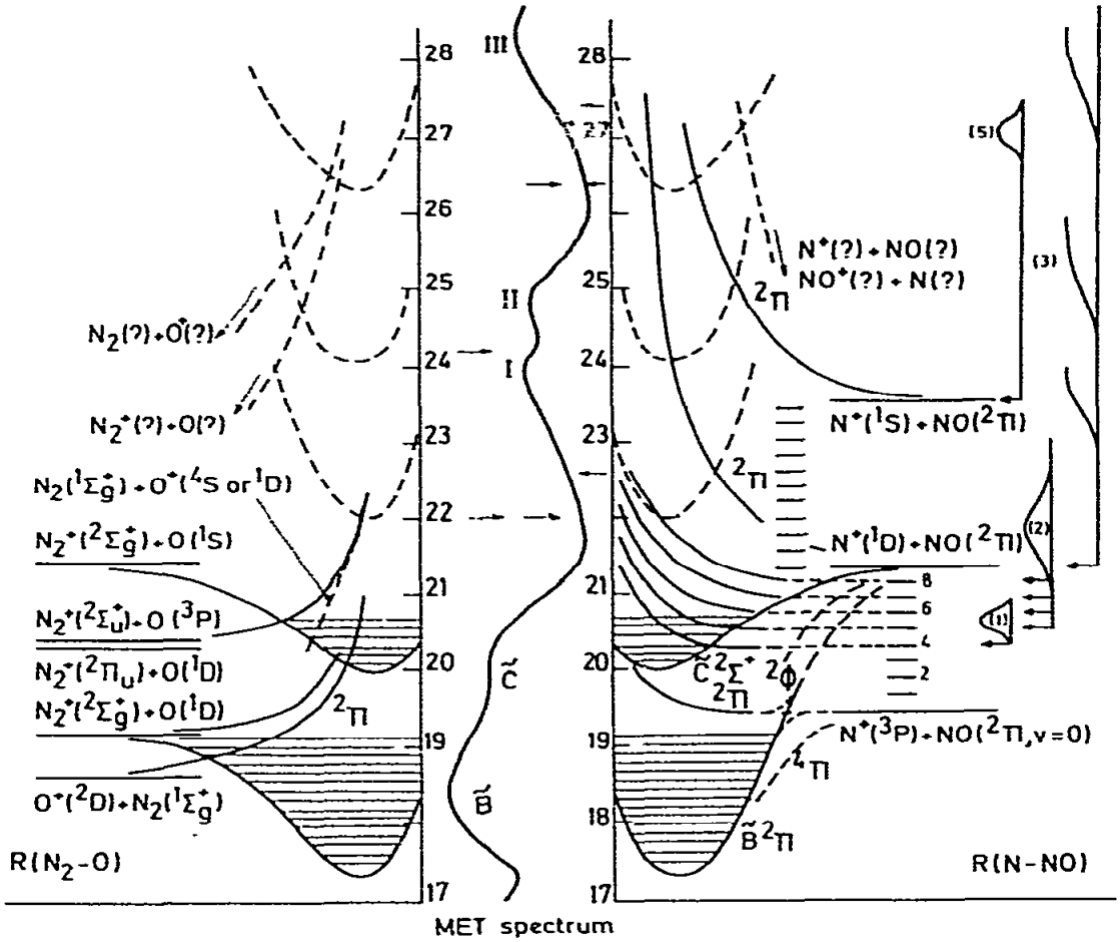


Figure 5.21 Potential energy surfaces for the formation of N^+ and O^+ from N_2O^+. The pathways discussed by Olivier *et al.* are also indicated. Reproduced from [235], with the permission of Elsevier under license 4930370443204.

Olivier *et al.* have previously reported a kinetic energy release distribution for N^+ following electron ionisation at 100 eV, allowing for a direct comparison to be made.[235] Qualitatively at least, there is little difference in the distribution they obtain. They observe a large thermal peak, broadened towards high ion kinetic energies, and observe a weak feature at around 4.1 eV. However, their results give a much higher relative intensity for ions with low kinetic energy than at higher energies than observed in the current work. This could be caused either by their experiment discriminating against the detection of ions with higher kinetic energy, or our experiment underestimating the number of ions formed with low kinetic energy. However, given that the count rate in our experiment is relatively low, we think

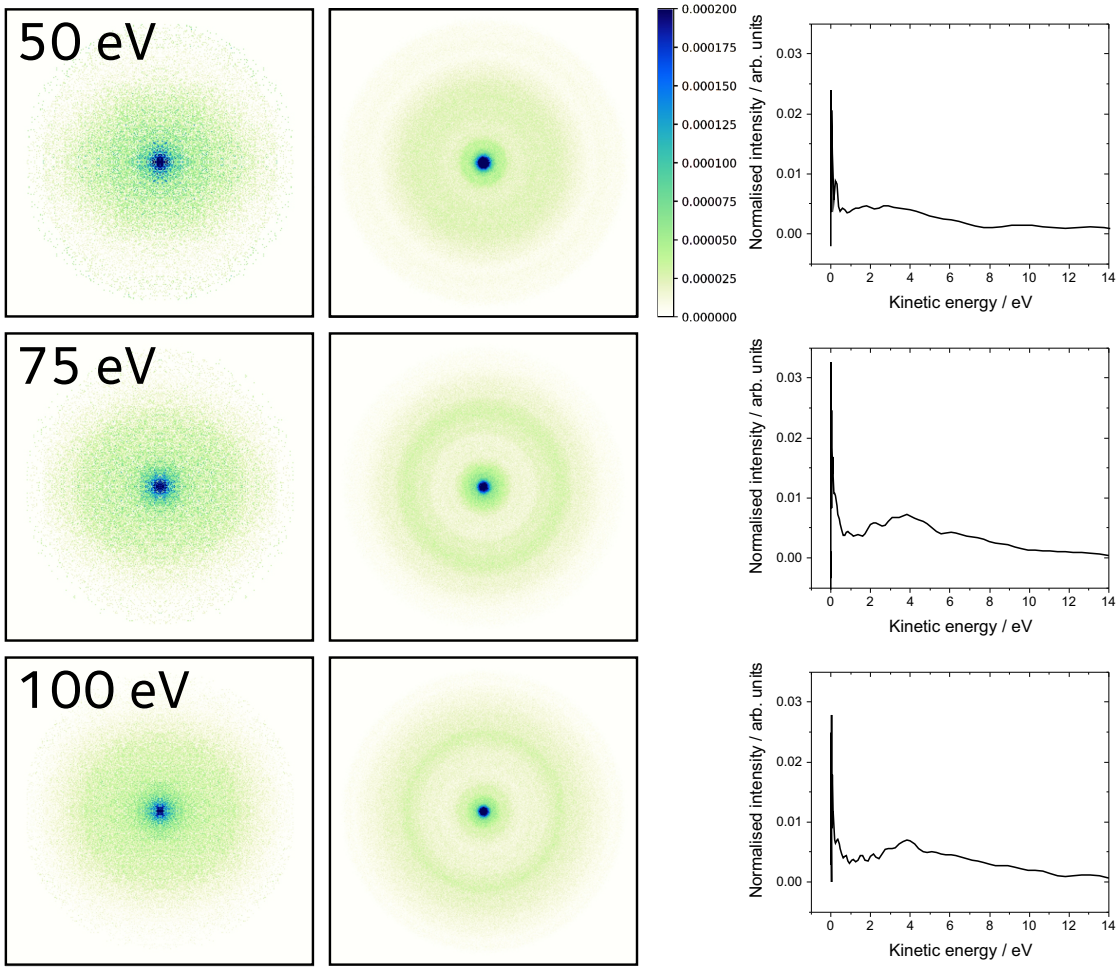


Figure 5.22 The scattering distribution recorded for O^+ produced from N_2O after ionisation by electrons of 50 eV, 75 eV, and 100 eV. The columns show the symmetrised image, the inverted image, and the kinetic energy distribution.

it is unlikely that our results show significant discrimination against ions with low kinetic energy.

Olivier *et al.* find that the onset for the formation of N^+ occurs at an electron energy of 20.26 eV. This corresponds to ionisation to the $\tilde{C}$ state of N_2O^+.[235] They proposed a pathway in which predissociation to a $^2\Pi$ state occurs, followed by dissociation to products in their electronic ground states, but with the NO fragment vibrationally excited. The same final states are found by Lebech *et al.* in their photoionisation study.[241] Other pathways discussed include excitation directly to the dissociative $^2\Pi$ state, and also one or more states occupied by multiple-electron transitions.

Figure 5.22 shows the scattering distribution obtained at three electron energies for the O^+ ion. We see a strong central feature, with a broad feature extending out to high kinetic energies. With increasing electron energy, a feature grows in at 4 eV and the tail extends to higher kinetic energies, both attributed to dissociation of doubly-charged N_2O.

Olivier *et al.* also provide kinetic energy distributions at 50 eV, 75 eV and 100 eV for the O^+ ion.[235] They find that the ion is predominantly formed with thermal energy, with shoulders at 0.6 eV, 1.6 eV and 3.2 eV at 75 eV and 100 eV, and a shoulder at 2.2 eV at 50 eV. They do not observe a peak at 4 eV, contrary to the findings of this work. In terms of dissociation pathways, they suggest that O^+ can be formed via dissociation of any of the $\tilde{A}$, $\tilde{B}$, and $\tilde{C}$ states (and the associated Rydberg series for each state), and also the states reached by multiple-electron transitions. They find that dissociation is predominantly from a $^4\Sigma^-$ state prepared by predissociation of the initial state, and also implicate a state of $^2\Pi$ symmetry for the more highly-excited states.

For photoionisation, Lebech *et al.* found that dissociation from the $\tilde{B}$ state resulted in the formation of products in their ground electronic states (energy $\sim$ 15.2 eV on the energy scale of figure 5.21),[240] whilst dissociation from the $\tilde{C}$ state primarily results in the formation of vibrationally-excited N_2 in its ground electronic state, and O^+ in its first excited electronic state. The intensity for dissociation from the $\tilde{B}$ state peaks at zero kinetic energy, whilst from the $\tilde{C}$ state, the intensity peaks at around 0.1 eV.

The parent ion, not shown here, appears as a well-defined point in our experiment, confirming that the experiment was operating under velocity-mapping conditions.

We will now discuss the dissociation of N_2O^{2+} using covariance analysis techniques.

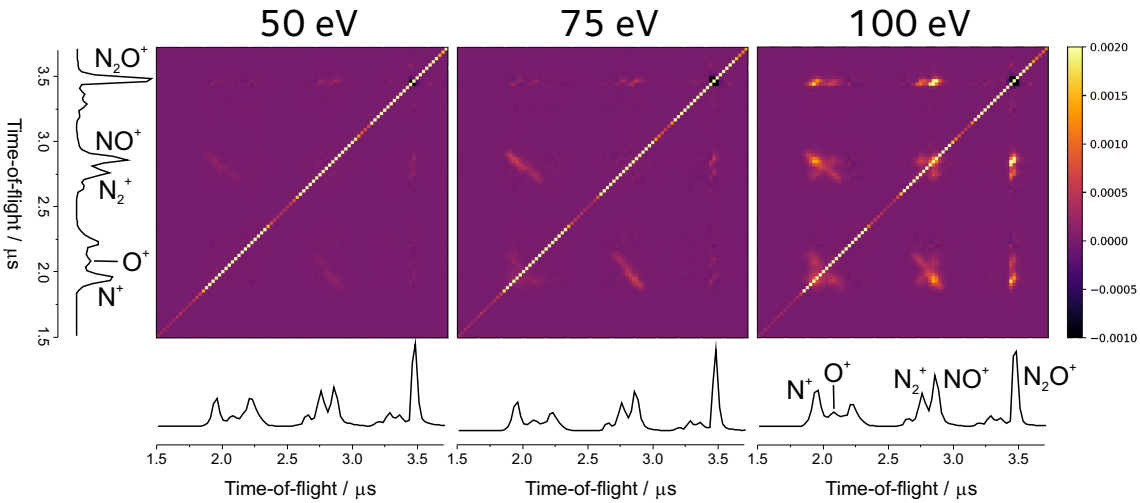


Figure 5.23 TOF-TOF covariance maps of N_2O recorded at electron energies of 50 eV, 75 eV, and 100 eV. The time-of-flight spectra used for the analysis is shown below the map, with the ions of interest indicated on the 100 eV TOF spectrum. Note that the TOF spectra are not background subtracted, so signal from background ions are also observed in the TOF spectra.

5.2.3 Covariance analysis of N_2O^{2+}

Figure 5.23 shows the TOF-TOF covariance map acquired from analysis of the PImMS data recorded following electron ionisation of N_2O at three electron energies. We see that, at 50 eV, the main features in the covariance map come from the two possible two-body dissociation pathways, with the signal corresponding to formation of NO^+ and N^+ being stronger than that for formation of $N_2{}^+$ and O^+. Upon moving to higher electron energies, we see the three-body dissociation pathways, i.e. the formation of N^+ and N^+, and the formation of N^+ and O^+ growing in. In the 100 eV covariance map, we see a significant amount of false covariance. Once we have implemented partial covariance mapping the 100 eV covariance map will need to be regenerated, but the current form is sufficient for the purposes of this discussion.

Now that we have established the four pathways for which we observe covariance, we will study each in turn using the recoil-frame covariance technique.

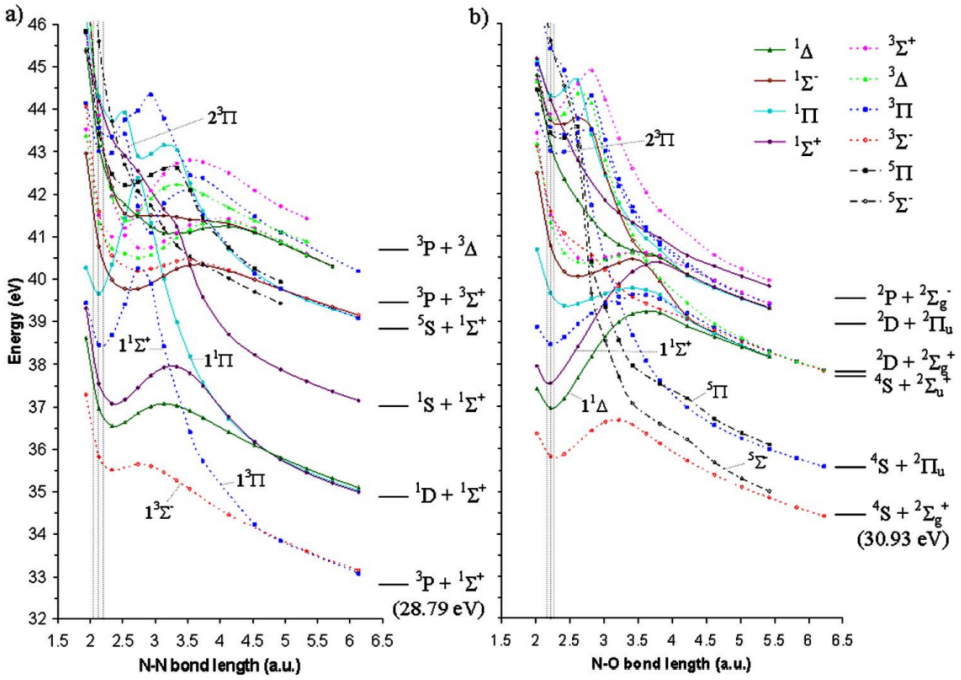


Figure 5.24 Potential energy surface of N_2O^{2+} in a collinear orientation, with the (a) N-N bond length, and (b) N-O bond length fixed. Note that the dissociation limits are displaced vertically, with the energy of the lowest final state indicated in brackets. Reproduced from [243] with the permission of AIP Publishing under license 4917840911689.

Two-body dissociation

There are two potential pathways by which N_2O^{2+} can dissociate via a two-body dissociation, namely

$$N_2O^{2+} \rightarrow NO^+ + N^+ \tag{5.8}$$

$$N_2O^{2+} \rightarrow N_2^+ + O^+ \tag{5.9}$$

Taylor *et al.* have determined potential energy surfaces for elongation of either the N-N bond and N-O bond in a collinear geometry, with the second bond length fixed.[243] These are reproduced in figure 5.24. It is immediately clear that the energy required to break the N-O bond is significantly higher than that required to break the N-N bond, i.e. the dominant dissociation pathway is pathway 5.8. This is entirely consistent with the relative signal intensities for these pathways observed in the

TOF-TOF covariance maps.

Figure 5.25 shows the covariance images and associated kinetic energy distributions obtained for pathway 5.8 (producing NO^+ and N^+) at incident electron energies of 50 eV, 75 eV, and 100 eV. We see that the two ions travel in opposite directions from each other, as is expected for a two-body dissociation. We also observe an unexpected isotropic feature with low kinetic energy release in the NO^+ covariance image at 100 eV. This is possibly due to the presence of a fluctuating parameter; we have already established that partial covariance analysis is required to obtain an accurate TOF-TOF covariance map here, and it follows that we should see a similar effect in the covariance images. The feature does match the scattering distribution of NO^+, which would be consistent with this conclusion. As N^+ has a more diffuse scattering distribution, this effect is less clear in the N^+ covariance image than in the NO^+ image, but we can still see this effect. We could also consider the possibility of dimer formation playing a role here, but are reserving further comment on this possibility until we have applied partial covariance analysis.

Other than the lower intensity for the NO^+ kinetic energy distribution at 100 eV due to the presence of the central feature, there is very little change in the kinetic energy distribution over the electron energy range. The peak of the kinetic energy release distribution is found to be around 6.5 eV, in excellent agreement with those reported in the literature, which range from 6.3 eV to 6.8 eV.[209,244–248] This dissociation is thought to occur predominantly via the $\tilde{X}^3\Sigma^-$ state of the dication.[243,244] We also see evidence for a second, significantly weaker feature, with a kinetic energy release of approximately 10 eV.

Figure 5.26 shows the covariance images and associated kinetic energy distributions obtained for pathway 5.9 (producing $N_2{}^+$ and O^+) at three electron energies. The signal level at 50 eV is relatively low, which means the kinetic energy distribution is relatively noisy, and we also see a low-energy isotropic feature in the 100 eV covariance image for N_2^+, presumably for the same reason as postulated for the NO^+

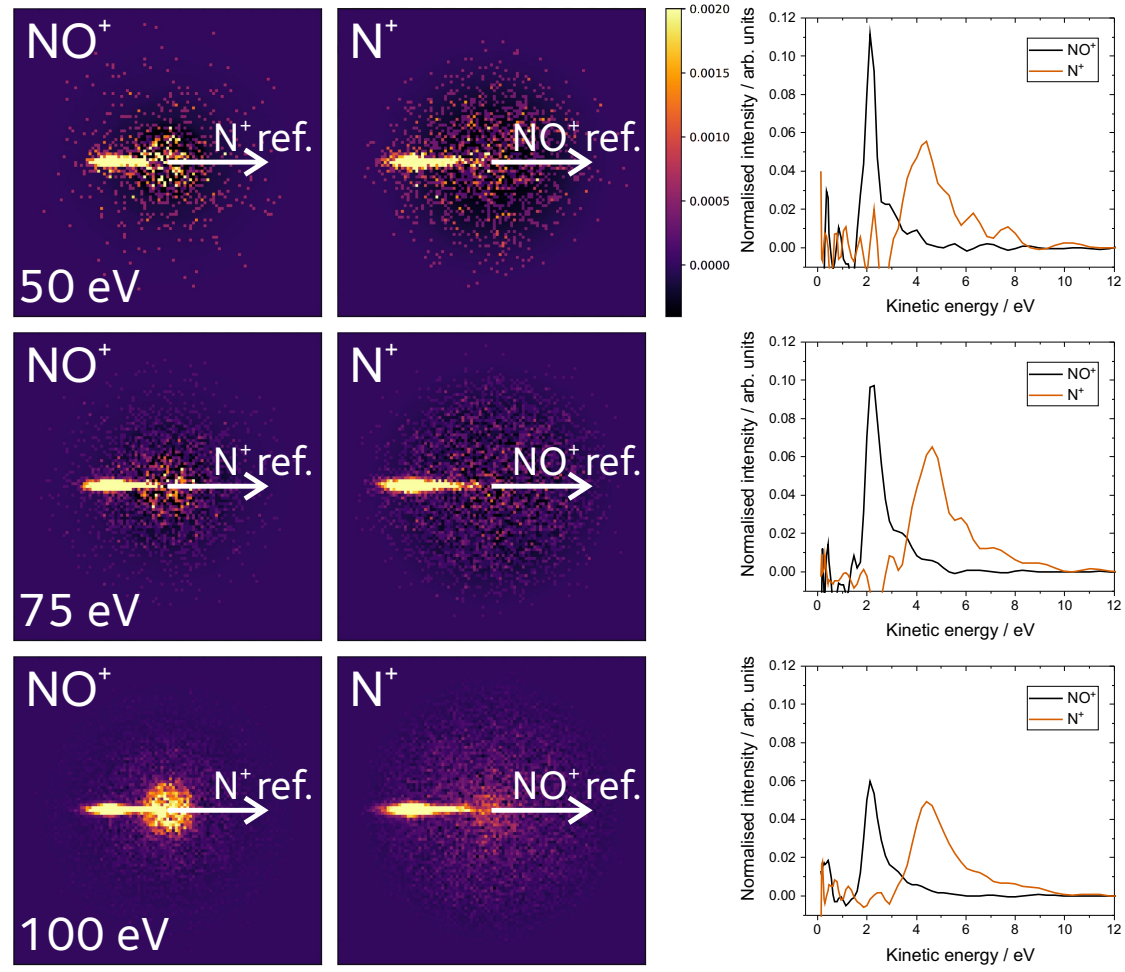


Figure 5.25 Recoil-frame covariance images for the formation of NO^+ and N^+ from N_2O^{2+} at three electron energies, along with the associated kinetic energy distributions (a). The label in the kinetic energy distribution corresponds to the signal ion, obtained using the inversion method discussed in section 3.5.1. (b) shows the kinetic energy release, which has been determined from the kinetic energy distribution of each signal ion independently, based on conservation of momentum.

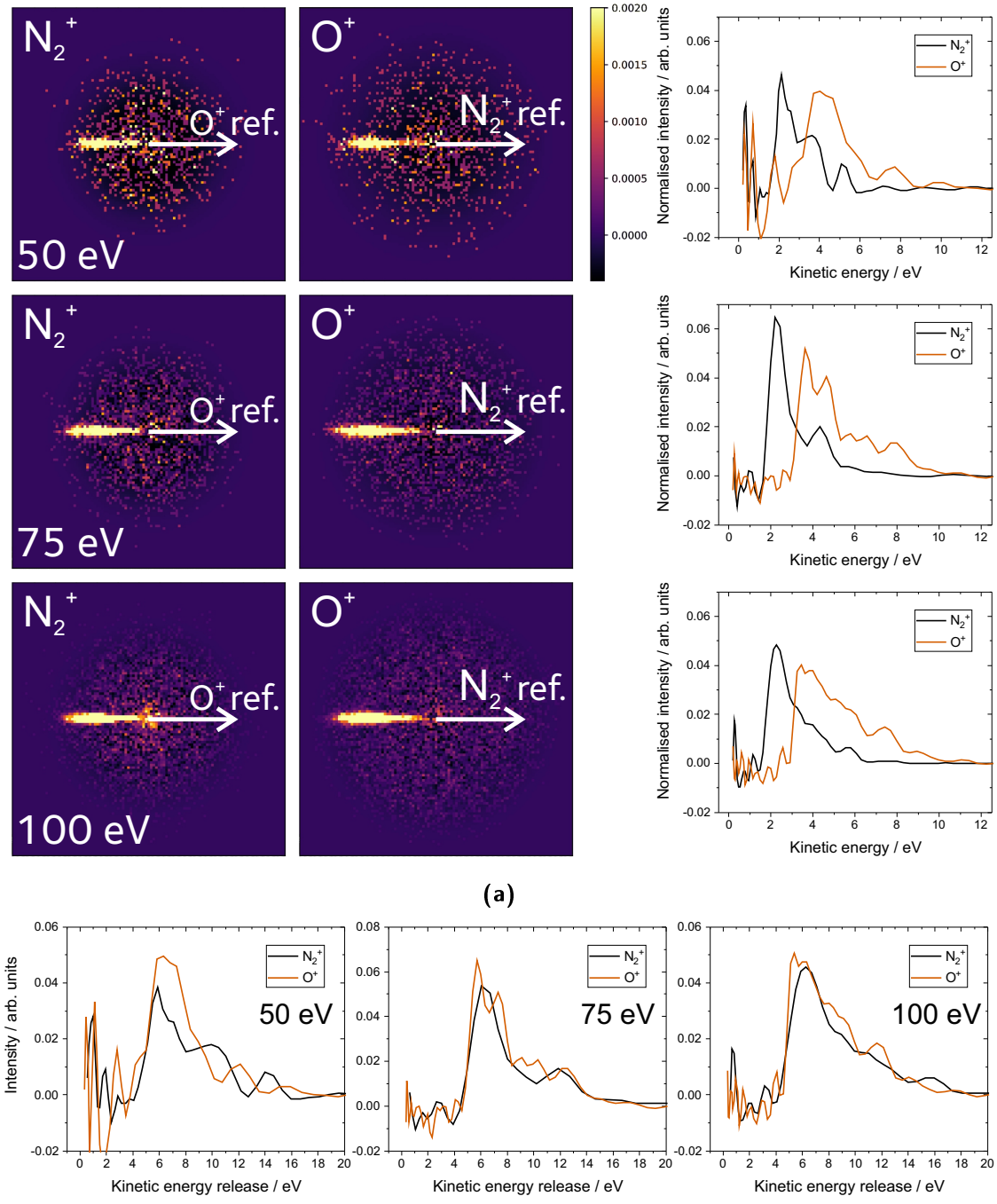


Figure 5.26 Recoil-frame covariance images for the formation of N_2^+ and O^+ from N_2O^{2+} at three electron energies, along with the associated kinetic energy distributions (a). The label in the kinetic energy distribution corresponds to the signal ion. (b) shows the kinetic energy release, which has been determined from the kinetic energy distribution of each signal ion independently, based on conservation of momentum.

covariance image, discussed above.

The kinetic energy distributions remain similar across the energy range considered. The modal kinetic energy release is found to be approximately 5.8 eV, with further channels occurring with higher kinetic energy release. Others have reported modal kinetic energy releases in the region of 5.6 eV to 6.2 eV,[209,244–248] in excellent agreement with our modal kinetic energy release.

Price *et al.* report a trimodal kinetic energy release distribution, consisting of Gaussians centred at 3.2 eV, 5.8 eV, and 8.5 eV, weighted in a 2:9:2 ratio, following photoionisation using 40.8 nm photons.[244] Our data is fairly noisy, making it difficult to identify channels with low-intensity signals with any confidence, but we do appear to observe signal at around 1 eV in the N_2^+ kinetic energy distribution, and at around 2 eV in the O^+ kinetic energy distribution at all electron energies, which would be consistent with the peak they observed at 3.2 eV in the kinetic energy release distribution. A kinetic energy release of 8.5 eV corresponds to a kinetic energy of 3.1 eV in the N_2^+ kinetic energy distribution and 5.4 eV in the O^+ kinetic energy distribution. There appear to be shoulders at approximately these energies, which would be consistent with their findings.

Kubel *et al.* report a main peak at 5.8 eV, with a shoulder observed at 7.2 eV, following strong-field ionisation at a wavelength of 750 nm.[248] The latter peak would correspond to signal appearing at 2.6 eV in the N_2^+ kinetic energy distribution and 4.6 eV in the O^+ kinetic energy distribution. We do potentially see a shoulder at these energies, most noticeably at lower electron energies, which would be consistent with their results. Kubel *et al.* attribute the two channels to dissociation from the lowest-lying $^3\Sigma^-$ state and the $^3\Pi$ state, respectively.[248]

Three-body dissociation

Very little was found on the dissociation of the dication N_2O^{2+} via three-body decay in the literature. Based on the other molecules we have studied, it seems likely that

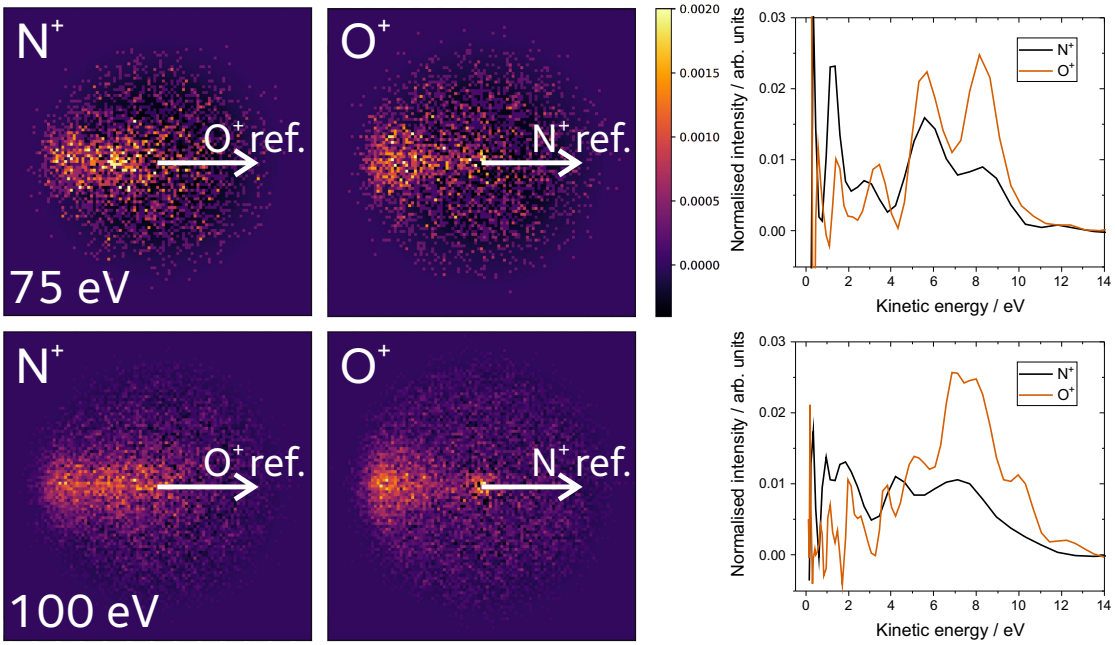


Figure 5.27 Recoil-frame covariance images for the formation of N^+ and O^+ from N_2O^{2+} at two electron energies, along with the associated kinetic energy distributions. The label in the kinetic energy distribution corresponds to the signal ion.

the major three-body dissociation pathway will be via dissociation of the dication following electron ionisation. However, other studies (albeit photoionisation studies) have primarily focussed on dissociation of the trication (for example [164, 172, 245, 246]). We will nonetheless focus on the dissociation of the dication, as we believe this to be the most probable source of our covariance signal.

Figure 5.27 shows the covariance images and associated kinetic energy distributions obtained for the dissociation of N_2O^{2+} into N^+, O^+ and N. There are a number of possible mechanisms by which this process could occur

$$N_2O^{2+} \rightarrow N^+ + O^+ + N \tag{5.10}$$

$$N_2O^{2+} \rightarrow NO^+ + N^+ \rightarrow N^+ + O^+ + N \tag{5.11}$$

$$N_2O^{2+} \rightarrow N_2^+ + O^+ \rightarrow N^+ + O^+ + N \tag{5.12}$$

$$N_2O^{2+} \rightarrow NO^{2+} + N \rightarrow N^+ + O^+ + N \tag{5.13}$$

From our TOF-TOF covariance map, we determine a gradient of approximately -1

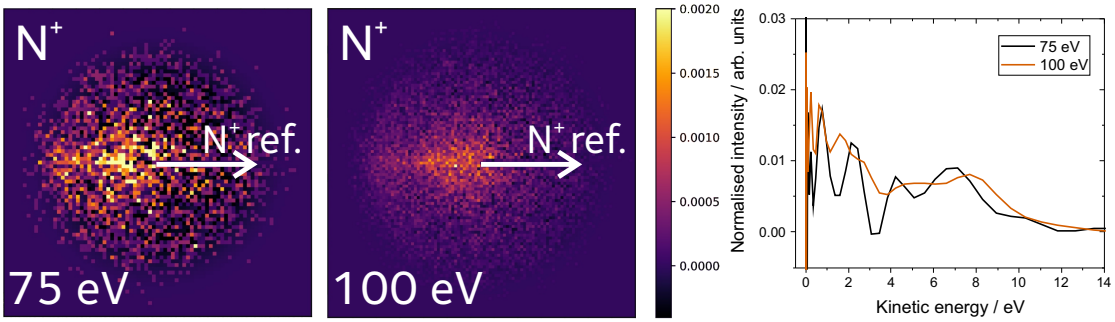


Figure 5.28 Recoil-frame covariance images for the formation of N^+ and N^+ from N_2O^{2+} at two electron energies, along with the associated kinetic energy distributions. The label in the kinetic energy distribution corresponds to the signal ion.

for N^+ and O^+ in agreement with Hsieh and Eland,[221] eliminating the two initial charge separation pathways (5.11 and 5.12), which would have gradients of -0.53 and -0.5 respectively, as dominant dissociation processes, and also the concerted mechanism (5.10) where the charge ends on the central nitrogen atom, for which we would expect a gradient of less than one, with the gradient dependent on the momentum gained by the terminal neutral N atom produced. This leaves us with either a concerted dissociation where the charges end on the two terminal atoms, with the central neutral N gaining almost no kinetic energy in the process, or a deferred charge separation (mechanism 5.13). The covariance images we obtain would be consistent with either mechanism, so we are unable to conclude which mechanism is dominant, although the relatively low angular spread of the features implies a low kinetic energy release in the first step of the deferred charge separation process to obtain.

We also observe signal at lower kinetic energy, particularly for N^+ at 100 eV. Some of the signal can be attributed to the false covariance previously noted, but this may not fully account for the observed signal. Without an implementation of partial covariance analysis it is difficult to draw any concrete conclusions on the source of this signal, but it is certainly possible that one or more of the discounted mechanisms discussed above makes a minor contribution to this covariance channel.

Figure 5.28 shows the covariance images and associated kinetic energy distribu-

tions obtained for the dissociation of N_2O^{2+} into N^+, N^+ and O. The signal level is relatively low for this channel, and this increases the effect of the false covariance on the data, making the interpretation challenging. As we cannot discuss potential mechanisms with any confidence using this data, we have decided to wait until we have implemented partial covariance analysis before we interpret the covariance images for this channel.

Comparison to CO_2

At this point, it is worth comparing and contrasting the dynamics observed following electron ionisation of N_2O and CO_2. The two molecules are isoelectronic, so differences in dynamics will only be caused by the differing atomic nuclei present.

It is clear that N_2O dissociation preferentially proceeds via the breaking of the N-N bond, whereas there is no distinction between the two C-O bonds in CO_2. If we take a look at the scattering distributions themselves however, there are certainly similarities between the two. Starting with the diatomic ionic fragments, the scattering distributions of NO^+, $N_2{}^+$, and CO^+ all show a strong central feature, decaying away at higher energies, with a feature from the doubly-charged molecule appearing at an energy of approximately 2 eV. However, the CO^+ scattering distribution falls off more quickly than those of the diatomic ions obtained from N_2O, and NO^+ shows multiple peaks at low kinetic energy not observed in the CO^+ scattering distribution.

Moving on to the atomic ion fragments, the scattering distributions of O^+ from the two molecules show striking similarities, with the only real difference being that the central feature following dissociation of CO_2 is significantly more pronounced. There are two different environments of N in N_2O, so we do not expect the distribution to match either the C^+ or O^+ scattering distributions from CO_2, but we might expect to observe aspects of these scattering distributions in the N^+ scattering distribution. To some extent at least, this seems to be the case, as in the N^+ scattering

distribution we see a strong central feature, as observed in the C^+ and O^+ scattering distributions, with the decay from this feature being similar to that observed in the C^+ scattering distribution. However, there is an extra 'bump' on the decay in the N^+ scattering distribution, as is seen in the O^+ scattering distribution from CO_2. All in all, we find that the dissociation dynamics of the singly-charged parent ions are similar for the two molecules, although evidently not identical.

We do see some differences in the three-body dissociation processes of the dication. The formation of C^+ and O^+ in covariance with one another clearly showed evidence of occurring via an initial charge separation process, whilst for the equivalent with N_2O, N^+ and O^+, we see no evidence for this mechanism. There are also some similarities however; we observe a concerted dissociation in which the two terminal atoms are ionised in both cases.

5.2.4 Summary

We have reported partial ionisation cross-sections, scattering distributions, and recoil-frame covariance images for nitrous oxide. We have discussed the scattering distributions in the context of the literature, and have used covariance analysis techniques to obtain new insight into the dissociation of multiply-charged parent ions. We have also compared and contrasted these results with those obtained for the isoelectronic CO_2.

5.3 Carbonyl sulphide (OCS)

Carbonyl sulphide (OCS) was first detected in the interstellar medium in 1971 by Jefferts *et al.*.[249] Since then, it has been detected in a wide variety of environments, including cold molecular clouds, protostellar ices, protostellar hot core gas, and cometary comas.[250] It is known that OCS is readily produced (and destroyed) by irradiation of interstellar ices containing CO and CO_2 as carbon sources and H_2S

or SO_2 as sulphur sources.[251] OCS has also been detected in extraterrestrial atmospheres, for example that of Jupiter (following impact of a comet),[252] and Venus.[253]

In Earth's atmosphere, OCS has been found to be the most abundant sulphur-containing gas.[254–256] It is relatively stable in the atmosphere, having a lifetime of approximately two years,[257] and is known to be transported to the stratosphere, where it can dissociate and form aerosol particles of H_2SO_4.[257] It is evident that OCS plays a role in a number of environments, thus it is important we understand the dynamics induced by the interaction of OCS with electrons.

Scattering distributions were recorded for electron ionisation products at electron energies of 50 eV, 75 eV and 100 eV using an extractor potential of 2 kV and a repeller potential of 1.612 kV. The electron beam pulse lengths were set to 550 ns, 450 ns and 350 ns at electron energies of 50 eV, 75 eV and 100 eV, respectively, and the timing of the ion optics pulse adjusted accordingly. A total of 800,000, 2,600,000, and 4,000,000 acquisition cycles were recorded at electron energies of 100 eV, 75 eV, and 50 eV, respectively, and an equal number of acquisition cycles of background data were recorded. Signal and background acquisitions were alternated every 50,000 acquisition cycles to reduce the effect of any experimental drift on the background subtraction. Neat OCS was used to form the molecular beam when recording 75 eV and 100 eV data, and a 50 % mixture with helium was used when recording the 50 eV data, due to the gas cylinder pressure falling below the typical operation pressure of the experiment.

Mass spectra were also recorded by using a photomultiplier tube (PMT) to detect the optical signal from the scintillator at electron energies ranging from 40 eV to 100 eV in 5 eV steps, using an extractor potential of 1.652 kV and a repeller potential of 2 kV. We have sufficient signal to present data above an electron energy of 50 eV. Data acquisition was carried out by alternating between recording 500 acquisition cycles of signal and background, for a total of 5,000 acquisition cycles of signal, and the background signal was subtracted from the signal to give the final mass

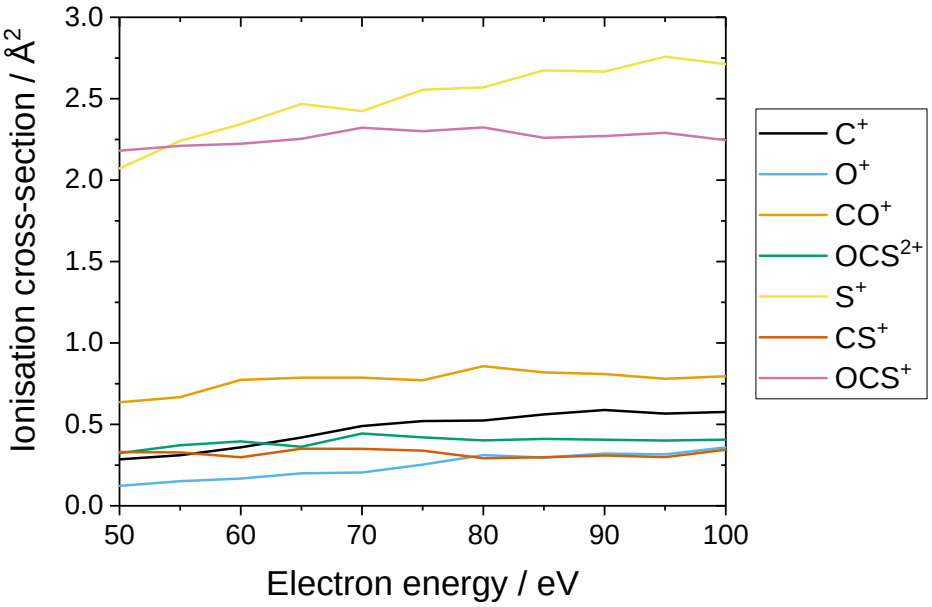


Figure 5.29 Partial ionisation cross-sections obtained for OCS following electron ionisation by electrons at energies ranging from 50 eV to 100 eV.

spectrum.

We will first present the partial ionisation cross-sections of OCS and compare our results to those found in the literature. Next, we will discuss the scattering distributions we obtain, and finally the results of the covariance analysis between the detected fragment ions.

5.3.1 Partial ionisation cross-sections

Figure 5.29 shows the partial ionisation cross-sections we obtain from fitting the mass spectra, as described previously. The sum of the partial cross-sections has been normalised to the total ionisation cross-sections recorded by Hudson *et al.*.[192] We see that as the electron energy increases, there is an increased probability that atomic ions are formed, which seems logical given that there is more energy available. The cross-sections of OCS^{2+} and CO^+ increase slightly across the energy range, whilst those of OCS^+ and CS^+ remain largely flat. It is immediately clear that the CS bond breaks preferentially to the CO bond, given that the cross-sections for formation of both S^+ and CO^+ are significantly higher than those for formation of

O^+ and CS^+. To our knowledge, no previous partial ionisation cross-sections have been reported for electron ionisation. However, we can compare our results to mass spectra obtained by electron ionisation.

The NIST Mass Spectrometry Data Centre provides a mass spectrum for OCS with the following ion abundances: OCS^+ (100.0), S^+ (57.7), CO^+ (13.7), CS^+ (7.5), and O^+ (1.2), and do not observe the presence of C^+ or OCS^{2+}.[258] It is not entirely clear which electron energy was used to obtain their mass spectrum, but given that the standard electron energy used in electron ionisation mass spectrometry is 70 eV,[259] we have assumed that this was the electron energy used to obtain the NIST spectrum. We have therefore normalised their data to the total ionisation cross-section of OCS at 70 eV reported by Hudson *et al.*,[192] and obtain partial ionisation cross-sections of 3.89 Å(OCS^+), 2.25 Å(S^+), 0.53 Å(CO^+), 0.29 Å(CS^+), and 0.05 Å(O^+). Unfortunately, there isn't very good agreement with our data. We see that formation of both C^+ and OCS^{2+} occur at with a cross-section similar to that of CS^+, so it is surprising that these are not observed in their data.

Wang and Vidal provide cross-sections for electron ionisation at 200 eV; they obtain partial ionisation cross-sections of 2.09 Å(S^+), 1.52 Å(OCS^+), 0.64 Å(CO^+), 0.47 Å(C^+), 0.40 Å(O^+ / S^{2+}), 0.12 Å(CS^+), and 0.10 (OCS^{2+}).[260] They also observe other ions, but with cross-sections around two orders of magnitude smaller than that of OCS^{2+}. Significant extrapolation is required to compare these values with our data, so only qualitative comparisons can be made. Note that the total ionisation cross-section at an electron energy of 200 eV is lower than that at 100 eV, and this is reflected in the partial ionisation cross-sections. The ordering of the cross-sections is in good agreement with the current work, and all the ions observed in the current work have been reported.

Figure 5.30 shows the fitted mass spectrum we obtain for an electron energy of 100 eV. We see peaks for all possible singly-charged fragmentations products of OCS, along with a peak at an m/z of 34. Part of the peak can be attributed to

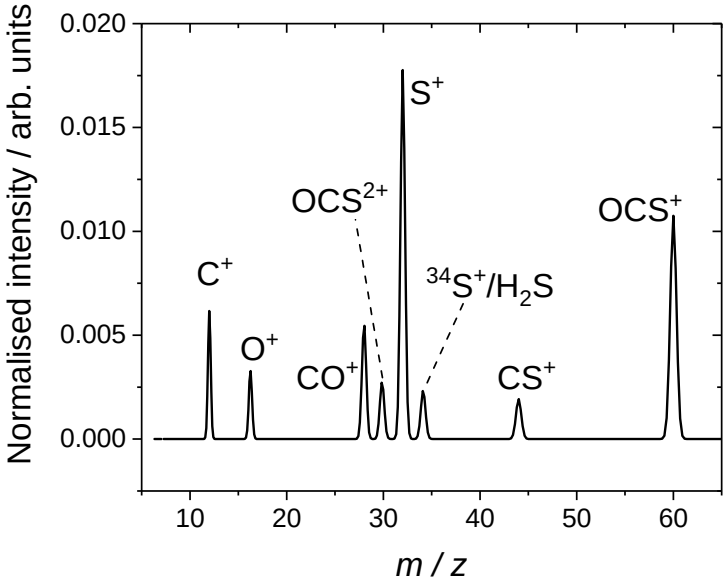


Figure 5.30 Mass spectrum obtained by fitting the PMT spectrum recorded following electron ionisation of OCS at an energy of 100 eV.

the presence of ^{34}S, which has an abundance of 4.2 %.[261] However when we study the scattering distribution, the signal appears to show similar features to that of a parent ion. We attribute this to the presence of an H_2S impurity, possibly due to interaction of OCS with water, which is known to produce H_2S and CO_2.[262]

Having determined the partial ionisation cross-sections, we will now study each of the scattering distributions in turn.

5.3.2 Scattering distributions resulting from electron ionisation of OCS

Figure 5.31 shows the scattering distributions obtained at three electron energies for the S^+ ion. The scattering distribution is dominated by dissociation channels imparting low kinetic energy to the S^+ ion, with the distribution consisting of a sharp central feature with a shoulder at all electron energies, consistent with at least one dissociation channel which proceeds via a statistical process, and one dissociation channel that proceeds via an impulsive dissociation. There is also a weaker feature at

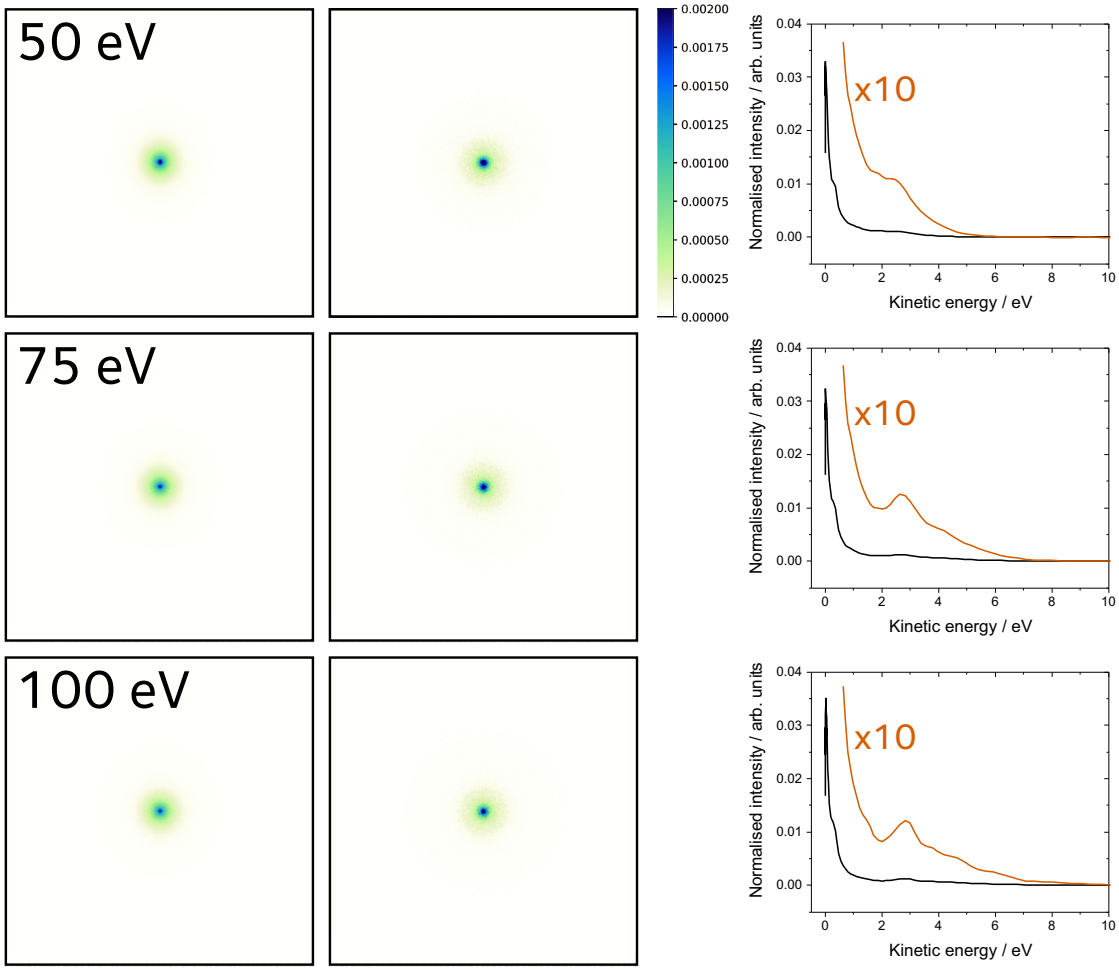


Figure 5.31 The scattering distribution recorded for S^+ produced from OCS after ionisation by electrons of 50 eV, 75 eV, and 100 eV. The columns show the symmetrised image, the inverted image, and the kinetic energy distribution.

a kinetic energy of approximately 3 eV which becomes more intense with increasing electron energy, which is attributed to dissociation of OCS^{2+}. The length of the tail in the kinetic energy distribution again increases with increasing electron energy, consistent with being able to access more highly excited states of OCS^{2+}, and states of OCS^{3+}.

S^+ is by far the most abundant fragment ion produced following electron ionisation of OCS. Energetically, it can be produced from almost all electronic states, as can be seen from the potential energy surface shown in figure 5.32. Eland found that the vast majority of molecules formed in the $\tilde{A}$, $\tilde{B}$, and $\tilde{C}$ states of OCS^+ do not remain as parent ions, but instead dissociate. Given that the $\tilde{A}$ and $\tilde{B}$ states lie

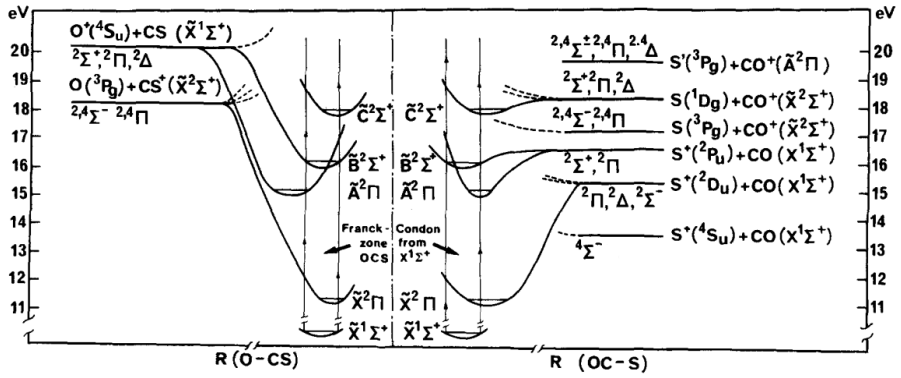


Figure 5.32 Potential energy surface including the first four electronic states of OCS^+. Reproduced from [263], with the permission of Elsevier under license 4917570601547. Figure also present in [264].

below the appearance potential of any other fragment ions, ions prepared in these states must fragment to produce S^+.[265] Below the energy of the S^+ (^2D_u) + CO (X $^1\Sigma^+$) state, it is evident that the dissociation must occur on the $^4\Sigma^-$ potential energy surface. It has been found that the $\tilde{A}$ state does not couple well to the $^4\Sigma^-$ state, so instead undergoes internal conversion to the $\tilde{X}$ state, followed by predissociation to the $^4\Sigma^-$ state. Above the limit for the formation of S^+ (^2D) + CO (X $^1\Sigma^+$), the $\tilde{X}$ state can also undergo direct dissociation after the internal conversion step.[263,266] From the $\tilde{B}$ state, it is thought dissociation occurs either via direct dissociation after internal conversion to the $\tilde{X}$ state, or via transfer to the $\tilde{A}$ state via a conical intersection, followed by crossing to a repulsive $^2\Delta$ state.[266,267] S^+ is also known to be formed from the $\tilde{C}$ state,[268,269] and can also be produced, along with the other possible fragment ions, from a series of electronic states resulting from multiple-electron transitions (MET), i.e. where one valence electron is removed from the molecule, and one or more valence electrons are promoted to antibonding orbitals.[268,270,271] The mechanism most consistent with the observed scattering distributions would be the population of either the $\tilde{A}$ or $\tilde{B}$ state, followed by internal conversion to the $\tilde{X}$ state and subsequent direct dissociation, as the kinetic energy gained by the S^+ ion in each of these cases would be low, and the Franck-Condon overlap in this region is good.

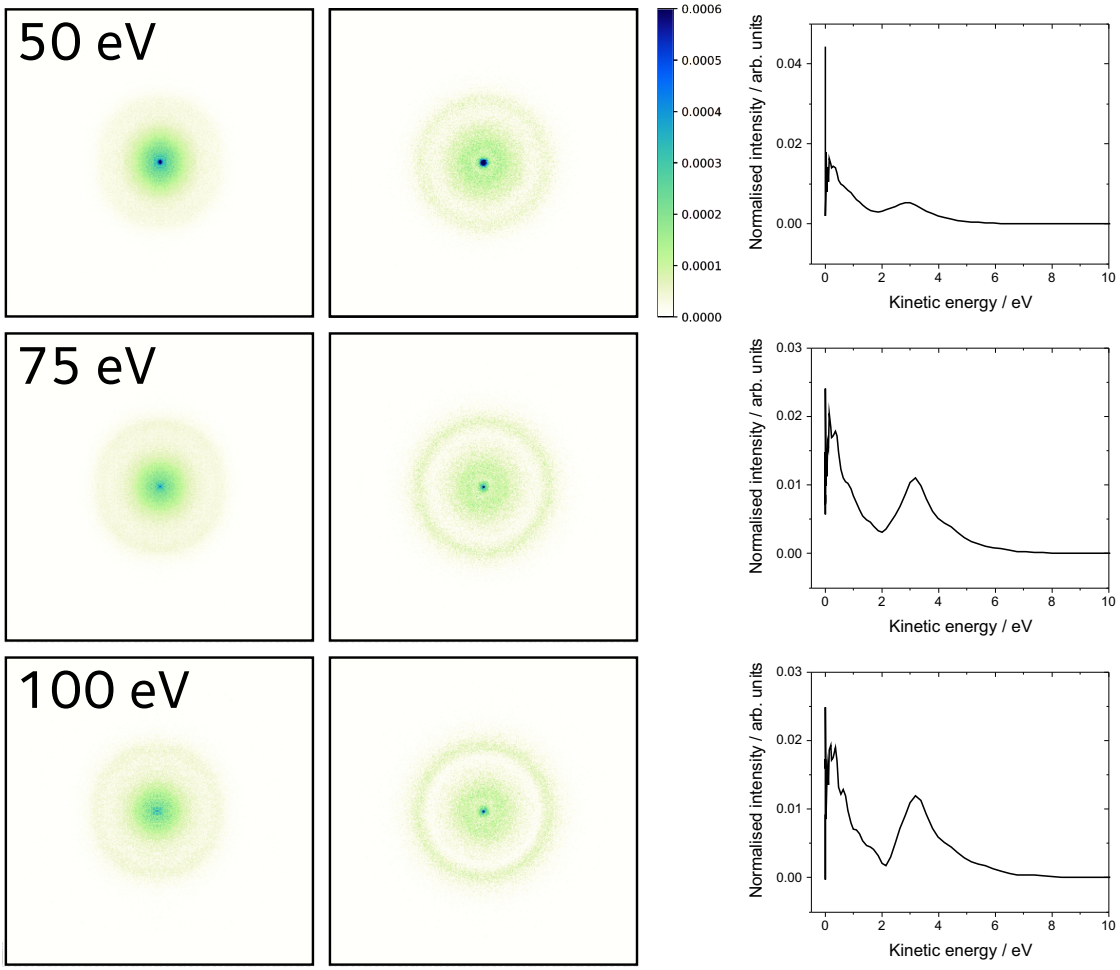


Figure 5.33 The scattering distribution recorded for CO^+ produced from OCS after ionisation by electrons of 50 eV, 75 eV, and 100 eV. The columns show the symmetrised image, the inverted image, and the kinetic energy distribution.

Figure 5.33 shows the scattering distribution obtained at three electron energies for the CO^+ ion. We see a central feature, and evidence for a number of dissociation channels at low kinetic energy, with little change being observed in this region over the energy range considered here. Again, we see the growth of a peak from dissociation of OCS^{2+} with increasing electron energy, at a kinetic energy of around 3 eV.

We can see from the potential energy surface shown in figure 5.32 that, of the well-defined electronic states of OCS^+, only the $\tilde{C}$ state lies above the lowest thermodynamic limit for the formation of CO^+. It is known that CO^+ is indeed formed from the $\tilde{C}$ state,[266,268,269] and is known to produce CO^+ in its first two vibrational

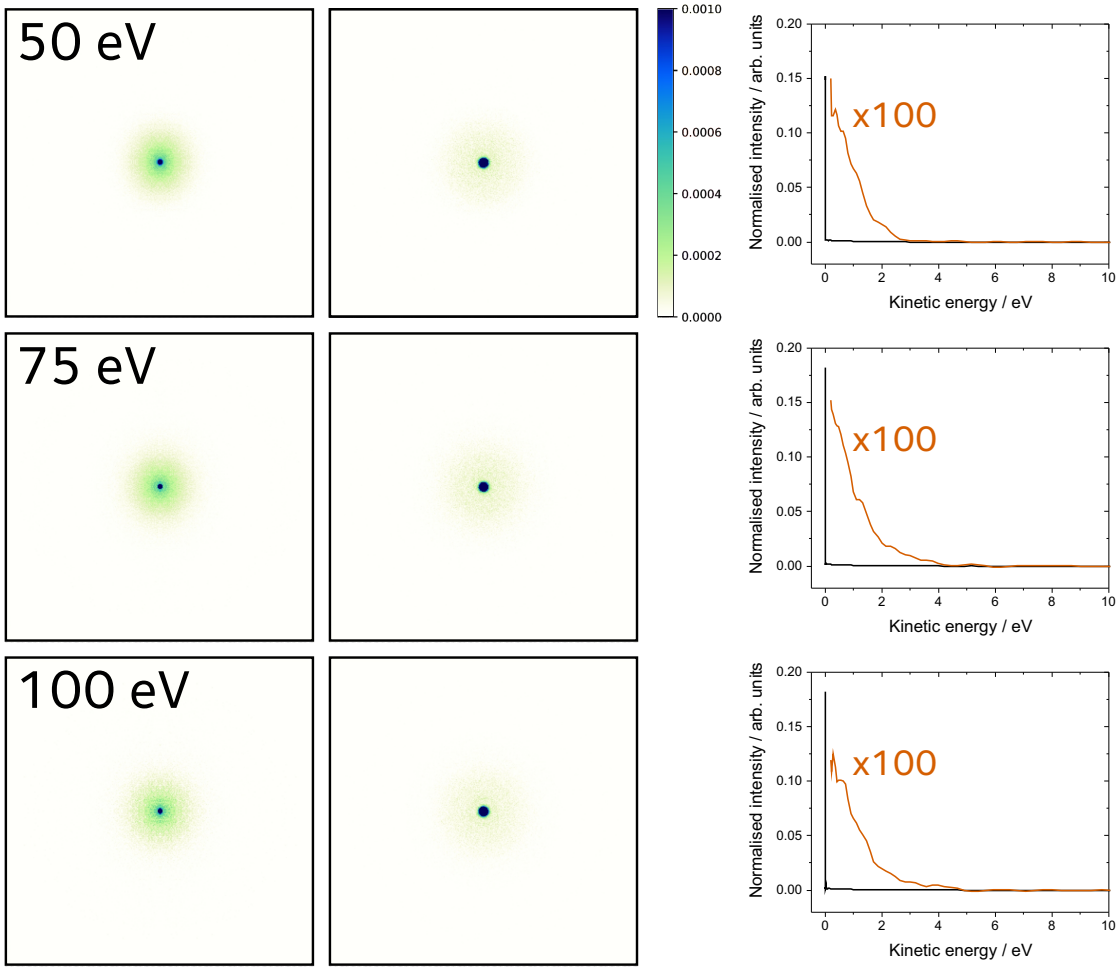


Figure 5.34 The scattering distribution recorded for CS^+ produced from OCS after ionisation by electrons of 50 eV, 75 eV, and 100 eV. The columns show the symmetrised image, the inverted image, and the kinetic energy distribution.

states.[269] The states accessed by multiple-electron transitions may also play a role in the production of CO^+, with Carnovale *et al.* estimating that around 15 % of ion fragments resulting from population of MET states result in the formation of CO^+. Dissociation from the $\tilde{C}$ state would be consistent with the observed kinetic energy distribution, and from our previous conclusions that the dissociation dynamics are dominated by low-lying states, it is likely to be the dominant formation pathway for CO^+.

Figure 5.34 shows the scattering distribution obtained at three electron energies for the CS^+ ion. We see a strong signal at zero kinetic energy at all electron energies, with a relatively weak signal extending out to higher electron energies. The central

feature may be from an impurity of CO_2 which, as we will see from the covariance analysis, is present in our sample. However, without repeating the experiment with a purer sample, we cannot easily determine the extent to which the central peak is caused by the presence of CO_2 and cannot discount the possibility that there is a central feature caused by CS^+. Based on the other low-energy signal, we assume that at least one of the dissociation pathways available proceeds via a statistical dissociation pathway, although it is likely that more than one dissociation pathway will lead to the formation of CS^+.

As can be seen from the potential energy surface shown in figure 5.32, the energetic threshold for formation of CS^+ lies slightly above the ground vibrational level of the $\tilde{C}$ state of OCS^+. The only realistic method of forming CS^+ from this state would be if the ion is produced with energy above this threshold, then either undergoes internal conversion to the $\tilde{X}$ state from which the ion can then fragment into CS^+, or predissociates via some other state which correlates with the electronic ground state of $CS^+ + O$. As was the case for CO^+, dissociation from the $\tilde{C}$ state is likely to be the dominant formation pathway for CS^+.

Alternative formation pathways for CS^+ include dissociation of highly excited neutral OCS into O and CS, followed by autoionisation of the CS fragment, and the MET states discussed previously. It is known that the latter produce CS^+,[268,269] with Carnovale *et al.* estimating that approximately 10 % of the fragment ions generated by dissociation of MET states result in formation of CS^+.[268]

Figure 5.35 shows the scattering distribution obtained at three electron energies for the O^+ ion. We see a feature in the centre of the image at each electron energy, surrounded by a ring which appears at increasing kinetic energy with increasing electron energy. The outer ring is largely attributed to dissociation of OCS^{2+} although some of the intensity will undoubtably result from the fragmentation of OCS^+.

Figure 5.36 shows the scattering distribution obtained at three electron energies for the C^+ ion. We see what appears to be a statistical dissociation, with the growth

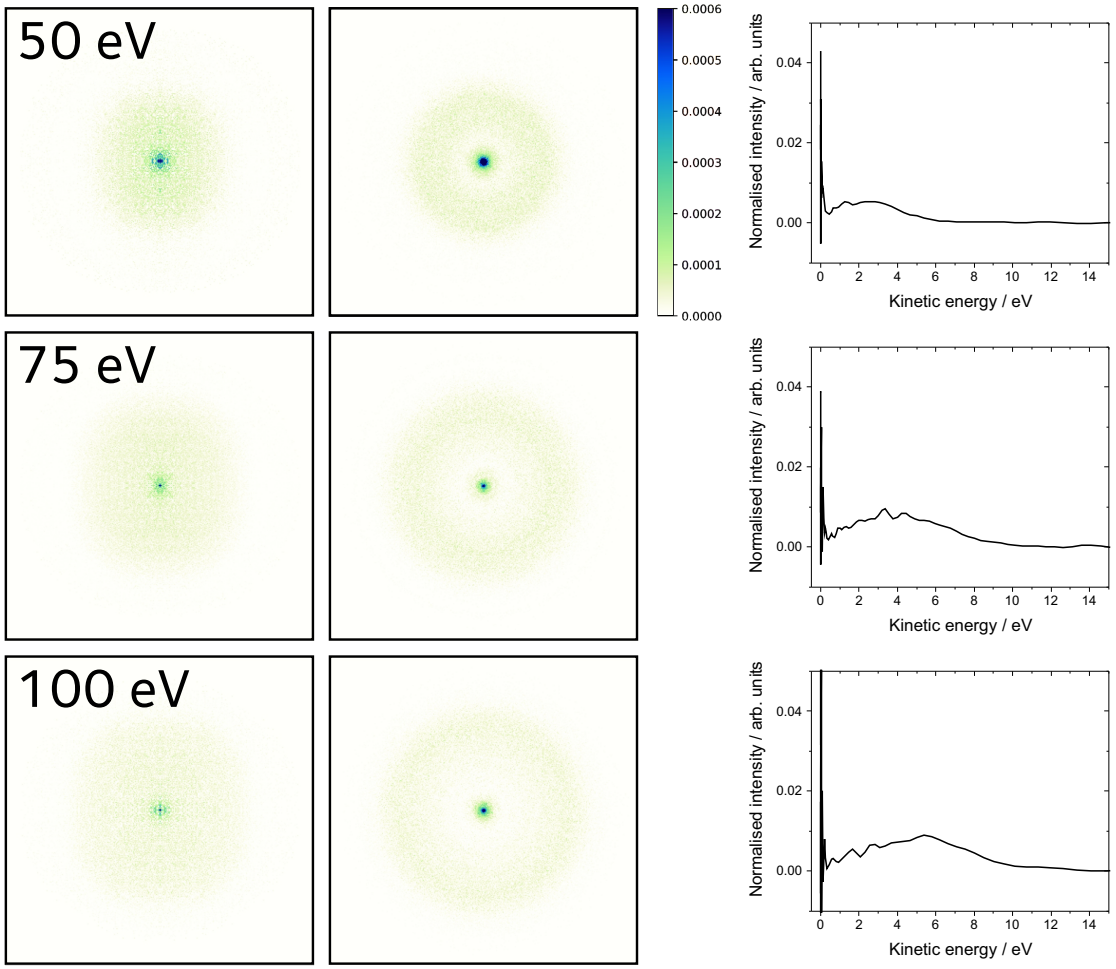


Figure 5.35 The scattering distribution recorded for O^+ produced from OCS after ionisation by electrons of 50 eV, 75 eV, and 100 eV. The columns show the symmetrised image, the inverted image, and the kinetic energy distribution.

of a feature corresponding to double ionisation at an energy of approximately 3 eV with increasing electron energy.

The energetic thresholds for the formation of both C^+ and O^+ lie above the energy of the $\tilde{C}$ state, so these ions are largely formed either by dissociation from the multiple-electron transition states,[268] or by dissociation of OCS^{2+}. Carnovale *et al.* found that around 13 % of the fragment ions produced from dissociation from OCS prepared in the MET states results in the formation of either C^+ and O^+, but did not specify an approximate branching ratio between the two. They also note that C^+ and O^+ are formed from particular groups of MET states.[268]

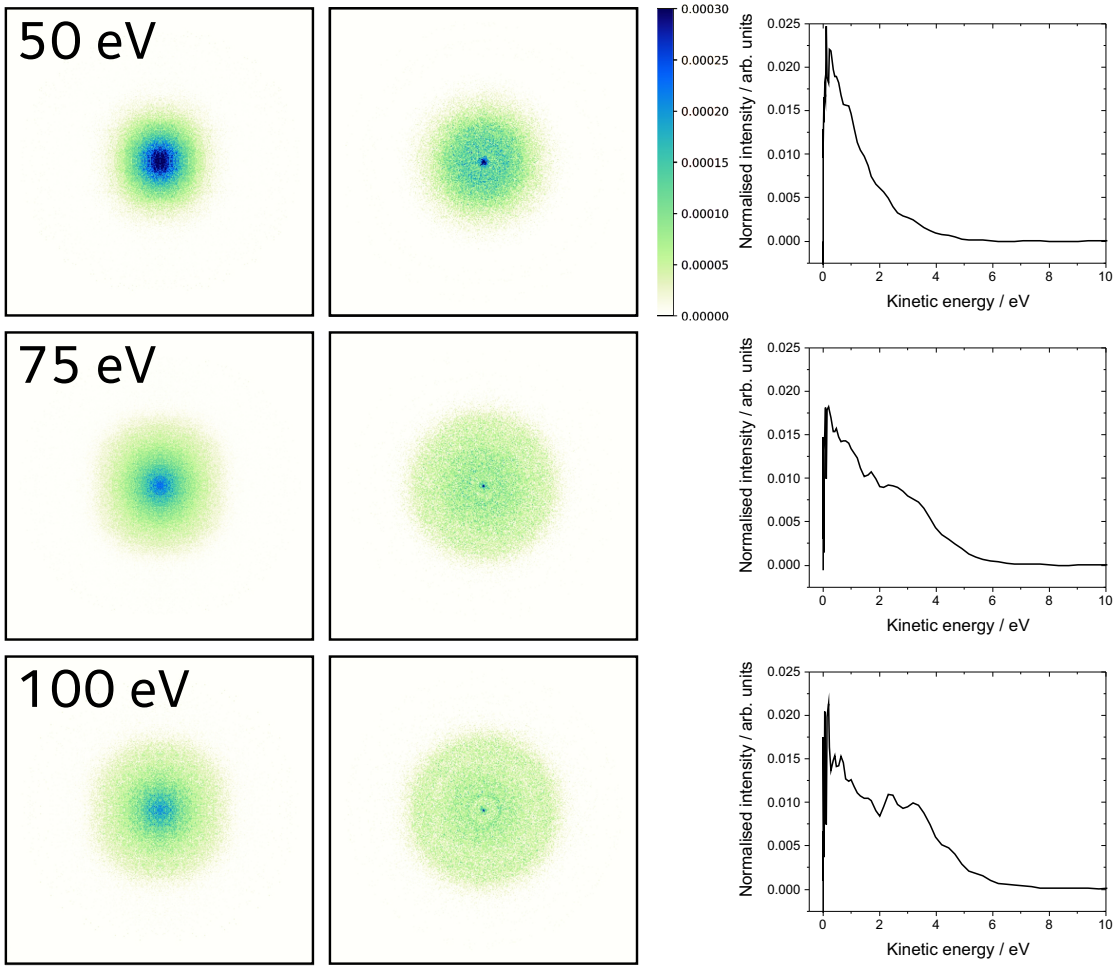


Figure 5.36 The scattering distribution recorded for C^+ produced from OCS after ionisation by electrons of 50 eV, 75 eV, and 100 eV. The columns show the symmetrised image, the inverted image, and the kinetic energy distribution.

Now that we have studied the scattering distributions of the ions we observe, we will turn our attention to the dissociation of multiply-charged OCS.

5.3.3 Covariance analysis of OCS^{2+}

We observe a number of covariant channels resulting from the electron ionisation of OCS. Figure 5.37 shows the TOF-TOF covariance map acquired from analysis of the PImMS data recorded at three electron energies. We see that the dissociation pathway $OCS^{2+} \rightarrow CO^+ + S^+$ is the dominant dissociation pathway of the dication at all electron energies considered here. The next most abundant pathway is $OCS^{2+} \rightarrow C^+ + S^+ + O$, which is also observed at all energies. The dissociation

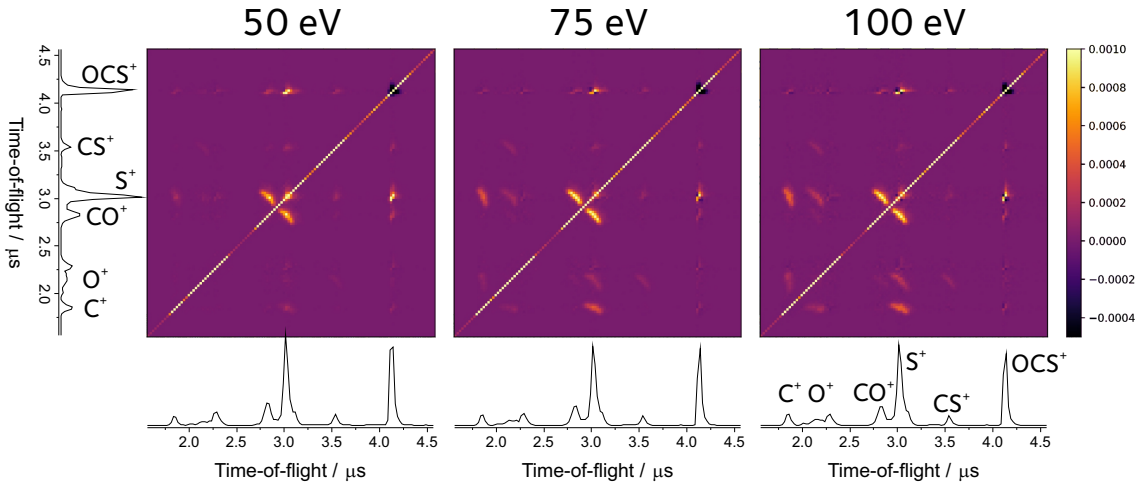
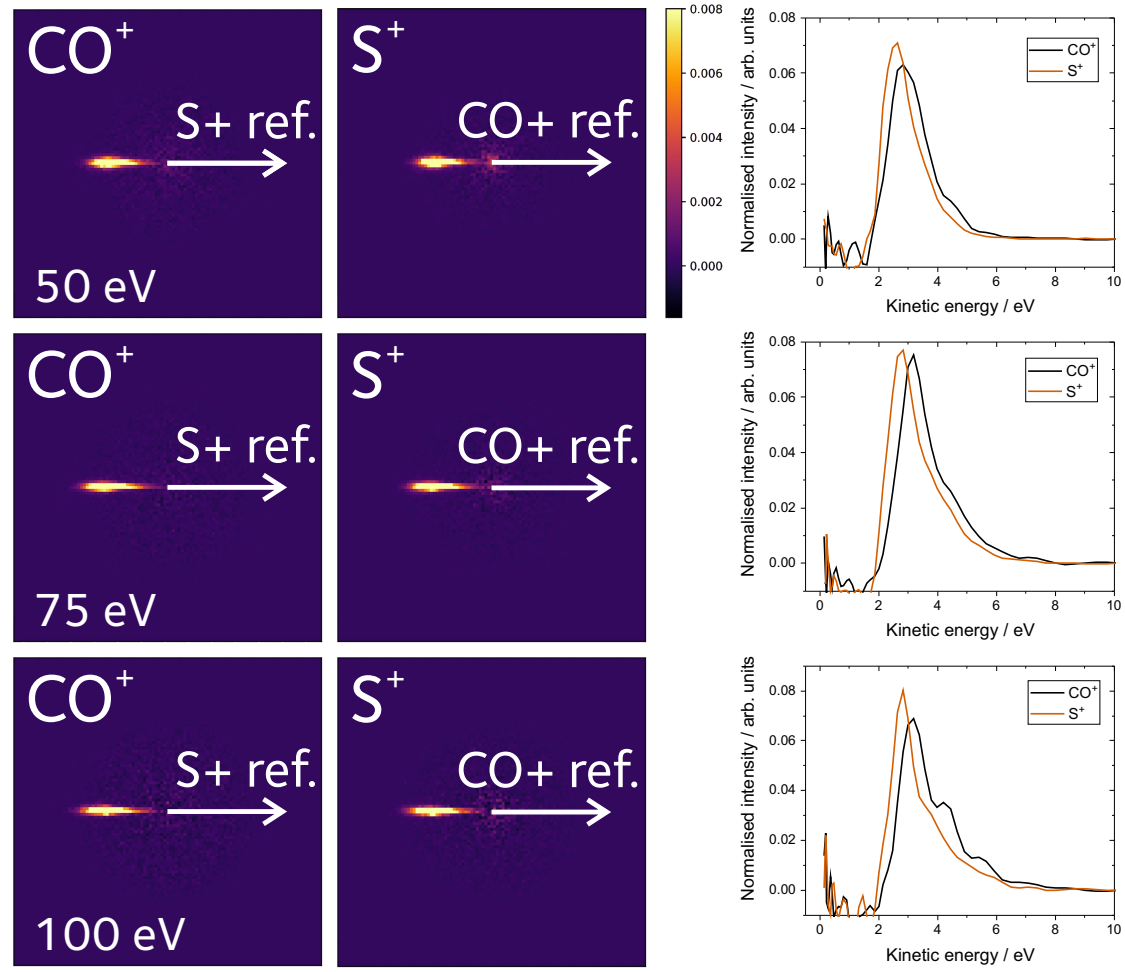


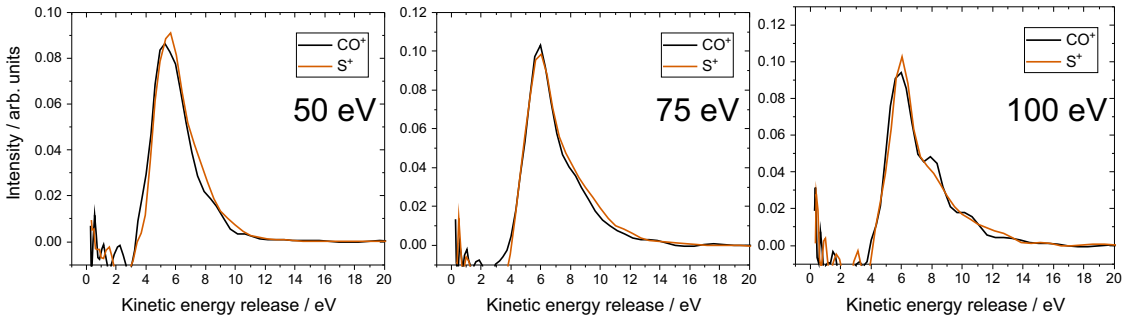
Figure 5.37 TOF-TOF covariance maps of OCS recorded at electron energies of 50 eV, 75 eV, and 100 eV. The time-of-flight spectra used for the analysis are shown below the map, with the ions of interest indicated on the 100 eV TOF spectrum. Note that the TOF spectra are not background subtracted, so signal from background ions is also observed in the TOF spectra.

pathway $OCS^{2+} \rightarrow O^+ + CS^+$ is also observed at all electron energies considered here, but is a much weaker dissociation channel than the previous two pathways. Above 75 eV, we also observe the presence of the pathways $OCS^{2+} \rightarrow C^+ + O^+ +$ S and $OCS^{2+} \rightarrow O^+ + S^+ + C$.

We have already established the presence of a small impurity of H_2S in the sample. From the covariance analysis, we can also determine that there is a small impurity of CO_2 present, as we see a weak covariance signal between CO^+ and O^+. Given that this is the strongest covariance signal observed in the CO_2 TOF-TOF covariance map (see figure 5.7), but appears as a very weak feature in the OCS TOF-TOF covariance map, it is thought that the contribution of ${CO_2}^{2+}$ to the $C^+ + O^+$ covariance feature in the OCS data will be negligible.

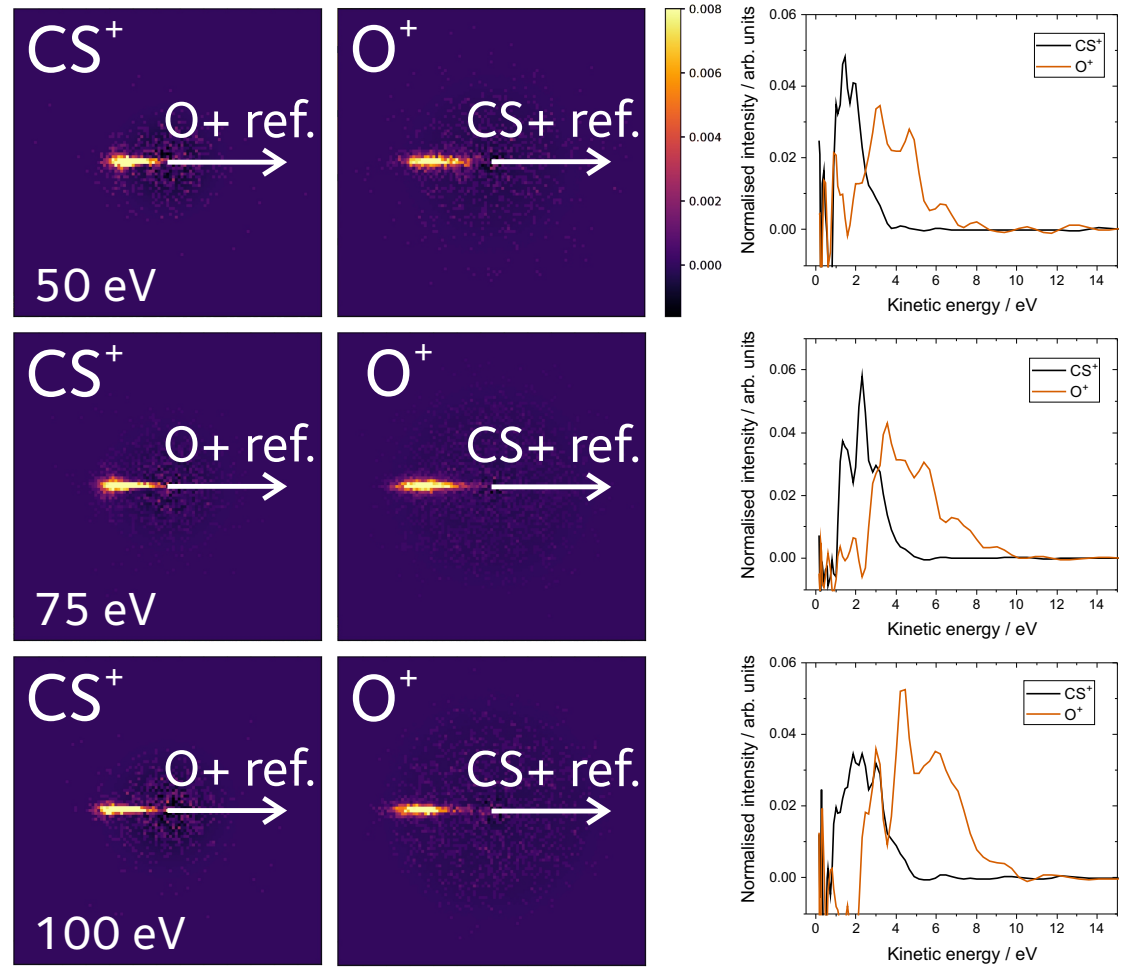


(a)

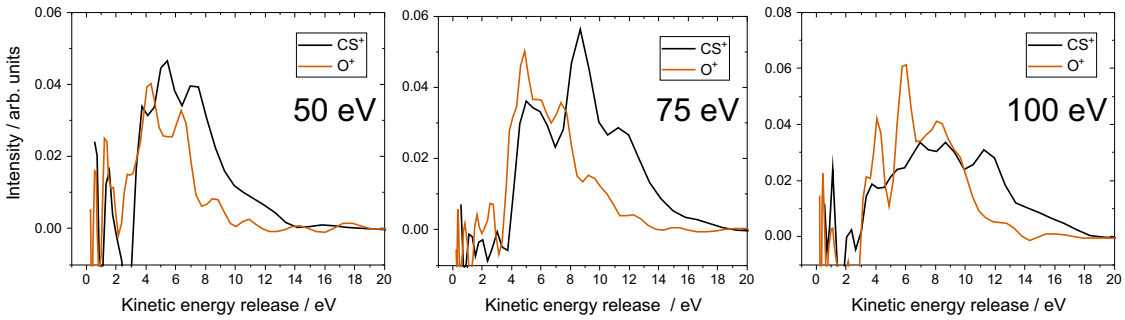


(b)

Figure 5.38 Recoil-frame covariance images for the formation of CO^+ and S^+ from OCS^{2+} at three electron energies, along with the associated kinetic energy distributions (a). The label in the kinetic energy distribution corresponds to the signal ion, obtained using the inversion method discussed in section 3.5.1. (b) shows the kinetic energy release, which has been determined from the kinetic energy distribution of each signal ion independently, based on conservation of momentum.



(a)



(b)

Figure 5.39 Recoil-frame covariance images for the formation of CS^+ and O^+ from OCS^{2+} at three electron energies, along with the associated kinetic energy distributions (a). The label in the kinetic energy distribution corresponds to the signal ion, obtained using the inversion method discussed in section 3.5.1. (b) shows the kinetic energy release, which has been determined from the kinetic energy distribution of each signal ion independently, based on conservation of momentum.

Two-body dissociation

We observe two pairs of two-body dissociation products after electron ionisation of OCS. The recoil-frame covariance image obtained for the processes

$$OCS^{2+} \rightarrow CO^{+} + S^{+} \tag{5.14}$$

$$OCS^{2+} \rightarrow CS^{+} + O^{+} \tag{5.15}$$

are shown in figures 5.38 and 5.39. We see that for pathway 5.14 the main dissociation channel observed has a kinetic energy release of 6.0 eV at 75 eV and 100 eV, and 5.5 eV at 50 eV. Previously, Curtis and Eland has reported a kinetic energy release of 5.7 eV,[209] and Eland has reported a kinetic energy release of 5.3 eV[155] following photoionisation at 40.8 eV. Masuoka *et al.* report an average kinetic energy release of 5.4 eV at a photon energy of 45 eV, and note that there is very little deviation in the kinetic energy distribution when the photon energy is increased to 50 eV.[272] Our kinetic energy release at an electron energy of 50 eV is consistent with these data.

It is also clear from the results of Masuoka *et al.* that the kinetic energy release at 45 eV is bimodal.[272] Brites *et al.* suggest that the dominant electronic states of OCS^{2+} involved in pathway 5.14 are the lowest energy $^{1}\Delta$ and $^{1}\Sigma^{+}$ states of OCS^{2+}, for which they compute kinetic energy releases of 5.44 eV, and 6.58 eV, respectively.[273] This would be consistent with the bimodal distribution obtained by Masuoka *et al.*, and a change in the relative intensities of the two pathways would be consistent with the increase in kinetic energy release with electron energy we observe in our data.

We also see evidence for a number of other channels with higher kinetic energy release, which are attributed to the dissociation of a number of higher-lying electronic states.

The kinetic energy distributions obtained for pathway 5.15 ($OCS^{2+} \rightarrow CS^{+} +$

O^+) are much noisier than those obtained for pathway 5.14 due to the significantly lower signal level. However, we can determine that the modal kinetic energy release is approximately 6 eV at 75 eV and 100 eV, and is around 5 eV at 50 eV, although there is significant uncertainty in these values. Again, we see higher energy features appearing at higher electron energies.

Eland reports a kinetic energy release of 6.3 eV following photoionisation at 40.8 eV,[155] and Masuoka *et al.* report a mean kinetic energy release of around 6 eV following photoionisation at 50 eV.[272] Brites *et al.* also state that they obtain a kinetic energy release of 6 eV from their PEPIPICO data.[273] These kinetic energy release values are consistent with those obtained in the present work.

From the potential energy surfaces calculated by Brites *et al.* it is clear that the barrier to dissociation via breaking the C-O bond is significantly higher than that via breaking the C-S bond.[273] This is entirely consistent with the relative signal intensities of the two channels.

Three-body dissociation

As noted previously, the dominant three-body dissociation pathway is found to be

$$OCS^{2+} \rightarrow C^+ + S^+ + O \tag{5.16}$$

Figure 5.40 shows the covariance images obtained for this pathway. The signal-to-noise ratio at 50 eV is relatively low, but in general we see little change in the images or kinetic energy distribution with increasing electron energy, with the exception of the kinetic energy distribution extending to higher energies for higher incident electron energies. We find that the mode of the total kinetic energy of the S^+ and C^+ ions is approximately 7 eV.

Eland reports a kinetic energy of 6.4 eV for photoionisation at 40.8 eV.[155] Masuoka *et al.* present kinetic energy release distributions which vary with photon energy, with peaks appearing at around 4 eV, 6.5 eV, and 9 eV at different relative

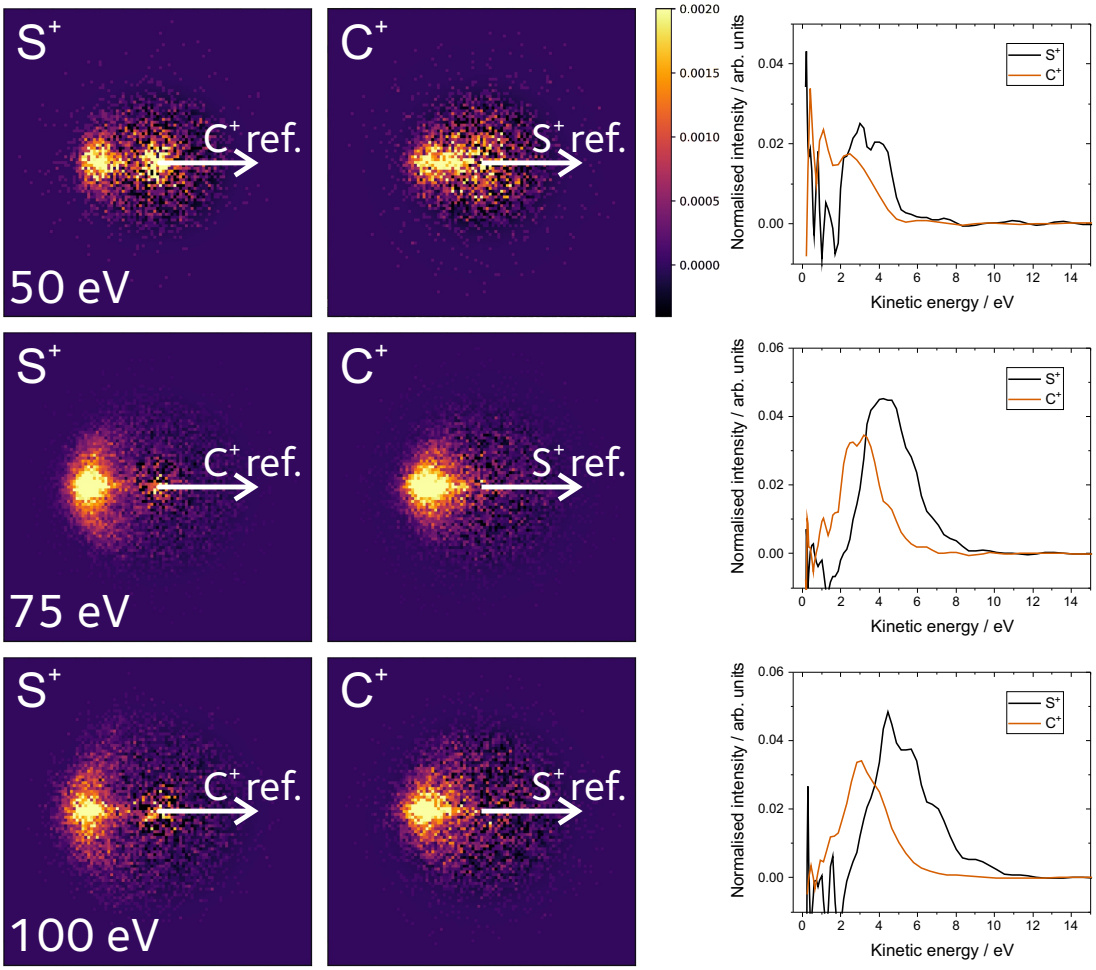


Figure 5.40 Recoil-frame covariance images for the formation of C^+, S^+ and O from OCS2+ at three electron energies, along with the associated kinetic energy distributions. The label in the kinetic energy distribution corresponds to the signal ion.

intensities for photon energies in the range 45 eV to 100 eV.[272]

From figure 5.37, we can see that the slope of the TOF-TOF covariance map for this pathway is evidently not -1. We determine the gradient to be approximately -0.45, although due to the resolution of our covariance map, it is difficult to determine the exact value. Eland has previously reported a gradient of -0.52,[155], Masuoka a value of -0.46 at photon energies of 48 eV and 60 eV, and -0.43 at 80 eV,[274] and Wang and Vidal a value of -0.4 following electron ionisation by 200 eV electrons.[260] For an initial charge separation mechanism where the resulting CO^+ ion dissociates at a random orientation, we would expect a gradient of -0.43, which is consistent with the gradients obtained. The covariance images are also consistent with this

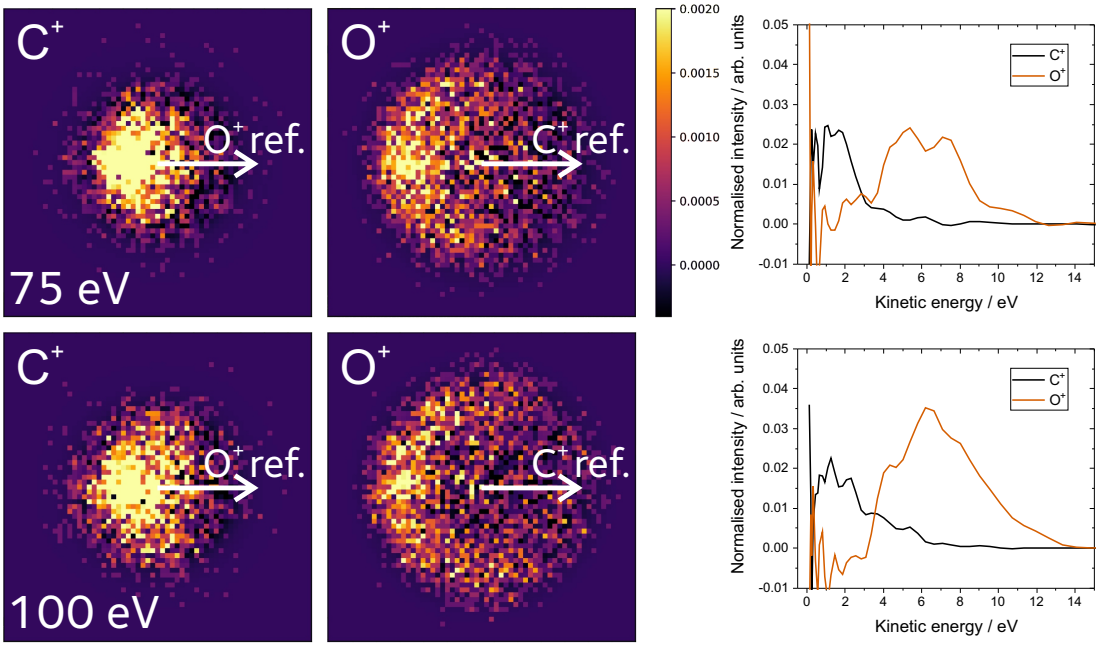


Figure 5.41 Recoil-frame covariance images for the formation of C^+, O^+ and S from OCS2+ at two electron energies, along with the associated kinetic energy distributions. The label in the kinetic energy distribution corresponds to the signal ion.

designation, and in this case would show at least two dissociation channels of the CO^+ fragment. Hsieh and Eland also suggest a mechanism by which dissociation occurs in a concerted manner, but from an asymmetric initial geometry, prepared by indirect transition onto a dication potential energy surface.[221] This mechanism could also be consistent with our results, however, we believe that an initial charge separation gives the best match to the observed experimental data here, in accord with both Masuoka[274] and Wang and Vidal.[260]

Figure 5.41 shows the covariance images obtained for the pathway

$$OCS^{2+} \rightarrow C^+ + O^+ + S \tag{5.17}$$

From the covariance images, we immediately see that the intensity in the O^+ image appears as an arc at constant radius, and the feature in the C^+ image is circular. This would be entirely consistent with an initial charge separation process, as can be seen from the simulations carried out in section 3.4.5. We estimate the gradient of

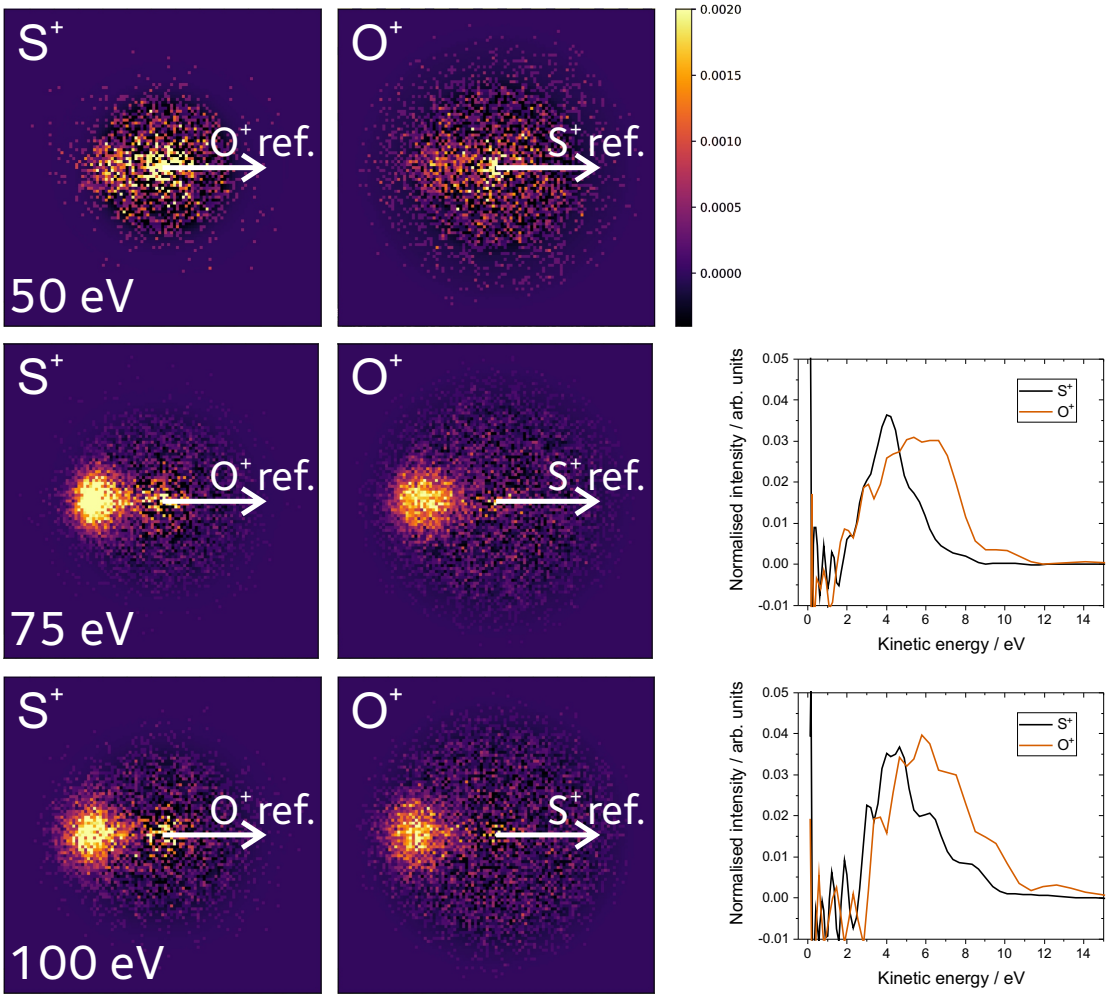


Figure 5.42 Recoil-frame covariance images for the formation of O^+, S^+ and C from OCS2+ at three electron energies, along with the associated kinetic energy distributions where the signal level allows. The label in the kinetic energy distribution corresponds to the signal ion.

the corresponding features in the TOF-TOF covariance map, shown in figure 5.37, to be approximately −0.23 from our data, which is in good agreement with the expected gradient of −0.27 expected for an initial charge separation process. This finding is also consistent with the results of Wang *et al.*, who report a gradient of −0.26 following electron ionisation at 200 eV.[260]

In contrast to this, Masuoka reports gradients of −0.06 and −0.08 following photoionisation at 60 eV and 80 eV, respectively. He suggests that the mechanism by which dissociation occurs involves a simultaneous three-body dissociation of the OCS^{2+} and/or OCS^{3+} cation, where the C^+ ion acts as a spectator.[274]

Figure 5.42 shows the covariance images obtained for the pathway

$$OCS^{2+} \rightarrow O^+ + S^+ + C \tag{5.18}$$

The kinetic energy distributions involve formation from a number of states. The modal value for the total kinetic energy of the O^+ and S^+ ion is approximately 10 eV, but this is by no means a complete description of the dynamics observed. We see reasonable agreement with the results obtained by Masuoka *et al.* via photoionisation, who reported multiple peaks in the fragment kinetic energy distributions, consistent with dissociation from a number of electronic states.[272] It is trickier to compare the kinetic energy values, as Masuoka *et al.* report kinetic energy releases, but on casual inspection it appears that peaks appear in approximately the same locations as in our data. Eland reports a kinetic energy release of 5.9 eV for this channel following photoionisation at 40.8 eV.[155] We do not see a clear signal at this point in our data, which suggests that a number of higher-lying electronic states are responsible for the signal we observe.

From the TOF-TOF covariance map, we obtain a gradient of -1 for this dissociation channel. This would be consistent with either a deferred charge separation, or a concerted dissociation. Given that the formation of OS^{2+} would require significant rearrangement of the OCS dication, and that we would expect to see less circular features in the covariance images due to the OS^{2+} ion gaining kinetic energy in the first step of the dissociation, the covariance images are best explained by a concerted dissociation pathway. Eland reports a slope of -1.1,[155] Masuoka a slope of -0.97 and -0.9 at photon energies of 60 eV and 80 eV, respectively,[274] and Wang and Vidal report a gradient of -0.83 following electron ionisation at 200 eV. All suggest a concerted dissociation mechanism, in agreement with our assignment.

5.3.4 Comparison to CO_2

At this point, it seems logical to draw comparisons with the dynamics observed for electron ionisation of CO_2. Both molecules are linear in the ground state, and contain a central carbon atom double-bonded to both an oxygen atom and either a sulphur atom or a second oxygen atom. Thus, we might expect to observe similar dissociation dynamics for the two molecules.

The scattering distributions obtained for C^+ in both cases are almost identical at 50 eV. At higher energies, we see a higher relative contribution from double ionisation in the OCS scattering distribution, so greater differences are seen at higher energies. The scattering distributions of O^+ and S^+ obtained via ionisation of OCS are also very similar to those obtained for O^+ from CO_2, although the O^+ scattering distribution of OCS shows significant contributions from dissociation of OCS^{2+}. The scattering distributions of CS^+ from OCS and CO^+ from CO_2 show excellent agreement, although there was found to be a contribution of CO_2^+ to the signal observed at zero kinetic energy in the CS^+ scattering distribution. The CO^+ scattering distributions obtained from OCS also show reasonable agreement with their CO_2 counterpart, although show slightly higher kinetic energy releases in the low-energy region, and a greater extent of double ionisation.

The covariance analysis shows that dissociation of doubly-charged ions proceed via the same mechanisms in both cases, albeit with OCS^{2+} preferentially proceeding via fragmentation of the CS bond. We also see that double-ionisation is much more common in the case of OCS, which is unsurprising given that the double ionisation potential of CO_2 to the lowest-lying electronic state of CO_2^{2+} is 38.1 eV,[275] whilst the equivalent for OCS is 30.0 eV.[275]

We can conclude that, on the whole, replacing an oxygen atom with a sulphur atom makes little qualitative difference to the dissociation mechanisms in this case. It is evident that the loss of symmetry inevitably results in certain bonds being broken preferentially upon dissociation, and that the introduction of an atom which

is more readily ionised increases the cross-section for double ionisation. We can also conclude that the presence of an extra set of s and p orbitals on a terminal atom does not seem to have a huge effect on the potential surfaces involved in the ionisation and fragmentation processes observed in this case.

5.3.5 Summary

We have reported partial ionisation cross-sections, scattering distributions, and recoil-frame covariance images for carbonyl sulphide. To our knowledge, these are the first partial ionisation cross-sections reported for electron ionisation of OCS. We have discussed the scattering distributions we obtain and discussed potential dissociation pathways using results in the literature obtained through photoelectron spectroscopy, and have used covariance analysis techniques to probe the dissociation of multiply-charged OCS, and compared our results to those available in the literature. We have also compared the dissociation dynamics with those obtained for CO_2.

5.4 Sulphur dioxide (SO_2)

Sulphur dioxide (SO_2) was first detected in the interstellar medium in 1975 by Snyder *et al.*[276] Since then, it has been found to have a relatively high abundance in a number of molecular clouds under various conditions.[277–281] It is known to be a significant component of the surface frost and atmosphere of Jupiter's moon Io,[282] and, along with SO, is a likely source for the plasma torus described by Io's orbital path.[283] Closer to home, SO_2 plays an important part in the sulphur cycle, and is known to be emitted from man-made sources on a scale exceeding that of natural sources.[284] It is an atmospheric pollutant,[285] with the main industrial source being from the burning of fossil fuels.[284] It is well known that atmospheric sulphur dioxide can be converted to sulphuric acid, which can then fall as acid rain. Work has been carried out to attempt to remove sulphur dioxide from flue gases of power stations,

to reduce the atmospheric concentration of SO_2.[286] SO_2 is a bent molecule, belonging to the C_{2v} point group, and has a bond angle of approximately 120°.

In the present work, scattering distributions for the electron ionisation products of SO_2 were recorded at electron energies of 50 eV, 75 eV and 100 eV using an extractor potential of 2 kV and a repeller potential of 1.612 kV. The electron beam pulse lengths were set to 750 ns, 550 ns and 350 ns at electron energies of 50 eV, 75 eV and 100 eV, respectively, and the timing of the ion optics pulse adjusted accordingly. A total of 800,000, 2,400,000, and 3,800,000 acquisition cycles were recorded at electron energies of 100 eV, 75 eV, and 50 eV, respectively, and an equal number of acquisition cycles of background data were recorded. Signal and background acquisitions were alternated every 50,000 acquisition cycles to reduce the effect of any experimental drift on the background subtraction. SO_2 was seeded in helium at a ratio between 10 % and 20 %.

Mass spectra were also recorded using a photomultiplier tube (PMT) to record the optical signal from the scintillator screen at electron energies ranging from 50 eV to 100 eV in 5 eV steps, using an extractor potential of 1.652 kV and a repeller potential of 2 kV. We have sufficient signal to present data above an electron energy of 50 eV. Data acquisition was carried out by alternating between recording 500 acquisition cycles of signal and background, for a total of 5,000 acquisition cycles of signal, and the background signal subtracted from the signal to give the final mass spectrum.

We will first present the partial ionisation cross-sections of SO_2 and compare these to those found in the literature. Next, we will discuss the scattering distributions we obtain, and finally the results of the covariance analysis between the detected fragment ions.

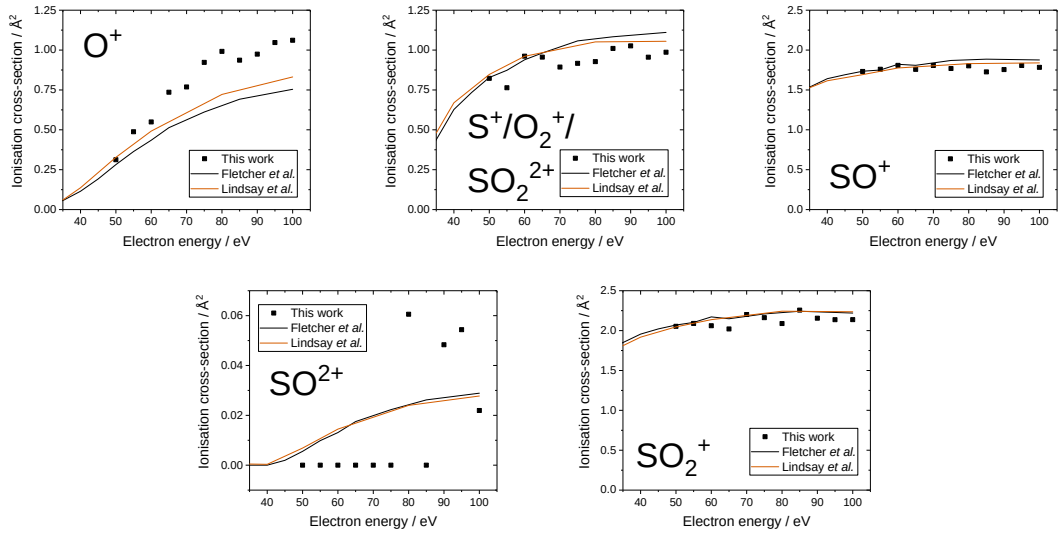


Figure 5.43 Partial ionisation cross-sections obtained for SO_2 by fitting our PMT traces with Gaussians convoluted with an exponential decay, and normalising to the total ionisation cross-section of Cadez *et al.*.[287] Also plotted are the cross-sections obtained by Fletcher *et al.*,[288] and Lindsay *et al.*,[289] which have been normalised in the same way.

5.4.1 Partial ionisation cross-sections

Figure 5.43 shows the partial ionisation cross-sections we obtain, with comparison to the results of Fletcher *et al.*,[288] and Lindsay *et al.*.[289] All cross-sections have been normalised to the total ionisation cross-sections recorded by Cadez *et al.*.[287] Our results agree well with the results from the literature, although we struggle to determine the cross-section of SO^{2+} with a high degree of accuracy due to the low signal level for this ion, making it difficult to achieve a good fit to this region of the PMT trace.

Fletcher *et al.* suggest that the ions with an m/z ratio of 32 are mostly S^+, based on the intensity of the ^{34}S peak relative to the mass 32 peak.[288] This is in contrast to the results of Basner *et al.*, who previously reported an approximately 2:1 contribution from S^+ and O_2^+, based on results obtained using a high-resolution mass spectrometer.[290] Both suggest that there is almost no contribution from SO_2^{2+}. From our data, we find that both S^+ and O_2^+ are formed, but cannot determine the

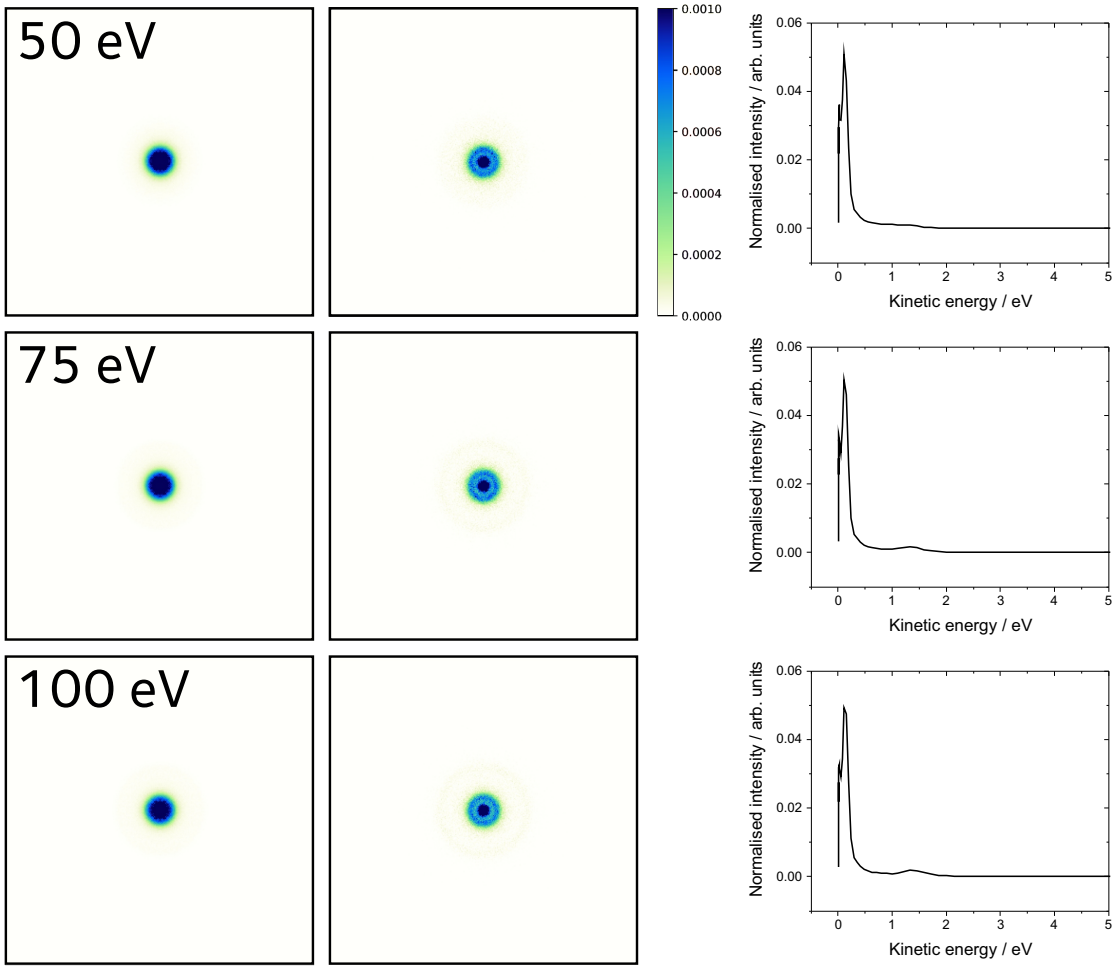


Figure 5.44 The scattering distribution recorded for SO^+ produced from SO_2 after ionisation by electrons of 50 eV, 75 eV, and 100 eV. The columns show the symmetrised image, the inverted image, and the kinetic energy distribution.

relative intensities of the two ions.

We will now study each of the scattering distributions obtained for the fragment ions formed by electron ionisation of SO_2.

5.4.2 Scattering distributions resulting from electron ionisation of SO_2

Figure 5.44 shows the scattering distribution obtained at three electron energies for the SO^+ ion. We see that there is little change in the centre of the scattering distribution over this energy range, but we do see the growth of a feature at around 1.5 eV, which is formed from the dissociation of SO_2^{2+}, as will be seen in the next

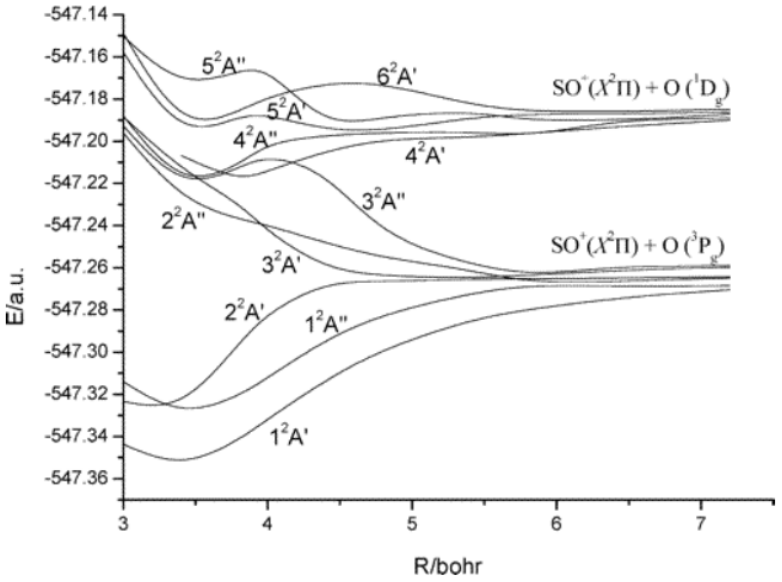


Figure 5.45 Potential energy surfaces calculated at the CASPT2/ANO-S level of theory for a number of states of SO_2^+ with $^2A_1$ and $^2A_2$ symmetry. Labels assigned by Li *et al.* have also been included. They also find that the $\tilde{A}$ state has $^2B_2$ symmetry, the $\tilde{C}$ state $^2B_1$, and the $\tilde{E}$ state $^2B_2$ symmetry.[295] Note that there is disagreement of the precise assignment of these labels between different sources. Reproduced with permission from [295]. © American Chemical Society.

section. It is clear that there are at least two pathways to form SO^+, as we observe a central feature, and a ring with a kinetic energy of approximately 0.1 eV. SO^+ is known to be produced after population of the $\tilde{C}$, $\tilde{D}$, and $\tilde{E}$ states of SO_2,[291–294] and is also known to be produced via autoionisation.[292] Zhang *et al.* propose that ions formed in the $\tilde{D}$ state predissociate to a repulsive state with $^2A_2$ symmetry.[294] Li and Huang have calculated potential energy surfaces for the dissociation of SO_2^+ for a number of states with $^2A'$ and $^2A''$ symmetry[295] (which correspond to states with $^2A_1$ and $^2A_2$ symmetry in the work of Zhang *et al.*), and their potential energy surfaces are shown in figure 5.45. Both Dujardin *et al.* and Zhang *et al.* have also suggested a mechanism for dissociation via a state of $^2B_2$ symmetry.

From our data, we can see that there is certainly a mechanism by which SO_2^+ dissociates on a repulsive surface; the peak at 0.1 eV is most consistent with a weakly impulsive dissociation, where there is not a significant barrier on the dissociative potential energy surface. The central peak is more consistent with a statistical

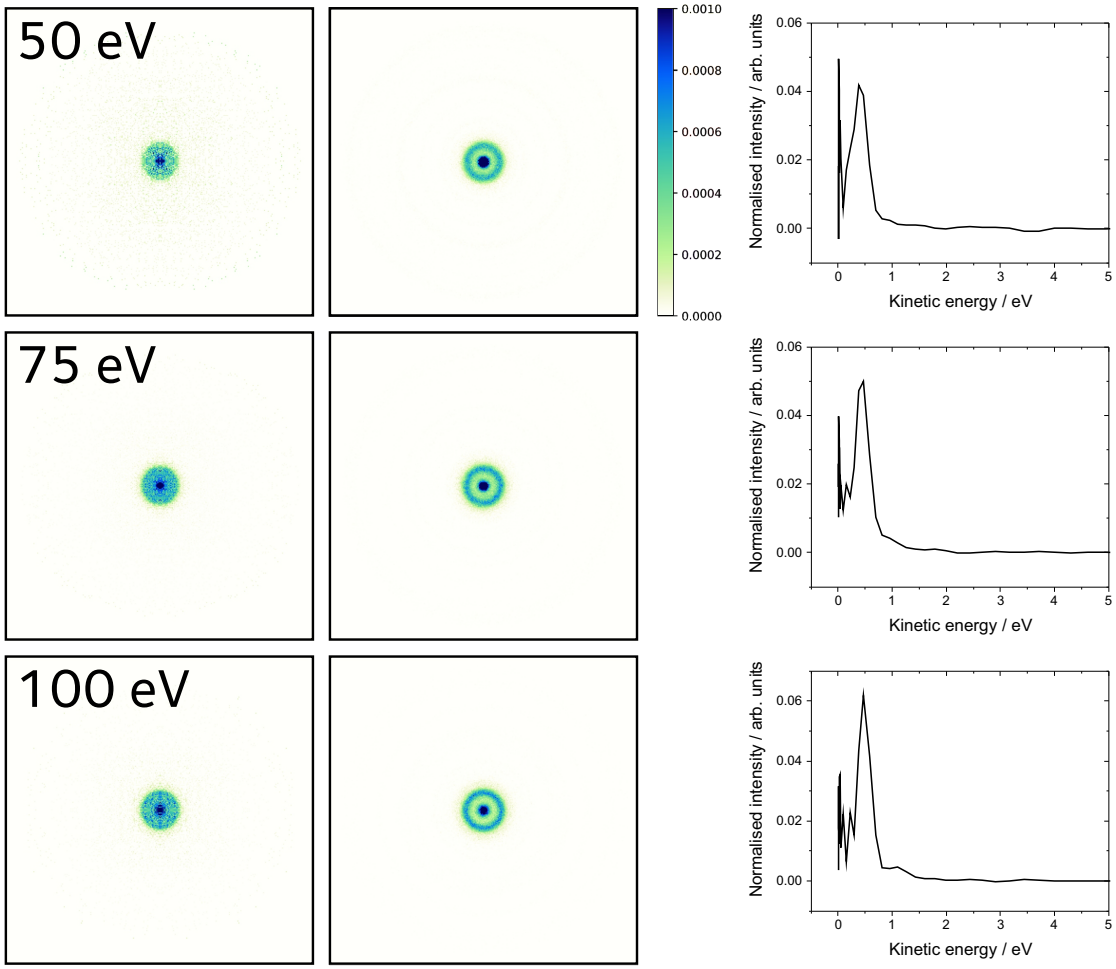


Figure 5.46 The scattering distribution recorded for SO^{2+} produced from SO_2 after ionisation by electrons of 50 eV, 75 eV, and 100 eV. The columns show the symmetrised image, the inverted image, and the kinetic energy distribution.

dissociation, so would most likely occur via a state with some barrier to dissociation.

Figure 5.46 shows the scattering distributions obtained for the SO^{2+} ion. We see that the general shape of the distribution is almost identical to that observed for SO^+, but with the ring at a slightly higher kinetic energy of approximately 0.5 eV. There is very little variation in the kinetic energy distribution across the electron energy range considered, although the outer feature does grow slightly stronger with respect to the central feature with increasing electron energy. Based on the appearance potential of approximately 35 eV for this ion,[293,296] the main formation

pathway has been determined to be the following

$$SO_2^{2+} \rightarrow SO^{2+} + O \tag{5.19}$$

Field and Eland have previously considered the formation of SO^{2+} produced via the photoionisation of SO_2 using 40.8 eV photons. They propose that the formation of SO^{2+} is concentrated below the threshold for the formation of $S^+ + O^+ + O$,[296] i.e. if SO^{2+} is produced in a sufficiently excited state, it will undergo further dissociation. Field and Eland also note that, at least in their experiment, the formation of SO^{2+} must either be via a diabatic dissociation of the parent dication, as none of the states of SO_2^{2+} available at a photon energy of 40.8 eV correlate with the ground state of SO^{2+} and O, or by dissociation of an excited singly-charged state, followed by subsequent autoionisation.

Figure 5.47 shows the scattering distributions obtained for the O^+ ion. The scattering distribution obtained at 50 eV has a rather unusual shape; usually a number of peaks are seen, but in this case there is a plateau at electron energies out to around 3 eV, before decaying by around 5 eV. We can clearly see the growth of a channel peaking at around 4 eV, due to dissociation of SO_2^{2+}. It is also unusual that the dissociation of doubly-charged parent makes such a large contribution to the cross-section for a given fragment ion, but is consistent with the cross-sections for the formation of O^+ via single and double ionisation obtained by Fletcher *et al.*[288]

O^+ can be formed either from a two-body or three-body decay, which have formation thresholds of 19.3 eV, and 24.4 eV respectively.[290] Basner and Schmidt suggest that the latter channel is the dominant channel, as only a shallow increase in the cross-section is seen below the threshold for the three-body dissociation.[290] Dujardin and Leach suggest that the $\tilde{F}$ state of SO_2 presents a pathway for the formation of O^+,[291] and Masuoka *et al.* also reach this conclusion.[293] Masuoka *et al.* also note that there is the possibility of formation of O^+ (and S^+) from a number of electronic states between the $\tilde{F}$ state and the double ionisation threshold.[293]

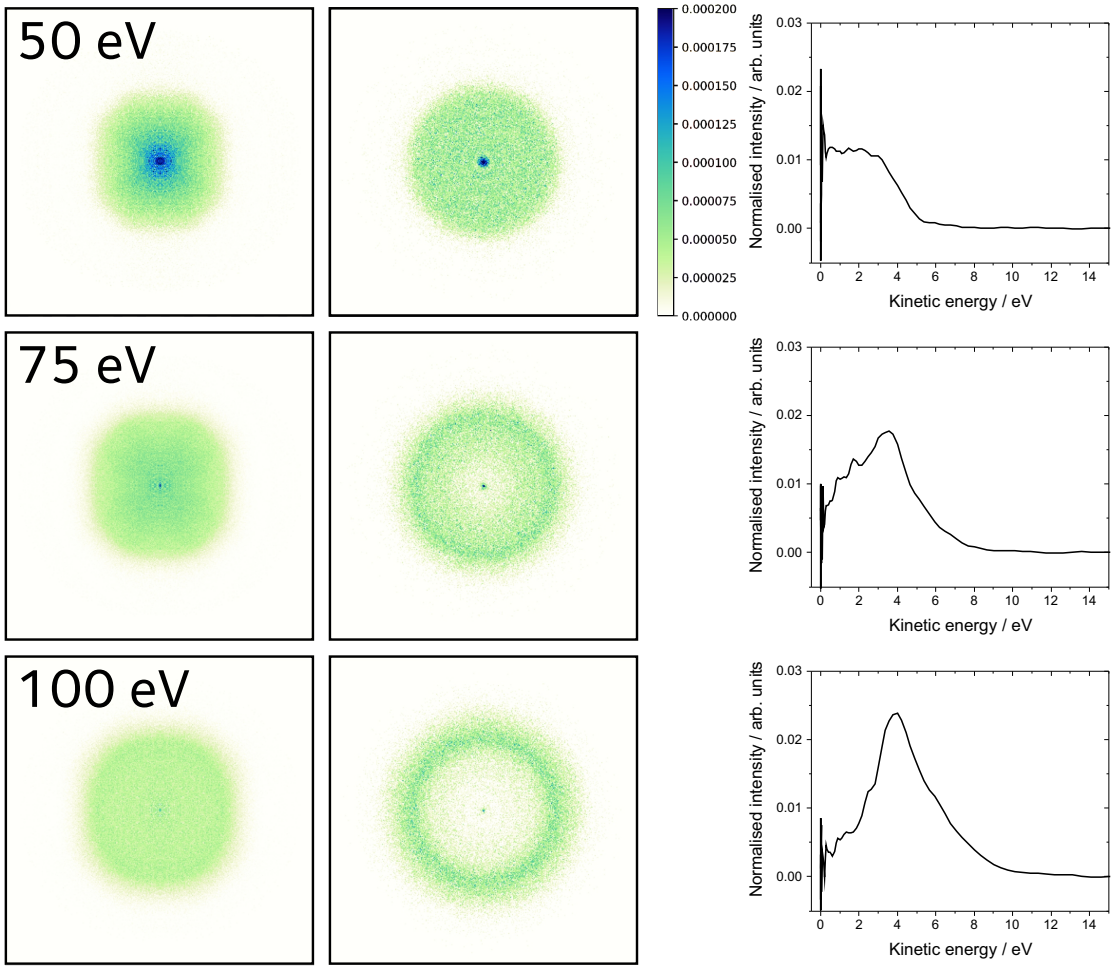


Figure 5.47 The scattering distribution recorded for O^+ produced from SO_2 after ionisation by electrons of 50 eV, 75 eV, and 100 eV. The columns show the symmetrised image, the inverted image, and the kinetic energy distribution.

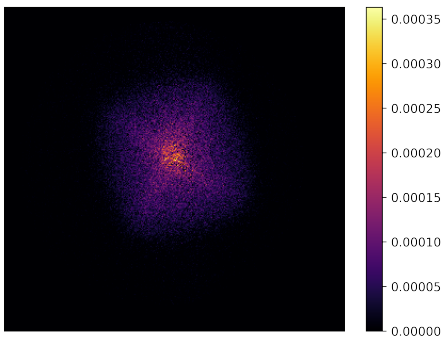


Figure 5.48 The unsymmetrised scattering distribution recorded for O^+ resulting from electron ionisation of SO_2 at an electron energy of 50 eV. It is apparent that the O^+ fragment does not velocity-map as well as would be expected in this case.

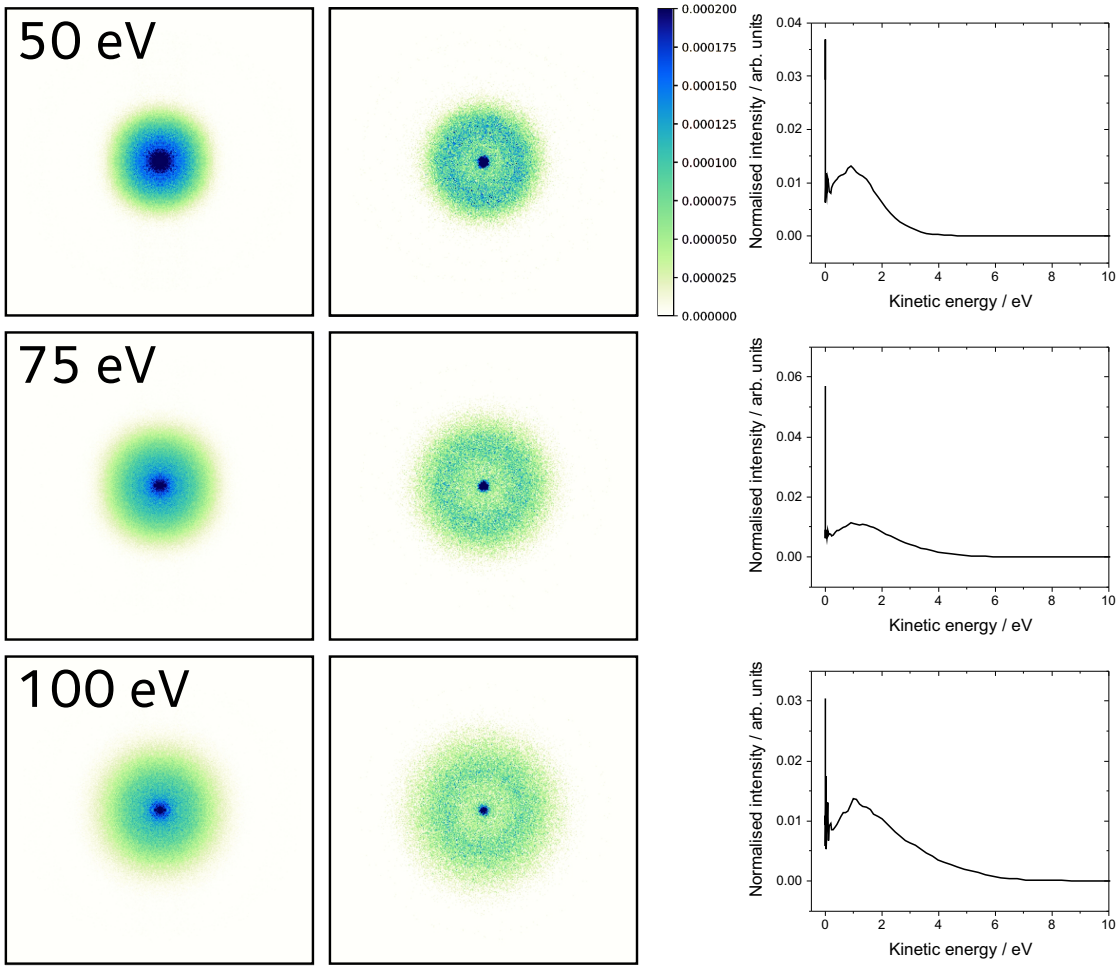


Figure 5.49 The scattering distribution recorded for S^+ produced from SO_2 after ionisation by electrons of 50 eV, 75 eV, and 100 eV. The columns show the symmetrised image, the inverted image, and the kinetic energy distribution.

If we look at the scattering distribution obtained for O^+ at 50 eV prior to symmetrisation, shown in figure 5.48, we can see that the velocity mapping is not as successful as for the other fragments in this case. One possible explanation could be that the dissociation occurs outside the region which can successfully be velocity-mapped. No reports of metastable decay were found in the literature however, which seems to contradict our hypothesis. We conclude that further work is required before we can identify the source of this feature. In any case, it is clear that the formation of O^+ cannot be adequately described by a dissociation from a single electronic state.

Figure 5.49 shows the scattering distribution for $m/z = 32$, which contains con-

tributions from the ions S^+, O_2^+, and SO_2^{2+}. We see a central feature, followed by a peak decaying out to higher kinetic energies. The length of the tail increases significantly as the electron energy increases.

Basner and Schmidt carried out an experiment to determine partial ionisation cross-sections for S^+ and O_2^+ by using a mass spectrometer with sufficient mass resolution to resolve the two peaks. They found that, in the energy range used in our work, the S^+ partial ionisation cross-section is a little under double that of O_2^+.[290] However, the conclusions of Fletcher *et al.* contradict these findings, suggesting that S^+ is almost exclusively formed, with O_2^+ only being a minor product.[288] A third determination of the cross-sections of these two fragments would be welcome, to allow the product ratio to be assigned with greater confidence.

Whilst at threshold the formation of S^+ is thought to proceed either via the $\tilde{C}$ or $\tilde{D}$ states of SO_2, at higher energies,[293] the dominant formation pathway at the energies considered in this thesis are thought, at least following photoionisation, to be via a number of states lying between the $\tilde{F}$ state and the double ionisation threshold.[293] As with O^+, it thus seems likely that a number of electronic states will result in the formation of S^+.

Finally, we might expect the central feature to be caused by SO_2^{2+}, as parent ions are expected to gain no kinetic energy. Basner and Schmidt find that they do not observe the presence of SO_2^{2+} below an electron energy of 90 eV.[290] If their conclusion is correct, the central feature cannot be caused by SO_2^{2+}, but must be caused by another process which results in the generation of an ion with almost no kinetic energy.

We also observe the parent ion, SO_2^+, which appears as a well-defined spot on the detector as is expected for a VMI experiment; the scattering distribution has not been included.

Now that we have studied the scattering distributions obtained through electron ionisation of SO_2, we will now use covariance analysis to gain a further insight into

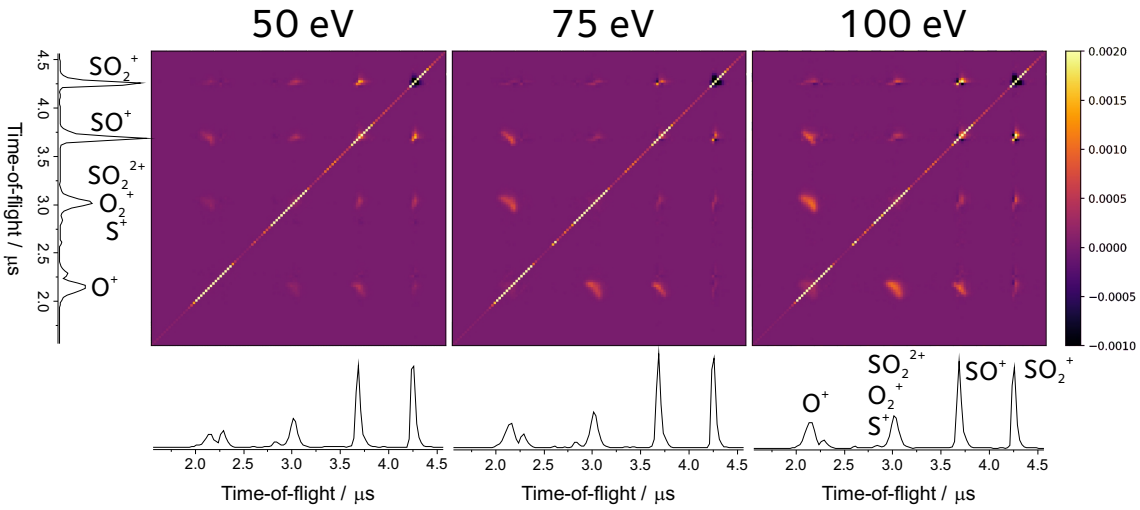


Figure 5.50 TOF-TOF covariance maps of SO_2 recorded at electron energies of 50 eV, 75 eV, and 100 eV. The time-of-flight spectra used for the analysis is shown below the map, with the ions of interest indicated on the 100 eV TOF spectrum. Note that the TOF spectra are not background subtracted, so signal from background ions are also observed in the TOF spectra.

the dissociation dynamics.

5.4.3 Covariance analysis of $SO_2{}^{2+}$

Again, double ionisation plays a significant role in the electron ionisation of SO_2. Figure 5.50 shows the TOF-TOF covariance maps obtained from the PImMS data recorded at three electron energies. We see that, at 50 eV, the main feature in the covariance map is the covariance between SO^+ and O^+, with weaker covariances visible between S^+ and O^+, and between S^+ and O_2^+. Upon moving to higher electron energies, the S^+ and O^+ channel appears to grow significantly stronger, and we also observe the introduction of a new feature between two O^+ fragments. We see no evidence for covariance of the SO^{2+} fragment with any other ion, which suggests that SO^{2+} is almost exclusively formed from the dissociation of SO_2^{2+}, rather than the triply-charged parent. This is consistent with the findings of Fletcher *et al.*, who found that SO_2^{3+} primarily dissociates to form three monocations, and that the partial ionisation cross-section for the formation of SO^{2+} from SO_2^{2+} is approximately two orders of magnitude greater than that for formation from SO_2^{3+}.

Now that we have established the four pathways for which we observe covariance, we will now study each in turn using the recoil-frame covariance technique.

Two-body dissociation

We observe two pairs of two-body dissociation products after electron ionisation of SO_2. The recoil-frame covariance images obtained for the process

$$SO_2^{2+} \rightarrow SO^+ + O^+ \tag{5.20}$$

are shown in figure 5.51. There is little change across the electron energy range considered, although there is evidence of at least two new dissociation pathways growing in at higher electron energies. The major dissociation channel has a kinetic energy release of 5.1 eV, in good agreement with the kinetic energy release of 4.7 eV reported by Masuoka,[297] Curtis and Eland,[209] and Dujardin *et al.*,[151] and 4.8 eV reported by Eland,[155] and Field and Eland.[296] The kinetic energy release of 4.2 eV reported by Fletcher *et al.*[288] is in less good agreement with our results. Dujardin *et al.* also report the presence of a second channel with a kinetic energy release of 7 eV. We also see evidence for this channel, which appears as a shoulder in the 75 eV and 100 eV plots at around 5 eV and 2 eV in the O^+ and SO^+ kinetic energy distributions, respectively.

Based on the appearance potential and the lack of change in kinetic energy distribution with ionisation energy, the main feature with a 5 eV kinetic energy release is known to be produced from one or more low-lying states of $SO_2{}^{2+}$, and results in the formation of SO^+ and O^+ in their ground electronic states, with the SO^+ fragment having little internal excitation.[151,296,297] Dujardin *et al.* also find that the feature with a kinetic energy release of 7 eV has an appearance potential of approximately 41 eV. After accounting for the kinetic energy release, five sets of product states were found to be energetically feasible, with the SO^+ ion carrying any excess energy as internal energy. They also note that, based on their data, the

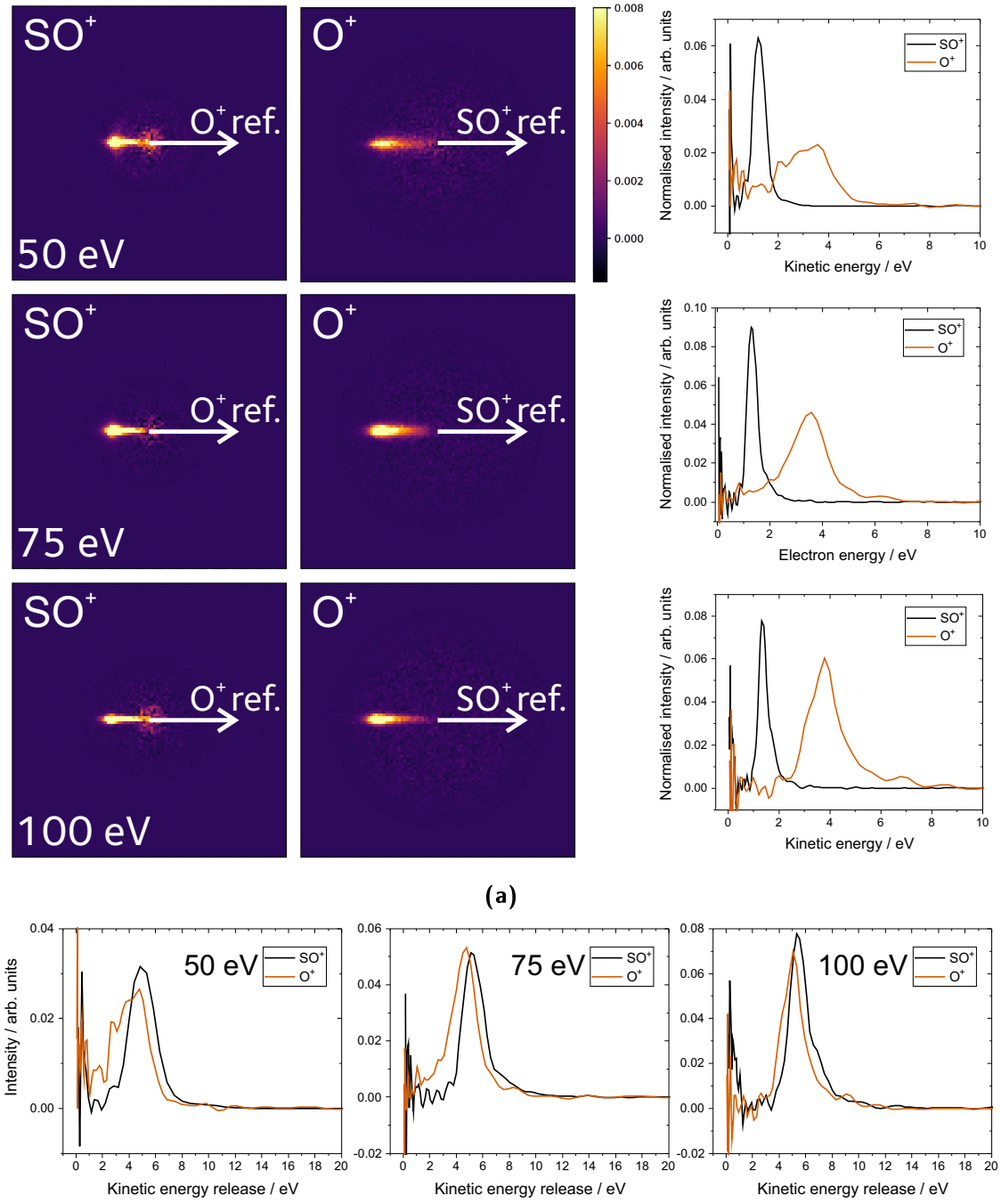


Figure 5.51 Recoil-frame covariance images for the formation of SO^+ and O^+ from SO_2^{2+} at three electron energies, along with the associated kinetic energy distributions (a). The label in the kinetic energy distribution corresponds to the signal ion. (b) shows the kinetic energy release, which has been determined from the kinetic energy distribution of each signal ion independently, based on conservation of momentum.

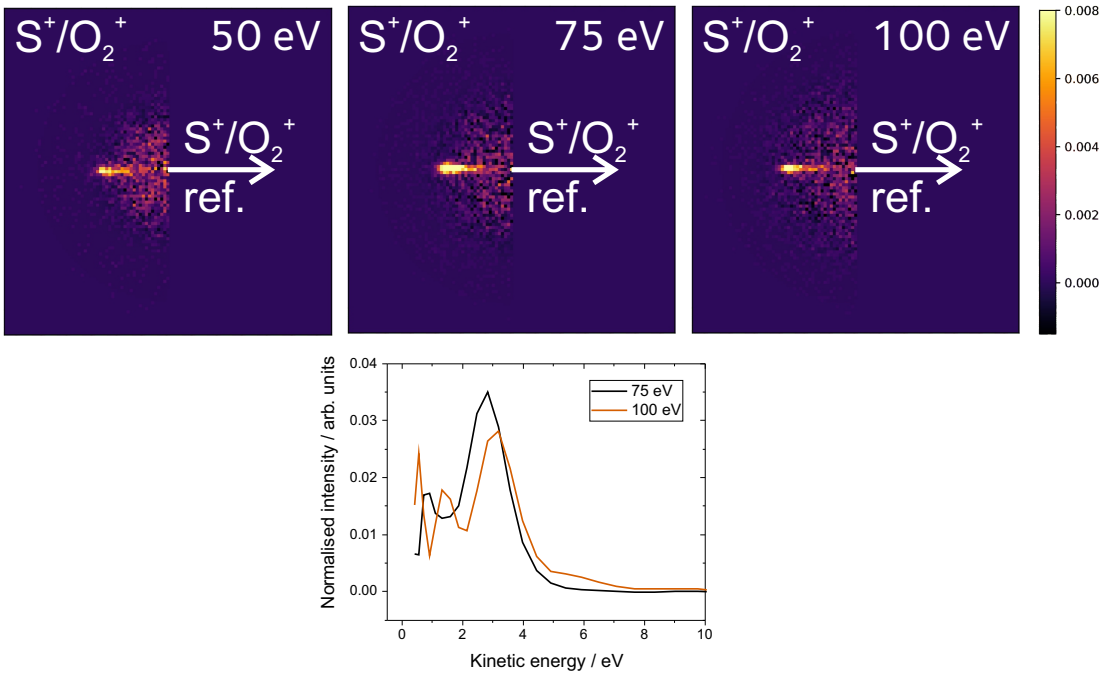


Figure 5.52 Recoil-frame covariance images for the formation of S^+ and O_2^+ from SO_2^{2+} at three electron energies, along with the associated kinetic energy distributions where statistics allow. The label in the kinetic energy distribution corresponds to the signal ion.

dissociation leads to the vast majority of the available energy being transformed to kinetic energy, with the SO^+ carrying very little of the available energy as internal energy. Based on this, the following two sets of electronic states

$$SO_2{}^{2+} \rightarrow SO^+(A^2\Pi) + O^+(^4S_u) \tag{5.21}$$

$$SO_2{}^{2+} \rightarrow SO^+(b^4\Sigma^-) + O^+(^4S_u) \tag{5.22}$$

were deemed to be the most likely final states for this dissociation pathway.[151] According to the correlation diagram of Hochlaf and Eland, there are a large number of electronic states in the energy range from 34 eV to 42 eV,[298] which makes it difficult to determine the exact pathway by which these two dissociation processes proceed.

The second two-body dissociation process we observe is

$$SO_2{}^{2+} \rightarrow S^+ + O_2^+ \tag{5.23}$$

The recoil-frame covariance images for this pathway are shown in figure 5.52. Unfortunately, we had insufficient signal to determine the product kinetic energy distribution for an electron energy of 50 eV, but based on the image we expect to see a similar kinetic energy distribution to that seen at higher electron energies. The kinetic energy release of the main feature appears at around 6 eV, increasing slightly with increasing electron energy. We also see the introduction of a minor dissociation channel with a kinetic energy release of approximately 12 eV in the 100 eV distribution.

Curtis and Eland report a kinetic energy release of 6 eV for this dissociation channel in their photoionisation study carried out at a photon energy of 40.8 eV, in excellent agreement with our data. They attribute this pathway to population of an electronic state of SO_2^{2+} with a lower energy limit of approximately 34.4 eV relative to the ground state of SO_2, based on the energy of the ground states of the products and the kinetic energy of the two fragments.[209] Field and Eland also place an upper limit for the appearance energy of this pathway at 36 eV,[296] which narrows down the potential electronic states from which dissociation may occur. Others had noted the presence of the $SO_2^{2+} \rightarrow S^+ + O_2^+$ channel, but no further determinations of the kinetic energy release of this process were found.

Three-body dissociation

We observe evidence for two different three-body dissociation pathways. Figure 5.53 shows the covariance images we obtain for the pathway

$$SO_2{}^{2+} \rightarrow S^+ + O^+ + O \tag{5.24}$$

There has been a significant amount of discussion on the precise mechanism of this dissociation pathway in the literature.[221,288,297] The final consensus was that the production of S^+ and O^+ proceeds via a non-direct process, in which the parent molecule is first ionised to SO_2^+ in an excited state, resulting in the lengthening of

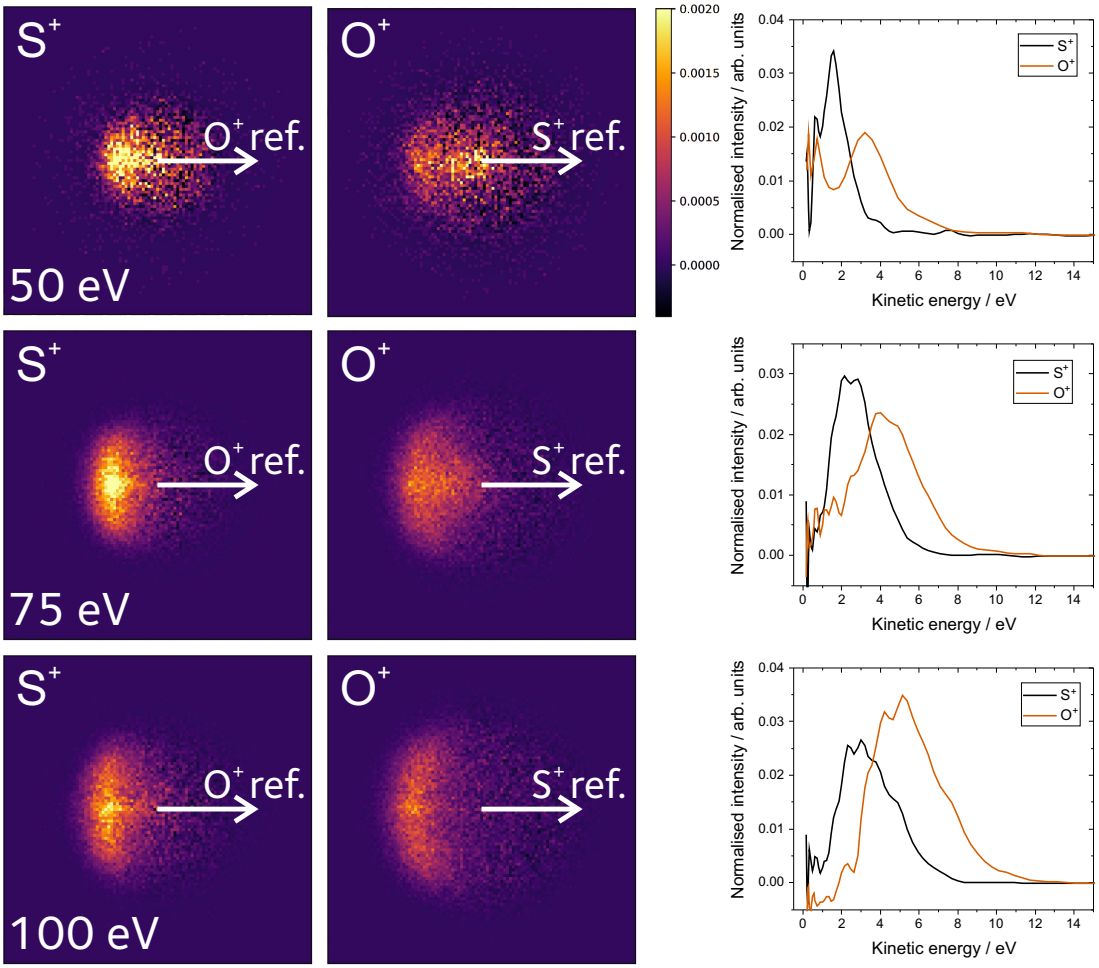


Figure 5.53 Recoil-frame covariance images for the formation of S^+, O^+ and O from SO_2^{2+} at two electron energies, along with the associated kinetic energy distributions. The label in the kinetic energy distribution corresponds to the signal ion.

the bonds. If the ion is produced in a sufficiently excited state, it can then undergo autoionisation. In the case of SO_2, Hsieh and Eland found that the best match was achieved if the charges were localised on the two atoms closest together, i.e. the mechanism proceeds via the formation of a very short-lived SO^{2+} intermediate.[221]

Whilst this mechanism is consistent with our data, it is clear from our covariance images that there is a significant change in the process resulting in the formation of S^+ and O^+ over the electron energy range of 50 eV to 100 eV. The explanation most consistent with our data is that at higher electron energies, the dissociation occurs preferentially from a state (or states) with shorter internuclear distance, and hence a greater Coulomb repulsion between the two ionic fragments at the point of double

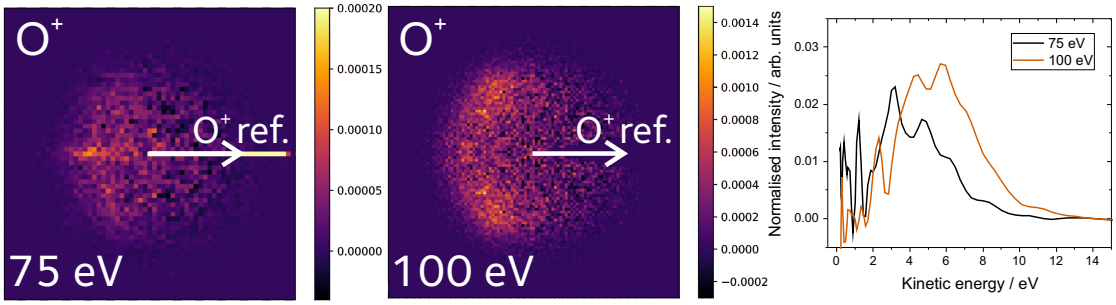


Figure 5.54 Recoil-frame covariance images for the formation of S, O^+ and O^+ from SO_2^{2+} at two electron energies, along with the associated kinetic energy distributions. The label in the kinetic energy distribution corresponds to the signal ion.

ionisation. We reach this conclusion as the kinetic energy of the two covariant ions increases with increasing electron energy, consistent with an increase in the Coulomb repulsion. This could be caused either by accessing a state from which autoionisation occurs on a faster timescale than at lower electron energies, or by being able to directly access a state of SO_2^{2+} which then dissociates via a concerted mechanism. Masuoka has calculated the total kinetic energy of the S^+ and O^+ ions after dissociation from a range of inter-charge distances, and dissociation from a separation equivalent to the bond length of neutral SO_2 results in a total kinetic energy value of approximately 10 eV.[297] At higher electron energies we observe total kinetic energy of the S^+ and O^+ ions which are both smaller and greater than this value, which suggests that both processes are occurring. At 100 eV, the highest total kinetic energy of the S^+ and O^+ ion we observe is at around 18 eV, which could potentially be produced by the dissociation of SO_2^{3+}.

The final covariant dissociation pathway we observe is

$$SO^{2+} \rightarrow S + 2O^+ \tag{5.25}$$

The covariance images for this pathway are shown in figure 5.54. It is also possible

that the dissociation leading to the observed products proceeds via the pathways

$$SO_2{}^{3+} \rightarrow S^+ + 2O^+ \tag{5.26}$$

$$SO_2{}^{3+} \rightarrow S^{2+} + O^+ + O \tag{5.27}$$

although these are presumed to make a smaller contribution due to the fact that the triple ionisation cross-sections are generally significantly lower than the double ionisation cross-sections.

The signal level at 75 eV is rather low, which suggests that the the electronic state(s) from which dissociation via pathway 5.25 are only populated to a small degree at this electron energy. The gradient of the corresponding feature in the TOF-TOF covariance map is -1, which rules out an initial charge separation process, leaving only a deferred charge separation or a concerted pathway as potential dissociation pathways. The main feature observed appears to lie in an opposite direction to the reference direction, which would be most consistent with the SO_2^{2+} molecule being produced in a linear electronic state, followed by a concerted dissociation where the S atom gains almost no kinetic energy. At an electron energy of 100 eV, the signal level is significantly higher, as can clearly be seen from the covariance image, and the dissociation pathway appears to have changed significantly from that observed at 75 eV. The covariance image now shows an arc-like feature, extending from an angle of approximately 120° to 240° with respect to the reference direction. Given that the gradient of the TOF-TOF covariance map is still approximately -1, and the recoil-frame covariance map is not at all consistent with the simulation for a deferred charge separation process, this dissociation pathway is attributed to the concerted dissociation of SO_2^{2+} from approximately the same geometry as the neutral SO_2. The angle at which the two O^+ are produced is also consistent with the bond angle of the neutral molecule, although this would require the neutral S to carry away sufficient energy to conserve momentum. It may also be the case that this dissociation is primarily proceeding via pathway 5.26, i.e. via

a Coulomb explosion. Based on both O^+ ions being produced with a kinetic energy of 6 eV (the maximum of the kinetic energy distribution) at an angle of 120° to one another, the S atom (or ion) would be expected to have a kinetic energy of 1.5 eV by conservation of momentum.

One potential method to determine the mechanism would be to use three-fold covariance to determine whether all three ions are produced simultaneously. It may also be possible to determine the approximate weightings of the two pathways, 5.25 and 5.26, based on the relative intensities of the two-fold and three-fold covariance images, and an estimate of the detection efficiency of the experiment. We are not yet in a position to run this analysis, but after we have successfully implemented three-fold covariance analysis software, we will be able to run simulations to determine how the intensity of two-fold and three-fold covariance images are related at different detection efficiencies.

No other data on the kinetic energy release of this channel was found in the literature, although a number of authors have noted its presence. Further work will be required to determine the exact mechanism by which this dissociation proceeds.

5.4.4 Summary

We have reported partial ionisation cross-sections, scattering distributions, and recoil-frame covariance images for sulphur dioxide. We have discussed the scattering distributions in the context of the literature, and have used covariance analysis techniques to obtain new insight into the dissociation of multiply-charged parent ions.

5.5 Deuterated benzene (C_6D_6)

Benzene is a well-known molecule, being routinely used to introduce the concept of aromaticity. Due to its highly symmetrical nature, and its importance as a model polycyclic aromatic hydrocarbon (PAH), benzene is an attractive molecule for study;

numerous studies on benzene have already been carried out. Benzene was previously used extensively as a solvent, but is now known to be a carcinogen[299] so finds less use in this role. It currently finds use as a chemical feedstock for producing a number of other useful products, including styrene, phenol, nylon, and aniline.[300] Benzene can be used as a model for PAHs, being a central building block for these molecules.[301] It has been suggested that as much as 30 % of the galactic interstellar carbon is in the form of PAHs,[301,302] and PAHs have been identified as potential sources of both the unidentified infrared emission bands, and diffuse interstellar bands (see [303–305], for example). Thus, it is important to understand the chemistry of the benzene molecule, both to give an insight into how PAHs may interact with electrons, and also into the formation processes of the PAHs.

In the present study, scattering distributions for the products of electron ionisation were recorded at an electron energy of 100 eV and 75 eV, using an extractor potential of 2.000 kV, a repeller potential of 1.611 kV and an electron beam pulse duration of 850 ns, and 900 ns for electron energies of 100 eV and 75 eV, respectively (with the timing of the ion optics pulse adjusted accordingly). A total of 850,000 and 4,360,000, acquisition cycles were recorded at electron energies of 100 eV and 75 eV, respectively, together with an equal number of acquisition cycles of background data. Signal and background acquisitions were alternated every 50,000 acquisition cycles to reduce the effect of any experimental drift on the background subtraction. The molecular beam was prepared by bubbling 1.2 bar helium through a sample of deuterated benzene, before the benzene-seeded helium was expanded through the solenoid valve. It has previously been shown that the dynamics of benzene and deuterated benzene are equivalent,[306] so we have opted for the deuterated molecule, as this allows us to more readily resolve the different mass peaks. Despite the improvement in mass resolution, there is still some overlap between peaks, particularly for heavier ions. The terms deuterated benzene and benzene are used interchangeably in the text.

Mass spectra were also recorded by using a photomultiplier tube (PMT) to measure the total signal from the phosphor screen at electron energies ranging from 60 eV to 100 eV in 5 eV steps, using an extractor potential of 1.74 kV and a repeller potential of 2.00 kV. Data acquisition was carried out by alternating between recording 500 acquisition cycles of signal and background, for a total of 7,500 acquisition cycles of signal, and the background signal subtracted from the signal to give the final mass spectrum.

We will first present the partial ionisation cross-sections of C_6D_6. We will then discuss the dissociation of singly-charged benzene using the obtained scattering distributions, followed by the dissociation of doubly-charged benzene using covariance analysis, both in the context of the available literature.

5.5.1 Partial ionisation cross-sections

Figure 5.55 shows the partial ionisation cross-sections obtained for deuterated benzene from an electron energy of 70 to 100 eV, obtained by fitting the recorded PMT trace with a number of Gaussians convoluted with an exponential decay as discussed previously. The fit of the mass spectrum recorded at an electron energy of 100 eV, and the associated deconvoluted mass spectrum, is shown in figure 5.56. We can see that the majority of peaks are very closely spaced, which makes the fitting much more difficult to achieve, leading to an increase in the uncertainty of the cross-sections. The partial ionisation cross-sections in figure 5.55 have been smoothed by a three-point moving average (i.e. for 95 eV, the mean of the partial ionisation cross-sections obtained at 90, 95, and 100 eV is used), to smooth the noise in the determined cross-sections. To improve the resolution, experiments could be carried out using a longer flight tube to aid the mass separation, or could use a faster phosphor, reducing the length of the decay and making the peaks easier to resolve.

We find that the parent ion is the most abundant ion, indicating that the ben-

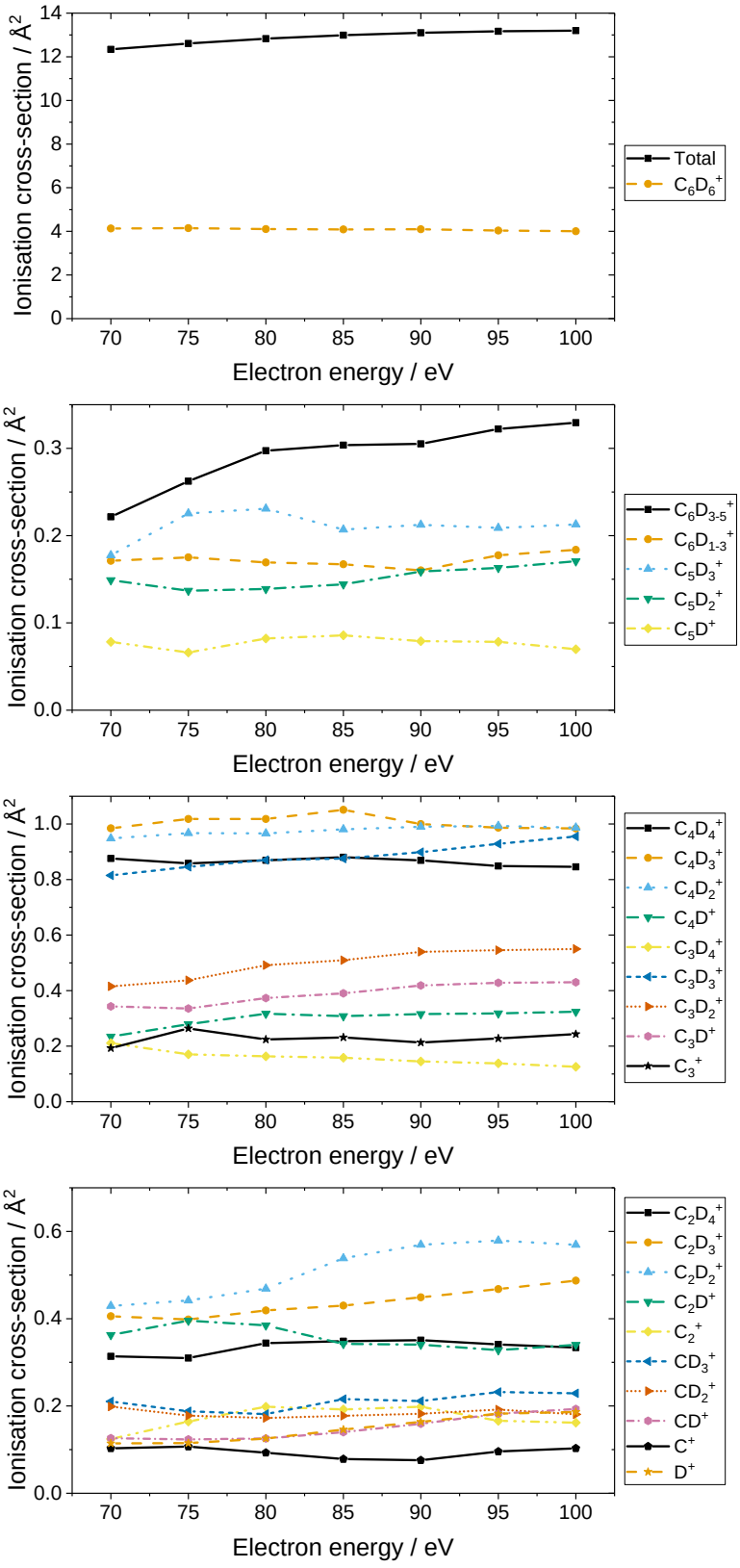


Figure 5.55 Partial ionisation cross-sections for electron ionisation of deuterated benzene. The partial ionisation cross-sections have been smoothed using a three-point moving average, and normalised to the total ionisation cross-section obtained by Zhou.[307]

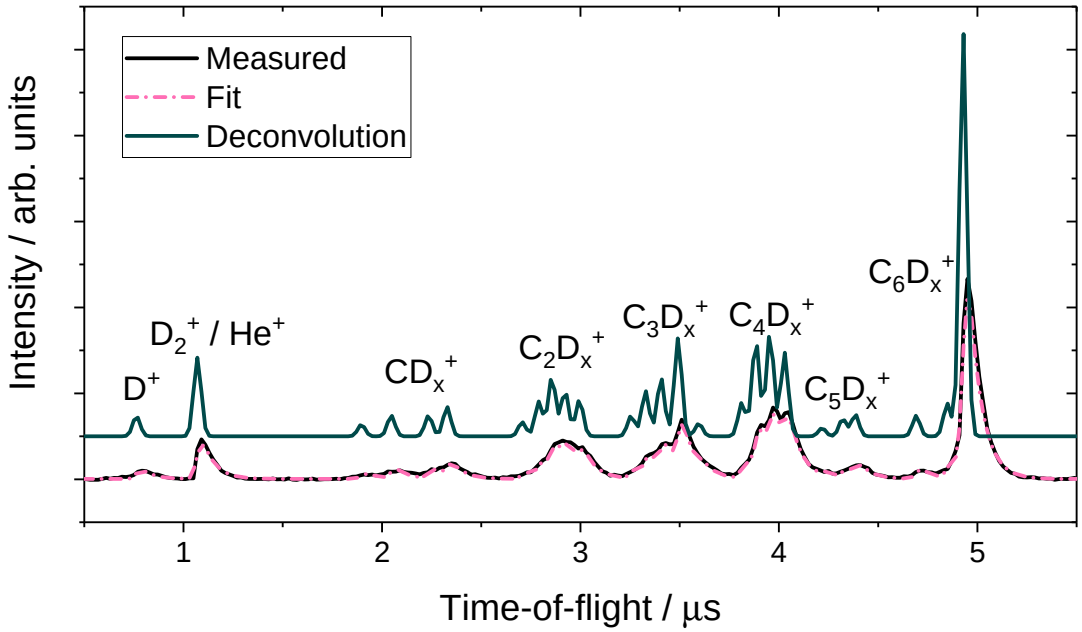


Figure 5.56 The fit achieved by fitting a number of Gaussians convoluted with an exponential decay for the PMT trace obtained following electron ionisation at an electron energy of 100 eV. The deconvoluted spectrum has been offset for clarity.

zene cation is relatively stable. The next most dominant set of ions are $C_4D_x{}^+$, where $x = 2 - 4$, suggesting acetylene loss, accompanied by neutral D loss, plays an important role in the dissociation of benzene. $C_3D_3{}^+$ also makes a major contribution. The partial ionisation cross-sections generally show little change across the electron energy range considered here.

We were unable to find any previous determination of the partial electron ionisation cross-sections of benzene for all ions for comparison. Fucaloro and Srivastava have previously reported the relative abundances of the ions of benzene following electron ionisation at electron energies of 20 eV, 40 eV, 75 eV, and 100 eV. They found $C_6H_5{}^+$ and $C_6H_6{}^+$ to be the dominant ions produced, followed by $C_4H_x{}^+$, where $x = 2 - 4$, and $C_3H_3{}^+$, as found in the current work. However, they do not provide abundances for all ions, and were unable to accurately determine the abundance of some of the lower-intensity ion signals.[308] Holland *et al.* have previously reported partial ionisation cross-sections for photoionisation.[309]

Now that we have established which fragments can be produced, and their relat-

ive intensities, we will now study the scattering distributions we measure using the electron-molecule crossed beam experiment.

5.5.2 Scattering distributions resulting from electron ionisation of C_6D_6

Benzene is the largest molecule studied in this thesis, and shows numerous possible fragmentation channels. We are unable to carry out as extensive an analysis of each fragment as we have for the previous molecules, but will discuss the overarching features and potential dissociation pathways in reference to the literature. We will also only focus on the data recorded at 100 eV; the equivalent data recorded at 75 eV can be found in appendix C.

Figure 5.57 shows the scattering distributions obtained for all fragment ions detected following electron ionisation at 100 eV. In general, we see a strong central feature, usually with one or more shoulders, and some contribution from the dissociation of $C_6D_6{}^{2+}$. Dissociation of $C_6D_6{}^{+}$ is dominated by statistical dissociation, i.e. the molecule has time for energy to be distributed between the various available modes before dissociation can occur. Due to isotopic labelling experiments, it is known that the molecular framework undergoes significant rearrangement prior to dissociation, with near or complete randomisation of the D atoms, and frequently the carbon framework as well.[306,310] It has also previously been shown that benzene and a number of linear isomers show remarkable similarity in their mass spectra, suggesting that the isomers dissociate via one or more common intermediates.[311] The kinetic energy of the fragment ion also shows a general increase with increasing loss of deuterium, presumably due to the loss of neutral D imparting extra kinetic energy on the fragment ion.

Jennings has previously used a double-focusing mass spectrometer to study the metastable decay of benzene, from which a metastable decay map is obtained. He observed that metastable decay provides a formation pathway for a number of the

Figure 5.57 Scattering distributions for all fragments of deuterated benzene recorded at an electron energy of 100 eV. The left column shows the symmetrised image, the central column the inverted image, and the right column the kinetic energy release. D^+ and $CD_x{}^+$.

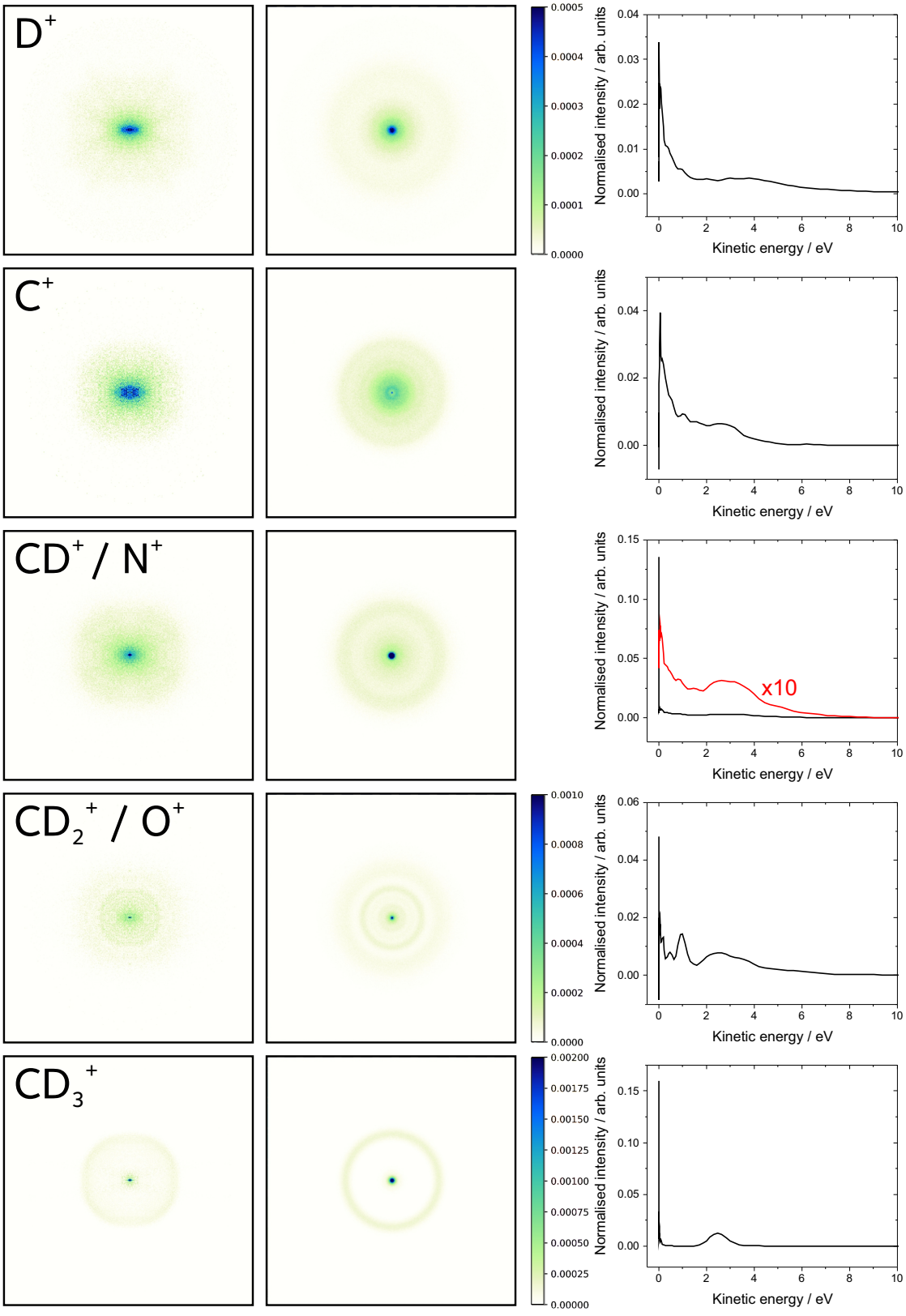


Figure 5.57 (continued) $C_2D_x{}^+$

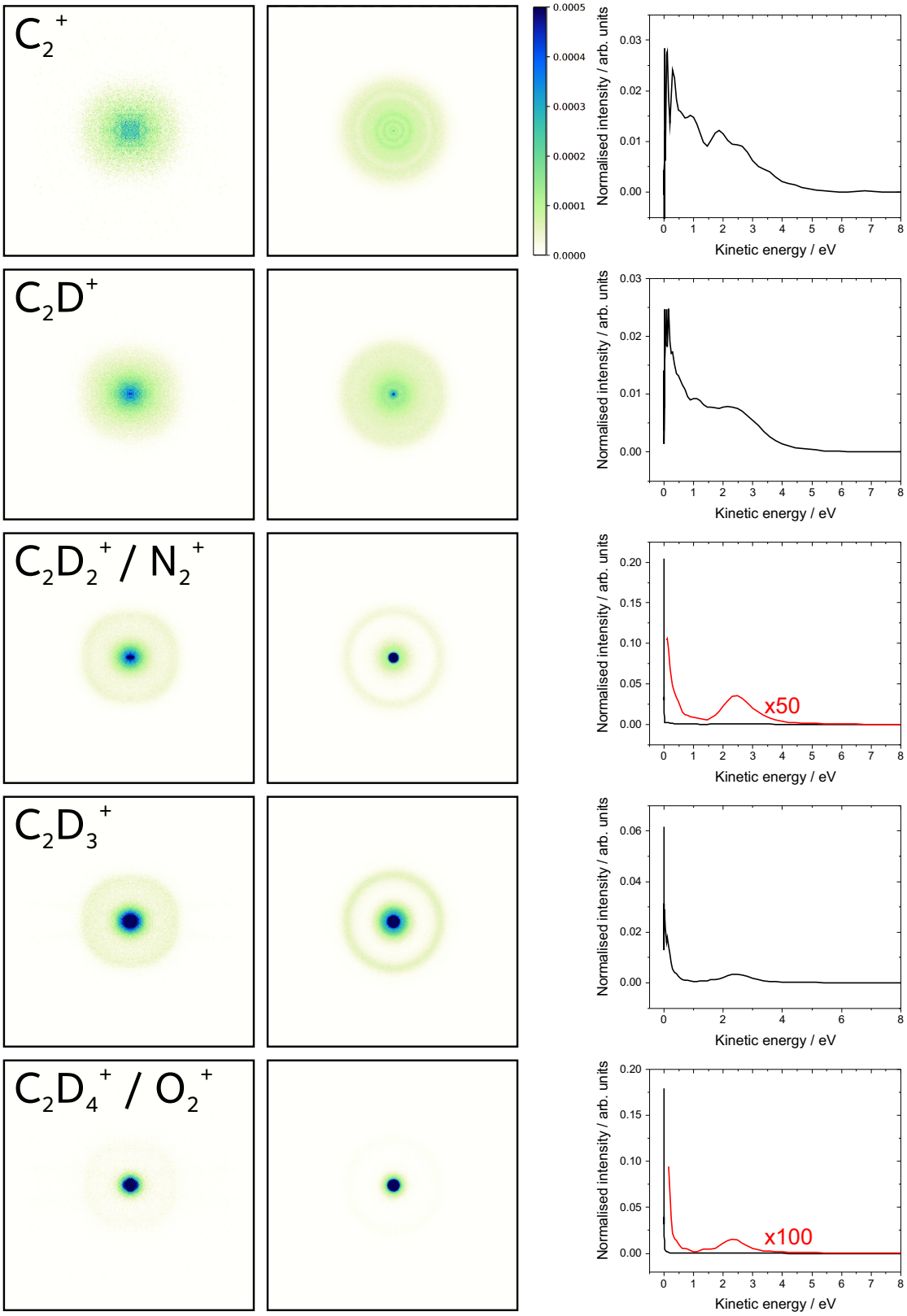


Figure 5.57 (continued) $C_3D_x^+$

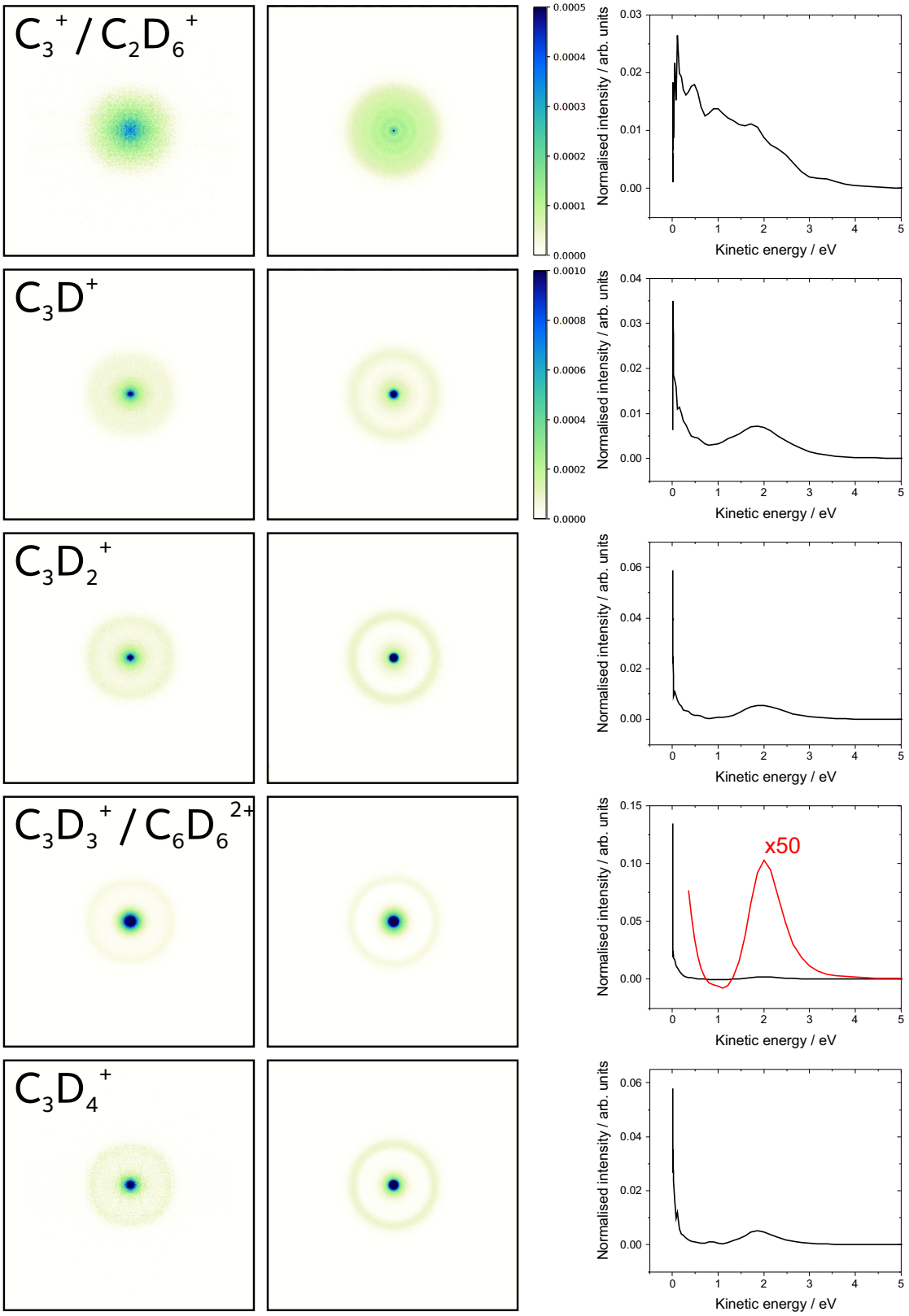


Figure 5.57 (continued) $C_4D_x{}^+$

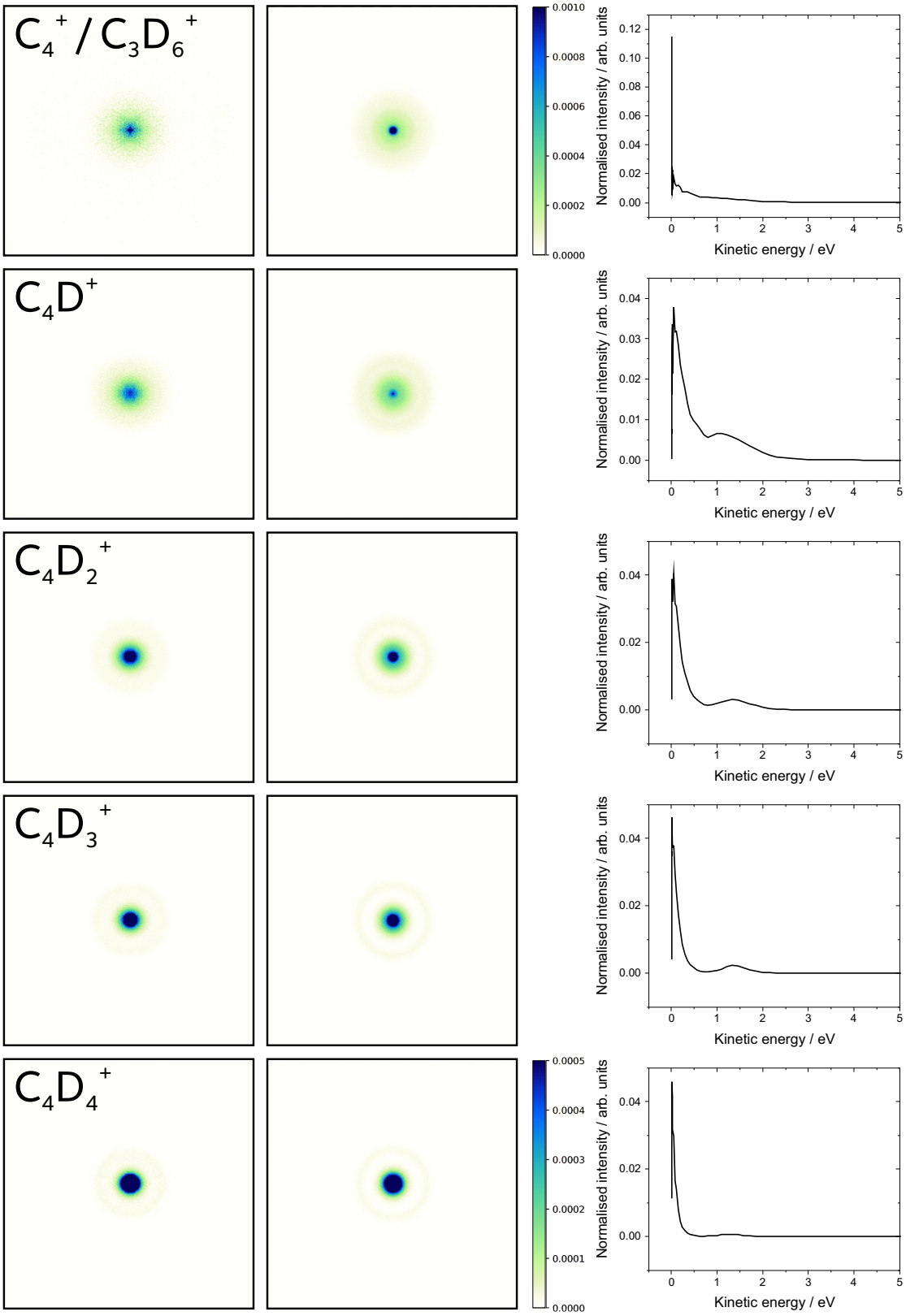
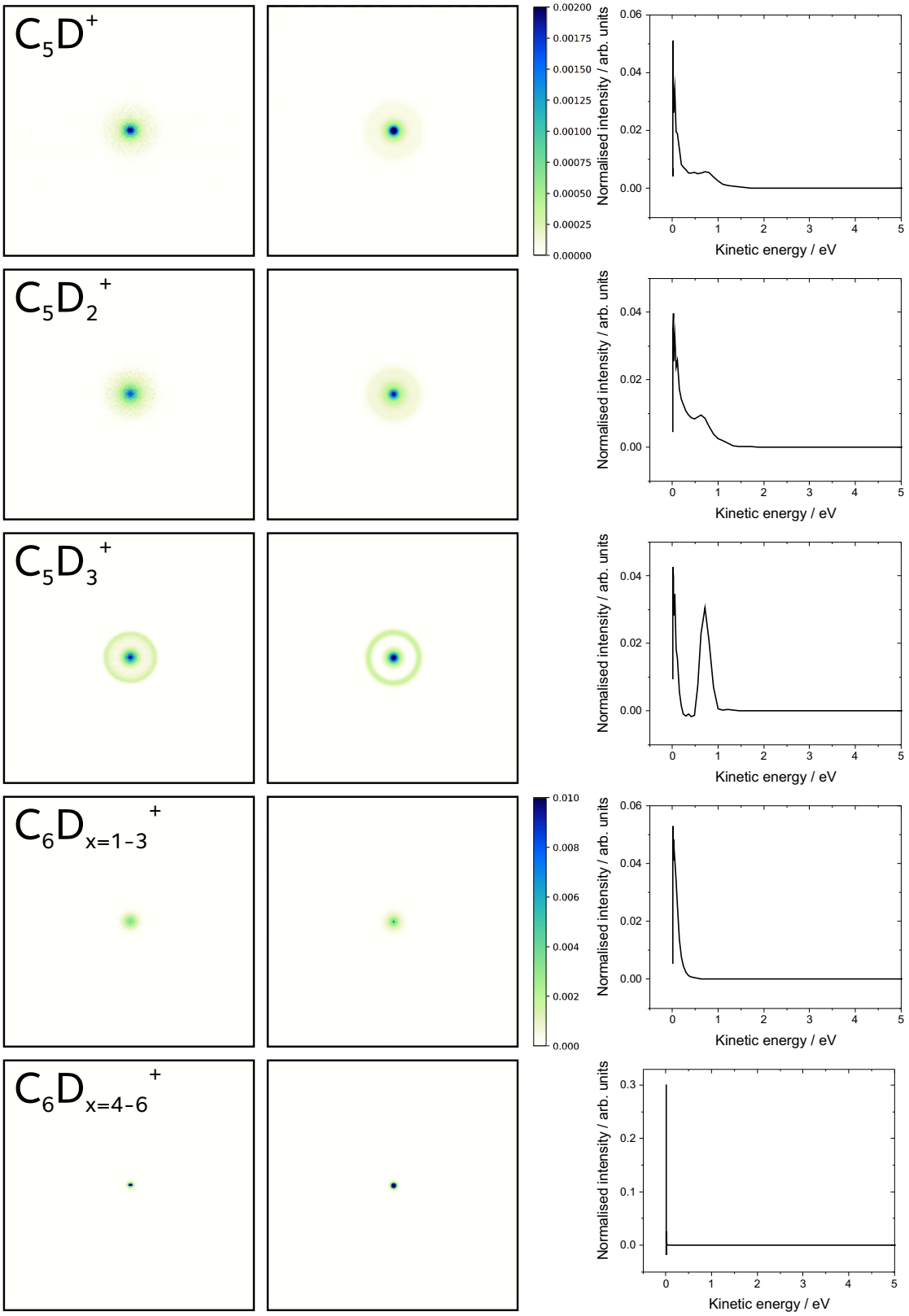


Figure 5.57 (continued) $C_5D_x^+$ / $C_6D_x^+$



ions detected in the current work, and we also see that metastable decay is dominated by the loss of either H, H_2, C_2H_2, or C_3H_3, and to some extent CH_3. We observe all of the ions seen by Jennings, as well as a number of other ions not included in his metastable decay map. We attempted to fit Gaussians to our data to identify different dissociation pathways in our data, but the results of this analysis were inconclusive. This may be due to the existence of multiple possible formation pathways with similar kinetic energy distributions, making the identification of distinct pathways difficult, or the broadening from D loss having only a small effect on the kinetic energy distribution.

$C_6D_x{}^+$ ions are formed from the loss of either D (for $C_6D_5{}^+$), D_2 ($C_6D_4{}^+$), or a mixture of the two (for $x < 4$).[308,309] The loss of an increasing number of deuterium atoms increases the kinetic energy of the larger ionic fragment. $C_5D_3{}^+$ ions can be formed via loss of CD_3,[308] with $C_5D_2{}^+$ and C_5D^+ being formed either by subsequent loss of D or D_2, or by loss of CD_4.[308,309]

The $C_4D_4{}^+$ ion is known to be formed by the loss of neutral acetylene.[308,309] Holland *et al.* identify four possible structures for the cation, namely the methylene cyclopropene, cyclobutadiene, 1,2,3-butatriene, and 1-buten-3-yne cations.[309] Theoretical studies have calculated the barriers for formation of each of the isomers.[312] Only the methylene cyclopropene cation, which has the lowest barrier to formation, and the 1-buten-3-yne cation have been detected. Van der Hart found that the three other isomers, other than methylene cyclopropene, had similar barriers to formation, so attributed the latter to a much more direct formation pathway.[312] Holland *et al.* found that the most consistent product with the appearance potential of the $C_4D_4{}^+$ to be the formation of 1-buten-3-yne. The $C_4D_3{}^+$ ion is thought to be produced either by loss of a further D, or by loss of C_2D and D_2,[308,309] and possibly also by loss of C_2D_3.[308] The $C_4D_2{}^+$ ion is most likely formed either by neutral acetylene loss, followed by D_2 loss, or by neutral ethene loss.[308,309] The cation is assumed to take the 1,3-butadiyne structure.[309] The C_4D^+ ion can be formed with a variety of

neutral co-fragments, but the cation is thought to take a linear structure similar to that observed for $C_4D_2{}^+$.

$C_3D_3{}^+$ ions are found to be formed primarily from the loss of neutral C_3D_3.[308,309] Holland *et al.* only find one channel lying below the appearance potential for the $C_3D_3{}^+$ ion, from the formation of the cyclopropenyl cation and propargyl neutral radical.[309] According to the ab initio calculations of van der Hart, these products can be produced following isomerisation of the benzene cation to the fulvene structure (a five-membered ring double-bonded to a sixth carbon), followed by ring opening and ring closing to the allyl-cyclopropene cation, followed by loss of neutral C_3D_3.[313] $C_3D_2{}^+$ and C_3D^+ are both thought to be formed via sequential decomposition. Holland *et al.* suggest that the neutral co-fragments could also consist of various combinations of C_2D_2, C_2D_3, C, CD, and D.[309]

$C_2D_x{}^+$ ions can be formed with a significant number of possible co-fragments. This can be narrowed down to some extent based on the appearance energies of the ions, but it is still expected that numerous formation pathways contribute to the formation of $C_2D_x{}^+$ ions. Holland *et al.* provide thermochemical thresholds for formation with a number of neutral co-fragments.[309] $CD_3{}^+$ has been found to primarily be formed from $C_6D_6{}^{2+}$.[309] In figure 5.57, we see that there is a central feature in the scattering distribution which cannot come from dissociation of the doubly-charged ion however. There are two possible sources for this feature: either there is a channel forming $CD_3{}^+$ not discussed by Holland *et al.*, or our background subtraction of H_2O is not perfect. For the formation of D^+, there are any number of potential partner fragments from which the ion could be produced, and thus we see formation of D^+ with a wide range of kinetic energies.

Given we are unable to observe the neutral fragments, and cannot at present run experiments near threshold, we are unable to add significantly to the details of the fragmentation process, other than confirming that the benzene molecule undergoes significant rearrangement before dissociation, which occurs in a statistical manner.

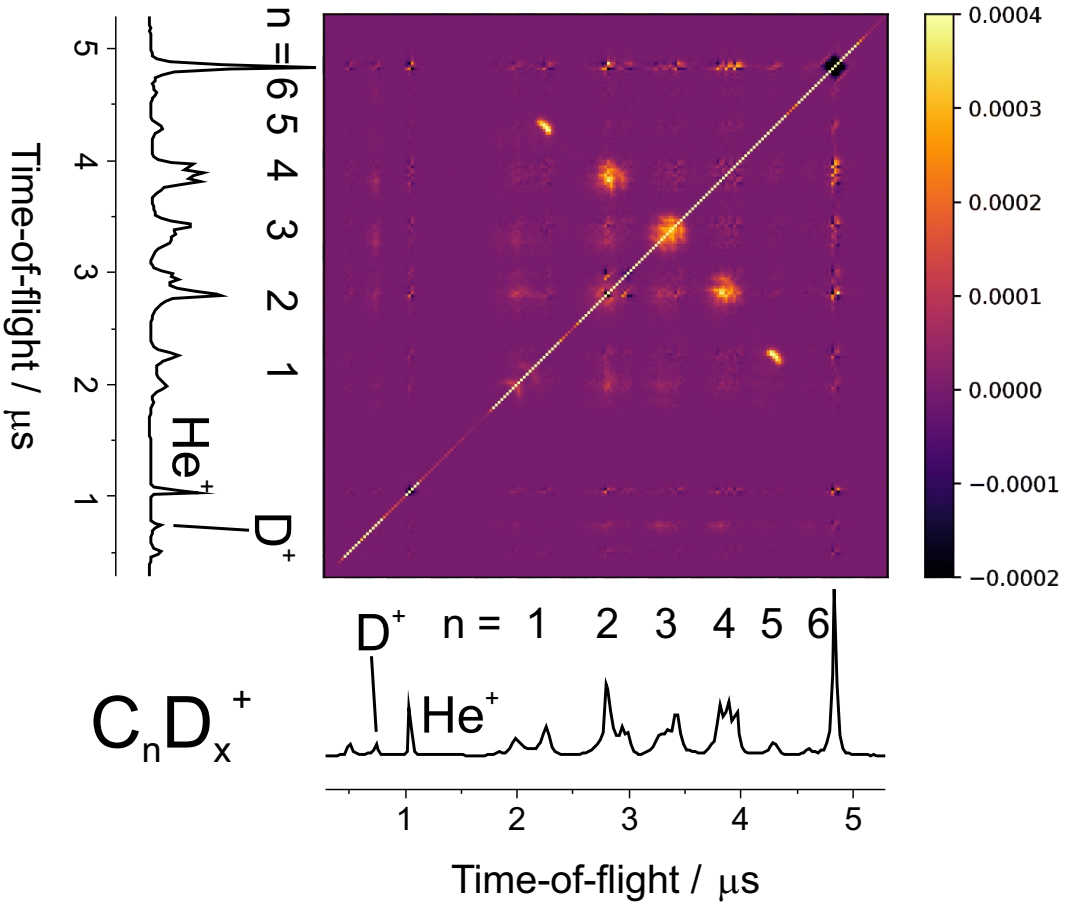


Figure 5.58 TOF-TOF covariance map of C_6D_6 recorded at an electron energy of 100 eV. The time-of-flight spectra used for the analysis is shown below the map, with the ions of interest indicated on the 100 eV TOF spectrum. Note that the TOF spectra are not background subtracted, so signal from background ions are also observed in the TOF spectra.

We also see a broadening of the kinetic energy distribution with increased neutral loss. We have also seen significant contribution from the dissociation of doubly-charged benzene, which we will now discuss.

5.5.3 Dissociation of $C_6D_6{}^{2+}$

With an appearance potential of 24.65 eV,[314] $C_6D_6{}^{2+}$ is accessible at all electron energies considered in this thesis. Unlike the triatomic molecules considered previously, there are a myriad of potential ion pairs that could be formed, and there exists the possibility that the parent ion can dissociate into more than three fragments.

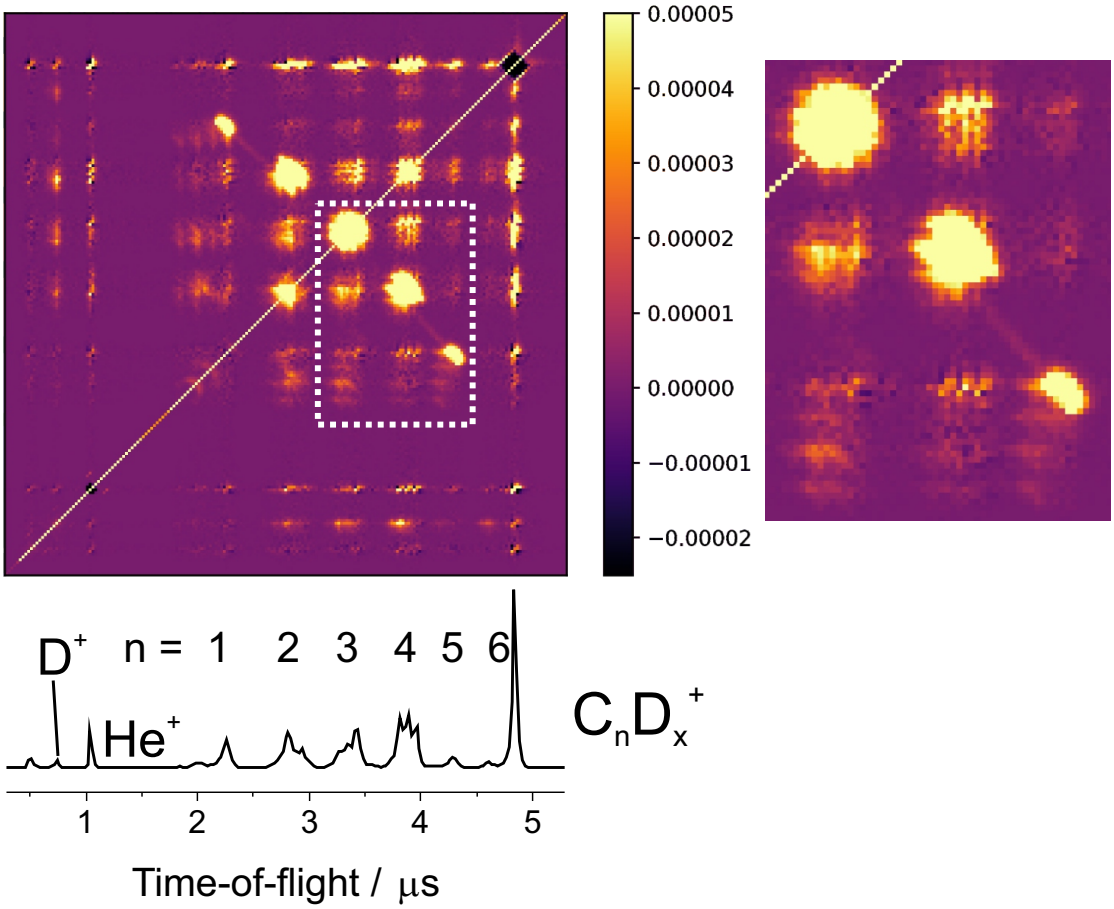


Figure 5.59 TOF-TOF covariance map of C_6D_6 recorded at an electron energy of 75 eV. The area bounded by a white dotted line has been magnified on the right. A metastable decay feature observed due to delayed decay of $C_6D_6{}^{2+}$ into $C_5D_3{}^+$ and $CD_3{}^+$ is seen extending diagonally from the $C_5D_3{}^+/CD_3{}^+$ covariance signal (the bottom-right saturated feature in the magnified region).

Figure 5.58 shows the TOF-TOF covariance map we obtain following electron ionisation at 100 eV. We see that the dominant features are those which correspond to a two-body decay of the carbon framework, either with or without the loss of one or more neutral D fragments. We also see two features corresponding to m/z ratios of 14 and 16, which we attribute to a contamination of N_2 and O_2, as will be discussed in the context of the recoil-frame covariance image below. Other features are relatively weak, but we do see covariance between $C_2D_x{}^+$ and itself, between $CD_x{}^+$ and both $C_2D_x{}^+$ and $C_3D_x{}^+$, and between C_2D_x+ and $C_3D_x{}^+$.

We also see evidence of metastable decay in the TOF-TOF covariance, i.e. where

the doubly-charged parent ion dissociates outside of the velocity-mapping region after it has started accelerating towards the detector. If the resulting ion is still within the extraction field, the signal is observed as a tail extending from the position of the ion pair to the point on the diagonal corresponding to the doubly-charged parent ion. If the ion has reached the field-free region before dissociation, the time-of-flight is dictated by the mass of the doubly-charged parent, and thus will be observed as two diagonal features,[315] which would appear as an 'X-shaped' feature in our TOF-TOF covariance map. In the work of Field and Eland, it would instead appear as a 'V-shaped' feature; due to their experiment being run under coincidence conditions, the arrival time of the first ion, t_1, must always be earlier than the arrival time of the second ion, t_2, so their coincidence plot is only defined where $t_1 < t_2$. Figure 5.59 shows the TOF-TOF covariance map recorded at 75 eV, with a the section bounded by the white dotted line shown magnified on the right. We see a clear feature extending from the covariance feature CD_3^+ and $C_5D_3^+$ towards the location of $C_6D_6^{2+}$ on the self-covariance diagonal, consistent with dissociation of $C_6D_6^{2+}$ whilst still in the extraction field. The same feature is observed in the 100 eV TOF-TOF covariance map, but is seen more clearly in the 75 eV covariance map. Metastable decay has previously been observed for this channel (see [316, 317], for example), with Richardson *et al.* suggesting that there are a range of lifetimes for the precursor state, corresponding to a range of internal energy states.[316]

Turning to the recoil-frame covariance analysis, we find that we observe covariance between a large number of fragments, as shown in figure 5.60. It is impractical to show the covariance map between each pair of fragments individually, and we have instead grouped the ions by number of carbons, i.e. we would use CD_x^+ to represent C^+, CD^+, CD_2^+, and CD_3^+. This also eliminates the problem of closely-spaced ion arrival times, which can lead to signal from neighbouring fragments contaminating each other.

Richardson *et al.* report that they observe weak covariance between H^+ and

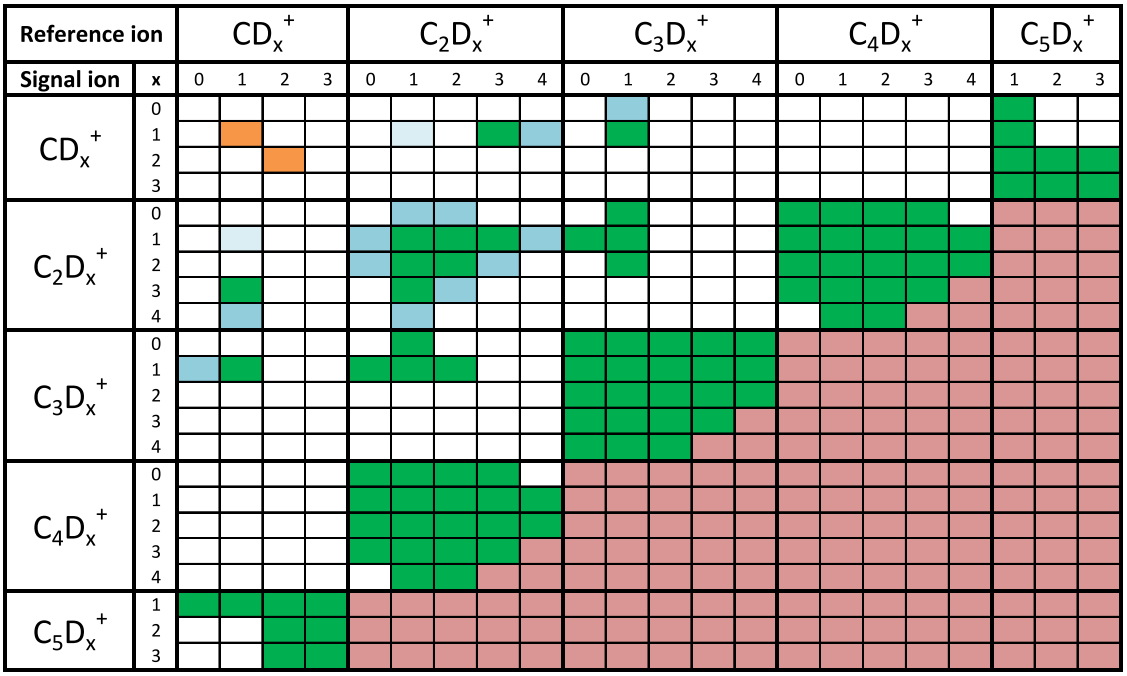


Figure 5.60 A plot of all fragments between which covariance is observed for benzene at 100 eV. Cells highlighted green show covariance, cells highlighted blue show weak covariance, cells highlighted orange are thought to be due to contaminants, as discussed below, and cells highlighted red are impossible to form based on dissociation of the parent ion.

either $C_6H_x{}^+$, $C_4H_x{}^+$, or $C_3H_x{}^+$,[316] but we do not see any covariance between D^+ and the other fragments. This could either be because the signal is too weak, and thus we have insufficient statistics to observe it, or because the D^+ ion is significantly lighter than the other fragments, so does not appear in a well-defined location with respect to the partner ion.

Two-body dissociation

As noted previously, it is clear that the vast majority of dissociation of $C_6D_6{}^{2+}$ occurs via two-body dissociation. Figure 5.61 shows the combined recoil-frame covariance images for the pairs $C_5D_x{}^+$ and $CD_x{}^+$, $C_4D_x{}^+$ and $C_2D_x{}^+$, and $C_3D_x{}^+$ and $C_3D_x{}^+$. The kinetic energy of each ion has also been determined by inverting the covariance image, and the modal kinetic energy release determined from the peak positions. For $CD_x{}^+$ and $C_5D_x{}^+$, we obtain a kinetic energy release for the

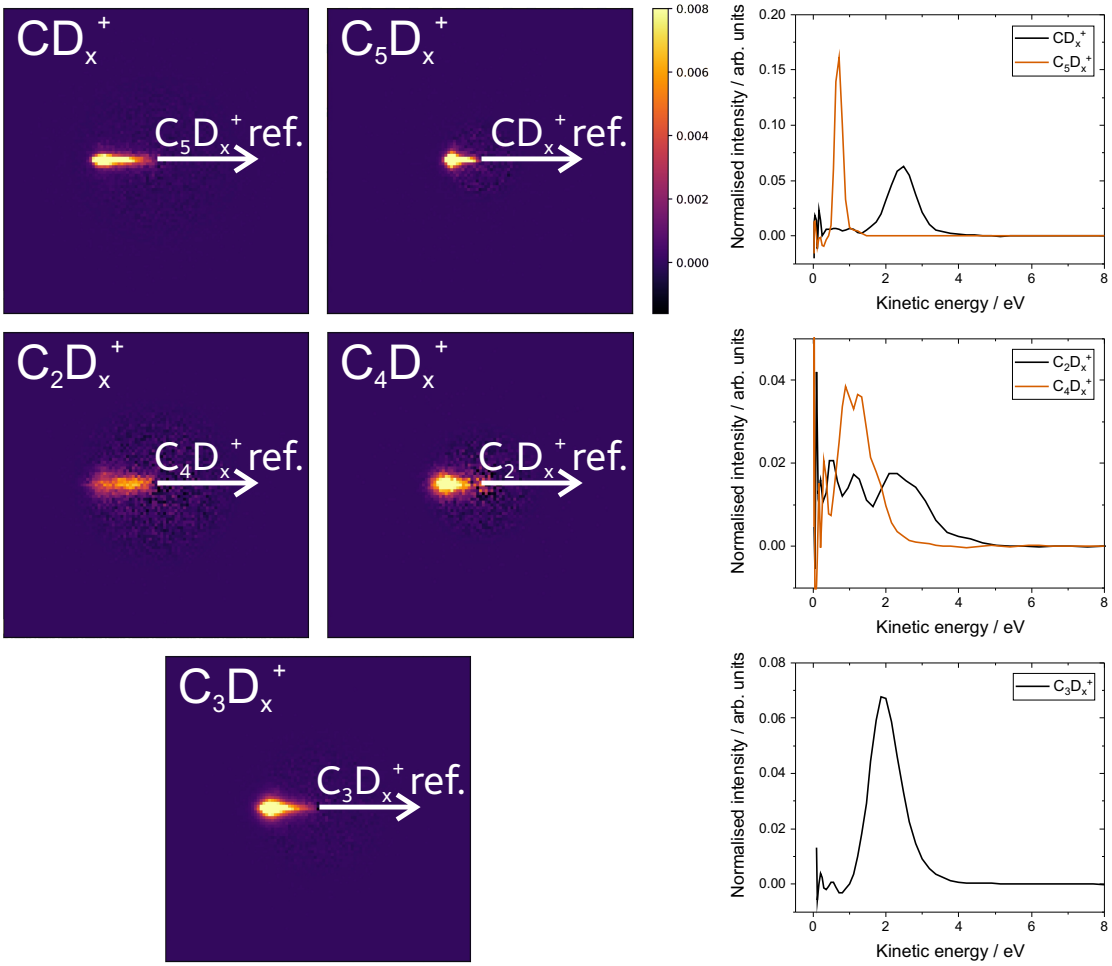


Figure 5.61 Recoil-frame covariance maps for two-body dissociation of benzene at an electron energy of 100 eV, along with the corresponding kinetic energy distribution of each fragment in the covariance image (the signal ion is labelled in the kinetic energy distribution plot).

two ions of 3.2 eV, in good agreement with previous values of 3.0 eV,[316] 3.1 eV (with $x = 3$),[309] and 2.9 eV (also with $x = 3$),[317] for $C_2D_x{}^+$ and $C_4D_x{}^+$, we obtain a kinetic energy release for the two ions of approximately 3.5 eV, in good agreement with the literature values of 3.8 eV[316] and 3.2 eV and 3.5 eV (for formation of $C_4H_4{}^+$ and $C_2H_2{}^+$),[317] and for $C_3D_x{}^+$ and $C_3D_x{}^+$, we obtain a kinetic energy release for the two ions of 3.9 eV, also in good agreement with the literature value of 4.2 eV.[316] In agreement with Richardson *et al.*, we do not see any appreciable change in the kinetic energy release on the loss of extra D atoms.[316]

It seems likely that the molecule undergoes significant rearrangement before

dissociation, as was the case for the dissociation of $C_6D_6{}^+$, with the formation of the $CD_3{}^+$ fragment requiring at least two deuterium atoms to migrate; Richardson *et al.* suggest a substantial rearrangement prior to the formation of $CH_3{}^+$ and $C_5H_3{}^+$, but suggest distorted cyclic precursors could be valid precursors for formation of the other two pairs of ions.[316] Alagia *et al.* have also calculated the energetics of a number of possible C_4H_4 and C_4H_3 structures,[317] the majority of which require significant rearrangement to form. Anand *et al.* have carried out a detailed study of the three major dissociation channels, also finding significant rearrangement was required to form the reaction products.[318]

Whilst deuterium has a mass significantly smaller than the fragments, we would expect that loss of deuterium will have a small but noticeable effect on the covariance image, 'blurring' the covariance signal from the axis opposite to the reference ion, with the effect increasing with loss of an increasing number of D atoms. This is indeed the case; figure 5.62 shows the recoil-frame covariance maps for each of the $C_3D_x{}^+$ ion pairs. We see increased blurring as the number of deuterium atoms shared between the covariant ions decreases. We can conclude that the dissociation involves a charge separation process and loss of neutral deuterium, but we cannot determine the ordering of the steps; unfortunately, the change in momentum of the ionic species following D loss is insufficient to allow us to obtain this information from the covariance images, as was achieved for the triatomic molecules.

Multi-body dissociation

We also observe a number of other covariant channels between various fragments, considerably weaker than those discussed above. Figure 5.63 shows the recoil-frame covariance maps between the groups of ions. It is again rather difficult to determine the dissociation mechanism here, given that it is possible that the dissociation occurs in one or more steps, and the statistics are rather low. The signal in the TOF-TOF covariance map is not sufficiently well-defined for us to be able to obtain a gradient

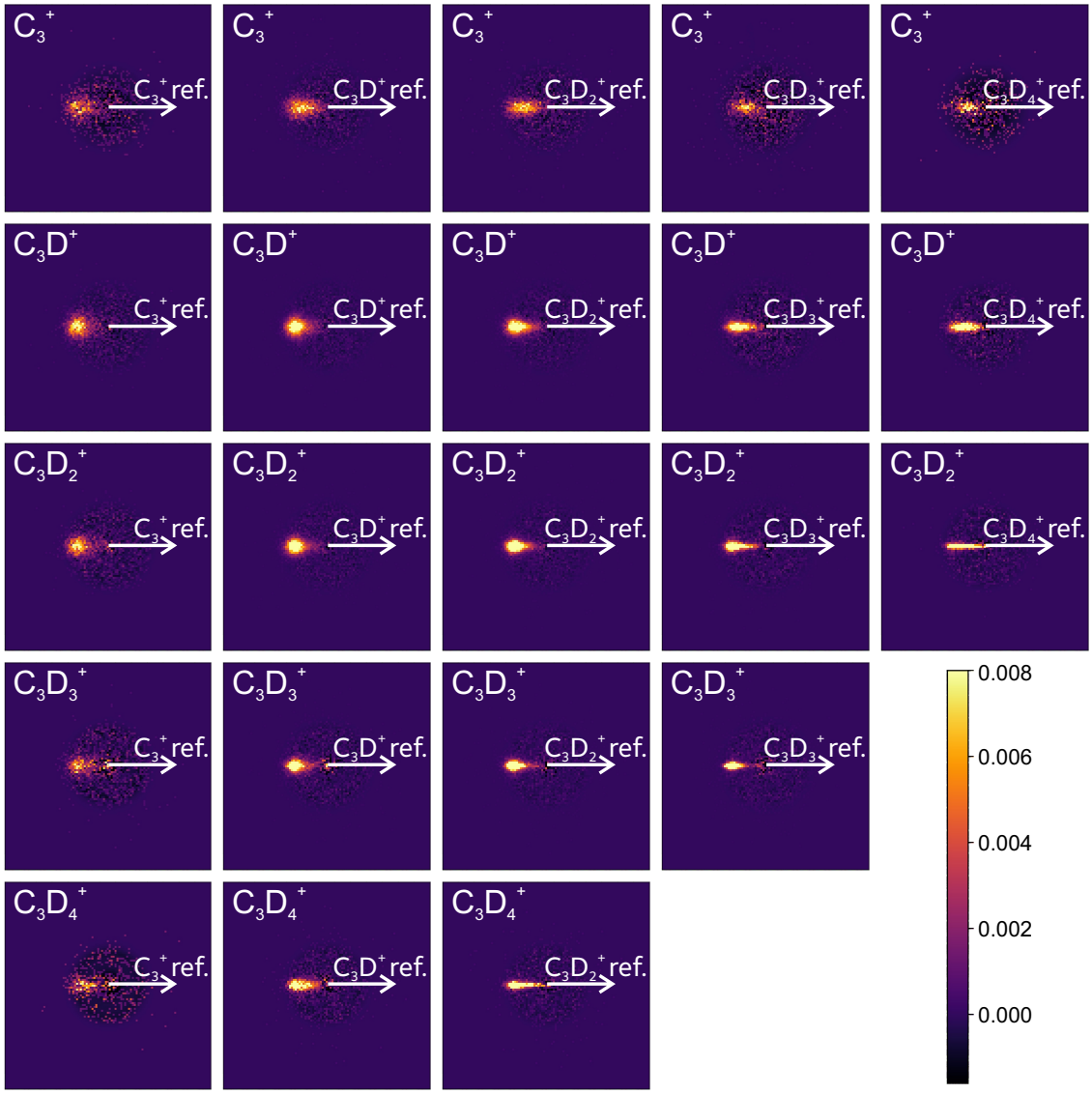


Figure 5.62 Recoil-frame covariance maps for two-body dissociation of benzene into two $C_3D_x{}^+$ fragments at an electron energy of 100 eV. We see that the signal spreads from the x axis to a greater degree as the number of deuterium atoms lost increases.

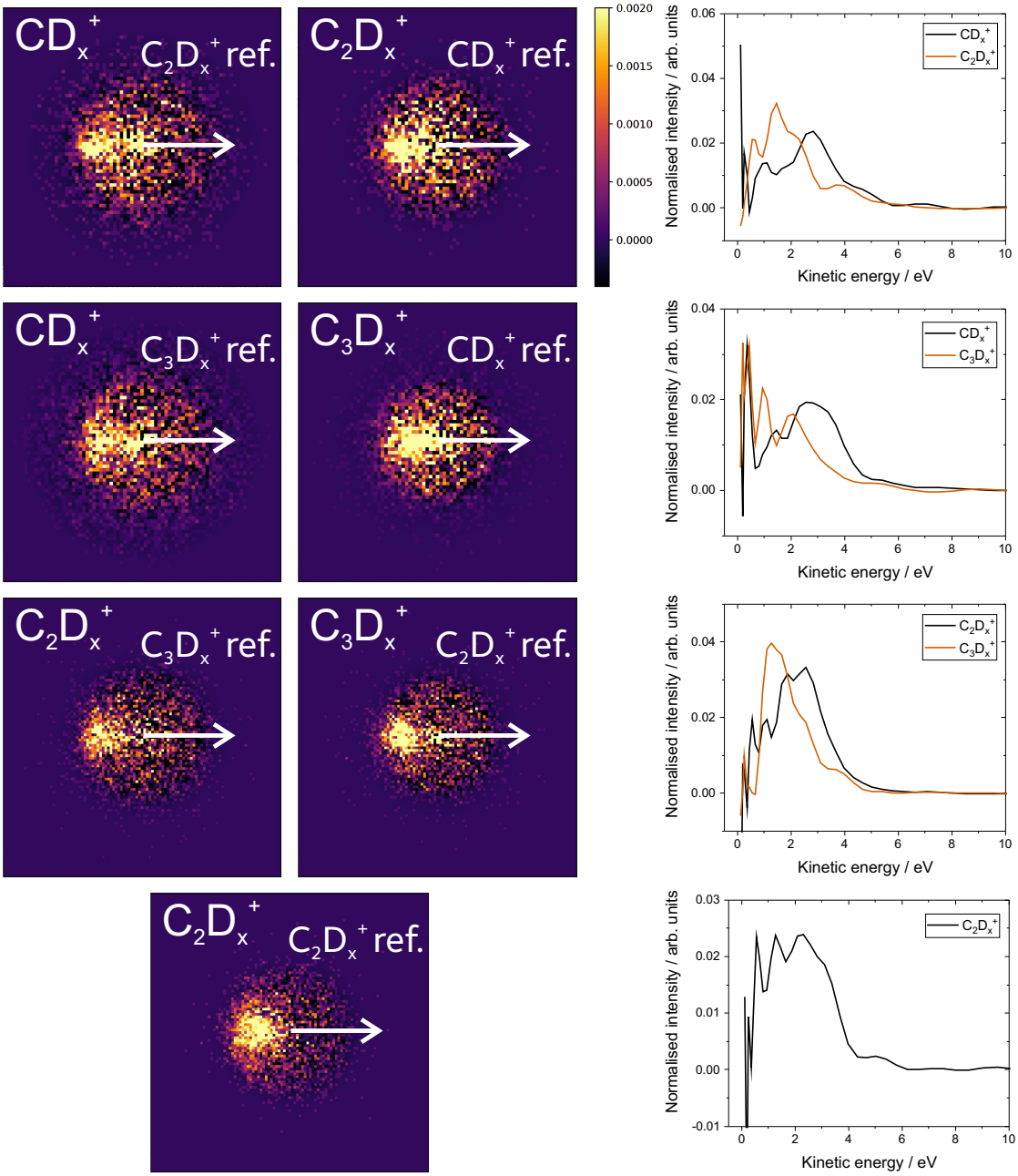


Figure 5.63 Recoil-frame covariance maps for multi-body dissociation of benzene at an electron energy of 100 eV. The kinetic energy of each signal ion with respect to the reference ion is plotted on the right.

either, so at present we just acknowledge the existence of these channels.

Recently, our group has also participated in two beamtimes headed by Melanie Schnell, in which the Free-Electron Laser in Hamburg (FLASH) of the Deutsches Elektronen-Synchrotron (DESY) was used to study the photo-induced dissociation dynamics of the molecules flourene, phenanthrene, and pyrene. Ionisation of the sample molecules was carried out by a 40.9 eV XUV photon, and the scattering distribution of the resulting ions were recorded using velocity-map imaging with a PImMS sensor, in a similar way to that employed in this work. It was found that all three molecules could undergo fragmentation of the carbon framework into two singly-charged ions, as is observed in this work. We also found that these singly-charged ions formed following fragmentation of the doubly-charged parent could also lose an even number of carbon units (typically two or four), consistent with the loss of neutral acetylene.[319] We observe a similar effect here, with covariance observed between $C_2D_x^+$ and itself, and $C_3D_x^+$ and CD_x^+, for example.

The most widely accepted mechanism for PAH formation is the hydrogen abstraction acetylene addition (HACA) mechanism.[320–322] The mechanism consists of initial abstraction of a hydrogen atom from an aromatic hydrocarbon, followed by subsequent addition of acetylene to the radical site, followed by loss of a hydrogen atom.[320] A similar mechanism involving the addition of diacetylene has also been proposed for the formation of larger PAHs.[323] Based on this information, we can conclude that the formation and destruction of PAHs proceed via a similar energetic pathways, as would be expected.

Finally, we should touch on the $CD_x{}^+$ self-covariance channel. We previously stated that the signal was caused by a contaminant, and we will now discuss the reasoning for this. Figure 5.64 shows the recoil-frame covariance map obtained for this channel. It is clear that the covariance map shows the two fragments travelling in opposite directions with very little deviation, which seems highly unlikely for the formation of two $CD_x{}^+$ fragments from $C_6D_6{}^{2+}$. If we look at the individual

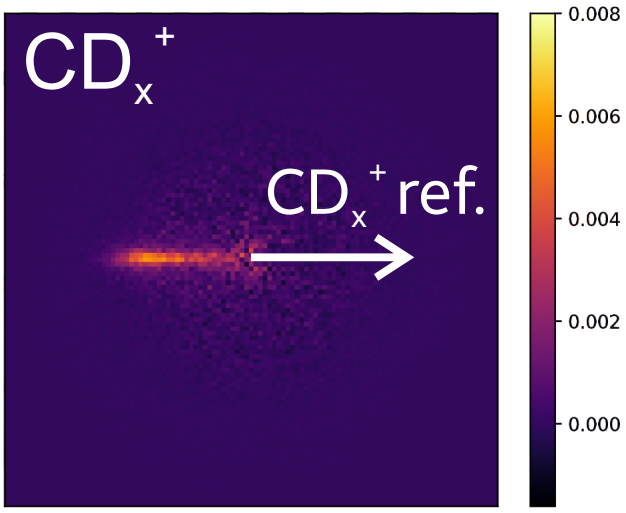


Figure 5.64 Recoil-frame covariance map for the formation of CD_x^+ and CD_x^+ from $C_6D_6^{2+}$. The well-defined recoil direction is inconsistent with the amount of fragmentation required to form the two ions.

fragments which contribute (see figure 5.60), we see that ions of m/z 14 and 16 show self-covariance, and there are no other ion pairs for which covariance is observed. The signal for this channel also decreases significantly in the 75 eV data, recorded after the 100 eV data. The most likely explanation here is that there was a small leak of gas into the foreline following the freeze-pump-thaw process which introduced N_2 and O_2 into the foreline, the dissociation of which would be consistent with the observed covariance signal. Over time, the concentration of these gases in the foreline would also decrease, which would be consistent with the observed decrease in intensity over time.

5.5.4 Summary

In this section, we have first presented partial ionisation cross-sections for benzene. We have then discussed the scattering distributions obtained in the context of the literature, finding that benzene undergoes significant rearrangement before dissociating statistically, and we established that numerous fragmentation pathways are available for benzene. Finally, we used covariance analysis to study the dissociation

of $C_6D_6{}^{2+}$, identifying that dissociation occurs primarily via two-body processes, frequently with loss of D. We also identified a number of covariance channels that have not previously been observed, to the best of our knowledge.

5.6 Summary

In this chapter, we have presented scattering distributions for carbon dioxide, nitrous oxide, carbonyl sulphide, sulphur dioxide, and (deuterated) benzene. We have obtained the partial ionisation cross-sections for each molecule, and have used the scattering distributions and covariance analysis to probe the dynamics of each of the molecules.

We have established some general features of electron ionisation. Whilst we observe a change in the dissociation of doubly-charged parent ions with respect to singly-charged parent ions, the contribution to the kinetic energy distribution from dissociation of singly-charged molecules does not appreciably change over the electron energy range used in this thesis. This implies that the dissociation is probably occurring on a small set of low-lying potential energy surfaces, the topology of which dictates the dissociation dynamics. We also observe that the kinetic energy of the ions is generally small in comparison with the energy of the incident electron. Whilst some energy is required to promote the molecule to an excited state, and the molecule can be internally excited, this is still not enough to account for all the energy available. We do not know how much energy is transferred from the incident electron to the molecule, but given the short timescale (on the order of tens to hundreds of attoseconds) it takes for the electron to traverse the length of the molecule at the electron energies considered here, we believe that the incident electron interacts primarily with the electron density of the molecule, and very little of the energy of the incident electron is transferred to the molecular framework. We can thus conclude that the incident and ejected electrons carry away the majority of the energy of the incident electron as kinetic energy.

In the next chapter, we will outline some possible plans for the future using the electron-molecule crossed beam experiment.

6

Future work

Of course, there are always many possibilities for further work on an experiment. Before we conclude, we will propose a number of potential avenues for experimental development for the electron-molecule crossed beam experiment, and identify a selection of target molecules which could be studied in future.

6.1 Experimental development

There are a number of ways in which our experimental setup could be improved to allow us to either increase the signal-to-noise ratio of the experiment (and hence improve acquisition times), or to improve the quality of our data. We will now highlight three potential upgrades to the experiment which could be made to this end.

6.1.1 Electron source

As was noted in section 2.2.2, the electron current produced by our current electron source rapidly decreases as the electron energy is decreased. When coupled with the fall in total ionisation cross-section as electron energy is decreased, this means

that the signal-to-noise ratio at 50 eV is significantly lower than at 100 eV. This can be circumvented to some degree by lengthening the electron pulse so that more electrons pass through the interaction region, but ideally there should be no requirement to change the electron beam pulse length. At present, we need to record for around 800,000 acquisition cycles to have good statistics at an electron energy of 100 eV, but have to record around three times that at an electron energy of 50 eV. Recording 800,000 acquisition cycles, plus the associated background, takes around a day running the experiment at a frequency 20 Hz. Whilst the experiment is rather stable, it is still likely that there will be experimental drift, particularly for the lower electron energies. A higher signal level would allow us to shorten the acquisition time, and more readily pick out low-intensity signals, which suffer most from a low signal-to-noise ratio.

We would also like to be able to run experiments at higher electron energies. This would increase the amount of information we can obtain from the experiment, and may allow us to examine a number of previously inaccessible dissociation pathways. For example, whilst we have observed products formed as a result of triple ionisation before,[207] triple ionisation cross-sections are generally low at an electron energy of 100 eV, and are more readily detected at higher electron energies. Measurements at higher energies would also help to inform some of the general conclusions we have made with regard to electron ionisation.

With an electron source able to provide a suitable electron current at lower electron energies, we would be able to more readily determine the electronic states responsible for the production of each ionic species. By studying electron ionisation using electron energies near the threshold of the formation threshold of various ions, we would be able to gain further insight into which states are dominant at higher electron energies, furthering our understanding of the electron ionisation process.

We would like to find a pulsed electron source which has both a higher and consistent electron current and tunable energy from around 10 eV to 250 eV or higher,

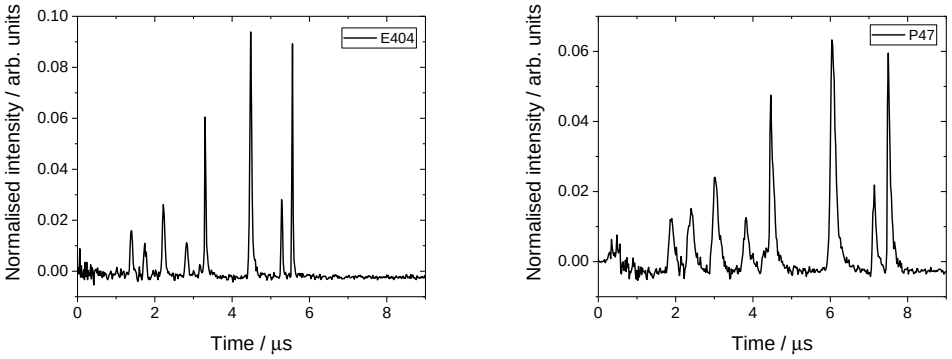


Figure 6.1 Comparison between mass spectra recorded using a PMT when using an E404 (left) and P47 (right) scintillator. Note that the mass spectrum was recorded with a repeller potential of 4 kV when using the E404 scintillator and 2 kV when using the P47 scintillator.

which focuses into a small region and has a pulse length of 100 ns or less. Naturally there are some challenges associated with delivering our desired properties, due to the charges on the electrons; space-charge repulsion means that it is difficult to create a narrow focus with high electron density using an electron beam. Nonetheless, we should be able to obtain an improved electron source, which will improve the quality of our future experiments.

6.1.2 Ultra-fast scintillator

In the present work, the scintillator P47 has been used to detect the electrons emitted by the MCPs after an ion arrives at the detector. As has been noted previously, P47 has a decay lifetime of around 70 ns.[189] Whilst this is an acceptable decay time when the arrival times of different ions are well spaced, for more complex ions it becomes much more difficult to distinguish peaks. The fact that the PImMS camera triggers on the rising edge of the scintillator signal does mitigate the problem to a large degree, but the intensity of light needs to drop below a certain threshold before a given pixel on the PImMS sensor can trigger again, so a faster scintillator allows hits in the same location in quick succession to be recorded more readily.

A significant amount of effort was made to fabricate and install a scintillator

based on an Exalite dye (E404) on our experiment. E404 has a decay lifetime of 3.7 ns, and has previously been shown to offer performance surpassing that of P47,[84] making it an ideal candidate for our experiment. An E404 scintillator was prepared on a indium tin oxide- (ITO) coated glass screen, and mounted in a detector assembly with three chevron-mounted MCPs. A mass spectrum recorded using the PMT for CF_3I is shown in figure 6.1, along with that recorded using the P47 scintillator. Note that the spectrum recorded using the P47 scintillator was measured with a repeller potential half that used when recording the spectrum using the E404 scintillator, hence the arrival times are more spread out for the P47 spectrum. We see that the decay lifetime is significantly improved, and is no longer the limiting factor in the quality of the mass spectrum. However, when we attempted to record images using the PImMS camera, we were unable to observe any signal.

To confirm whether this was a camera-specific issue, a CCD camera was installed in place of the PImMS camera, and signal was successfully observed. Thus, we can conclude that for some reason the PImMS camera is unable to detect the photons emitted from the E404 scintillator. The emission wavelength of E404 is shifted towards the blue relative to the emission wavelength of P47; our current hypothesis is that some element of the optics used in the PImMS setup, i.e. the camera lens and the on-sensor microlenses, is absorbing the light to some degree before it is detected.

The next steps for the installation of the fast scintillator are first to disassemble the detector and check for damage to the E404 scintillator. Whilst it seems unlikely there is a problem, given both the CCD camera and PMT recorded signal, it still would be worth ensuring there was no problem with the assembly. Next, the wavelength response of the PImMS camera should be checked using a tunable light source. This will allow us to confirm whether our hypothesis is accurate, and inform the choice of a new scintillator if it is. Finally, a number of scintillator candidates which are compatible with the PImMS setup should be assessed to determine whether they are suitable candidates for use in ion imaging.

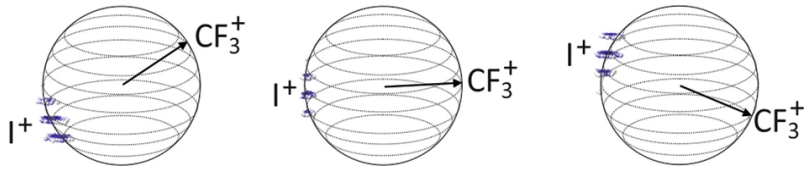


Figure 6.2 3D covariance-map images for I^+ with reference to CF_3^+. The dotted circles refer to time bins in the PImMS data, and the black arrow the direction of the reference ion. Reproduced from [324] under the Creative Commons Attribution 4.0 International License (`http://creativecommons.org/licenses/by/4.0/`).

6.1.3 Sliced imaging

The sliced imaging technique, first introduced by Gebhardt *et al.*,[71] has already been introduced as a method of obtaining the three-dimensional scattering distribution without requiring the use of an inversion method. Rather than compressing the scattering distribution for each mass-to-charge ratio such that the constituent ions arrive at the same time, i.e. the scattering distribution is 'crushed', instead, the scattering distribution is stretched out, such that ions of the same mass-to-charge arrive over a wider range of times. Initially, this technique was used in conjunction with fast gating of the detector to record a 'slice' of the scattering distribution. If the gate is set to coincide with the middle of the arrival time of the scattering distribution, i.e. the central slice of the scattering distribution, there is no longer any requirement to invert the scattering distribution to determine the central slice. The time position of the detector gate could also be stepped through the entire scattering distribution, allowing the full 3D scattering distribution to be recorded, which allows the scattering distribution of systems without an axis of cylindrical symmetry in the detector plane to be determined.

We have recently published work demonstrating the use of three-dimensional covariance-map imaging, carried out at the ARTEMIS laser within the Central Laser Facility in Harwell, Oxfordshire.[324] In this experiment, CF_3I was ionised using a RedDragon 1 kHz Ti:Sapphire laser operating at 800 nm. Due to the high laser power used in the experiment, the sample molecule was ionised via strong-field

ionisation.[325] This leads to the formation of parent molecule in a number of charge states, which then go on to dissociate into a number of fragments, which are then accelerated towards the detector by the sliced imaging optics discussed above. As we are using a multi-mass imaging sensor, in this case the PImMS sensor, we no longer need to set a detector gate, and can instead record the entire scattering distribution in one experiment. The slices of the scattering distribution will then be obtained in a number of adjacent time bins. In and of itself this is extremely useful, but also allows us to use recoil-frame covariance between slices, and hence determine a three-dimensional covariance map; for each slice of the reference scattering distribution, the recoil-frame covariance image is determined for all slices of the signal image. Figure 6.2 shows an example of this technique for the dissociation of CF_3I^{2+} into CF_3^+ and I^+. We can see that the two ions travel in opposite directions in all cases, as would be expected from a two-body dissociation. The use of this method may allow us to obtain further structural information from our data in future.

Another exciting possibility for this technique is the possibility of utilising three-fold covariance. In three-fold covariance, covariance between three ions can be determined. A schematic of the process is shown in figure 6.3. First, a reference ion is first chosen and a rotation carried out so that the reference ions point along a reference direction, as with the recoil-frame covariance discussed in this thesis. However, as we have recorded the entire 3D scattering distribution, the rotation is determined in 3D space, and is then applied to the two other selected ions. One of these two ions is then chosen to be a second reference ion, and is confined to lie in a plane which includes the original reference direction. The location of the third ion is then determined. This allows the further structural information to be extracted from the recorded scattering distribution.

This technique has previously been used experimentally using crushed imaging following strong-field ionisation by a high-power 800 nm laser, where the molecule of interest has been aligned to a specific axis.[176] Simulations carried out by Dr Jason

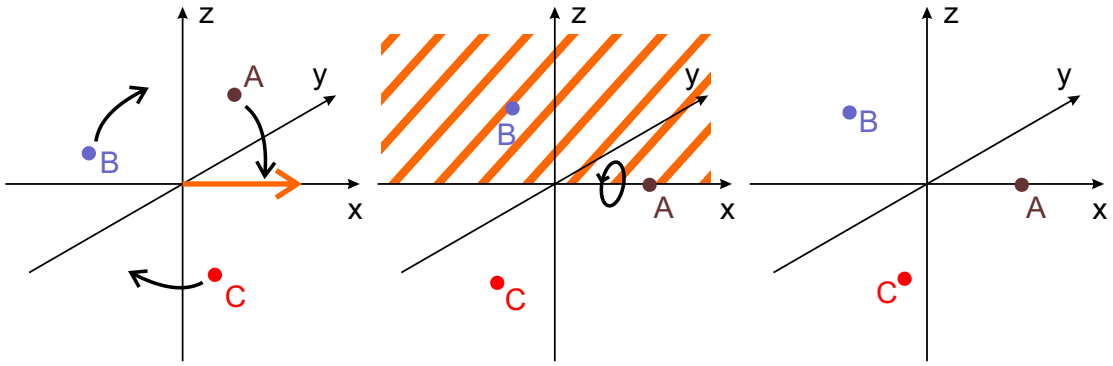


Figure 6.3 Example of the rotations required for three-fold covariance for a three-dimensional data set. Left: an ion is first selected as a reference ion, in this case ion A, and the rotation to make the ion lie along the x axis is determined. All ions are then rotated by this angle. Centre: a second reference ion is then chosen, in this case ion B, the rotation required to make this ion lie in the xz plane is determined, and the system is rotated by this angle. Right: the final position of the signal ion, in this case ion C, has been found. This process is repeated for each pair of reference ions detected in each experimental cycle.

Lee have also shown that this technique is compatible with sliced imaging, although proof-of-concept experiments using sliced imaging have not yet been carried out. Whilst the main use of three-fold covariance will be for the study of photo-induced Coulomb explosion, as the technique readily prepares the parent molecule in the highly charged states required for fragmentation to result in the formation of three or more ions, it may also be possible to use the technique in conjunction with electron ionisation. With regard to the experiments carried out in this thesis, we would require both access to higher electron energies and higher electron currents, to both work in a region with a higher ionisation cross-section for the triple ionisation pathways required to observe three-fold covariance, and to increase the signal level.

To allow access to more advanced covariance techniques such as discussed above, it would be beneficial to install ion optics which allow sliced imaging in the electron-molecule scattering experiment. The ion optics can still operate in a crushed imaging regime, as has been used in this thesis, but gives the option of carrying out sliced imaging experiments in addition to this.

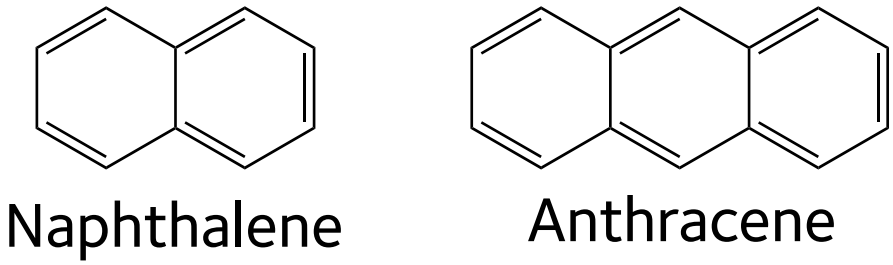


Figure 6.4 Two future targets for the crossed electron-molecular beam experiment.

6.2 Future target systems

As has previously been noted, our study of benzene is our first real foray into larger molecules, a feat made possible by the installation of a multi-mass imaging sensor on the experiment, and the study of small molecules allowing us to gain an understanding of the intricacies of electron-molecule scattering. This is intended as the first of a series of measurements on PAH-type molecules of increasing complexity. Our next two targets in this series are naphthalene and anthracene, the molecular structures of which are shown in figure 6.4. These experiments will allow us to compare and contrast the dissociation dynamics observed through the series, giving us an insight into the processes which may be occurring in the interstellar medium.

As noted previously, our group has also participated in two beamtimes headed by Melanie Schnell, in which the Free-Electron Laser in Hamburg (FLASH) of the Deutsches Elektronen-Synchrotron (DESY) was used to study the photo-induced dissociation dynamics of the molecules flourene, phenanthrene, and pyrene, as part of a multinational collaboration. In these experiments, the molecule of interest was first pumped into an excited state using photons of wavelength 30.3 nm from the FEL, before being probed by an 810 nm laser. The time between the two laser pulses was varied, allowing the evolution of the pumped molecule to be determined on a sub-picosecond timescale. Publications on this work are currently under preparation by other members of the collaboration. For our work, this study presents us with an excellent opportunity to look for similarities and differences between photon- and

electron-induced processes.

Whilst this thesis has focused on molecules of atmospheric and astrochemical relevance, there are a number of other systems in which ionisation plays a key role. For example, fluorocarbon plasmas play a key role in the etching of SiO_2, required in the manufacture of integrated circuits.[326,327] As such, it is important that we understand the composition of the plasmas to better understand the etching process. There are also environmental issues associated with plasma etching, as many of the molecules used have significant lifetimes, and strongly absorb in the infra-red, making them potent greenhouse gases.[327,328] Efforts have been made to find alternative molecules to use as etchants; one such molecule is CF_3I, which is known to have a lifetime of less than a day, significantly reducing its potency as a greenhouse gas.[329,330] We have previously studied CF_3I[206,207] and C_2F_6 (unpublished) with our crossed electron-molecular beam experiment.

It is known that DNA damage on irradiation of the skin by UV photons is caused by secondary electrons released as a result of photoionisation by the incident photon, rather than being damaged directly by the photon.[331–334] Whilst the majority of electrons produced have energies below 20 eV,[331] electrons with kinetic energies up to 100 eV are produced.[332] Using our experiment, we will be able to determine the dynamics of any ionised products resulting from electron scattering of a number of small molecules which can be considered the 'building blocks' of DNA. Previous work in our group determined total ionisation cross-sections for a number of such molecules.[100] It may be the case that excited states of the neutral molecule and/or its fragments may also play a role in DNA damage; these states could potentially be studied by using a laser to ionise the neutral species. By studying the scattering distributions of these molecules, we may be able to shed some light on the mechanism by which DNA damage occurs, which could then facilitate the development of methods both to detect damage at an earlier stage, and to protect the DNA from being damaged in the first place.

There are of course numerous other potential series of molecules which we could explore, but those we have identified serve to show that electron ionisation plays a role in a wide variety of systems.

7

Conclusion

In this thesis, we have discussed the electron-induced dynamics of a number of molecules of atmospheric and astrochemical relevance, using the BEB model to calculate theoretical total ionisation cross-sections, and an electron-molecule crossed beam experiment to obtain partial ionisation cross-sections and probe the dissociation dynamics of a range of molecules. It is clear that we can gain further insight into the dynamics of electron ionisation using these techniques.

The BEB model was already known to produce total ionisation cross-sections in good agreement with experimental results, provided the molecule contains only first- or second-row atoms. By calculating total ionisation cross-sections for a large number of molecules found in the interstellar medium, we hope to provide high-quality data for those modelling the interstellar medium, and have also fitted the calculated cross-sections with a frequently used analytical function to aid the integration of our data into their models.

We have found that we can obtain partial ionisation cross-sections which agree well with those found in the literature, and have reported what we believe to be the

first set of partial electron ionisation cross-sections for two molecules, namely carbonyl sulphide and benzene. We have also identified possible improvements which would allow us to improve the accuracy of our partial ionisation cross-sections, including replacing the current phosphor with a faster phosphor, or increasing the flight time of the ions. We also intend to explore the possibility of using the PImMS camera to obtain partial ionisation cross-sections, which could also be used to eliminate the contribution from the phosphor decay.

The scattering distributions obtained following electron scattering at a range of electron energies have been reported for five molecules: carbon dioxide, nitrous oxide, carbonyl sulphide, sulphur dioxide, and deuterated benzene. We have reached a number of conclusions based on our results. It has been observed that there is very little change in the kinetic energy of the fragment ions produced following single ionisation of the parent molecule with increasing electron energy, leading us to the conclusion that the dissociation is dominated by dissociation of only a small set of electronic states, with the kinetic energy of the fragment dictated by the topology of these states. Given that the kinetic energy of the fragments is typically only a small fraction of the kinetic energy of the incident electron, it is clear that the majority of the energy is carried away by the ionising and ejected electrons.

We have found that the decay of doubly-charged parent ions plays a significant role in the dissociation dynamics following electron ionisation, particularly at higher electron energies. We have utilised the multi-mass imaging capabilities of the PImMS sensor to record all ions produced in each experimental cycle in a single experiment, allowing us to employ both TOF-TOF covariance and recoil-frame covariance techniques. The recoil-frame covariance technique has been extensively characterised, and we concluded that recoil-frame covariance images give us information purely on covariant channels, and the positive and negative covariance seen in the image then describes the dynamics of the dissociation within the covariant channel, consistent with previous arguments for TOF-TOF covariance. We have

also identified that, on the basis of the recoil-frame covariance maps, we are able to distinguish between different decay pathways for three-body decay in most cases.

To allow us to obtain the kinetic energy of the two covariant fragments from the recoil-frame covariance images, we have developed an inversion method based on the fitting of the radial distribution of the covariance image with basis functions generated from the 2D projection of shells of differing radius. Provided the original distribution is isotropic, we have shown that we are able to obtain the kinetic energy distribution from a recoil-frame covariance map. The new inversion method can also be used to invert the 2D projection of isotropic scattering distributions, and has been used throughout this thesis. We hope to generalise the inversion method to allow us to invert anisotropic recoil-frame covariance maps in the relatively near future.

Finally, we have outlined some future directions in which the experiment could be taken over the coming years. There are a number of exciting possibilities to be explored, allowing us to further increase the amount of information we can obtain from our experiments. We have now laid the groundwork to allow for the study of larger and more complex molecular systems; electon-molecule scattering is currently an attractive area for further research.

References

(1) A. J. Dempster, *Physical Review*, 1918, **11**, 316–325.

(2) J. N. Gushue, in *Comprehensive Analytical Chemistry*, ed. I. Ferrer and E. M. Thurman, Elsevier, 2013, vol. 61, pp. 255–270.

(3) H. D. Voss, W. L. Imhof, M. Walt, J. Mobilia, E. E. Gaines, J. B. Reagan, U. S. Inan, R. A. Helliwell, D. L. Carpenter, J. P. Katsufrakis and H. C. Chang, *Nature*, 1984, **312**, 740–742.

(4) I. A. Mironova, A. A. Artamonov, G. A. Bazilevskaya, E. V. Rozanov, G. A. Kovaltsov, V. S. Makhmutov, A. L. Mishev and A. V. Karagodin, *Geophysical Research Letters*, 2019, **46**, 990–996.

(5) W. Köhnlein, *Reviews of Geophysics*, 1978, **16**, 341–354.

(6) C. Vallance, *Astrochemistry*, World Scientific (Europe), 2015, p. 228.

(7) T. A. Nordheim, L. R. Dartnell, L. Desorgher, A. J. Coates and G. H. Jones, *Icarus*, 2015, **245**, 80–86.

(8) K. Hensley, P. Withers, Z. Girazian, M. Pätzold, S. Tellmann and B. Häusler, *Journal of Geophysical Research: Space Physics*, 2020, **125**, e2019JA027167.

(9) H. S. Müller, C. P. Endres, P. Schilke and S. Schlemmer, *Molecules in Space*, 2001.

(10) H. S. Müller, S. Thorwirth, D. A. Roth and G. Winneswisser, *Astronomy and Astrophysics*, 2001, **370**, L49–L52.

(11) H. S. Müller, F. Schlöder, J. Stutzki and G. Winnewisser, *Journal of Molecular Structure*, 2005, **742**, 215–227.

(12) C. P. Endres, S. Schlemmer, P. Schilke, J. Stutzki and H. S. Müller, *Journal of Molecular Spectroscopy*, 2016, **327**, 95–104.

(13) N. J. Mason, B. Nair, S. Jheeta and E. Szymańska, *Faraday Discussions*, 2014, **168**, 235–247.

(14) S. M. Pimblott and J. A. LaVerne, *Radiation Physics and Chemistry*, 2007, **76**, 1244–1247.

(15) B. T. Draine and C. D. Kreisch, *The Astrophysical Journal*, 2018, **862**, 30.

(16) V. Pierrard and M. Lazar, *Solar Physics*, 2010, **267**, 153–174.

(17) J. L. Burch, R. Goldstein, T. E. Cravens, W. C. Gibson, R. N. Lundin, C. J. Pollock, J. D. Winningham and D. T. Young, *Space Science Reviews*, 2007, **128**, 697–712.

(18) M. Vivekanand and R. Narayan, *Journal of Astrophysics and Astronomy*, 1982, **3**, 399–412.

(19) S. Redfield and J. L. Linsky, *The Astrophysical Journal*, 2008, **673**, 283–314.

(20) I. T. Ho, L. J. Kewley, M. A. Dopita, A. M. Medling, J. T. Allen, J. Bland-Hawthorn, J. V. Bloom, J. J. Bryant, S. M. Croom, L. M. Fogarty, M. Goodwin, A. W. Green, I. S. Konstantopoulos, J. S. Lawrence, R. López-Sánchez, M. S. Owers, S. Richards and R. Sharp, *Monthly Notices of the Royal Astronomical Society*, 2014, **444**, 3894–3910.

(21) M. Kaasinen, F. Bian, B. Groves, L. J. Kewley and A. Gupta, *Monthly Notices of the Royal Astronomical Society*, 2017, **465**, 3220–3234.

(22) L. J. Kewley, D. C. Nicholls, R. Sutherland, J. R. Rigby, A. Acharya, M. A. Dopita and M. B. Bayliss, *The Astrophysical Journal*, 2019, **880**, 16.

(23) A. Acharyya, L. J. Kewley, J. R. Rigby, M. Bayliss, F. Bian, D. Nicholls, C. Federrath, M. Kaasinen, M. Florian and G. A. Blanc, *Monthly Notices of the Royal Astronomical Society*, 2019, **488**, 5862–5886.

(24) A. Harshan, A. Gupta, K.-V. Tran, L. Y. Alcorn, T. Yuan, G. G. Kacprzak, T. Nanayakkara, K. Glazebrook, L. J. Kewley, I. Labbé and C. Papovich, *The Astrophysical Journal*, 2020, **892**, 77.

(25) S. K. Ocker, J. M. Cordes and S. Chatterjee, *The Astrophysical Journal*, 2020, **897**, 124.

(26) C. Vallance, *Molecular Reaction Dynamcis*, URL: `http://vallance.chem.ox.ac.uk/pdfs/ReactionDynamicsLectureNotes2015.pdf`. Last visited on 01/09/2020, University of Oxford, Department of Chemistry, 2015, pp. 1–38.

(27) M. Born and R. Oppenheimer, *Annalen der Physik*, 1927, **389**, 457–484.

(28) P. W. Atkins and R. S. Friedman, *Molecular Quantum Mechanics*, Oxford University Press, Fifth Ed., 2010, p. 560.

(29) P. Atkins, *Physical Chemistry*, OUP Oxford, Fourth Ed., 1992.

(30) *IUPAC Compendium of Chemical Terminology*, 2009.

(31) L. Meitner, *Zeitschrift für Physik*, 1922, **9**, 131–144.

(32) P. Auger, *Comptes rendus de l'Académie des Sciences*, 1923, **177**, 169–171.

(33) P. Persson, S. Lunell, A. Szöke, B. Ziaja and J. Hajdu, *Protein Science*, 2001, **10**, 2480–2484.

(34) J. W. Lee, D. Phil. University of Oxford, 2014.

(35) R. J. Van Brunt and L. J. Kieffer, *The Journal of Chemical Physics*, 1974, **60**, 3057–3063.

(36) C. R. Claydon, G. A. Segal and H. S. Taylor, *The Journal of Chemical Physics*, 1970, **52**, 3387–3398.

(37) P. J. Chantry, *The Journal of Chemical Physics*, 1972, **57**, 3180–3186.

(38) A. G. Harrison, *Chemical Ionization Mass Spectrometry, Second Edition*, Taylor & Francis, 1992.

(39) L. G. Christophorou, *Electron—Molecule Interactions and Their Applications: Volume 2*, Elsevier Science, 2013.

(40) M. Dantus, R. M. Bowman and A. H. Zewail, *Nature*, 1990, **343**, 737–739.

(41) J. W. Otvos and D. P. Stevenson, *Journal of the American Chemical Society*, 1956, **78**, 546–551.

(42) D. K. Jain and S. P. Khare, *Journal of Physics B: Atomic and Molecular Physics*, 1976, **9**, 1429–1438.

(43) S. P. Khare and W. J. Meath, *Journal of Physics B: Atomic and Molecular Physics*, 1987, **20**, 2101–2116.

(44) K. N. Joshipura, M. Vinodkumar and U. M. Patel, *Journal of Physics B: Atomic, Molecular and Optical Physics*, 2001, **34**, 509–519.

(45) K. N. Joshipura, M. Vinodkumar, C. G. Limbachiya and B. K. Antony, *Physical Review A - Atomic, Molecular, and Optical Physics*, 2004, **69**, 6.

(46) H. Deutsch and T. D. Märk, *International Journal of Mass Spectrometry and Ion Processes*, 1987, **79**, R1–R8.

(47) D. Margreiter, H. Deutsch, M. Schmidt and T. D. Märk, *International Journal of Mass Spectrometry and Ion Processes*, 1990, **100**, 157–176.

(48) H. Deutsch, K. Becker, S. Matt and T. D. Märk, *International Journal of Mass Spectrometry*, 2000, **197**, 37–69.

(49) Y. K. Kim and M. E. Rudd, *Physical Review A*, 1994, **50**, 3954–3967.

(50) W. Hwang, Y. K. Kim and M. E. Rudd, *Journal of Chemical Physics*, 1996, **104**, 2956–2966.

(51) A. L. Hughes and E. Klein, *Physical Review*, 1924, **23**, 450–463.

(52) P. T. Smith, *Physical Review*, 1930, **36**, 1293–1302.

(53) J. T. Tate and P. T. Smith, *Physical Review*, 1932, **39**, 270–277.

(54) D. D. Briglia and D. Rapp, *The Journal of Chemical Physics*, 1965, **42**, 3201–3213.

(55) D. Rapp, P. Englander-Golden and D. D. Beiglia, *The Journal of Chemical Physics*, 1965, **42**, 4081–4085.

(56) D. Rapp and P. Englander-Golden, *The Journal of Chemical Physics*, 1965, **43**, 1464–1479.

(57) W. W. Lozier, *Physical Review*, 1930, **36**, 1285–1292.

(58) G. E. Busch, R. T. Mahoney, R. I. Morse and K. R. Wilson, *The Journal of Chemical Physics*, 1969, **51**, 449–450.

(59) R. W. Diesen, J. C. Wahr and S. E. Adler, *The Journal of Chemical Physics*, 1969, **50**, 3635–3636.

(60) R. N. Zare and P. J. Dagdigian, *Science*, 1974, **185**, 739 LP –747.

(61) J. L. Kinsey, *The Journal of Chemical Physics*, 1977, **66**, 2560–2565.

(62) G. E. Hall, N. Sivakumar, R. Ogorzalek, G. Chawla, H. P. Haerri, P. L. Houston, I. Burak and J. W. Hepburn, *Faraday Discussions of the Chemical Society*, 1986, **82**, 13–24.

(63) D. W. Chandler, P. L. Houston and D. H. Parker, *Journal of Chemical Physics*, 2017, **147**, 13601.

(64) D. W. Chandler and P. L. Houston, *The Journal of Chemical Physics*, 1987, **87**, 1445–1447.

(65) B. Y. Chang, R. C. Hoetzlein, J. A. Mueller, J. D. Geiser and P. L. Houston, *Review of Scientific Instruments*, 1998, **69**, 1665–1670.

(66) A. T. Eppink and D. H. Parker, *Review of Scientific Instruments*, 1997, **68**, 3477–3484.

(67) R. Zenobi and R. Knochenmuss, *Mass Spectrometry Reviews*, 1998, **17**, 337–366.

(68) M. Brouard, A. J. Johnsen, A. Nomerotski, C. S. Slater, C. Vallance and W. H. Yuen, *Journal of Instrumentation*, 2011, **6**, C01044–C01044.

(69) M. Brouard, E. Halford, A. Lauer, C. S. Slater, B. Winter, W. H. Yuen, J. J. John, L. Hill, A. Nomerotski, A. Clark, J. Crooks, I. Sedgwick, R. Turchetta, J. W. Lee, C. Vallance and E. Wilman, *Review of Scientific Instruments*, 2012, **83**, 114101.

(70) E. Halford, B. Winter, M. D. Mills, S. P. Thompson, V. Parr, J. J. John, A. Nomerotski, C. Vallance, R. Turchetta and M. Brouard, *Rapid Communications in Mass Spectrometry*, 2014, **28**, 1649–1657.

(71) C. R. Gebhardt, T. P. Rakitzis, P. C. Samartzis, V. Ladopoulos and T. N. Kitsopoulos, *Review of Scientific Instruments*, 2001, **72**, 3848–3853.

(72) D. Townsend, M. P. Minitti and A. G. Suits, *Review of Scientific Instruments*, 2003, **74**, 2530–2539.

(73) J. B. Anderson and J. B. Fenn, *Physics of Fluids*, 1965, **8**, 780–787.

(74) W. Christen, K. Rademann and U. Even, *Journal of Physical Chemistry A*, 2010, **114**, 11189–11201.

(75) J. Ladislas Wiza, *Nuclear Instruments and Methods*, 1979, **162**, 587–601.

(76) Hamamatsu, *MCP Assembly Technical Information*, 2006.

(77) M. Lampton and F. Paresce, *Review of Scientific Instruments*, 1974, **45**, 1098–1105.

(78) M. Yamamoto, *Radioisotopes*, 1975, **24**, 386–390.

(79) R. Allemand and G. Thomas, *Nuclear Instruments and Methods*, 1976, **137**, 141–149.

(80) M. Lampton and C. W. Carlson, *Review of Scientific Instruments*, 1979, **50**, 1093–1097.

(81) M. Lampton, O. Siegmund and R. Raffanti, *Review of Scientific Instruments*, 1987, **58**, 2298–2305.

(82) C. Martin, P. Jelinsky, M. Lampton, R. F. Malina and H. O. Anger, *Review of Scientific Instruments*, 1981, **52**, 1067–1074.

(83) G. Veshapidze, T. Nishide, H. Shiromaru, N. Kobayashi and T. Mizogawa, *Japanese Journal of Applied Physics, Part 1: Regular Papers and Short Notes and Review Papers*, 2002, **41**, 871–875.

(84) B. Winter, S. J. King, M. Brouard and C. Vallance, *Review of Scientific Instruments*, 2014, **85**, 23306.

(85) E. S. Wilman, S. H. Gardiner, A. Nomerotski, R. Turchetta, M. Brouard and C. Vallance, *Review of Scientific Instruments*, 2012, **83**, 13304.

(86) A. Nomerotski, M. Brouard, E. Campbell, A. Clark, J. Crooks, J. Fopma, J. J. John, A. J. Johnsen, C. Slater, R. Turchetta, C. Vallance, E. Wilman and W. H. Yuen, *Journal of Instrumentation*, 2010, **5**, C07007.

(87) I. Sedgwick, A. Clark, J. Crooks, R. Turchetta, L. Hill, J. J. John, A. Nomerotski, R. Pisarczyk, M. Brouard, S. H. Gardiner, E. Halford, J. Lee, M. L. Lipciuc, C. Slater, C. Vallance, E. S. Wilman, B. Winter and W. H. Yuen, 2012 IEEE 10th International New Circuits and Systems Conference, NEWCAS 2012, 2012, pp. 497–500.

(88) J. John, M. Brouard, A. Clark, J. Crooks, E. Halford, L. Hill, L. Lee, A. Nomerotski, R. Pisarczyk, I. Sedgwick, S. Slater, R. Turchetta, C. Vallance, E. Wilman, B. Winter and H. Yuen, *Journal of Instrumentation*, 2012, **7**, C08001.

(89) X. Llopart, R. Ballabriga, M. Campbell, L. Tlustos and W. Wong, *Nuclear Instruments and Methods in Physics Research, Section A: Accelerators, Spectrometers, Detectors and Associated Equipment*, 2007, **581**, 485–494.

(90) M. De Gaspari, J. Alozy, R. Ballabriga, M. Campbell, E. Fröjdh, J. Idarraga, S. Kulis, X. Llopart, T. Poikela, P. Valerio and W. Wong, *Journal of Instrumentation*, 2014, **9**, C01037.

(91) T. Poikela, J. Plosila, T. Westerlund, M. Campbell, M. D. Gaspari, X. Llopart, V. Gromov, R. Kluit, M. V. Beuzekom, F. Zappon, V. Zivkovic, C. Brezina, K. Desch, Y. Fu and A. Kruth, *Journal of Instrumentation*, 2014, **9**, C05013.

(92) R. Signorell and F. Merkt, *Molecular Physics*, 1997, **92**, 793–804.

(93) N. F. Mott and R. H. Fowler, *Proceedings of the Royal Society of London. Series A, Containing Papers of a Mathematical and Physical Character*, 1930, **126**, 259–267.

(94) L. Vriens, in *Case studies in atomic collision physics*, ed. E. McDaniel and M. McDowell, North-Holland Publishing Company, Amsterdam, 1969, vol. 1, p. 335.

(95) H. Bethe, *Annalen der Physik*, 1930, **397**, 325–400.

(96) D. Heathcote, Part II, University of Oxford, 2016.

(97) D. Heathcote and C. Vallance, *Journal of Physics B: Atomic, Molecular and Optical Physics*, 2018, **51**, 195203.

(98) Y. K. Kim, W. Hwang, N. M. Weinberger, M. A. Ali and M. E. Rudd, *Journal of Chemical Physics*, 1997, **106**, 1026–1033.

(99) J. N. Bull, P. W. Harland and C. Vallance, *Journal of Physical Chemistry A*, 2012, **116**, 767–777.

(100) J. N. Bull, J. W. Lee and C. Vallance, *Physical Chemistry Chemical Physics*, 2014, **16**, 10743–10752.

(101) D. R. Hartree and W. Hartree, *Proceedings of the Royal Society of London. Series A - Mathematical and Physical Sciences*, 1935, **150**, 9–33.

(102) C. C. Roothaan, *Reviews of Modern Physics*, 1951, **23**, 69–89.

(103) J. A. Pople and R. K. Nesbet, *The Journal of Chemical Physics*, 1954, **22**, 571–572.

(104) R. McWeeny and G. Diercksen, *The Journal of Chemical Physics*, 1968, **49**, 4852–4856.

(105) J. V. Ortiz, *Journal of Chemical Physics*, 1996, **104**, 7599–7605.

(106) T. H. Dunning, *The Journal of Chemical Physics*, 1989, **90**, 1007–1023.

(107) R. A. Kendall, T. H. Dunning and R. J. Harrison, *The Journal of Chemical Physics*, 1992, **96**, 6796–6806.

(108) D. E. Woon and T. H. Dunning, *The Journal of Chemical Physics*, 1993, **98**, 1358–1371.

(109) W. M. Huo and Y. K. Kim, *Chemical Physics Letters*, 2000, **319**, 576–586.

(110) J. N. Bull, J. W. Lee and C. Vallance, *Physical Review A - Atomic, Molecular, and Optical Physics*, 2015, **91**, 22704.

(111) M. E. McHenry and D. E. Laughlin, in *Physical Metallurgy: Fifth Edition*, ed. D. E. Laughlin and K. Hono, Elsevier, Oxford, 2014, vol. 1, pp. 1881–2008.

(112) Q. Wang, M. Guo and C. Li, *Integrated Ferroelectrics*, 2016, **172**, 49–58.

(113) P. V. Technology, *ELS 100 Electron Gun*, 2020, `http://www.pspvacuum.com/files/els100outline1.pdf` (visited on 12/08/2020).

(114) K. Sasaki, R. Engeln and E. V. Barnat, *Journal of Physics D: Applied Physics*, 2018, **51**, 40202.

(115) R. Álvarez, A. Rodero and M. C. Quintero, *Spectrochimica Acta - Part B Atomic Spectroscopy*, 2002, **57**, 1665–1680.

(116) S. Shi, K. Finch, Y. She and G. Gamez, *Journal of Analytical Atomic Spectrometry*, 2020, **35**, 117–125.

(117) B. Hubert, C. Opitom, D. Hutsemékers, E. Jehin, G. Munhoven, J. Manfroid, D. V. Bisikalo and V. I. Shematovich, *Icarus*, 2016, **277**, 237–256.

(118) R. N. Bracewell, *Australian Journal of Physics*, 1956, **9**, 198.

(119) R. N. Bracewell and A. C. Riddle, *The Astrophysical Journal*, 1967, **150**, 427.

(120) G. A. Hajj, R. Ibañez-Meier, E. R. Kursinski and L. J. Romans, *International Journal of Imaging Systems and Technology*, 1994, **5**, 174–187.

(121) W. S. Schreiner, S. V. Sokolovskiy, C. Rocken and D. C. Hunt, *Radio Science*, 1999, **34**, 949–966.

(122) M. Hernandez-Pajares, J. M. Juan and J. Sanz, *Geophysical Research Letters*, 2000, **27**, 2473–2476.

(123) M. Garcia-Fernandez, M. Hernandez-Pajares, M. Juan and J. Sanz, *Journal of Geophysical Research: Space Physics*, 2003, **108**, DOI: `10/c8dk9n`.

(124) R. N. Zare and W. G. Harter, *Angular Momentum: Understanding Spatial Aspects in Chemistry and Physics*, Wiley, New York, N.Y., 1988, vol. 42, p. 368.

(125) B. Ritchie, *Physical Review A*, 1976, **13**, 1411–1415.

(126) I. Powis, *Journal of Chemical Physics*, 2000, **112**, 301–310.

(127) N. H. Abel, *Journal fur die Reine und Angewandte Mathematik*, 1826, **1826**, 153–157.

(128) A. T. J. B. Eppink, S.-m. Wu and B. J. Whitaker, in *Imaging in Molecular Dynamics: Technology and Applications*, ed. B. J. Whitaker, Cambridge University Press, Cambridge, 2003, pp. 65–112.

(129) E. W. Hansen and P.-L. Law, *Journal of the Optical Society of America A*, 1985, **2**, 510.

(130) R. E. Kalman, *Transactions of the ASME–Journal of Basic Engineering*, 1960, **82**, 35–45.

(131) *Larousse gastronomique*, ed. J. Robuchon, London : Hamlyn, London, 2009.

(132) C. J. Dasch, *Applied Optics*, 1992, **31**, 1146–1152.

(133) C. Bordas, F. Paulig, H. Helm and D. L. Huestis, *Review of Scientific Instruments*, 1996, **67**, 2257–2268.

(134) K. Zhao, T. Colvin, W. T. Hill and G. Zhang, *Review of Scientific Instruments*, 2002, **73**, 3044.

(135) G. M. Roberts, J. L. Nixon, J. Lecointre, E. Wrede and J. R. Verlet, *Review of Scientific Instruments*, 2009, **80**, 53104.

(136) A. N. Tikhonov, *Doklady Akademii Nauk SSSR*, 1943, **39**, 195–198.

(137) D. L. Phillips, *Journal of the ACM (JACM)*, 1962, **9**, 84–97.

(138) A. N. Tikhonov, *Doklady Akademii Nauk SSSR*, 1963, **151**, 501–504.

(139) A. N. Tikhonov and V. Y. Arsenin, *Solutions of ill-posed problems*, V. H. Winston & Sons, Washington, D.C.: John Wiley & Sons, New York, 1977.

(140) V. Dribinski, A. Ossadtchi, V. A. Mandelshtam and H. Reisler, *Review of Scientific Instruments*, 2002, **73**, 2634.

(141) G. A. Garcia, L. Nahon and I. Powis, *Review of Scientific Instruments*, 2004, **75**, 4989–4996.

(142) T. Gerber, Y. Liu, G. Knopp, P. Hemberger, A. Bodi, P. Radi and Y. Sych, *Review of Scientific Instruments*, 2013, **84**, 33101.

(143) M. J. Bass, M. Brouard, A. P. Clark and C. Vallance, *Journal of Chemical Physics*, 2002, **117**, 8723–8735.

(144) R. N. Dixon, *The Journal of Chemical Physics*, 1986, **85**, 1866–1879.

(145) D. A. Dahl, *International Journal of Mass Spectrometry*, 2000, **200**, 3–25.

(146) R. N. Bannister, *Quarterly Journal of the Royal Meteorological Society*, 2008, **134**, 1951–1970.

(147) P. Danaher, D. Paul and P. Wang, *Biometrika*, 2015, **102**, 533–544.

(148) L. J. Frasinski, K. Codling and P. A. Hatherly, *Science*, 1989, **246**, 1029–1031.

(149) K. E. McCulloh, T. E. Sharp and H. M. Rosenstock, *The Journal of Chemical Physics*, 1965, **42**, 3501–3509.

(150) B. Brehm and E. V. Puttkamer, *Zeitschrift fur Naturforschung - Section A Journal of Physical Sciences*, 1967, **22**, 8–10.

(151) G. Dujardin, S. Leach, O. Dutuit, P. M. Guyon and M. Richard-Viard, *Chemical Physics*, 1984, **88**, 339–353.

(152) J. H. Eland, F. S. Wort and R. N. Royds, *Journal of Electron Spectroscopy and Related Phenomena*, 1986, **41**, 297–309.

(153) J. H. Eland, S. S. Ho and H. L. Worthington, *Chemical Physics*, 2003, **290**, 27–34.

(154) J. H. Eland, *Chemical Physics*, 2003, **294**, 171–186.

(155) J. H. D. Eland, *Molecular Physics*, 1987, **61**, 725–745.

(156) R. Dalitz, *The London, Edinburgh, and Dublin Philosophical Magazine and Journal of Science*, 1953, **44**, 1068–1080.

(157) D. Dehnhard, D. Kamke and P. Kramer, *Physics Letters*, 1962, **3**, 52–55.

(158) J. L. Quebert and L. Marquez, *Nuclear Physics, Section A*, 1969, **126**, 646–670.

(159) B. May, K. D. Duch, M. Heel, H. Kalinowsky, F. Kayser, E. Klempt, J. Reifenröther, O. Schreibei, P. Weidenauer, M. Ziegler, D. Bailey, S. Barlag, J. M. Butler, U. Gastaldi, R. Landua, C. Sabev, W. Dahme, F. Feld-Dahme, U. Schaefer, W. R. Wodrich, J. C. Bizot, B. Delcourt, J. Jeanjean, H. Nguyen, E. G. Auld, D. A. Axen, K. L. Erdman, B. Howard, R. Howard, B. L. White, S. Ahmad, M. Comyn, G. M. Marshall, G. Beer, L. P. Robertson, M. Botlo, C. Laa, H. Vonach, C. Amsler, M. Doser, J. Riedlberger, U. Straumann and P. Truöl, *Zeitschrift für Physik C Particles and Fields*, 1990, **46**, 203–213.

(160) L. M. Wiese, O. Yenen, B. Thaden and D. H. Jaecks, *Physical Review Letters*, 1997, **79**, 4982–4985.

(161) C. Maul and K. H. Gericke, *Journal of Physical Chemistry A*, 2000, **104**, 2531–2541.

(162) M. Schulz, T. Ferger, D. Fischer, R. Moshammer and J. Ullrich, *Physical Review A - Atomic, Molecular, and Optical Physics*, 2006, **74**, 42705.

(163) A. Matsuda, E. J. Takahashi and A. Hishikawa, *Journal of Chemical Physics*, 2007, **127**, 114318.

(164) R. Karimi, É. Bisson, B. Walles, S. Beaulieu, M. Giguère, Z. Long, W. K. Liu, J. C. Kieffer, F. Légaré and J. Sanderson, *Journal of Chemical Physics*, 2013, **138**, 204311.

(165) X. Wang, Y. Zhang, D. Lu, G. C. Lu, B. Wei, B. H. Zhang, Y. J. Tang, R. Hutton and Y. Zou, *Physical Review A - Atomic, Molecular, and Optical Physics*, 2014, **90**, 62705.

(166) A. Khan, L. C. Tribedi and D. Misra, *Physical Review A*, 2017, **96**, 12703.

(167) A. Ramadhan, B. Wales, R. Karimi, I. Gauthier, M. Macdonald, L. Zuin and J. Sanderson, *Journal of Physics B: Atomic, Molecular and Optical Physics*, 2016, **49**, 215602.

(168) L. J. Frasinski, *Journal of Physics B: Atomic, Molecular and Optical Physics*, 2016, **49**, 152004.

(169) L. J. Frasinski, A. J. Giles, P. A. Hatherly, J. H. Posthumus, M. R. Thompson and K. Codling, *Journal of Electron Spectroscopy and Related Phenomena*, 1996, **79**, 367–371.

(170) W. J. Krzanowski, *Principles of multivariate analysis : a user's perspective*, Oxford University Press, Oxford, Rev., 2000.

(171) V. Zhaunerchyk, L. J. Frasinski, J. H. Eland and R. Feifel, *Physical Review A - Atomic, Molecular, and Optical Physics*, 2014, **89**, 53418.

(172) L. J. Frasinski, P. A. Hatherly and K. Codling, *Physics Letters A*, 1991, **156**, 227–232.

(173) J. L. Hansen, J. H. Nielsen, C. B. Madsen, A. T. Lindhardt, M. P. Johansson, T. Skrydstrup, L. B. Madsen and H. Stapelfeldt, *Journal of Chemical Physics*, 2012, **136**, 204310.

(174) C. S. Slater, S. Blake, M. Brouard, A. Lauer, C. Vallance, J. J. John, R. Turchetta, A. Nomerotski, L. Christensen, J. H. Nielsen, M. P. Johansson and H. Stapelfeldt, *Physical Review A - Atomic, Molecular, and Optical Physics*, 2014, **89**, 11401.

(175) C. S. Slater, S. Blake, M. Brouard, A. Lauer, C. Vallance, C. S. Bohun, L. Christensen, J. H. Nielsen, M. P. Johansson and H. Stapelfeldt, *Physical Review A - Atomic, Molecular, and Optical Physics*, 2015, **91**, 53424.

(176) J. D. Pickering, K. Amini, M. Brouard, M. Burt, I. J. Bush, L. Christensen, A. Lauer, J. H. Nielsen, C. S. Slater and H. Stapelfeldt, *Journal of Chemical Physics*, 2016, **144**, 161105.

(177) S. Gibson, D. D. Hickstein, R. Yurchak, M. Ryazanov, D. Das and G. Shih, *PyAbel/PyAbel: v0.8.3*, version v0.8.3, 2019.

(178) S. E. Huber, A. Mauracher, I. Sukuba, J. Urban, T. Maihom and M. Probst, *European Physical Journal D*, 2017, **71**, 335.

(179) H. C. Straub, P. Renault, B. G. Lindsay, K. A. Smith and R. F. Stebbings, *Physical Review A - Atomic, Molecular, and Optical Physics*, 1996, **54**, 2146–2153.

(180) E. Krishnakumar and S. K. Srivastava, *Journal of Physics B: Atomic, Molecular and Optical Physics*, 1990, **23**, 1893–1903.

(181) N. Durić, I. Čadež and M. Kurepa, *International Journal of Mass Spectrometry and Ion Processes*, 1991, **108**, R1–R10.

(182) O. J. Orient and S. K. Strivastava, *Journal of Physics B: Atomic and Molecular Physics*, 1987, **20**, 3923–3936.

(183) H. C. Straub, D. Lin, B. G. Lindsay, K. A. Smith and R. F. Stebbings, *Journal of Chemical Physics*, 1997, **106**, 4430–4435.

(184) W. Zhong and J. D. Haigh, *Weather*, 2013, **68**, 100–105.

(185) L. B. D'Hendecourt and M. Jourdain de Muizon, *Astronomy and Astrophysics*, 1989, **223**, L5–L8.

(186) M. Minissale, E. Congiu, G. Manicò, V. Pirronello and F. Dulieu, *Astronomy and Astrophysics*, 2013, **559**, A49.

(187) E. L. Gibb, D. C. B. Whittet, A. C. A. Boogert and A. G. G. M. Tielens, *The Astrophysical Journal Supplement Series*, 2004, **151**, 35–73.

(188) W. A. Schutte, *Advances in Space Research*, 2002, **30**, 1409–1417.

(189) G. F. Knoll, *Radiation detection and measurement*, John Wiley & Sons, New York, 4th ed., 2010.

(190) H. C. Straub, B. G. Lindsay, K. A. Smith and R. F. Stebbings, *Journal of Chemical Physics*, 1996, **105**, 4015–4022.

(191) S. J. King and S. D. Price, *International Journal of Mass Spectrometry*, 2008, **272**, 154–164.

(192) J. E. Hudson, C. Vallance and P. W. Harland, *Journal of Physics B: Atomic, Molecular and Optical Physics*, 2004, **37**, 445–455.

(193) J. H. Eland and J. Berkowitz, *The Journal of Chemical Physics*, 1977, **67**, 2782–2787.

(194) M. T. Praet, J. C. Lorquet and G. Raşeev, *The Journal of Chemical Physics*, 1982, **77**, 4611–4618.

(195) R. Bombach, J. Dannacher, J. P. Stadelmann and J. C. Lorquet, *The Journal of Chemical Physics*, 1983, **79**, 4214–4220.

(196) J. Liu, W. Chen, M. Hochlaf, X. Qian, C. Chang and C. Y. Ng, *Journal of Chemical Physics*, 2003, **118**, 149–163.

(197) P. Johnsson, W. Siu, A. Gijsbertsen, J. Verhoeven, A. S. Meijer, W. Van Der Zande and M. J. Vrakking, *Journal of Modern Optics*, 2008, **55**, 2693–2709.

(198) M. Yang, L. Zhang, X. Zhuang, L. Lai and S. Yu, *Journal of Chemical Physics*, 2008, **128**, 164308.

(199) Q. Meng, M. B. Huang and H. B. Chang, *Journal of Physical Chemistry A*, 2009, **113**, 12825–12830.

(200) R. Mao, C. He, M. Chen, D. na Zhou, Q. Zhang and Y. Chen, *Chinese Journal of Chemical Physics*, 2017, **30**, 123–127.

(201) H. Ehrhardt and A. Kresling, *Z. Naturforschg.*, 1967, **22a**, 2036–2043.

(202) A. Crowe and J. W. McConkey, *Journal of Physics B: Atomic and Molecular Physics*, 1974, **7**, 349–361.

(203) R. Velotta, P. D. Girolamo, V. Berardi, N. Spinelli and M. Armenante, *Journal of Physics B: Atomic, Molecular and Optical Physics*, 1994, **27**, 2051–2061.

(204) R. Locht and M. Davister, *International Journal of Mass Spectrometry and Ion Processes*, 1995, **144**, 105–129.

(205) J. W. McConkey, C. P. Malone, P. V. Johnson, C. Winstead, V. McKoy and I. Kanik, *Physics Reports*, 2008, **466**, 1–103.

(206) H. Köckert, D. Phil. University of Oxford, 2019.

(207) H. Köckert, D. Heathcote, J. W. Lee and C. Vallance, *Molecular Physics*, 2020, e1811909.

(208) C. Tian and C. R. Vidal, *Physical Review A - Atomic, Molecular, and Optical Physics*, 1998, **58**, 3783–3795.

(209) D. M. Curtis and J. H. Eland, *International Journal of Mass Spectrometry and Ion Processes*, 1985, **63**, 241–264.

(210) G. Dujardin and D. Winkoun, *The Journal of Chemical Physics*, 1985, **83**, 6222–6228.

(211) T. Masuoka, *Physical Review A*, 1994, **50**, 3886–3894.

(212) T. Masuoka, E. Nakamura and A. Hiraya, *Journal of Chemical Physics*, 1996, **104**, 6200–6207.

(213) A. E. Slattery, T. A. Field, M. Ahmad, R. I. Hall, J. Lambourne, F. Penent, P. Lablanquie and J. H. Eland, *Journal of Chemical Physics*, 2005, **122**, 84317.

(214) Z. D. Pešić, D. Rolles, M. Perri, R. C. Bilodeau, G. D. Ackerman, B. S. Rude, A. L. Kilcoyne, J. D. Bozek and N. Berrah, *Journal of Electron Spectroscopy and Related Phenomena*, 2007, **155**, 155–159.

(215) M. Alagia, P. Candori, S. Falcinelli, M. Lavollée, F. Pirani, R. Richter, S. Stranges and F. Vecchiocattivi, *Journal of Physical Chemistry A*, 2009, **113**, 14755–14759.

(216) M. Alagia, P. Candori, S. Falcinelli, M. Lavollée, F. Pirani, R. Richter, S. Stranges and F. Vecchiocattivi, *Physical Chemistry Chemical Physics*, 2010, **12**, 5389–5395.

(217) C. Wu, G. Zhang, C. Wu, Y. Yang, X. Liu, Y. Deng, H. Liu, Y. Liu and Q. Gong, *Physical Review A - Atomic, Molecular, and Optical Physics*, 2012, **85**, 63407.

(218) S. Larimian, S. Erattupuzha, S. Mai, P. Marquetand, L. González, A. Baltuška, M. Kitzler and X. Xie, *Physical Review A*, 2017, **95**, 11404.

(219) J. Long, F. J. Furch, J. Durá, A. S. Tremsin, J. Vallerga, C. P. Schulz, A. Rouzée and M. J. Vrakking, *Journal of Chemical Physics*, 2017, **147**, 13919.

(220) M. Hochlaf, F. R. Bennett, G. Chambaud and P. Rosmus, *Journal of Physics B: Atomic, Molecular and Optical Physics*, 1998, **31**, 2163–2175.

(221) S. Hsieh and J. H. Eland, *Journal of Physics B: Atomic, Molecular and Optical Physics*, 1997, **30**, 4515–4534.

(222) V. Lew, E. McKay and M. Maze, *British Medical Bulletin*, 2018, **125**, 103–119.

(223) V. Zakirov, M. Sweeting, T. Lawrence and J. Sellers, *Acta Astronautica*, 2001, **48**, 353–362.

(224) D. Ehhalt, M. Prather, F. Dentener, R. Derwent, E. Dlugokencky, E. Holland, I. Isaksen, J. Katima, V. Kirchhoff, P. Matson, P. Midgley, M. Wang, T. Berntsen, I. Bey, G. Brasseur, L. Buja, W. Collins, J. Daniel, W. DeMore, N. Derek, R. Dickerson, D. Etheridge, J. Feichter, P. Fraser, R. Friedl, J. Fuglestvedt, M. Gauss, L. Grenfell, A. Grübler, N. Harris, D. Hauglustaine, L. Horowitz, C. Jackman, D. Jacob, L. Jaeglé, A. Jain, M. Kanakidou, S. Karlsdottir, M. Ko, M. Kurylo, M. Lawrence, J. Logan, M. Manning, D. Mauzerall, J. McConnell, L. Mickley, S. Montzka, J. Müller, J. Olivier, K. Pickering, G. Pitari, G. Roelofs, H. Rogers, B. Rognerud, S. Smith, S. Solomon, J. Staehelin, P. Steele, D. Stevenson, J. Sundet, A. Thompson, V. M., R. Weele, V. Kuhlmann, Y. Wang, D. Weisenstein, T. Wigley, O. Wild, D. Wuebbles, R. Yantosca, F. Joos and M. McFarland, in *Climate Change 2001: The Scientific Basis. Contribution of Working Group I to the Third Assessment Report of the Intergovernmental Panel on Climate Change*, ed. J. Houghton, Y. Ding, D. Griggs, M. Noguer, P. van der Linden, X. Dai, K. Maskell and C. Johnson, Cambridge University Press, Cambridge, 2001, ch. 4, p. 881.

(225) R. L. Thompson, L. Lassaletta, P. K. Patra, C. Wilson, K. C. Wells, A. Gressent, E. N. Koffi, M. P. Chipperfield, W. Winiwarter, E. A. Davidson, H. Tian and J. G. Canadell, *Nature Climate Change*, 2019, **9**, 993–998.

(226) P. J. Crutzen, *Quarterly Journal of the Royal Meteorological Society*, 1970, **96**, 320–325.

(227) A. R. Ravishankara, J. S. Daniel and R. W. Portmann, *Science*, 2009, **326**, 123–125.

(228) L. M. Ziurys, A. J. Apponi, J. M. Hollis and L. E. Snyder, *The Astrophysical Journal*, 1994, **436**, L181.

(229) D. T. Halfen, A. J. Apponi and L. M. Ziurys, *The Astrophysical Journal*, 2001, **561**, 244–253.

(230) C. S. Jamieson, C. J. Bennett, A. M. Mebel and R. I. Kaiser, *The Astrophysical Journal*, 2005, **624**, 436–447.

(231) I. Iga, M. V. Rao and S. K. Srivastava, *Journal of Geophysical Research E: Planets*, 1996, **101**, 9261–9266.

(232) B. G. Lindsay, R. Rejoub and R. F. Stebbings, *Journal of Chemical Physics*, 2003, **118**, 5894–5900.

(233) N. A. Love and S. D. Price, *Physical Chemistry Chemical Physics*, 2004, **6**, 4558–4565.

(234) J. L. Olivier, R. Locht and J. Momigny, *Chemical Physics*, 1982, **68**, 201–211.

(235) J. L. Olivier, R. Locht and J. Momigny, *Chemical Physics*, 1984, **84**, 295–309.

(236) R. Locht and J. Schopman, *International Journal of Mass Spectrometry and Ion Physics*, 1974, **15**, 361–378.

(237) M. Richard-Viard, O. Atabek, O. Dutuit and P. M. Guyon, *The Journal of Chemical Physics*, 1990, **93**, 8881–8892.

(238) H. Xu, Y. Guo, Q. Li, Y. Shi, S. Liu and X. Ma, *Journal of Chemical Physics*, 2004, **121**, 3069–3073.

(239) H. Wang, X. Zhou, S. Liu, B. Jiang, D. Dai and X. Yang, *Journal of Chemical Physics*, 2010, **132**, 244309.

(240) M. Lebech, J. C. Houver, D. Dowek and R. R. Lucchese, *Journal of Chemical Physics*, 2004, **120**, 8226–8240.

(241) M. Lebech, J. C. Houver, D. Dowek and R. R. Lucchese, *Journal of Chemical Physics*, 2002, **117**, 9248–9257.

(242) X. Tang, M. Niu, X. Zhou, S. Liu, F. Liu, X. Shan and L. Sheng, *Journal of Chemical Physics*, 2011, **134**, 54312.

(243) S. Taylor, J. H. Eland and M. Hochlaf, *Journal of Chemical Physics*, 2006, **124**, 204319.

(244) S. D. Price, J. H. Eland, P. G. Fournier, J. Fournier and P. Millie, *The Journal of Chemical Physics*, 1988, **88**, 1511–1515.

(245) A. Hishikawa, A. Iwamae, K. Hoshina, M. Kono and K. Yamanouchi, *Research on Chemical Intermediates*, 1998, **24**, 765–784.

(246) M. Ueyama, H. Hasegawa, A. Hishikawa and K. Yamanouchi, *Journal of Chemical Physics*, 2005, **123**, 154305.

(247) X. Zhou, P. Ranitovic, C. W. Hogle, J. H. Eland, H. C. Kapteyn and M. M. Murnane, *Nature Physics*, 2012, **8**, 232–237.

(248) M. Kübel, A. S. Alnaser, B. Bergues, T. Pischke, J. Schmidt, Y. Deng, C. Jendrzejewski, J. Ullrich, G. G. Paulus, A. M. Azzeer, U. Kleineberg, R. Moshammer and M. F. Kling, *New Journal of Physics*, 2014, **16**, 65017.

(249) K. B. Jefferts, A. A. Penzias, R. W. Wilson and P. M. Solomon, *The Astrophysical Journal*, 1971, **168**, L111.

(250) S. B. Charnley, P. Ehrenfreund and Y. J. Kuan, *Spectrochimica Acta - Part A: Molecular and Biomolecular Spectroscopy*, 2001, **57**, 685–704.

(251) R. F. Ferrante, M. H. Moore, M. M. Spiliotis and R. L. Hudson, *The Astrophysical Journal*, 2008, **684**, 1210–1220.

(252) E. Lellouch, G. Paubert, R. Moreno, M. C. Festou, B. Bézard, D. Bockelée-Morvan, P. Colom, J. Crovisier, T. Encrenaz, D. Gautier, A. Marten, D. Despois, D. F. Strobel and A. Sievers, *Nature*, 1995, **373**, 592–595.

(253) B. Bézard, C. De Bergh, D. Crisp and J. P. Maillard, *Nature*, 1990, **345**, 508–511.

(254) M. Chin and D. D. Davis, *Journal of Geophysical Research*, 1995, **100**, 8993–9005.

(255) S. A. Montzka, P. Calvert, B. D. Hall, J. W. Elkins, T. J. Conway, P. P. Tans and C. S. Sweeney, *Journal of Geophysical Research Atmospheres*, 2007, **112**, DOI: 10.1029/2006JD007665.

(256) S. Hattori, K. Kamezaki and N. Yoshida, *Proceedings of the National Academy of Sciences*, 2020, **117**, 202007260.

(257) C. Brühl, J. Lelieveld, P. J. Crutzen and H. Tost, *Atmospheric Chemistry and Physics*, 2012, **12**, 1239–1253.

(258) W. E. Wallace, in *NIST Chemistry WebBook, NIST Standard Reference Database Number 69*, ed. P. Linstrom and W. Mallard, retrieved 16th October 2020, National Institute of Standards and Technology, Gaithersburg MD, 20899.

(259) O. D. Sparkman, Z. E. Penton and F. G. Kitson, in, ed. O. D. Sparkman, Z. E. Penton, F. G. B. T. G. C. Kitson and M. S. (Edition), Academic Press, Amsterdam, 2011, pp. 89–148.

(260) P. Wang and C. R. Vidal, *Journal of Chemical Physics*, 2003, **118**, 5383–5389.

(261) J. R. De Laeter, J. K. Böhlke, P. De Bièvre, H. Hidaka, H. S. Peiser, K. J. Rosman and P. D. Taylor, *Pure and Applied Chemistry*, 2003, **75**, 683–800.

(262) T. E. Graedel, G. W. Kammlott and J. P. Franey, *Science*, 1981, **212**, 663–665.

(263) M. J. Hubin-Franskin, J. Delwiche, P. M. Guyon, M. Richard-Viard, M. Lavollée, O. Dutuit, J. M. Robbe and J. P. Flament, *Chemical Physics*, 1996, **209**, 143–157.

(264) J. Delwiche, M. J. Hubin-Franskin, P. M. Guyon and I. Nenner, *The Journal of Chemical Physics*, 1981, **74**, 4219–4227.

(265) J. H. Eland, *International Journal of Mass Spectrometry and Ion Physics*, 1973, **12**, 389–395.

(266) D. M. Hirst, *Molecular Physics*, 2006, **104**, 55–60.

(267) C. Chang, C. Y. Luo and K. Liu, *Journal of Physical Chemistry A*, 2005, **109**, 1022–1025.

(268) F. Carnovale, A. P. Hitchcock, J. P. Cook and C. E. Brion, *Chemical Physics*, 1982, **66**, 249–259.

(269) S. Morse, M. Takehashi, J. H. Eland and L. Karsson, *International Journal of Mass Spectrometry*, 1999, **184**, 67–74.

(270) J. P. D. Cook, M. G. White, C. E. Brion, W. Domcke, J. Schirmer, L. S. Cederbaum and W. von Niessen, *Journal of Electron Spectroscopy and Related Phenomena*, 1981, **22**, 261–270.

(271) M. G. White, K. T. Leung and C. E. Brion, *Journal of Electron Spectroscopy and Related Phenomena*, 1981, **23**, 127–145.

(272) T. Masuoka, I. Koyano and N. Saito, *The Journal of Chemical Physics*, 1992, **97**, 2392–2399.

(273) V. Brites, J. H. Eland and M. Hochlaf, *Chemical Physics*, 2008, **346**, 23–33.

(274) T. Masuoka, *The Journal of Chemical Physics*, 1993, **98**, 6989–6994.

(275) R. G. Cooks, D. T. Terwilliger and J. H. Beynon, *The Journal of Chemical Physics*, 1974, **61**, 1208–1213.

(276) L. E. Snyder, J. M. Hollis, B. L. Ulich, F. J. Lovas, D. R. Johnson and D. Buhl, *The Astrophysical Journal*, 1975, **198**, L81.

(277) F. P. Schloerb, W. M. Irvine, P. Friberg, A. Hjalmarson and B. Hoglund, *The Astrophysical Journal*, 1983, **264**, 161.

(278) W. M. Irvine, J. C. Good and F. P. Schloerb, *Astronomy and Astrophysics*, 1983, **127**, L10–L13.

(279) J. E. Dickens, W. M. Irvine, R. L. Snell, E. A. Bergin, F. P. Schloerb, P. Pratap and M. P. Miralles, *The Astrophysical Journal*, 2000, **542**, 870–889.

(280) P. Schilke, D. J. Benford, T. R. Hunter, D. C. Lis and T. G. Phillips, *The Astrophysical Journal Supplement Series*, 2001, **132**, 281–364.

(281) J. Cernicharo, A. Spielfiedel, C. Balança, F. Dayou, M.-L. Senent, N. Feautrier, A. Faure, L. Cressiot-Vincent, L. Wiesenfeld and J. R. Pardo, *A&A*, 2011, **531**.

(282) C. Laver and I. de Pater, *Icarus*, 2008, **195**, 752–757.

(283) A. L. Broadfoot, M. J. Belton, P. Z. Takacs, B. R. Sandel, D. E. Shemansky, J. B. Holberg, J. M. Ajello, S. K. Atreya, T. M. Donahue, H. W. Moos, J. L. Bertaux, J. E. Blamont, D. F. Strobel, J. C. McConnell, A. Dalgarno, R. Goody and M. B. McElroy, *Science*, 1979, **204**, 979–982.

(284) C. F. Cullis and M. M. Hirschler, *Atmospheric Environment (1967)*, 1980, **14**, 1263–1278.

(285) A. L. Barbu, A. J. Segers, M. Schaap, A. W. Heemink and P. J. Builtjes, *Atmospheric Environment*, 2009, **43**, 1622–1631.

(286) Y. N. Novoselov, G. A. Mesyats and D. L. Kuznetsov, *Journal of Physics D: Applied Physics*, 2001, **34**, 1248–1255.

(287) I. M. Cadez, V. M. Pejcev and M. V. Kurepa, *Journal of Physics D: Applied Physics*, 1983, **16**, 305–314.

(288) J. D. Fletcher, M. A. Parkes and S. D. Price, *Journal of Chemical Physics*, 2013, **138**, 184309.

(289) B. G. Lindsay, H. C. Straub, K. A. Smith and R. F. Stebbings, *Journal of Geophysical Research: Planets*, 1996, **101**, 21151–21156.

(290) R. Basner, M. Schmidt, H. Deutsch, V. Tarnovsky, A. Levin and K. Becker, *The Journal of Chemical Physics*, 1995, **103**, 211–218.

(291) G. Dujardin and S. Leach, *The Journal of Chemical Physics*, 1981, **75**, 2521–2531.

(292) J. Erickson and C. Y. Ng, *The Journal of Chemical Physics*, 1981, **75**, 1650–1657.

(293) T. Masuoka, Y. Chung, E. M. Lee and J. A. Samson, *Journal of Chemical Physics*, 1998, **109**, 2246–2253.

(294) L. Zhang, Z. Wang, J. Li, F. Wang, S. Liu, S. Yu and X. Ma, *Journal of Chemical Physics*, 2003, **118**, 9185–9191.

(295) W. Z. Li and M. B. Huang, *Journal of Physical Chemistry A*, 2004, **108**, 6901–6907.

(296) T. A. Field and J. H. Eland, *International Journal of Mass Spectrometry*, 1999, **192**, 281–288.

(297) T. Masuoka, *International Journal of Mass Spectrometry*, 2001, **209**, 125–131.

(298) M. Hochlaf and J. H. Eland, *Journal of Chemical Physics*, 2004, **120**, 6449–6460.

(299) R. Baan, Y. Grosse, K. Straif, B. Secretan, F. El Ghissassi, V. Bouvard, L. Benbrahim-Tallaa, N. Guha, C. Freeman, L. Galichet and V. Cogliano, *The lancet oncology*, 2009, **10**, 1143–1144.

(300) A. M. Niziolek, O. Onel and C. A. Floudas, *AIChE Journal*, 2016, **62**, 1531–1556.

(301) B. M. Jones, F. Zhang, R. I. Kaiser, A. Jamal, A. M. Mebel, M. A. Cordiner and S. B. Charnley, *Proceedings of the National Academy of Sciences of the United States of America*, 2011, **108**, 452–457.

(302) C. Joblin and G. Mulas, *EAS Publications Series*, 2009, **35**, 133–152.

(303) S. Schlemmer, D. J. Cook, J. A. Harrison, B. Wurfel, W. Chapman and R. J. Saykally, *Science*, 1994, **265**, 1686–1689.

(304) W. W. Duley, *Faraday Discussions*, 2006, **133**, 415–425.

(305) H. Linnartz, J. Cami, M. Cordiner, N. L. Cox, P. Ehrenfreund, B. Foing, M. Gatchell and P. Scheier, *Journal of Molecular Spectroscopy*, 2020, **367**, 111243.

(306) K. R. Jennings, *Zeitschrift fur Naturforschung - Section A Journal of Physical Sciences*, 1967, **22**, 454–459.

(307) W. Zhou, D. Phil. University of Oxford, 2018.

(308) A. F. Fucaloro and S. K. Srivastava, *Journal Of The Brazilian Chemical Society*, 1993, **4**, 7–13.

(309) D. M. Holland, D. A. Shaw, I. Sumner, M. A. Bowler, R. A. Mackie, L. G. Shpinkova, L. Cooper, E. E. Rennie, J. E. Parker and C. A. Johnson, *International Journal of Mass Spectrometry*, 2002, **220**, 31–51.

(310) J. H. Beynon, R. M. Caprioli, W. O. Perry and W. E. Baitinger, *Journal of the American Chemical Society*, 1972, **94**, 6828–6833.

(311) H. M. Rosenstock, J. Dannacher and J. F. Liebman, *Radiation Physics and Chemistry*, 1982, **20**, 7–28.

(312) W. J. van der Hart, *International Journal of Mass Spectrometry*, 1998, **176**, 23–38.

(313) W. J. van der Hart, *International Journal of Mass Spectrometry and Ion Processes*, 1997, **171**, 269–272.

(314) J. H. Eland, *Chemical Physics*, 2008, **345**, 82–86.

(315) T. A. Field and J. H. Eland, *Chemical Physics Letters*, 1993, **211**, 436–442.

(316) P. J. Richardson, J. H. Eland and P. Lablanquie, *Organic Mass Spectrometry*, 1986, **21**, 289–294.

(317) M. Alagia, P. Candori, S. Falcinelli, F. Pirani, M. S. Mundim, R. Richter, M. Rosi, S. Stranges and F. Vecchiocattivi, *Physical Chemistry Chemical Physics*, 2011, **13**, 8245–8250.

(318) S. Anand and H. B. Schlegel, *Journal of Physical Chemistry A*, 2005, **109**, 11551–11559.

(319) J. W. L. Lee, D. S. Tikhonov, P. Chopra, S. Maclot, A. L. Steber, S. Gruet, F. Allum, R. Boll, X. Cheng, B. Erk, D. Garg, L. He, D. Heathcote, M. Johny, M. M. Kazemi, H. Köckert, J. Lahl, A. K. Lemmens, D. Loru, R. Mason, E. M. Müller, T. Mullins, P. Olshin, C. Passow, J. Peschel, D. Ramm, D. Rompotis, N. Schirmel, S. Trippel, J. Wiese, F. Ziaee, S. Bari, M. Burt, J. Küpper, A. M. Rijs, D. Rolles, P. Johnsson, M. Brouard, C. Vallance, B. Manschwetus and M. Schnell, 'Time-Resolved Relaxation and Fragmentation of Polycyclic AromaticHydrocarbons Investigated in the Ultrafast XUV-IR Regime', in preparation.

(320) D. S. Parker, R. I. Kaiser, T. P. Troy and M. Ahmed, *Angewandte Chemie - International Edition*, 2014, **53**, 7740–7744.

(321) T. Yang, T. P. Troy, B. Xu, O. Kostko, M. Ahmed, A. M. Mebel and R. I. Kaiser, *Angewandte Chemie - International Edition*, 2016, **55**, 14983–14987.

(322) T. Yang, R. I. Kaiser, T. P. Troy, B. Xu, O. Kostko, M. Ahmed, A. M. Mebel, M. V. Zagidullin and V. N. Azyazov, *Angewandte Chemie - International Edition*, 2017, **56**, 4515–4519.

(323) A. K. Lemmens, D. B. Rap, J. M. Thunnissen, B. Willemsen and A. M. Rijs, *Nature Communications*, 2020, **11**, 269.

(324) J. W. Lee, H. Köckert, D. Heathcote, D. Popat, R. T. Chapman, G. Karras, P. Majchrzak, E. Springate and C. Vallance, *Communications Chemistry*, 2020, **3**, 72.

(325) M. Y. Ivanov, M. Spanner and O. Smirnova, *Journal of Modern Optics*, 2005, **52**, 165–184.

(326) B.-O. Cho, S.-W. Hwang, G.-R. Lee and S. H. Moon, *Journal of Vacuum Science & Technology A: Vacuum, Surfaces, and Films*, 2000, **18**, 2791–2798.

(327) J. H. Kim, J. S. Park and C. K. Kim, *Applied Surface Science*, 2020, **508**, 144787.

(328) M. B. Chang and S. J. Yu, *Environmental Science and Technology*, 2001, **35**, 1587–1592.

(329) A. Misra, J. Sees, L. Hall, R. A. Levy, V. B. Zaitsev, K. Aryusook, C. Ravindranath, V. Sigal, S. Kesari and D. Rufin, *Materials Letters*, 1998, **34**, 415–419.

(330) S. Karecki, L. Pruette, R. Reif, T. Sparks, L. Beu and V. Vartanian, *Journal of The Electrochemical Society*, 1998, **145**, 4305–4312.

(331) B. Boudaïffa, P. Cloutier, D. Hunting, M. A. Huels and L. Sanche, *Science*, 2000, **287**, 1658–1660.

(332) M. A. Huels, B. Boudaïffa, P. Cloutier, D. Hunting and L. Sanche, *Journal of the American Chemical Society*, 2003, **125**, 4467–4477.

(333) L. Sanche, *European Physical Journal D*, 2005, **35**, 367–390.

(334) E. Alizadeh and L. Sanche, *Chemical Reviews*, 2012, **112**, 5578–5602.

(335) W. F. Miller and R. L. Platzman, *Proceedings of the Physical Society. Section A*, 1957, **70**, 299–303.

(336) J. Thomson, *The London, Edinburgh, and Dublin Philosophical Magazine and Journal of Science*, 1912, **23**, 449–457.

(337) M. Gryziński, *Physical Review*, 1965, **138**, A305–A321.

(338) H. Deutsch, K. Becker and T. D. Mark, *International Journal of Mass Spectrometry*, 1998, **177**, 47–50.

(339) H. Deutsch, K. Becker and T. D. Märkc, *International Journal of Mass Spectrometry*, 1999, **185**, 319–326.

(340) R. S. Mulliken, *Journal de Chimie Physique*, 1949, **46**, 497–542.

(341) R. S. Mulliken, *Journal de Chimie Physique*, 1949, **46**, 675–713.

(342) R. S. Mulliken, *The Journal of Chemical Physics*, 1955, **23**, 1833–1840.

(343) A. Einstein, *Jahrbuch der Radioaktivität und Elektronik*, 1907, **4**, 411–462.

Appendices

A

Theoretical determination of total ionisation cross-sections

A number of theoretical methods exist for determining total ionisation cross-sections. We will now review a number of the methods available to calculate total ionisation cross-sections.

A.1 The Jain-Khare semi-empirical formalism

The Jain-Khare semi-empirical formalism, developed by Jain and Khare,[42,43] combines Mott[93] and Born-Bethe cross-sections[95] to obtain an expression for the ionisation cross-section. The two cross-sections are combined to give the following

equation for the ionisation cross-section

$$\sigma(E,\xi) = \frac{4\pi a_0 R}{E}\left[\frac{1}{1+I/E}\left(1-\frac{\xi}{E-I}\right)\frac{R}{w}\frac{df_i(w,0)}{dw}\ln\left(1+C\left(E-I\right)\right)+ S\frac{\left(E-I\right)R}{E\left(\xi^3+\xi_0^3\right)}\left(\xi-\frac{\xi^2}{E-\xi}+\frac{\xi^3}{\left(E-\xi\right)^2}\right)\right] \quad \text{(A.1)}$$

where E is the energy of the incident electron, ξ is the energy of the secondary electron, a_0 is the Bohr radius, R is the Rydberg constant, I is the ionisation energy, w is the energy loss of the incident electron, $df(w,0)/dw$ is the optical oscillator strength for the production of an ion by a photon of wavelength w, C is a collision parameter defined by Miller and Platzman,[335] and ξ_0 is a mixing parameter, chosen such that theoretical results are in best agreement with experimental data for a given molecule.

Khare and Meath also discuss the extension of the model to attempt to predict partial ionisation cross-sections.[43] By integrating equation A.1 over values of ξ from 0 to $\frac{(E-I)}{2}$, an expression of the partial ionisation cross-section can be obtained. This requires dipole oscillator strengths for the production of each ion as a function of energy. However, they found that the partial ionisation cross-sections obtained greatly underestimated experimentally-determined cross-sections.

A.2 The complex scattering potential-ionisation contribution (CSP-ic) method

The complex scattering potential-ionisation contribution (CSP-ic) method determines the total ionisation cross-section from a calculated inelastic cross-section.[44,45] The inelastic cross-section has two main contributions, one from the total excitation cross-sections for all available transitions, and the other from the total ionisation cross-section. First, the complex scattering potential is determined, consisting of a real part consisting of the static, exchange and polarisation potentials, and an

imaginary part accounting for electronic excitation and ionisation, and is used to determine the inelastic and elastic cross-sections for the system under study.

To estimate the total ionisation cross-section, Joshipura *et al.* define the ratio between the ionisation and inelastic cross-sections at an incident electron energy E_i as follows

$$R(E_i) = \frac{\sigma_{\text{ion}}(E_i)}{\sigma_{\text{inel}}(E_i)} \tag{A.2}$$

where $\sigma_{\text{ion}}(E_i)$ and $\sigma_{\text{inel}}(E_i)$ are the ionisation and inelastic cross-section, respectively. It is necessary that below the ionisation energy, $R(E_i)$ should equal zero, and that $R(E_i)$ should tend to one as E_i tends to infinity, with some continuous function describing its behaviour at intermediate energies. They also note that at the peak of the inelastic cross-section, $R(E_i)$ is generally found to take a value of around 0.7 to 0.8, and have thus set $R(E_i)$ equal to 0.7. They then define a function for $R(E_i)$ based on three variable parameters

$$R(E_i) = 1 - C_1 \left[\frac{C_2}{U + a} + \frac{\ln U}{U} \right] \tag{A.3}$$

where $U = \frac{E_i}{I}$, I is the ionisation energy, and a, C_1 and C_2 are dimensionless parameters that reflect the properties of the target molecule. The two terms in the square brackets account for different energy regimes, with the first term largely determining the behaviour at low and intermediate incident electron energies, whilst the second term determining the behaviour at high incident electron energies. As there are three conditions and three unknowns, it is possible to determine a, C_1, and C_2 by using the peak of the inelastic cross-section, determined in the first step or experimentally. The cross-sections generally show good agreement with experimentally-determined total ionisation cross-sections.

A.3 The Deutsch-Märk formalism

The Deutsch-Märk formalism, developed by Deutsch, Märk, and co-workers,[46,48] has its origin in Thompson's classical binary-encounter approximation.[336] By assuming the atomic electron has a continuous velocity distribution, Gryziński found a new expression for the total electron ionisation cross-section[337] which is given by[48]

$$\sigma = \sum_{n,l} 4\pi a_0^2 \xi_n \left(\frac{R}{E_{nl}}\right)^2 f(U) \tag{A.4}$$

$$f(U) = d\left(\frac{1}{U}\right)\left[\frac{U-1}{U+1}\right]^a \times \left(b + c\left[1 - \left(\frac{1}{2U}\right)\right]\ln\left[2.7 + (U-1)^{0.5}\right]\right) \tag{A.5}$$

$$\tag{A.6}$$

where a_0 is the Bohr radius, ξ_n is the number of electrons in the n^{th} atomic subshell, R is the Rydberg constant, E_{nl} is the ionisation energy of the n^{th} subshell, U is the reduced energy given by $\frac{E}{E_{nl}}$, where E is the energy of the incident electron, and a, b, c and d are parameters dependent on the shell from which the electrons are ejected, but in the initial formulation of the model they took the values $\frac{3}{2}$, one, $\frac{2}{3}$, and one, respectively. Deutsch and Märk postulated that the term $4a_0^2$ could be replaced by $g_{nl}(r_{nl})^2$, where g_{nl} is a weighting factor and r_{nl} the mean square radius of the subshell described by the principal quantum number n and the angular quantum number l. Initially, the weighting factor was determined to be three for s electrons and 0.5 otherwise. Subsequent studies lead to refinements to this initial formulation; both the weighting factors g_{nl} and the parameters a, b, c, and d[338,339] were adjusted to improve the model.

The model can also be extended to molecules by utilising the additivity rule. Margreiter *et al.* determine the cross-section of each molecular orbital by calculating the cross-section of each atomic orbital, identifying the contribution of each atomic orbital to the molecular orbitals by carrying out a Mulliken population analysis,[340–342] and then using the effective occupancy of each orbital to determine

the total cross-section.[47] As the valence orbitals of each molecule largely determine the ionisation cross-section, the method is highly sensitive to the quality of the Mulliken analysis carried out; differences in Mulliken representation can lead to large variation in both peak height and position for the cross-section.[48]

B

Non-critical derivations

B.1 Beer-Lambert law

The Beer-Lambert law is used to describe a cross-section with a related change in flux. Perhaps the most widespread application of this law is in colourimetric analysis, where it can be used to describe the absorption of light by a medium, but this is not the only system to which this law can be applied. For example, it can be used to describe the ionisation cross-section of a molecule, as is the case for the beam-gas experiment discussed in the introduction of this thesis. A general derivation is given below.

Consider a container filled with some absorbing sample, with an absorption cross-section σ and number density n. Radiation of intensity I_0 and a cross-sectional area A propagates through the sample, travelling a length l, after which the intensity is I. We can take an infinitesimally thin slice of length dl at a position x along the length l, the change in intensity at x, dI_x, is given by the intensity at position x, I_x, multiplied by the absorption in the slice dl, A_{dl}, i.e.

$$dI_x = I_x A_{dl} \tag{B.1}$$

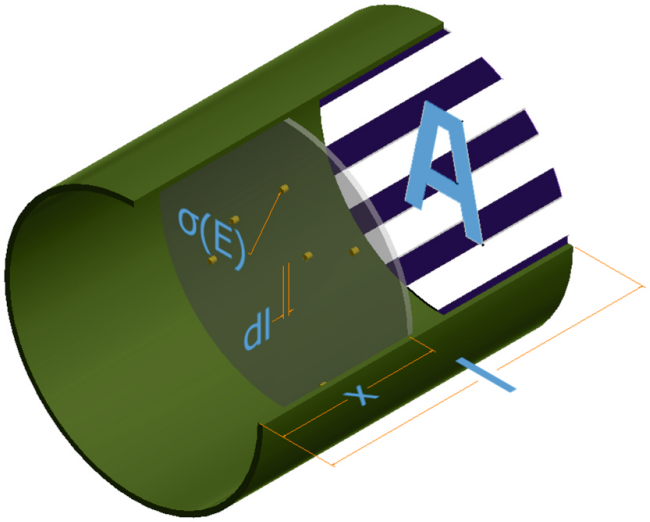


Figure B.1 A depiction of the various dimensions required in the derivation of the Beer-Lambert law. Note that the relative sizes of the dimensions will be significantly different to these in a real system.

A_{dl} is found by multiplying the number density by the volume of the slice to give the total number of absorbing particles in the slice, and the contribution of each molecule is described by the absorption cross-section. This is then divided by the area of the propagating radiation, to give

$$A_{dl} = \frac{n\sigma A\ dl}{A} \tag{B.2}$$

Thus, it follows that

$$dI_x = -I_x n\sigma\ dl \tag{B.3}$$

This expression can be rearranged and the two integrals carried out as follows

$$\int_I^{I_0} \frac{1}{I_x}\ dl = \int_l^0 n\sigma\ dl \tag{B.4}$$

$$\log_e \frac{I}{I_0} = -n\sigma l \tag{B.5}$$

$$\frac{I}{I_0} = e^{-n\sigma l} \tag{B.6}$$

$$\tag{B.7}$$

This is the Beer-Lambert law.

B.2 Dalitz plots

Dalitz plots[156] are used to describe three-body decays. They reduce the twelve-dimensional problem to just two degrees of freedom, allowing the three-body scattering process to be easily displayed in graphical form. This can be justified in the following way:

Consider the dissociation P $\rightarrow$ A + B + C. Each of the product ions can be described by a four-momentum of the form:

$$\left[\frac{E}{c},\ p_x,\ p_y,\ p_z\right] \tag{B.8}$$

This results in three four-vectors, giving a total of twelve dimensions. The energy E is famously given by the expression $E = mc^2$, where c is the speed of light, and m is the mass at velocity v, given by the expression $m = \gamma m_0$, where γ is given by

$$\gamma = \frac{1}{\left(1 - \frac{v^2}{c^2}\right)^{0.5}} \tag{B.9}$$

and m_0 is the rest, or intrinsic, mass of the object.[343] It also follows from Einstein's work that momentum is given by $\mathbf{p} = m\mathbf{v}$, and from this the energy-momentum relation can be established:

$$E^2 = (pc)^2 + \left(m_0c^2\right)^2 \tag{B.10}$$

For the three-body dissociation, energy and momentum must be conserved, the rest mass of A, B and C must remain constant, and the spatial orientation is unimportant. Using these constraints, from equation B.10, it is apparent that the energy is constrained by m_0 and $\mathbf{p}$, removing three degrees of freedom. Momentum must be conserved, which allows another three degrees of freedom to be removed. The

dissociation must occur in a plane, so provided the x, y and z components of the momentum are all measured, we can rotate the system such that one of the components is zero in all cases, reducing the number of degrees of freedom by two. Finally, we can rotate the system about the origin such that one of the momenta always lies along a given axis, further reducing the number of degrees by two, leaving only two degrees of freedom in the system. This serves to demonstrate that a three-body dissociation can be described fully by two variables.

Of course, there are multiple other ways of defining the two degrees of freedom of the system, and the degrees of freedom are chosen depending on the goal of the analysis. In Dalitz's original work on the decay of a τ-meson at rest,[156] the x co-ordinate was chosen to be $\frac{3^0.5(E_A - E_B)}{Q}$ and the y co-ordinate was chosen to be $\frac{(2E_C - E_A - E_B)}{Q}$, where Q is the total kinetic energy, given by $Q = (m_P - m_A - m_B - m_C)\, c^2$.

C

Scattering distributions and recoil-frame covariance maps recorded for benzene at 75 eV

As noted in the main text, we chose to only include the data recorded at an electron energy of 100 eV in the benzene section (section 5.5). Here, we provide both the scattering distributions and recoil-frame covariance maps recorded for deuterated benzene at an electron energy of 75 eV.

Figure C.1 Scattering distributions for all fragments of deuterated benzene recorded at an electron energy of 75 eV. The left column shows the symmetrised image, the central column the inverted image, and the right column the kinetic energy release. D^+ and $CD_x{}^+$.

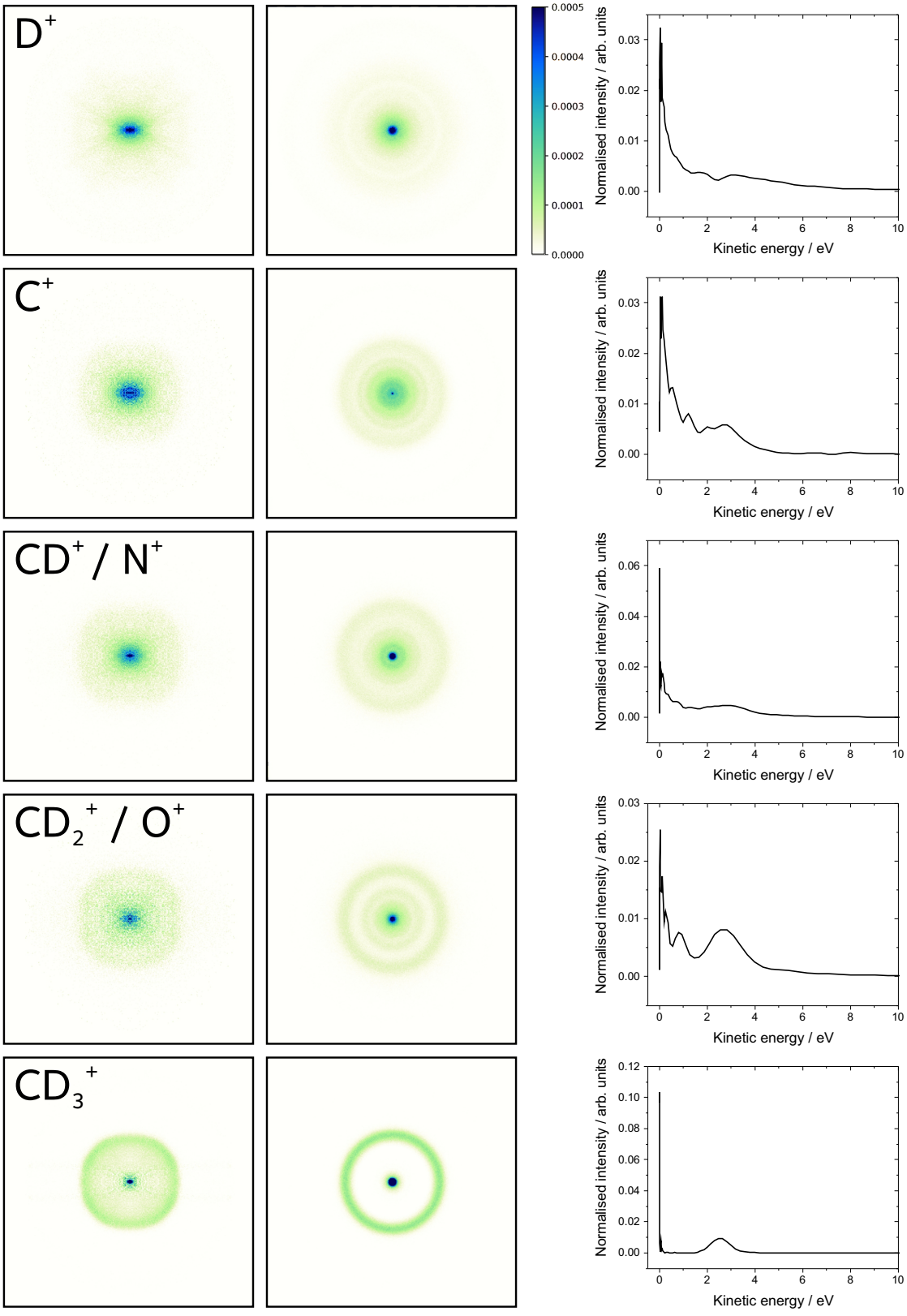


Figure C.1 (continued) C_2D_x $^+$

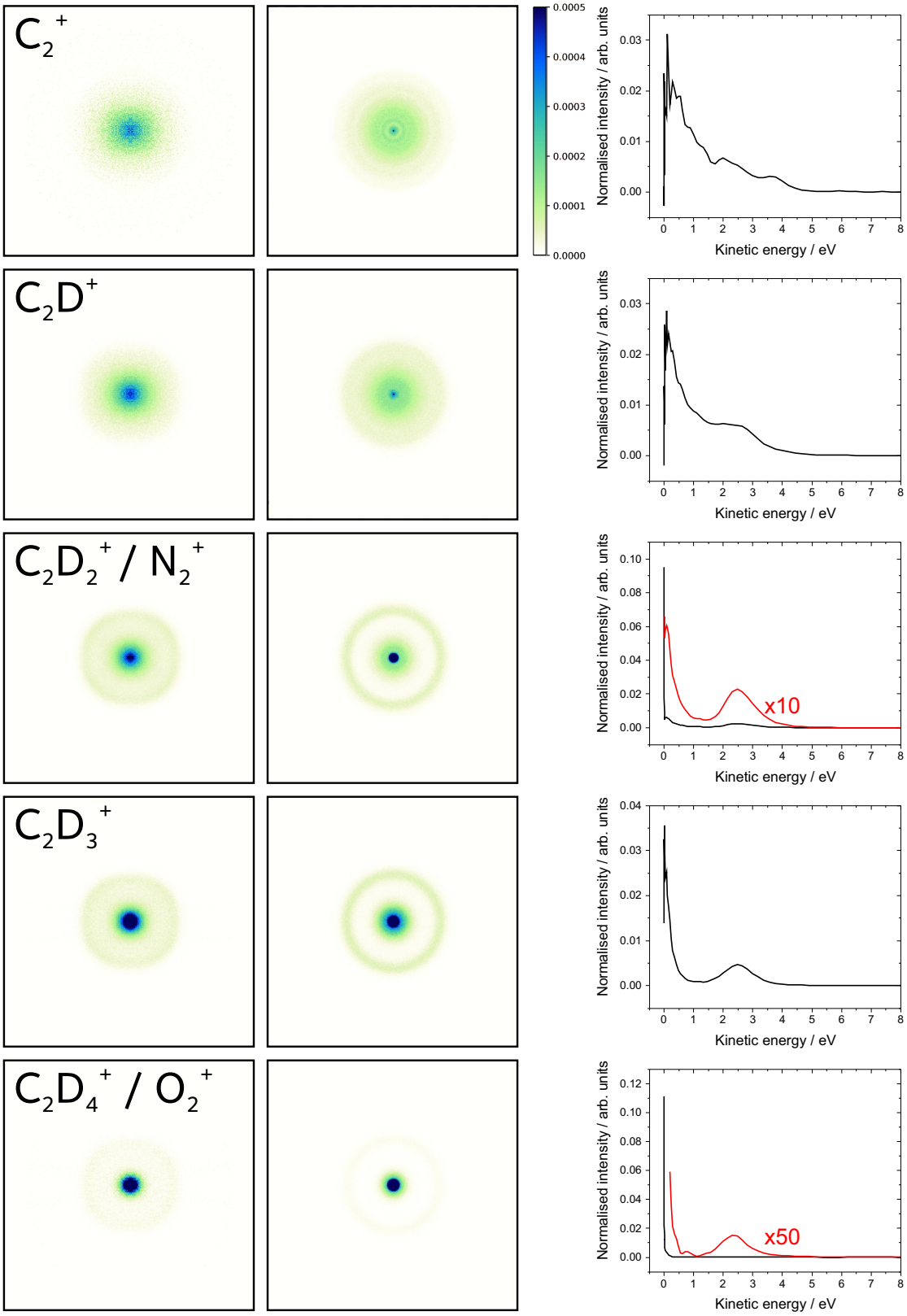


Figure C.1 (continued) $C_3D_x^+$

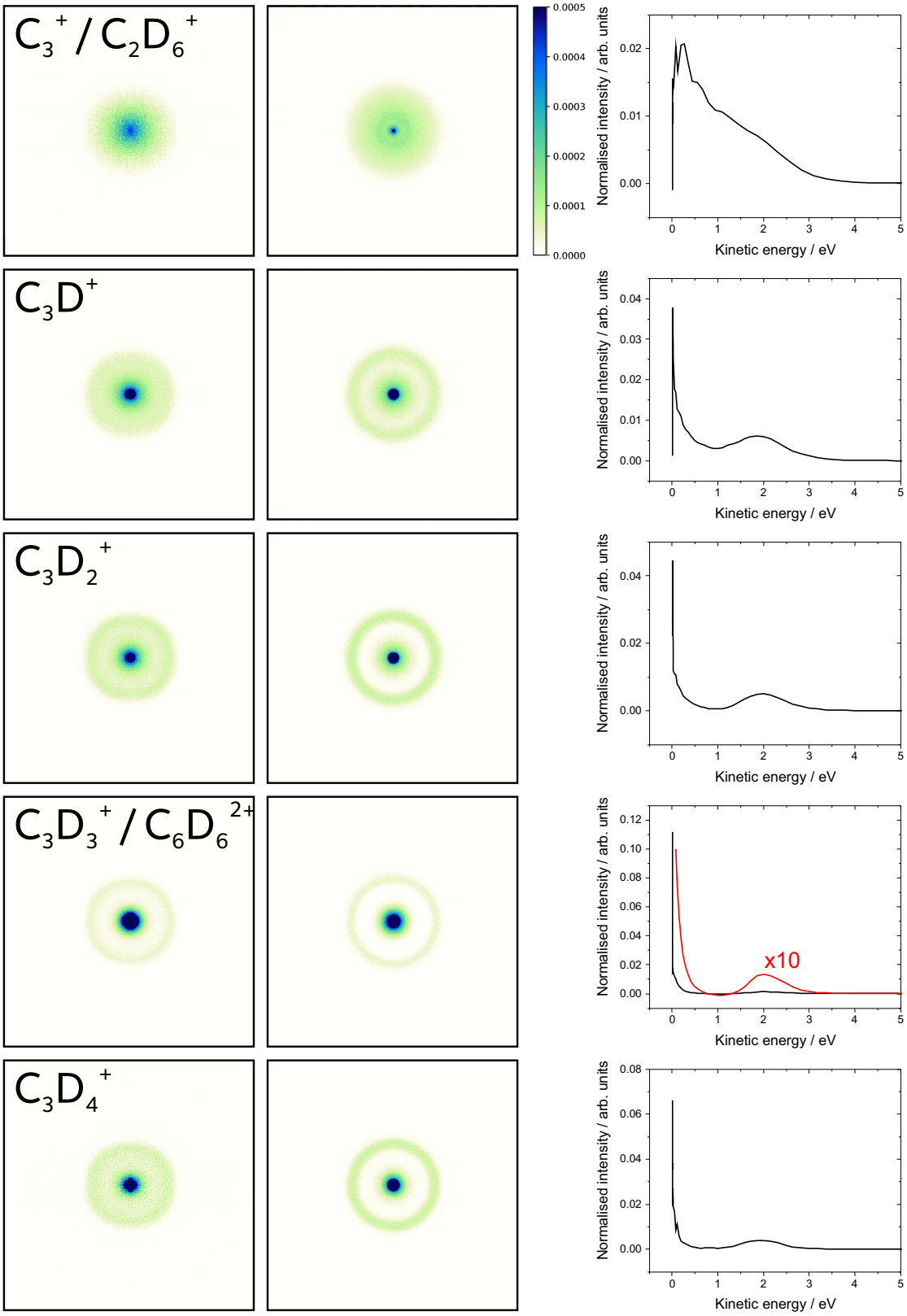


Figure C.1 (continued) $C_4D_x{}^+$

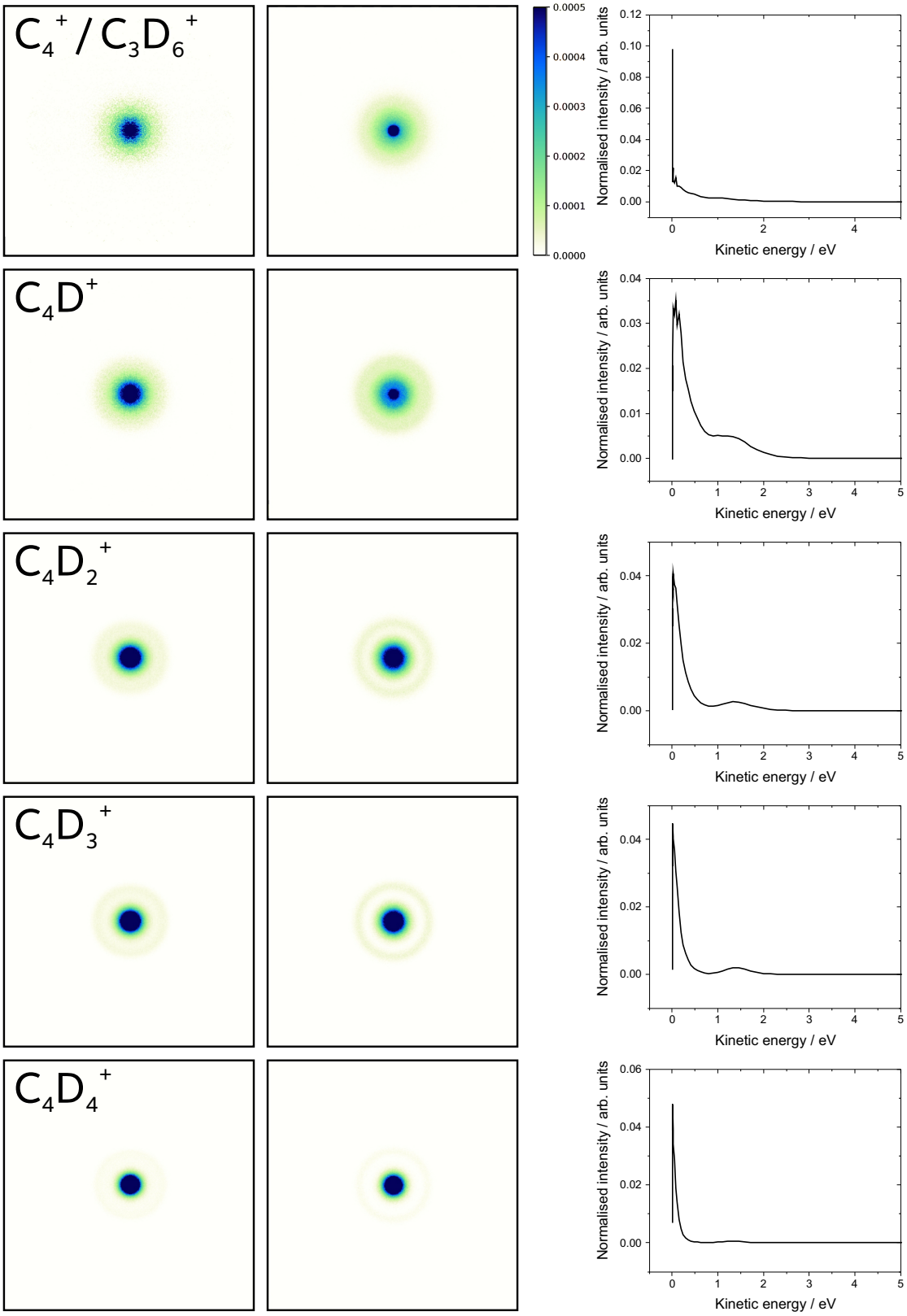
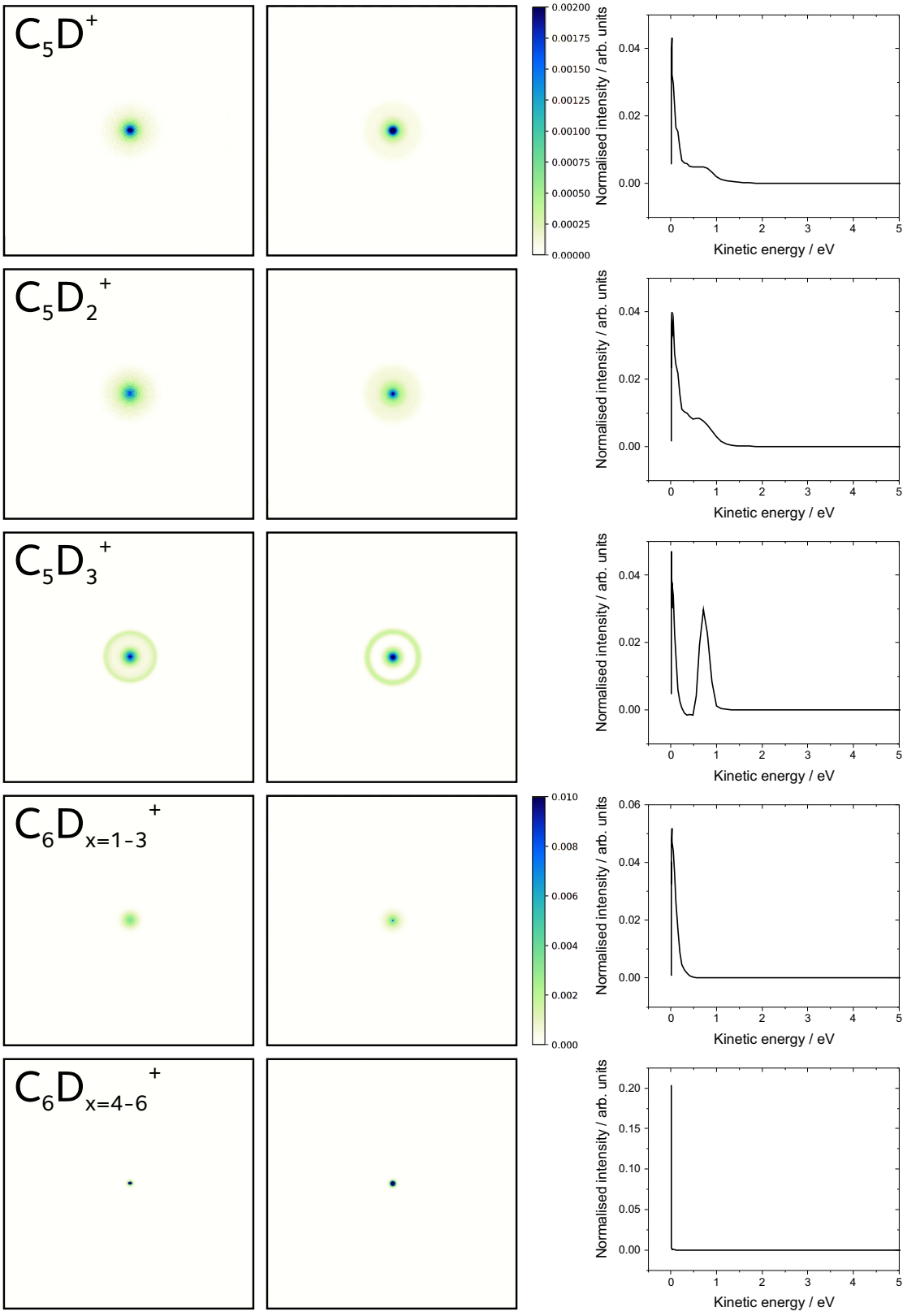


Figure C.1 (continued) $C_5D_x^+$ / $C_6D_x^+$



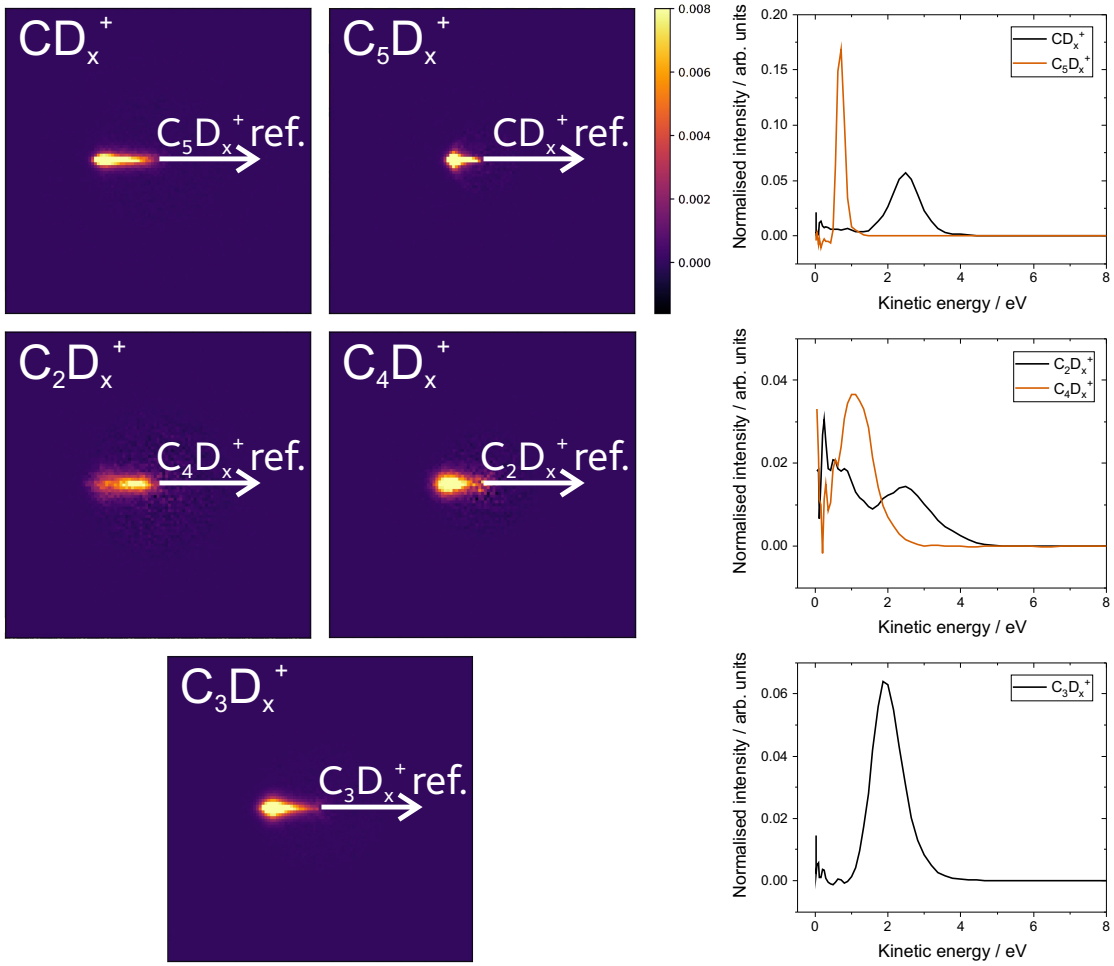


Figure C.2 Recoil-frame covariance maps for two-body dissociation of benzene at an electron energy of 75 eV, along with the corresponding kinetic energy distribution of each fragment in the covariance image (the signal ion is labelled in the kinetic energy distribution plot).

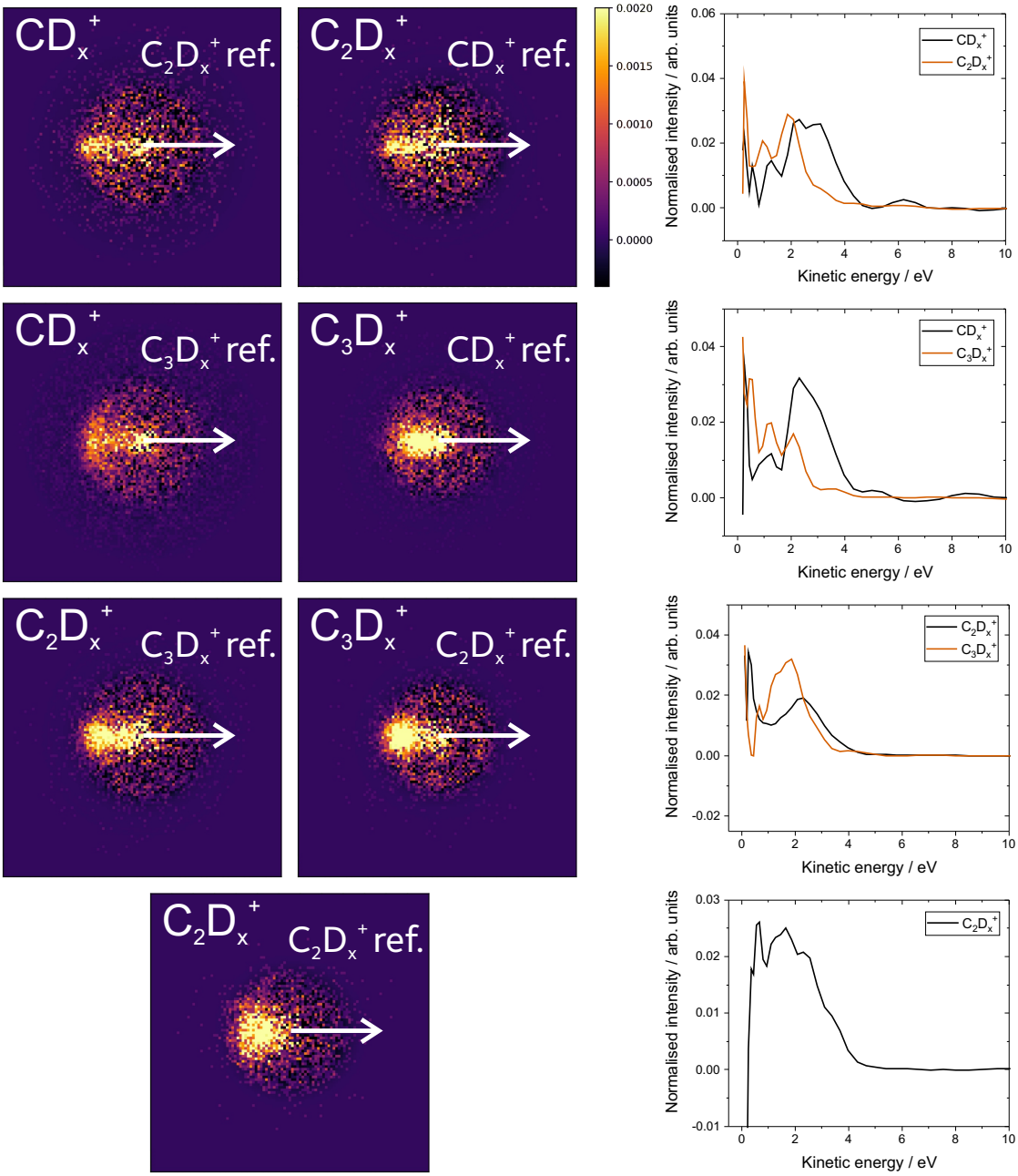


Figure C.3 Recoil-frame covariance maps for multi-body dissociation of benzene at an electron energy of 75 eV. The kinetic energy of each signal ion with respect to the reference ion is plotted on the right.

D

Key codes for data analysis

D.1 Imgread

This package contains code for reading both PImMS and delimited text files.

```
import numpy as np

class pimms():
    """Class which can process binary PImMS files (to some extent at least!).

    Requires:
        filename - the path to a PImMS file

    Optional:
        frames_to_skip - Defaults to zero. Must be an integer
        frames_to_proc - Defaults to all (-1). Must be an integer

        **Please note that there is no check to see if this combination actually
        processes any frames, so be careful when selecting values**

    Provides the following functions:
        read_full_data()
                - Adds full_image, no_frames, tof variables to class
                - Reads the entire PImMS file, stores an image for each timecode

        read_full_image_data()
                - Adds full_image and no_frames to the class
                - Reads the entire PImMS file, stores an image for each timecode
```

```
24
25          read_full_image_data_legacy()
26                  - A slower version of read_full_image_data() {
    approx. 10x}
27                  - Do not use this. Included for completeness
28
29          read_image_data_subset(minimum_timecode,maximum_timecode)
30                  - Adds subset_image, time_codes and no_frames to
    the class
31                  - Same as read_full_image_data, but only reads
    between the provided
32                      limits (inclusively)
33                  - time_codes variable is used to keep track of the
    timecodes for
34                      each image in the subset_image array
35
36          read_image_data_subset_single_image(minimum_timecode,
    maximum_timecode)
37                  - Adds subset_image and no_frames to the class
38                  - Same as read_full_image_data, but only reads
    between the provided
39                      limits (inclusively)
40
41          read_ranges_image_data(timecode_ranges)
42                  - Adds image_data and no_frames variables to class
43                  - Requires pairs of timecodes
44                  - Image produced between the two timecodes (
    inclusive)
45
46          read_ranges_image_data_subset_tof(timecode_ranges)
47                  - Adds image_data and no_frames variables to class
48                  - Requires pairs of timecodes
49                  - Image produced between the two timecodes (
    inclusive)
50                  - Similar to read_ranges_image_data(), but is more
    efficient when
51                      reading multiple ranges and a subset of the TOF
52
53          read_ranges_image_data_with_frame_intensities(bin_ranges)
54                  - Adds image_data, no_frames and intensity
    variables to class
55                  - Requires pairs of timecodes
56                  - Image produced between the two timecodes
57                  - For each pair of timecodes, the intensity is
    recorded for each
58                      frame
59                  - Other than recording the intensity, this is
    identical to
60                      read_ranges_image_data
61
62          read_tof_only()
63                  - Adds tof variable to the class
64                  - Just reads the time-of-flight from the PImMS file
65
66          read_pimms_file()
67                  - The function which reads the PImMS file
```

```
68              - Called by the other functions. Can also be called
    externally
69              - Acts as a generator for each PImMS frame
70      """
71      def __init__(self, filename, frames_to_skip = 0, frames_to_proc
    = -1):
72          self.filename = filename
73          self.frames_to_skip = frames_to_skip
74          self.frames_to_proc = frames_to_proc
75
76      def read_full_data(self):
77          """Read an entire PImMS image into an array, along with TOF
78
79          Reads the entire PImMS image into a numpy array, which is
    stored in full_image, a 324 x 324 x 4096 array. Also produces
    the time-of-flight spectrum.
80
81          Does not return anything, but adds the variables tof,
    full_data and no_frames
82          to the class.
83          """
84          #Reinitialise generator
85          data_gen = self.read_pimms_file()
86          #Define a variable for the full data set
87          self.full_image = np.zeros([324,324,4096]) #Zeros is one
    indexed
88          #Define a variable for the TOF
89          self.no_frames = 0
90          #Read in the data, populate the image array
91          try:
92              i = 0
93              while True:
94                  frame_data = next(data_gen)
95                  i += 1
96                  self.full_image[np.array(frame_data[:,1]),np.array(
    frame_data[:,0]),np.array(frame_data[:,2])] += 1
97          except ValueError:
98              self.no_frames = i
99          except StopIteration:
100             self.no_frames = i
101
102         try:
103             del event; del frame_data
104         #If there was no event, this catches the error
105         except UnboundLocalError:
106             pass
107
108         self.tof = self.full_image.sum(axis=(0,1))
109
110     def read_full_image_data_legacy(self):
111         """Legacy version of read_full_image_data()
112
113         ****************************************
114         Use read_full_image_data instead, it is around 10x faster
    and uses the same memory.
115         ****************************************
```

```
116
117         Reads the entire PImMS image into a numpy array, which is
    stored in full_image, a 324 x 324 x 4096 array. A TOF can be
    trivially extracted by summing the array for each time bin,
    although you can just use the read_full_data function for that.
118         """
119         #Reinitialise generator
120         data_gen = self.read_pimms_file()
121         #Define a variable for the full data set
122         self.full_image = np.zeros([324,324,4096]) #Zeros is one
    indexed
123         self.no_frames = 0
124         #Read in the data, populate the image array
125         try:
126             i = 0
127             while True:
128                 frame_data = next(data_gen)
129                 i += 1
130                 for event in frame_data:
131                     self.full_image[event[1],event[0],event[2]] +=
    1
132         except ValueError:
133             self.no_frames = i
134         except StopIteration:
135             self.no_frames = i
136
137         try:
138             del event; del frame_data
139         #If there was no event, this catches the error
140         except UnboundLocalError:
141             pass
142
143     def read_full_image_data(self):
144         """Read an entire PImMS image into an array
145
146         Reads the entire PImMS image into a numpy array, which is
    stored in full_image, a 324 x 324 x 4096 array. A TOF can be
    trivially extracted by summing the array for each time bin,
    although you can just use the read_full_data function for that.
147
148         Does not return anything, but adds the variables full_data
    and no_frames
149         to the class.
150         """
151         #Reinitialise generator
152         data_gen = self.read_pimms_file()
153         #Define a variable for the full data set
154         self.full_image = np.zeros([324,324,4096]) #Zeros is one
    indexed
155         self.no_frames = 0
156         #Read in the data, populate the image array
157         try:
158             i = 0
159             while True:
160                 frame_data = next(data_gen)
161                 i += 1
```

```
                self.full_image[np.array(frame_data[:,1]),np.array(
frame_data[:,0]),np.array(frame_data[:,2])] += 1
        except ValueError:
            self.no_frames = i
        except StopIteration:
            self.no_frames = i

        try:
            del event; del frame_data
        #If there was no event, this catches the error
        except UnboundLocalError:
            pass

    def read_image_data_subset(self,minimum_timecode=0,
maximum_timecode=4095):
        """Read a subset of a PImMS image into an array

        Reads a subset of the PImMS image into a numpy array, which
 is stored in subset_image, a 324 x 324 x n array, where n is
the maximum timecode - minimum timecode + 1 (provided as
variables, which default to the same behaviour as
read_full_image_data, +1 to include the maximum timecode as well
). The TOF should be read using the read_full_data function, as
there is little memory impact there.

        Does not return anything, but adds the variables
subset_data, time_codes and no_frames
        to the class.

        Parameters required:
            minimum_timecode - an integer in the range 0 - 4095
corresponding to the minimum timecode
                               to include in the dataset
            maximum_timecode - an integer in the range 0 - 4095
corresponding to the maximum timecode
                               to include in the dataset

        Added to class:
            subset_image - a 324 x 324 x (maximum_timecode-
minimum_timecode+1) array
                           containing PImMS data for each timecode
from minimum_timecode
                           to maximum_timecode, inclusive. Use
time_codes variable to
                           check which timecode each 324 x 324
array corresponds to
            time_codes   - a 1D array of the timecodes to which
subset_data corresponds
            no_frames    - the number of frames in the PImMS file
        """
        # Validation of the provided timecodes
        for timecode in [minimum_timecode,maximum_timecode]:
            if not isinstance(timecode, int):
                print('Please provide integer bin edges.')
                return -1
            elif timecode < 0:
```

```
202                 print('Cannot have a negative bin edge (time codes start at 0).')
203                 return -1
204             elif timecode > 4095:
205                 print('Bin edges must not exceed 4095 (4096 time codes, zero indexed).')
206                 return -1
207 
208         #Reinitialise generator
209         data_gen = self.read_pimms_file()
210         #Define a variable for the full data set. Note zeros is one indexed
211         self.subset_image = np.zeros([324,324,maximum_timecode-minimum_timecode+1])
212         self.no_frames = 0
213 
214         # Set the time_codes array
215         self.time_codes = np.linspace(minimum_timecode, maximum_timecode, maximum_timecode-minimum_timecode + 1).astype('uint16')
216 
217         #Read in the data, populate the image array
218         try:
219             i = 0
220             while True:
221                 frame_data = next(data_gen)
222                 i += 1
223 
224                 #Adjust for smaller array
225                 frame_data = frame_data[np.isin(frame_data[:,2], self.time_codes)]
226                 frame_data[:,2] -= minimum_timecode
227 
228                 self.subset_image[np.array(frame_data[:,1]),np.array(frame_data[:,0]),np.array(frame_data[:,2])] += 1
229         except ValueError:
230             self.no_frames = i
231         except StopIteration:
232             self.no_frames = i
233 
234         try:
235             del event; del frame_data
236         #If there was no event, this catches the error
237         except UnboundLocalError:
238             pass
239 
240     def read_image_data_subset_single_image(self,minimum_timecode=0,maximum_timecode=4095):
241         """Read a subset of a PImMS image into an array (2D rather thnn 3D)
242 
243         Reads a subset of the PImMS image into a numpy array, which is stored in subset_image, a 324 x 324 array.
244 
245         Does not return anything, but adds the variables subset_data, time_codes and no_frames
```

```
246         to the class.
247 
248         Parameters required:
249             minimum_timecode - an integer in the range 0 - 4095
    corresponding to the minimum timecode
250                                to include in the dataset
251             maximum_timecode - an integer in the range 0 - 4095
    corresponding to the maximum timecode
252                                to include in the dataset
253 
254         Added to class:
255             subset_image - a 324 x 324 array containing PImMS data
    summed for all timecodes
256                            from minimum_timecode to
    maximum_timecode, inclusive.
257             no_frames    - the number of frames in the PImMS file
258         """
259         # Validation of the provided timecodes
260         for timecode in [minimum_timecode,maximum_timecode]:
261             if not isinstance(timecode, int):
262                 print('Please provide integer bin edges.')
263                 return -1
264             elif timecode < 0:
265                 print('Cannot have a negative bin edge (time codes
    start at 0).')
266                 return -1
267             elif timecode > 4095:
268                 print('Bin edges must not exceed 4095 (4096 time
    codes, zero indexed).')
269                 return -1
270 
271         #Reinitialise generator
272         data_gen = self.read_pimms_file()
273         #Define a variable for the full data set. Note zeros is one
     indexed
274         self.subset_image = np.zeros([324,324])
275         self.no_frames = 0
276 
277         # Set the time_codes array
278         time_codes = np.linspace(minimum_timecode, maximum_timecode
    , abs(maximum_timecode-minimum_timecode) + 1).astype('uint16')
279 
280         #Read in the data, populate the image array
281         try:
282             i = 0
283             while True:
284                 frame_data = next(data_gen)
285                 i += 1
286 
287                 #Adjust for smaller array
288                 frame_data = frame_data[np.isin(frame_data[:,2],
    time_codes)]
289                 frame_data[:,2] -= minimum_timecode
290 
291                 self.subset_image[np.array(frame_data[:,1]),np.
    array(frame_data[:,0])] += 1
```

```
292         except ValueError:
293             self.no_frames = i
294         except StopIteration:
295             self.no_frames = i
296 
297         try:
298             del event; del frame_data
299         #If there was no event, this catches the error
300         except UnboundLocalError:
301             pass
302 
303     def read_ranges_image_data(self,bin_ranges):
304         """Read PImMS image for specified time range(s) into array(
    s)
305 
306         Reads images recorded with a PImMS camera within the
    specified bin ranges
307         into a numpy array, which is stored in image_data, an n x
    324 x 324 array,
308         where n is the number of bin ranges specified. Note that
    this function
309         does not read the time-of-flight.
310 
311         Note that it will read from the lower bin limit to the
    upper bin limit,
312         inclusively. So for a single bin, provide [1,1], for
    example.
313 
314         Requires a numpy array of bin ranges to be provided, with
    one dimension
315         of two. For example, the below would be accepted:
316 
317         np.array([[1,2],    np.array([1,2])     np.array([[1],
318                   [3,4]])                                 [2]])
319 
320         Where the array provided is 2 x 2, the first dimension
    would specify each
321         pair, so the bin ranges from the first example above would
    be [1,2] and
322         the second [3,4].
323 
324         Does not return anything, but adds the variables image_data
     and no_frames
325         to the class.
326         """
327         #Make sure the bin range is formatted correctly. Otherwise
    returns.
328         bin_ranges = self.sort_dimensions_of_bin_ranges(bin_ranges)
329 
330         #Get a ValueError trying to do a comparison with an array,
    so catch it.
331         try:
332             bin_ranges == -1
333             #Just in case an error is not raised
334             if bin_ranges == -1:
335                 return
```

```
336         except ValueError:
337             pass
338 
339         #Reinitialise generator
340         data_gen = self.read_pimms_file()
341 
342         #Define an image for each bin range.
343         self.image_data = np.zeros([bin_ranges.shape[0],324,324]) #
    Zeros is one indexed
344         self.no_frames = 0
345 
346         #Define the bin range variable (contains all the included
    time bins)
347         included_time_bins = np.array([np.linspace(i[0],i[1],i[1]-i
    [0]+1).astype('uint16') for i in bin_ranges])
348 
349         try:
350             i = 0
351             while True:
352                 frame_data = next(data_gen)
353                 i += 1
354                 #Define the mask (specifies the events within the
    frame for each bin range)
355                 mask = np.array([np.isin(frame_data[:,2], cur_range
    ) for cur_range in included_time_bins])
356 
357                 #For each mask, increment the corresponding image
    pixels.
358                 for j in range(bin_ranges.shape[0]):
359                     #Need to use np.add.at, as just indexing
    results in any repeated pixels in a
360                     #frame only being incremented once.
361                     np.add.at(self.image_data[j],(np.array(
    frame_data[mask[j],1]),np.array(frame_data[mask[j],0])), 1)
362 
363         except ValueError:
364             self.no_frames = i
365         except StopIteration:
366             self.no_frames = i
367 
368         try:
369             del event; del frame_data
370         #If there was no event, this catches the error
371         except UnboundLocalError:
372             pass
373 
374     def read_ranges_image_data_subset_tof(self,bin_ranges):
375         """Read PImMS image for specified time ranges into arrays (
    see docs)
376 
377         IF YOU ARE NOT USING MULTIPLE BIN RANGES OR ARE LOOKING AT
    THE ENTIRE
378         TOF (CUMULATIVELY), PLEASE USE read_ranges_image INSTEAD!
379 
380         This is largely the same as read_ranges_image_data, but has
     been optimised
```

```
381         such that it runs more efficiently when only considering a
    subset of the
382         overall time-of-flight AND multiple bin ranges.
383 
384         Reads images recorded with a PImMS camera within the
    specified bin ranges
385         into a numpy array, which is stored in image_data, an n x
    324 x 324 array,
386         where n is the number of bin ranges specified. Note that
    this function
387         does not read the time-of-flight.
388 
389         Note that it will read from the lower bin limit to the
    upper bin limit,
390         inclusively. So for a single bin, provide [1,1], for
    example.
391 
392         Requires a numpy array of bin ranges to be provided, with
    one dimension
393         of two. For example, the below would be accepted:
394 
395         np.array([[1,2],    np.array([1,2])     np.array([[1],
396                   [3,4]])                                 [2]])
397 
398         Where the array provided is 2 x 2, the first dimension
    would specify each
399         pair, so the bin ranges from the first example above would
    be [1,2] and
400         the second [3,4].
401 
402         Does not return anything, but adds the variables image_data
     and no_frames
403         to the class.
404         """
405         #Make sure the bin range is formatted correctly. Otherwise
    returns.
406         bin_ranges = self.sort_dimensions_of_bin_ranges(bin_ranges)
407 
408         #Get a ValueError trying to do a comparison with an array,
    so catch it.
409         try:
410             bin_ranges == -1
411             #Just in case an error is not raised
412             if bin_ranges == -1:
413                 return
414         except ValueError:
415             pass
416 
417         #Reinitialise generator
418         data_gen = self.read_pimms_file()
419 
420         #Define an image for each bin range.
421         self.image_data = np.zeros([bin_ranges.shape[0],324,324]) #
    Zeros is one indexed
422         self.no_frames = 0
423 
```

```
424         #Define the bin range variable (contains all the included
    time bins)
425         included_time_bins = np.array([np.linspace(i[0],i[1],i[1]-i
    [0]+1).astype('uint16') for i in bin_ranges])
426 
427         # Define all the time bins within the bin ranges, so can
    ignore data outside this range
428         all_time_bins = np.unique(np.concatenate([i for i in
    included_time_bins]))
429 
430         try:
431             i = 0
432             while True:
433                 frame_data = next(data_gen)
434                 i += 1
435 
436                 #Remove any unused events from the list for the
    frame
437                 frame_data = frame_data[np.isin(frame_data[:,2],
    all_time_bins)]
438 
439                 try:
440                     #Define the mask (specifies the events within
    the frame for each bin range)
441                     mask = np.array([np.isin(frame_data[:,2],
    cur_range) for cur_range in included_time_bins])
442                 except IndexError:
443                     #If frame_data is now empty, catch the error
444                     continue
445 
446                 #For each mask, increment the corresponding image
    pixels.
447                 for j in range(bin_ranges.shape[0]):
448                     #Need to use np.add.at, as just indexing
    results in any repeated pixels in a
449                     #frame only being incremented once.
450                     np.add.at(self.image_data[j],(np.array(
    frame_data[mask[j],1]),np.array(frame_data[mask[j],0])), 1)
451 
452         except ValueError:
453             self.no_frames = i
454         except StopIteration:
455             self.no_frames = i
456 
457         try:
458             del event; del frame_data
459         #If there was no event, this catches the error
460         except UnboundLocalError:
461             pass
462 
463     def read_ranges_image_data_with_frame_intensities(self,
    bin_ranges):
464         """Read PImMS image for specified time range(s) into array(
    s), with intensity per frame
465 
```

```
466         Reads images recorded with a PImMS camera within the
    specified bin ranges
467         into a numpy array, which is stored in image_data, an n x
    324 x 324 array,
468         where n is the number of bin ranges specified. Note that
    this function
469         does not read the time-of-flight.
470 
471         Note that it will read from the lower bin limit to the
    upper bin limit,
472         inclusively. So for a single bin, provide [1,1], for
    example.
473 
474         Requires a numpy array of bin ranges to be provided, with
    one dimension
475         of two. For example, the below would be accepted:
476 
477         np.array([[1,2],    np.array([1,2])     np.array([[1],
478                   [3,4]])                                 [2]])
479 
480         Where the array provided is 2 x 2, the first dimension
    would specify each
481         pair, so the bin ranges from the first example above would
    be [1,2] and
482         the second [3,4].
483 
484         For each timebin range, the total intensity is read each
    frame and is
485         stored in the intensity variable, an n x no_frames array,
    where n is the
486         number of bin ranges specified.
487 
488         Does not return anything, but adds the variables image_data
     and no_frames
489         to the class.
490         """
491         #Make sure the bin range is formatted correctly. Otherwise
    returns.
492         bin_ranges = self.sort_dimensions_of_bin_ranges(bin_ranges)
493 
494         #Get a ValueError trying to do a comparison with an array,
    so catch it.
495         try:
496             bin_ranges == -1
497             #Just in case an error is not raised
498             if bin_ranges == -1:
499                 return
500         except ValueError:
501             pass
502 
503         #Reinitialise generator
504         data_gen = self.read_pimms_file()
505 
506         #Define an image for each bin range.
507         self.image_data = np.zeros([bin_ranges.shape[0],324,324]) #
    Zeros is one indexed
```

```
508         self.no_frames = 0
509 
510         #Define the bin range variable (contains all the included time bins)
511         included_time_bins = np.array([np.linspace(i[0],i[1],i[1]-i[0]+1).astype('uint16') for i in bin_ranges])
512 
513         #Define the intensity variable
514         intensity = []
515 
516         try:
517             i = 0
518             while True:
519                 frame_data = next(data_gen)
520                 i += 1
521                 #Define the mask (specifies the events within the frame for each bin range)
522                 mask = np.array([np.isin(frame_data[:,2], cur_range) for cur_range in included_time_bins])
523 
524                 #Append the intensity (equal to the sum of the mask) for each bin range
525                 intensity.append(mask.sum(axis=1))
526 
527                 #For each mask, increment the corresponding image pixels.
528                 for j in range(bin_ranges.shape[0]):
529                     #Need to use np.add.at, as just indexing results in any repeated pixels in a
530                     #frame only being incremented once.
531                     np.add.at(self.image_data[j],(np.array(frame_data[mask[j],1]),np.array(frame_data[mask[j],0])), 1)
532 
533         except ValueError:
534             self.no_frames = i
535         except StopIteration:
536             self.no_frames = i
537 
538         try:
539             del event; del frame_data
540         #If there was no event, this catches the error
541         except UnboundLocalError:
542             pass
543 
544         #Convert the intensity to a numpy array, and add it to the class
545         #Note that as the list consists of np arrays for each frame, you need to
546         #transpose to get the required dimensions for the variable
547         self.intensity = np.array(intensity).transpose()
548 
549     def read_tof_only(self):
550         """Read the time of flight from a PImMS image. Nothing else.
551 
```

```
552         Does not return anything, but adds the variables tof and
    no_frames
553         to the class.
554         """
555         #Reinitialise generator
556         data_gen = self.read_pimms_file()
557         #Define a variable for the full data set
558         self.tof = np.zeros([4096]) #Zeros is one indexed
559         self.no_frames = 0
560         #Read in the data, populate the image array
561         try:
562             i = 0
563             while True:
564                 frame_data = next(data_gen)
565                 i += 1
566                 unique_elements, counts_elements = np.unique(
    frame_data[:,2], return_counts=True)
567                 self.tof[np.array([unique_elements])] +=
    counts_elements
568         except ValueError:
569             self.no_frames = i
570         except StopIteration:
571             self.no_frames = i
572 
573         try:
574             del event; del frame_data
575         #If there was no event, this catches the error
576         except UnboundLocalError:
577             pass
578 
579     def read_pimms_file(self):
580         """Generator to read PImMS file
581 
582         The generator used to read in PImMS data. If you want to
    use this, set up a generator by
583         using generator_name = pimms.read_pimms_file() and iterate
    through the file with a loop,
584         calling next(generator_name) to get the data from the next
    frame.
585         """
586         #Defines generator to read in PImMS data
587         with open(self.filename, 'rb') as f:
588             for i in range(self.frames_to_skip):
589                 m, n = np.fromfile(f,dtype='int32',count=2)
590                 data = np.fromfile(f,dtype='uint16',count=(m*n))
591 
592             if self.frames_to_proc == -1:
593                 while True:
594                     m, n = np.fromfile(f,dtype='int32',count=2)
595                     data = np.fromfile(f,dtype='uint16',count=(m*n)
    )
596                     data = np.reshape(data, (-1,3))
597                     yield data
598 
599             else:
600                 for i in range(self.frames_to_proc):
```

```
                    m, n = np.fromfile(f,dtype='int32',count=2)
                    data = np.fromfile(f,dtype='uint16',count=(m*n)
)
                    data = np.reshape(data, (-1,3))
                    yield data


 def sort_dimensions_of_bin_ranges(self, bin_ranges):
     """Checks validity of timecode ranges

     Makes sure that a provided bin range is actually valid. For
 the purposes intended,
     this should be a range of PImMS time bins for which ion
images will be plotted.
     Could be used in conjunction with plotting a TOF, but would
 impact speed for
     little memory difference, so it is not advised.

     Parameters required:
         bin_ranges  - an array with one dimension of two, which
 contains a maximum
                       and minimum value. Should only contain
integers that fall
                       between 0 and 4096 (inclusive).

     Returns either:
         -1          - if the input is invalid
         bin_ranges  - a numpy array with dimensions (n, 2)
where n is the number
                       of bin ranges included in the array.
     """
     #Check the input is valid in various ways
     try:
         bin_ranges = np.array(bin_ranges)
     except:
         print('Cannot convert bin ranges to numpy array')
         return -1

     dimensions = bin_ranges.ndim

     if 2 not in bin_ranges.shape:
         print(str(bin_ranges.shape) + ' does not have a
dimension of two.')
         return -1
     elif dimensions != 1 and dimensions != 2:
         print(str(dimensions) + ' is an invalid number of
dimensions. Should be one or two.')
         return -1
     elif bin_ranges.dtype != 'int':
         print('Please provide integer bin edges.')
         return -1
     elif np.any(bin_ranges < 0):
         print('Cannot have a negative bin edge (time codes
start at 0).')
         return -1
     elif np.any(bin_ranges > 4095):
```

```
647             print('Bin edges must not exceed 4095 (4096 time codes, zero indexed).')
648             return -1
649         ###
650 
651         #Make the output bin ranges uniform
652         if dimensions == 1:
653             bin_ranges = np.array([bin_ranges])
654         else:
655             if bin_ranges.shape[1] != 2:
656                 bin_ranges = bin_ranges.transpose()
657 
658         #Make sure the limits are the correct way round (raises an error if not)
659         if np.any(bin_ranges[:,0] > bin_ranges[:,1]) == True:
660             print('Minimum bin must not exceed maximum bin.')
661             return -1
662 
663         return bin_ranges
664 
665 class dat_file():
666     """Class which reads in dat files
667 
668     Reads in an array from a delimited text file. Can be an image or, for example,
669     a time-of-flight PMT spectrum.
670 
671     Requires:
672         Filename
673 
674     Provides:
675         load_data(delimiter='\t', skiprows=0, dtype=float)
676             - Reads file provided to the class
677             - Columns are defined by splitting at the delimiter (defaults to tab)
678             - Can skip rows if a header is included (defaults to no skipping)
679             - Can specify data type (default is float)
680     """
681     def __init__(self, filename):
682         self.filename = filename
683 
684     def load_data(self, delimiter='\t', skiprows=0, dtype=float):
685         """Load text file into numpy array
686 
687         Read a delimited text file and converts it to a numpy array. This is
688         stored in the class instance as image_data (even if the code is not
689         being used to read an image)
690 
691         Optional parameters:
692             delimiter   - Delimiter between columns in the text file. Default \t
693             skiprows    - Number of rows to skip before reading. Default is 0
```

```
694             dtype       - Data type. Default is float
695         """
696         def iter_func():
697             with open(self.filename, 'r') as infile:
698                 for _ in range(skiprows):
699                     next(infile)
700                 for line in infile:
701                     line = line.rstrip().split(delimiter)
702                     for item in line:
703                         yield dtype(item)
704             self.rowlength = len(line)
705 
706         data = np.fromiter(iter_func(), dtype=dtype)
707         data = data.reshape((-1, self.rowlength))
708         del self.rowlength
709         self.image_data = data
```

D.2 A new inversion method for electron-molecule scattering experiments

Our implementation of our new inversion method, discussed in detail in the text.

D.2.1 Basis function generation

The code used to generate the basis functions used by the inversion method. The basis functions are defined as the radial distribution of the 2D projection of a sphere.

```
1  import numpy as np
2  import matplotlib.pyplot as plt
3  import tkinter as tk
4  from tkinter import filedialog
5  import PySimpleGUI as sg
6  import os
7  try:
8      import pyabel_caller
9  except ModuleNotFoundError:
10     from Inversion_functions import pyabel_caller
11 
12 def layout(max_r, step, sigma):
13     layout = [
14             [sg.Text('Maximum radius', size=(20, 1)),\
15             sg.Spin([i/2 for i in range(0,324)], initial_value=
   max_r, size=(4,1), key='max_radius')],
16             #
17             [sg.Text('Step size', size=(20, 1)),\
18             sg.Spin([i/2 for i in range(1,11)], initial_value=step,
    size=(4,1), key='step')],
19             #
20             [sg.Text('Basis sigma (st. dev. of r)', size=(20, 1)),\
21             sg.Spin([i/2 for i in range(0,12)], initial_value=sigma
   , size=(4,1), key='sigma')],
22             #
23             [sg.Text('Data points', size=(20, 1)),\
```

```
            sg.Spin([i*100000 for i in range(1,101)], initial_value
    =1000000, size=(10,1), key='no_points')],
            #
            [sg.Submit("Generate"), sg.Cancel()]]

    return layout

class generate_basis_sets():
    def __init__(self, max_r, step, sigma):
        self.window = sg.Window('Generate basis sets', layout(max_r
    ,step,sigma), finalize=True)

    def generate_data_2d_proj(self, radius, no_points, sigma):
        def get_radial_distribution():
            # Need to apply the Jacobian for conversion to polar
    coordinates.

            # Get the radial distribution
            radius, radial_intensity = pyabel_caller.
    angular_integration(\
            image_data, dr=1.0, Jacobian=False)

            return radial_intensity

        # Add width to radius if required (uses a normal
    distribution with
        # radius as the mean and sigma as the std. dev.)

        if radius == 0:
            return np.array([1] + [0] * 10000)

        # Work with a resolution of 1 to produce a 0.5-spaced basis
     function
        radius *= 2

        if sigma > 0:
            # Need to multiply sigma by two as spacing increased
    when calculating
            # the radial distribution
            radius = np.add(radius, np.random.randn(no_points) *
    sigma * 2)
        else:
            radius = radius * np.ones([no_points])

        # Check for any negative points and remove
        radius = radius[radius>0]
        no_points = len(radius)

        # Generate image array
        image_data = np.zeros([self.img_size * 2,self.img_size *
    2]).astype('int')

        # Generate the z and x coordinates
        z = (np.random.rand(no_points) - 0.5) * 2
        theta = np.random.rand(no_points) * 2 * np.pi
        r = np.sqrt(1 - np.power(z,2))
```

```
71          x = r * np.cos(theta)
72
73          # Scale to the appropriate radius
74          z *= radius; x *= radius
75
76          # Add to the image
77          np.add.at(image_data, (np.rint(self.img_size - 0.5 + x).
    astype('int'), np.rint(self.img_size - 0.5 + z).astype('int')),
    1)
78
79          # Get the radial distribution
80          radial_intensity = get_radial_distribution()
81
82          # Return the radial distribution
83          return radial_intensity / np.sum(radial_intensity)
84
85
86      def generate_inner_basis(self, basis_radius, no_points):
87          self.img_size = 140
88          # Set up basis set
89          inner_basis_set = np.zeros((10, len(basis_radius)))
90
91          # For each radius up to 4.5, generate a basis set with
    sigma 20x smaller
92          # than the radius. Cut from a larger distribution.
93          for i in range(10):
94              temp = self.generate_data_2d_proj(i*5, no_points, i/4)
    [::10]
95              temp = np.divide(temp, np.sum(temp))
96              try:
97                  inner_basis_set[i,:len(temp)] = temp
98              except ValueError:
99                  inner_basis_set[i] = temp[:len(basis_radius)]
100
101         # Save the inner distribution
102         # Generate the filename and save the data
103         foldername = os.path.join(os.getcwd(), os.path.dirname(
    __file__), 'Basis_sets')
104         filename = f'sph_harm_inner_basis_size_{basis_radius[-1]}'
105         filepath = os.path.join(foldername, filename)
106
107         self.write_data(inner_basis_set, filepath)
108
109         return inner_basis_set
110
111     def get_inner_basis(self, basis_radius, no_points):
112         # Find all possible basis sets
113         foldername = os.path.join(os.getcwd(), os.path.dirname(
    __file__), 'Basis_sets')
114         all_basis = os.listdir(foldername)
115
116         # Iterate through the list
117         for i, basis in enumerate(all_basis):
118             # If there is a basis set larger than or of the same
    size as that
119             # which is required, use that.
```

```
            try:
                if float(basis[26:-4]) < basis_radius[-1]:
                    continue
            except ValueError:
                continue

            basis_to_use = i
            break

        try:
            f = os.path.join(foldername,all_basis[basis_to_use])
            inner_basis_set = np.load(f)
        except UnboundLocalError:
            # Otherwise, generate a new basis set
            return self.generate_inner_basis(basis_radius,
no_points)

        # Cut down the read data to the correct size

        return inner_basis_set[:,:len(basis_radius)]

    def write_data(self, basis_sets, f):
        np.save(f, basis_sets)

    def __call__(self, show_plot):
        #Event loop
        while True:
            event, values = self.window.Read()

            if event in (None, 'Exit', 'Cancel'):
                break

            if event == 'Generate':
                # Get the parameters
                max_radius = float(self.window.FindElement('
max_radius').Get())
                step_size = float(self.window.FindElement('step').
Get())
                sigma = float(self.window.FindElement('sigma').Get
())
                no_points = int(self.window.FindElement('no_points'
).Get())


                # Find the radii of the basis function, and the
radii of all points included in the basis function
                basis_function_rs = np.arange(5, max_radius +
0.001, step_size)
                basis_radius = np.arange(0, int(len(
basis_function_rs + 10) * 1.2)*step_size + step_size + 0.001,
0.5)

                # Increase the basis function res slightly at low r
                if step_size > 1:
                    basis_function_rs = np.insert(basis_function_rs
,1,5+step_size/2)
```

```
166
167             basis_set_array = np.zeros((len(basis_function_rs)
    + 10, len(basis_radius)))
168
169             # Generate folder for basis function if it doesn't
    already exist
170             foldername = os.path.join(os.getcwd(), os.path.
    dirname(__file__), 'Basis_sets')
171             try:
172                 os.makedirs(foldername)
173             except FileExistsError:
174                 pass
175
176             # Load in the appropriate inner basis set
177             basis_set_array[:10] = self.get_inner_basis(
    basis_radius, no_points)
178
179             # Calcualte the image size
180             self.img_size = np.rint(max_radius).astype('int') *
     2 + 2 + 10*np.ceil(sigma).astype('int')
181
182             # Adjust sigma as function of r
183             self.sigma = sigma
184             sigma = np.arange(0.25, sigma, (sigma+step_size)
    *0.1)
185
186             # Increase the basis function res slightly for
    large steps
187             if step_size > 1:
188                 if self.sigma == 0:
189                     sigma = np.zeros(1)
190                 else:
191                     sigma = np.insert(sigma, 1, 0.25 + (self.
    sigma + step_size) * 0.05)
192                 # Make sure the generated sigma is not larger
    than the specified sigma
193                 sigma[sigma > self.sigma] = self.sigma
194
195             sigma = list(sigma) + [self.sigma] * (len(
    basis_function_rs) - len(sigma))
196
197             if show_plot:
198                 for i in basis_set_array[:10]:
199                     plt.plot(basis_radius,i)
200
201             for i, radius in enumerate(basis_function_rs):
202                 intense = self.generate_data_2d_proj(radius,
    no_points, sigma.pop(0))
203
204                 # Add to basis set array
205                 basis_set_array[i + 10] = intense[:len(
    basis_radius)]
206                 if show_plot:
207                     plt.plot(basis_radius,intense[:len(
    basis_radius)])
208
```

```
                # Generate the filename and save the data
                filename = f'sph_harm_max_r_{max_radius}_step_{step_size}_sig_{self.sigma}'

                filename = os.path.join(foldername, filename)
                self.write_data(basis_set_array, filename)

                if show_plot:
                    plt.show()

                if __name__ != '__main__':
                    self.window.Close()
                    return filename + '.npy'


def main(show_plot=False, *, init_max_r=161, init_step=1, init_sigma=1):
    gen_basis_gui = generate_basis_sets(init_max_r, init_step, init_sigma)
    return gen_basis_gui(show_plot)

if __name__ == '__main__':
    main(True)
```

D.2.2 Inversion code

The code used to invert the obtained scattering distributions. It uses linear regression to fit the generated basis functions to the raadial distribution of the recorded 2D projection of the scattering distribution, and then reconstructs the radial distribution of the 3D scattering distribution. The central slice of the scattering distribution can also be reconstructed from the radial distribution.

```
import numpy as np
from sklearn.linear_model import Ridge
from sklearn.pipeline import make_pipeline
from copy import deepcopy
import os
try:
    import generate_basis_sets
except ModuleNotFoundError:
    import Spherical_harmonics_inversion.generate_basis_sets as generate_basis_sets

def get_beta_scaling(n, r):
    if n == 2:
        return 0.75146 * np.power(r,2) - 0.00152 * r - 0.49854
    elif n == 4:
        return 1.59166 * np.power(r,4) + 0.06854 * np.power(r,3) - 1.90669 * np.power(r,2) + 0.00613 * r + 0.37695
    elif n == 6:
        return 13.27069 * np.power(r,5) - 22.17286 * np.power(r,4) + 7.72015 * np.power(r,3) + 1.40602 * np.power(r,2) + 0.18097 * r - 0.31589

    elif n < 6:
```

```
20          print('Only takes even n')
21          return np.ones(len(r))
22      else:
23          print('Only implemented basis set adjustment up to n = 6')
24          return np.ones(len(r))
25
26  def leg(l,x):
27      # Return the appropriate legendre polynomial. Adapted from the
28      # function used in pBASEX.
29      if l==2:
30          return (3*x**2-1)/2
31      elif l==4:
32          x2 = x**2
33          return ((35*x2-30)*x2+3)/8
34      elif l==6:
35          x2 = x**2
36          return (((231*x2-315)*x2+105)*x2-5)/16
37      elif l==8:
38          x2 = x**2
39          return ((((6435*x2-12012)*x2+6930)*x2-1260)*x2+35)/128
40      elif l % 2 == 0 and l < 30:
41          #Calculate the Legendre polynomial (only works up to 28,
    after that the
42          #precision causes issues)
43          #Uses 1/(2^n*n!) * d^n/dx^n (x^2 - 1)^n to generate the
    polynomials
44          legendre_poly = np.poly1d([1,0,-1]) ** l
45
46          for i in range(l):
47              legendre_poly = legendre_poly.deriv() / 2
48          return np.divide(legendre_poly(x), np.math.factorial(l))
49      else:
50          raise ValueError('l-value not implemented.')
51
52  class spherical_harmonic_transform():
53      def __init__(self, radial_dist_r, radial_dist_i, *, sigma, step
    , max_r, regularisation=True, reg_val = 0.001, basis_step=0.5):
54          self.radial_dist_r = radial_dist_r; self.radial_dist_i =
    radial_dist_i
55          self.sigma = sigma
56          self.step = step
57          self.max_r = max_r
58          self.reg = regularisation
59          self.reg_val = reg_val
60          self.basis_fn_step = basis_step
61
62      def check_appropriate_basis_exists(self):
63          basis_path = os.path.join(os.getcwd(), os.path.dirname(
    __file__), 'Basis_sets')
64          try:
65              os.makedirs(basis_path)
66          except FileExistsError:
67              pass
68          all_basis = os.listdir(basis_path)
69
70          for i, basis in enumerate(all_basis):
```

```
71              _ = basis.split('_')
72
73              try:
74                  if float(_[8][:-4]) != self.sigma:
75                      continue
76                  if self.step != float(_[6]):
77                      continue
78                  if float(_[4]) < self.max_r:
79                      continue
80              except IndexError:
81                  continue
82              except ValueError:
83                  continue
84
85              last_allowed_basis = i
86              break
87
88          try:
89              return os.path.join(basis_path,all_basis[
    last_allowed_basis])
90          except UnboundLocalError:
91              print('No appropriate basis function found. Generate an
     appropriate basis.')
92              return generate_basis_sets.main(False, init_max_r=self.
    max_r, init_step=self.step, init_sigma=self.sigma)
93
94      def load_basis(self, f):
95          basis_set = np.load(f)
96          basis_radius = np.arange(0,len(basis_set[0]) / 2,0.5)
97          return basis_radius, basis_set
98
99      def load_beta(self, beta_path):
100         read_beta = np.loadtxt(beta_path, delimiter='\t').T
101         beta_r = read_beta[0]; read_beta = read_beta[1:]
102
103         # Calculate the step in the radial distribution (should
    either be integer or 0.5)
104         beta_radial_step = np.rint(beta_r[2] - beta_r[0]) / 2
105
106         # Add points to make the beta distribution extend to a
    radius of zero if required
107         if beta_r[0] != 0:
108             # Make sure the first number is divisible by 0.5
109             cur_min = np.rint(beta_r[0] * 2) / 2
110
111             # Append the first beta value until the centre is
    reached
112             beta_min = read_beta[:,0].reshape(-1)
113             read_beta = np.insert(read_beta,0, [beta_min] * int(
    cur_min / beta_radial_step), axis=1)
114
115
116         # Redefine beta_r to have a step of 0.5
117         beta_r = np.arange(0, beta_r[-1] + 0.1, 0.5)
118
```

```
119         # Match to min separation of the basis functions (0.5).
    Then pick out
120         # the required values later.
121         if beta_radial_step == 0.5:
122             beta = read_beta
123         else:
124             # Generate a new array for beta
125             beta = np.zeros((len(read_beta),len(beta_r)))
126 
127             # The step with i is 0.5, so need to double
    beta_radial_step
128             beta_radial_step *= 2
129 
130             # Define the next position to look for beta
131             next_pos = 0; next_beta = read_beta[:,0]
132 
133             # Adjust each beta
134             for i in range(beta.shape[1]):
135                 if i % beta_radial_step == 0:
136                     # Set the next beta
137                     cur_beta = next_beta
138                     beta[:,i] = cur_beta
139                     try:
140                         next_pos += 1; next_beta = read_beta[:,
    next_pos]
141                     except IndexError:
142                         # This is to be expected for the last entry
143                         break
144                 else:
145                     # Extrapolate (linearly)
146                     beta[:,i] = cur_beta + (next_beta - cur_beta) *
     (i % beta_radial_step) / beta_radial_step
147 
148         return beta_r, beta
149 
150     def apply_beta_adjustment(self, basis_radius, basis_set,
    beta_path):
151         # If we multiply our basis function by 1 + b2f2(r/v) + ...,
     we are able
152         # to fit more complex distributions
153         # v is the actual velocity, r is the projection of the
    velocity
154 
155         # Generate an array containing the radius of each basis
    function. This
156         # is the v term
157         v = self.generate_radius()
158 
159         # Split beta into radius and beta parameters
160         beta_r, beta = self.load_beta(beta_path)
161 
162         # Find the appropriate beta parameter for each basis
    function
163         bn = beta[:,np.isin(beta_r,v)]
164 
```

```
165         # Maintain beta at the same value if the beta terms doesn't
     extend to as
166         # large a radius as v
167         if v[-1] > beta_r[-1]:
168             bn = np.append(bn,np.tile(bn[:,-1].reshape(-1,1),sum(v>
    beta_r[-1])),axis=1)
169 
170         # Multiply basis functions by 1 + b2f2(r/rmax) + ...
171         # fn(r) is the nth function of the rate of change of the
    ratio between
172         # the radial distribution for bn and the radial
    distribution for bn = 0
173         # with respect to beta
174 
175         # Define the limits for
176         if self.sigma == 0:
177             max_no_sigma_corr = len(v)
178         else:
179             max_no_sigma_corr = 10
180 
181         # Start with the inner basis sets (no convolution with
    sigma)
182         # Ignore the first four, as they are effectively delta
    functions anyway
183         # Will run this section for everything if sigma = 0
184         for i in range(3,max_no_sigma_corr):
185             # Define a scaling factor for the basis function
186             scaling_factor = np.ones(len(basis_radius))
187 
188             r_div_rmax = np.divide(basis_radius[basis_radius<= v[i
    ]], v[i])
189 
190             # Adjust the scaling factor according to beta values
191             for n in range(len(bn)):
192                 scaling_factor[basis_radius<= v[i]] += bn[n, i] *
    get_beta_scaling((n+1)*2, r_div_rmax)
193 
194             # Extend the scaling factor out by one (accounts for
    the fact that
195             # the radial distribution does not cut off immediately,
     even with
196             # sigma = 0)
197             _ = len(scaling_factor[basis_radius<= v[i]])
198             scaling_factor[_] = scaling_factor[_ - 1]
199             plt.figure(4)
200             plt.plot(basis_radius, scaling_factor)
201             plt.figure(5)
202             plt.plot(basis_radius, basis_set[i])
203             # Adjust the basis function
204             basis_set[i] = np.multiply(basis_set[i], scaling_factor
    )
205             basis_set[i] /= np.sum(basis_set[i])
206             plt.figure(6)
207             plt.plot(basis_radius, basis_set[i])
208 
209         # Redefine basis_radius to have a 10x greater resolution
```

```
210         orig_basis_radius = basis_radius
211         basis_radius = np.arange(0,basis_radius[-1]+0.00001,
    basis_radius[1] / 10)
212 
213         # Set up the generator for the gaussians of appropriate
    sigma
214         if max_no_sigma_corr != len(v):
215             gaussian = self.gaussian_generator(len(v) -
    max_no_sigma_corr, basis_radius[1])
216 
217         # Deal with cases where a sigma convolution is required
218         for i in range(max_no_sigma_corr,len(v)):
219             # Define a scaling factor for the basis function
220             scaling_factor = np.zeros(len(basis_radius))
221 
222             # Step size always uniform, so can use a step of
    basis_radius[1]
223             # Need to sample more frequently so the convolution
    works better
224             # when the change of gradient is greater
225             r_div_rmax = np.divide(basis_radius[basis_radius<= v[i
    ]], v[i])
226 
227             # Adjust the scaling factor according to beta values
228             for n in range(len(bn)):
229                 scaling_factor[basis_radius<= v[i]] += bn[n, i] *
    get_beta_scaling((n+1)*2, r_div_rmax)
230 
231             # Keep at final value to help with convolution
232             scaling_factor[basis_radius > v[i]] = scaling_factor[
    basis_radius<= v[i]][-1]
233 
234             plt.figure(3)
235             plt.plot(basis_radius, scaling_factor + 1)
236 
237             points, next_gaussian = next(gaussian)
238             scaling_factor = np.insert(scaling_factor, 0, np.tile(
    scaling_factor[0], points))
239 
240             # Apply a convolution of a gaussian with std. dev.
    sigma
241             scaling_factor = np.convolve(scaling_factor,
    next_gaussian, 'same')[points:]
242 
243             # Adjust the scaling factor so that it is the correct
    size for the basis set
244             scaling_factor = scaling_factor[::10] + 1
245 
246             plt.figure(4)
247             plt.plot(orig_basis_radius, scaling_factor)
248             plt.figure(5)
249             plt.plot(orig_basis_radius, basis_set[i])
250             # Adjust the basis function
251             basis_set[i] = np.multiply(basis_set[i], scaling_factor
    )
252             basis_set[i] /= np.sum(basis_set[i])
```

```
253             plt.figure(6)
254             plt.plot(orig_basis_radius, basis_set[i])
255 
256         self.bn = bn
257         return basis_set
258 
259 
260     def gaussian_generator(self, sigma_len, resolution):
261         if self.sigma < 0.25:
262             # All sigma will take the value of self.sigma if it is
    less than
263             # 0.25
264             sigma = np.zeros(3); sigma += self.sigma
265         else:
266             # Slowly increase sigma from 0.25 to its final value
    with inc r
267             sigma = np.arange(0.25, self.sigma, (self.sigma+self.
    step)*0.05)
268 
269         # Adjust the sigma smoothly to avoid a big step in the
    basis function shape
270         if self.step >= 1:
271             sigma = np.insert(sigma, 2, 0.25 + 3 * (self.sigma +
    self.step) * 0.025)
272             sigma = np.insert(sigma, 1, 0.25 + (self.sigma + self.
    step) * 0.025)
273 
274         # Make sure the generated sigma is not larger than the
    specified sigma
275         sigma[sigma > self.sigma] = self.sigma
276 
277         # Make the sigma array the correct length
278         sigma = list(sigma) + [self.sigma] * (sigma_len - len(sigma
    ))
279 
280         # Generate a gaussian for each sigma, and yield it
281         for _sig in sigma:
282             x = np.arange(-3*_sig, 3*_sig+0.1, resolution)
283             gaussian = np.exp(-np.square(x/_sig) / 2)
284             gaussian /= sum(gaussian)
285             yield len(x), gaussian
286 
287     def adjust_basis(self, beta_path):
288         # Need to account for the fact that the basis may not match
     the spacing
289         # of the radial distribution, and need to make sure that
    the size of the
290         # basis function actually matches that of the radial
    distribution
291 
292         # Load the basis set
293         f = self.check_appropriate_basis_exists()
294         basis_radius, basis_set = self.load_basis(f)
295 
296         # Calculate the step in the radial distribution
```

```
297         radial_step = np.rint(self.radial_dist_r[2] - self.
    radial_dist_r[0]) / 2
298 
299         # If a basis step for the function is provided, cut the
    basis set down accordingly
300         if self.basis_fn_step != 0.5:
301             cut_step = int(self.basis_fn_step / 0.5)
302             basis_radius = basis_radius[::cut_step]
303             basis_set = basis_set[:,::cut_step]
304 
305         # Adjust radial_dist accordingly as well
306         if radial_step < self.basis_fn_step:
307             cut_step = int(self.basis_fn_step / radial_step)
308             self.radial_dist_i = self.radial_dist_i[::cut_step]
309 
310         elif radial_step > self.basis_fn_step:
311             # In this case, basis_radius must be less than
    radial_step. Adjust
312             # the basis set appropriately
313             rebin = int(radial_step / basis_radius[1])
314             basis_radius = basis_radius[::rebin]
315             basis_set = basis_set[:,::rebin]
316 
317 
318         # Make sure the basis set and radial distribution have the
    same length
319         if len(basis_radius) > len(self.radial_dist_i):
320             basis_radius = basis_radius[:len(self.radial_dist_i)]
321 
322             # Need to adjust the basis set dimension containing the
     value at each r
323             basis_set = basis_set[:,:len(self.radial_dist_i)]
324 
325             # May also need to reduce the total number of r for
    which basis sets exist
326             if len(basis_set) > len(self.radial_dist_i):
327                 basis_set = basis_set[:len(self.radial_dist_i)]
328 
329         elif len(basis_radius) < len(self.radial_dist_i):
330             self.radial_dist_i = self.radial_dist_i[:len(
    basis_radius)]
331 
332         # Apply correction for beta if required
333         if beta_path != None:
334             basis_set = self.apply_beta_adjustment(basis_radius,
    basis_set, beta_path)
335 
336         self.basis_r = basis_radius
337         self.basis_set = basis_set
338 
339 
340     def generate_radius(self):
341         # Generate an array containing the radius at which each
    basis function
342         # has been generated.
```

```
343         # NOT TO BE CONFUSED WITH BASIS_RADIUS, THE RADIUS AT EACH
    POINT WITHIN
344         # THE BASIS FUNCTION
345         if self.step <= 1:
346             radius = np.concatenate((np.arange(0,5,0.5),\
347                         np.arange(5,self.max_r + 0.001,self.step)))
348         else:
349             radius = np.concatenate((np.arange(0,5.5,0.5),\
350                         [5 + self.step / 2],\
351                         np.arange(5+self.step,self.max_r + 0.001,
    self.step)))
352 
353         return radius
354 
355 
356     def fit_data(self):
357 
358         def analytical_inverse_function(radius):
359             if self.sigma < 0.25:
360                 # All sigma will take the value of self.sigma if it
     is less than
361                 # 0.25
362                 sigma = np.zeros(3); sigma += self.sigma
363             else:
364                 # Slowly increase sigma from 0.25 to its final
    value with inc r
365                 sigma = np.arange(0.25, self.sigma, (self.sigma+
    self.step)*0.05)
366 
367             # Adjust the sigma smoothly to avoid a big step in the
    basis function shape
368             if self.step >= 1:
369                 sigma = np.insert(sigma, 2, 0.25 + 3 * (self.sigma
    + self.step) * 0.025)
370                 sigma = np.insert(sigma, 1, 0.25 + (self.sigma +
    self.step) * 0.025)
371 
372             # Make sure the generated sigma is not larger than the
    specified sigma
373             sigma[sigma > self.sigma] = self.sigma
374 
375             sigma = np.insert(sigma, 0, [i / 20 for i in range(10)
    ])
376 
377             # Make the sigma array the correct length
378             sigma = list(sigma) + [self.sigma] * (len(radius) - len
    (sigma))
379 
380             # Generate a gaussian for each sigma, and yield it
381             for _sig, _rad in zip(sigma, radius):
382                 if _sig == 0:
383                     gaussian = np.zeros(len(radius))
384                     gaussian[radius == _rad] = 1
385                 else:
386                     gaussian = np.exp(-np.square((radius - _rad)/
    _sig) / 2)
```

```
                    gaussian /= sum(gaussian)
                yield gaussian

    if self.reg:
        # Regularisation is ridge regression, also known as Tikhonov regularization
        model = Ridge(alpha=self.reg_val, fit_intercept=True)
    else:
        # Setting alpha = 0 is the same as no regularisation
        model = Ridge(alpha=0, fit_intercept=True)

    model.fit(self.basis_set.T, self.radial_dist_i)

    fit = np.matmul(model.coef_,self.basis_set) + model.intercept_

    # Generate an array containing the radius of each basis function
    radius = self.generate_radius()

    # Multiply the weight by its analytical inverse
    gauss_gen = analytical_inverse_function(radius)
    inv_dist = np.zeros(len(radius))
    for _coef in model.coef_:
        inv_dist += next(gauss_gen) * _coef

    gauss_gen = analytical_inverse_function(radius)

    # Find the sum of the gaussians, to correct the intensity (as Gaussians
    # do not produce a distribution of uniform intensity)
    correction = np.zeros(len(radius))
    for _coef in model.coef_:
        correction += next(gauss_gen)

    # Adjust the correction based on the sampling rate
    correction[:10] *= 0.5 / self.step
    if self.step > 1:
        correction[10] *= (0.5 / self.step + 0.5) / 2
        correction[11] *= 0.5
        correction[12] *= 0.75
    else:
        correction[10] *= (0.5 / self.step + 1) / 2

    if __name__ == '__main__':
        plt.figure()
        plt.plot(correction)

        # Plot the output
        plt.figure()
        plt.plot(radius, model.coef_ + model.intercept_)

        plt.figure()
        plt.plot(radius, inv_dist / correction)

        # Plot the fit
```

```
439             plt.figure()
440             plt.plot(self.basis_r, fit, label='Fit')
441             plt.plot(self.basis_r, self.radial_dist_i, label='
    Original')
442             plt.legend()
443             plt.show()
444 
445         return radius, inv_dist/correction, self.basis_r, fit
446 
447 
448     def reconstruct_image(self, radius, fit, uniform_sig=True, *,
    no_points=100000):
449         # Uniform_sig uses a uniform sigma for the reconstruction.
    If False,
450         # the sigma of the basis function is used in the inner
    region.
451 
452         if not uniform_sig:
453             # Get the sigma for each radius
454             if self.sigma < 0.25:
455                 # All sigma will take the value of self.sigma if it
     is less than
456                 # 0.25
457                 sigma = np.zeros(3); sigma += self.sigma
458             else:
459                 # Slowly increase sigma from 0.25 to its final
    value with inc r
460                 sigma = np.arange(0.25, self.sigma, (self.sigma+
    self.step)*0.05)
461 
462             # Adjust the sigma smoothly to avoid a big step in the
    basis function shape
463             if self.step >= 1:
464                 sigma = np.insert(sigma, 2, 0.25 + 3 * (self.sigma
    + self.step) * 0.025)
465                 sigma = np.insert(sigma, 1, 0.25 + (self.sigma +
    self.step) * 0.025)
466 
467             # Make sure the generated sigma is not larger than the
    specified sigma
468             sigma[sigma > self.sigma] = self.sigma
469 
470             # Insert the sigma for the inner basis functions
471             sigma = np.insert(sigma, 0, [i / 20 for i in range(10)
    ])
472 
473             # Make the sigma array the correct length
474             sigma = list(sigma) + [self.sigma] * (len(radius) - len
    (sigma))
475 
476 
477 
478         # Get the size of the image you are creating and initialise
479         img_size = np.rint(self.max_r).astype('int') * 2 + 2 + 10*
    np.ceil(self.sigma).astype('int')
480         image = np.zeros((img_size, img_size))
```

```
481
482         fit_copy = deepcopy(fit)
483
484         # Make any negative values zero
485         fit_copy[fit<0] = 0
486
487         # Normalise the fit to the number of points
488         norm_fit = np.rint(fit / np.sum(fit_copy) * no_points).
    astype('int')
489
490         def uniform_distribution(image):
491             # Generate data for each r
492             for i, r in enumerate(radius):
493                 # Skip if zero or negative
494                 if norm_fit[i] <= 0:
495                     continue
496
497                 # Generate the r with sigma spread
498                 if uniform_sig:
499                     r = r + np.random.randn(norm_fit[i].astype('int
    ')) * self.sigma
500                 else:
501                     r = r + np.random.randn(norm_fit[i].astype('int
    ')) * sigma[i]
502
503                 # Generate the y and x coordinates
504                 theta = np.random.rand(len(r)) * 2 * np.pi
505                 x = r * np.cos(theta); y = r * np.sin(theta)
506
507                 # Add to the image
508                 np.add.at(image, (np.rint(img_size/2 - 0.5 + x).
    astype('int'), np.rint(img_size/2 - 0.5 + y).astype('int')), 1)
509
510             return image
511
512         def legendre_distribution(image):
513             theta = np.arange(0,2*np.pi,np.pi/500)
514
515             for i, r in enumerate(radius):
516                 # Skip if zero or negative
517                 if norm_fit[i] <= 0:
518                     continue
519
520                 # Generate the r with sigma spread
521                 if uniform_sig:
522                     r = r + np.random.randn(norm_fit[i]) * self.
    sigma
523                 else:
524                     r = r + np.random.randn(norm_fit[i]) * sigma[i]
525
526                 # Calculate the intensity at each theta
527                 intensity = np.ones(len(theta))
528                 for n in range(len(self.bn)):
529                     intensity += self.bn[n,i] * np.array(leg(2*(n
    +1), np.cos(theta)))
530
```

```
                # Get the cumulative distribution
                cum_dist = np.cumsum(intensity)

                # Pick thetas from the cumulative distribution
                sample_points = np.random.rand(norm_fit[i]) *
    cum_dist[-1]
                sample_theta = np.zeros(norm_fit[i])
                for j, _theta in enumerate(theta):
                    sample_theta[sample_points > cum_dist[j]] =
    _theta

                # Generate the x and y coordinates
                x = r*np.cos(sample_theta); y = r*np.sin(
    sample_theta)

                # Add to the image
                np.add.at(image, (np.rint(img_size/2 - 0.5 + x).
    astype('int'), np.rint(img_size/2 - 0.5 + y).astype('int')), 1)

            return image

        try:
            self.bn
            image = legendre_distribution(image)
        except AttributeError:
            image = uniform_distribution(image)

        if __name__ == '__main__':
            plt.figure()
            plt.imshow(image, origin='lower', cmap='inferno', vmax=
    np.max(image)/2)
            plt.show()

        return image

    def transform(self, beta_path=None):
        self.adjust_basis(beta_path)
        return self.fit_data()

# Caller function for the class
def transform(radial_dist_r, radial_dist_i, *, sigma, step, max_r,
    regularisation=True, reg_val = 0.001, disp_inv_im, im_no_points
    =100000, basis_step=0.5):
    # Does not do anything if max_r is too small
    if max_r < 5:
        return 0,0,0,0,np.zeros((1,1))

    # Initialise class
    sph_tran = spherical_harmonic_transform(radial_dist_r,\
                                            radial_dist_i,\
                                            sigma=sigma,\
                                            step=step,\
                                            max_r=max_r,\
                                            reg_val=reg_val,\
                                            basis_step=basis_step)

```

```
    # Transform the data
    radius, radial_intensity, fit_r, fit = sph_tran.transform()

    if disp_inv_im:
        # Reconstruct ion image
        inverted_image = sph_tran.reconstruct_image(radius, radial_intensity, no_points=im_no_points)

        return radius, radial_intensity, fit_r, fit, inverted_image

    return radius, radial_intensity, fit_r, fit, np.zeros((1,1))


if __name__ == '__main__':
    import matplotlib.pyplot as plt
    import tkinter; from tkinter import filedialog

    def load_radial_dist(f):
        data = np.loadtxt(f, delimiter='\t')
        return data[:,0], data[:,1]

    test_file = r''
    beta_path = r''

    radial_dist_r, radial_dist_i = load_radial_dist(test_file)

    test = spherical_harmonic_transform(radial_dist_r, radial_dist_i, sigma=0.5, step=0.5, max_r=161, reg_val=0.0005, basis_step=0.5)
    if beta_path == '':
        radius, radial_intensity, fit_r, fit = test.transform()
    else:
        radius, radial_intensity, fit_r, fit = test.transform(beta_path)

    # Choose whether to use the same sigma for the reconstruction, even in the inner
    # basis area, or to adjust the sigma in accordance with the basis function.
    reconstruct_uniform_sigma = True

    # Reconstruct ion image
    image_array = test.reconstruct_image(radius, radial_intensity, reconstruct_uniform_sigma)

    #Get rid of root from tkinter
    root = tkinter.Tk()
    root.withdraw()

    output_file = filedialog.asksaveasfilename(title='Set file name (radial distribution)',\
    filetypes = (("dat files","*.dat"),("All files","*.*")),\
    defaultextension = 'dat')

    if output_file == '':
        pass
```

```
628     else:
629         np.savetxt(output_file, np.array((radius, radial_intensity)
    ).T, delimiter='\t')
630         np.savetxt(output_file[:-4] + '_fit.dat', np.array((fit_r,
    fit)).T, delimiter='\t')
631         np.savetxt(output_file[:-4] + '_recon_image.dat',
    image_array, delimiter='\t')
```

D.3 PyAbel Caller

Pyabel caller contains functions to mask parts of an image, and to symmetrise an image. It can then call the inversion methods from the PyAbel package directly. It also provides the correct Jacobian for the radial distribution of both inverted and non-inverted scattering distributions.

```
1  import abel
2  import numpy as np
3
4  #NOTE THAT THE AXIS OF CYLINDRICAL SYMMETRY SHOULD BE VERTICAL
5  #IF RAW DATA IS PLOTTED WITH MATPLOTLIB WITH ORIGIN='LOWER'!!!
6
7  class Transform():
8      def __init__(self, *, method, transform_options, direction='
    inverse'):
9          #Tells the programme which inversion method is being used,
    and sets all
10         #the options.
11         self.method = method
12         self.transform_options = transform_options
13         self.direction = direction
14
15     def fold_image(self, raw_image, img_centre, symmetry_axis,
    use_quadrants,\
16     apply_detector_mask, mask_centre, mask_radius):
17         # Takes an image, image centre and directions to fold,
    folds the image and
18         # returns the folded image. A mask can also be applied to
    remove any contribution
19         # from outside the detector. Note it is always assumed that
     axis 0, defined
20         # below, is an axis of symmetry (indeed it must be for the
    inversion method
21         # to be used in the first place).
22         #
23         # Symmetry axis 0 is the vertical axis (axis of cylindrical
     symmetry) and
24         # axis 1 is the horizontal axis (when data is ploted with
    the origin in the
25         # bottom left corner of the image [origin='lower' in
    matplotlib]). Quadrants
26         # are ordered from top right in an anticlockwise direction
    (so
27         # theta = 0 -> pi/2, then theta = pi/2 -> pi etc.).
28         #
```

```
29          # The pyabel package treats the zero pixel as the central
    pixel. If the image
30          # centre is set to an integer, this will be used as the
    central column. If
31          # the image centre is set to, say, 161.5, a combination of
    columns 161 and 162
32          # will be used as the central column
33
34          def apply_mask(image):
35              #Create a grid of x and y coordinates
36              x,y = np.ogrid[:image.shape[0],:image.shape[1]]
37              cx, cy = mask_centre[0], mask_centre[1]
38
39              #Work out the r squaded value for each pixel
40              r_squared = (x-cx)**2 + (y-cy)**2
41
42              #Apply mask where radius greater than the size of the
    image
43              image[np.where(r_squared > mask_radius**2)] = np.nan
44
45              return image
46
47
48          def folding_function(raw_image, img_centre, symmetry_axis,
    use_quadrants):
49              class folder():
50                  def __init__(self, dim_zero, dim_one, fold_segments
    ):
51                      #Define the folded image, and the number of nan
     in each pixel
52                      self.folded_image = np.zeros((dim_zero, dim_one
    ))
53                      self.no_nan = np.zeros((dim_zero, dim_one))
54                      self.fold_segments = fold_segments
55
56                  def process_quadrant(self, data, use_quad):
57                      #Four quadrants, so up to four nan values in a
    pixel
58                      self.max_nan = 4
59
60                      #Assume that every point in the image is nan
61                      self.no_nan += 1
62
63                      #Check the quadrant is to be used
64                      if use_quad == False:
65                          return
66
67                      #Adjust the number of nan array. We assumed
    that all data were nan,
68                      #so start by subtracting one from all points
    within the image bounds.
69                      #Then, add one back on anywhere there was a nan
     included in the data.
70                      self.no_nan[:data.shape[0],:data.shape[1]] -= 1
71                      nan_location_array = np.isnan(data)
```

```
72                      self.no_nan[:data.shape[0],:data.shape[1]] +=
    nan_location_array.astype('uint8')
73
74                      #Set all nan equal to zero
75                      data[nan_location_array] = 0
76
77                      #Add in the new data
78                      self.folded_image[:data.shape[0], :data.shape
    [1]] += data
79
80
81                  def process_half(self, data, use_upper_quad,
    use_lower_quad):
82                      #Two halves, so up to two nan values in a pixel
83                      self.max_nan = 2
84
85                      if use_upper_quad and use_lower_quad:
86                          #If using both quadrants, no change
    required
87                          pass
88                      elif use_upper_quad or use_lower_quad:
89                          if use_upper_quad == False:
90                              #If not using upper quad
91                              data[img_centre[0]:] = np.nan
92                          else:
93                              #If not using lower quad
94                              data[:img_centre[0]] = np.nan
95                      else:
96                          # Case where not using either quadrant
    making up the half
97                          #Increment nan count on all pixels
98                          self.no_nan += 1
99                          return
100
101                     #Adjust the number of nan array. Add one to all
     points not included
102                     #in the current image, then add one for any nan
     in the data
103                     self.no_nan[:,data.shape[1]:] += 1
104                     nan_location_array = np.isnan(data)
105                     self.no_nan[:,:data.shape[1]] +=
    nan_location_array.astype('uint8')
106
107                     #Set all nan equal to zero
108                     data[nan_location_array] = 0
109
110                     #Add in the new data
111                     self.folded_image[:, :data.shape[1]] += data
112
113
114                 def finalise_image(self):
115                     #When normalising, need a non-zero divisor
116                     self.no_nan[np.where(self.no_nan == self.
    max_nan)] = self.max_nan - 1
117
```

```
                    #Divide by the number of image segments - the number of nans not contributing
                    self.folded_image = np.divide(self.folded_image, self.max_nan - self.no_nan)


            #Get the dimensions of the image
            img_dim_zero, img_dim_one = raw_image.shape[0], raw_image.shape[1]

            #Find the dimensions of the largest potential quadrant (img_centre has
            #one added due to zero-indexing, floor is to deal with half-integer centre)
            quadrant_dim_zero = np.floor(np.max([img_centre[0]+1, img_dim_zero-img_centre[0]])).astype('uint16')
            quadrant_dim_one = np.floor(np.max([img_centre[1]+1, img_dim_one-img_centre[1]])).astype('uint16')

            #Need to account for the difference in behaviour if the image centre
            #is between pixels or on a pixel. The former case needs no modification
            #to img_centre, whereas the latter requires one to be added when
            #indexing from the bottom (e.g. raw_image[:img_centre[0] + 1]).
            #This is because the same pixels need tobe included on more than
            #one occasion at the centre when the centre in either dimension is
            #on a pixel
            if img_centre[0] % 1 == 0:
                centre_zero = 1
                img_centre = (int(img_centre[0]), img_centre[1])
            else:
                centre_zero = 0
                img_centre = (np.round(img_centre[0] + 0.5).astype('uint16'), img_centre[1])

            if img_centre[1] % 1 == 0:
                centre_one = 1
                img_centre = (img_centre[0], int(img_centre[1]))
            else:
                centre_one = 0
                img_centre = (img_centre[0], np.round(img_centre[1] + 0.5).astype('uint16'))

            #There is an error if only a single number is put in the symmetry axis
            #tuple. Redefine symmetry_axis if this is the case.
            try:
                1 in symmetry_axis
            except TypeError:
                if symmetry_axis == (0):
                    symmetry_axis = (0,0)
```

```
158                 elif symmetry_axis == (1):
159                     symmetry_axis = (1,1)
160                 else:
161                     symmetry_axis = (0, 1)
162 
163             #If there is symmetric under reflection perpendicular
    to the axis of
164             #cylindrical symmetry, fold image into quadrants
165             if symmetry_axis == (0,1):
166                 folding_class = folder(quadrant_dim_zero,
    quadrant_dim_one, 4)
167 
168                 #Process each of the four quadrants in turn
169                 folding_class.process_quadrant(raw_image[img_centre
    [0]:,\
170                         img_centre[1]:],\
171                         use_quadrants[0])
172                 folding_class.process_quadrant(np.fliplr(raw_image[
    img_centre[0]:,\
173                         :img_centre[1] + centre_one]),\
174                         use_quadrants[1])
175                 folding_class.process_quadrant(np.fliplr(np.flipud(
    raw_image[:img_centre[0] + centre_zero,\
176                         :img_centre[1] + centre_one])),\
177                         use_quadrants[2])
178                 folding_class.process_quadrant(np.flipud(raw_image
    [:img_centre[0] + centre_zero,\
179                         img_centre[1]:]),\
180                         use_quadrants[3])
181 
182             #If there is only an axis of cylindrical symmetry, fold
     image into a half
183             #image. Still need to know quadrant_dim_zero for the
    use_quadrants bit.
184             else:
185                 # Need to transpose the image to fold it properly.
    Leave in transposed state (as this is the correct orientation
    for inversion).
186                 if 1 in symmetry_axis:
187                     raw_image = raw_image.transpose()
188                     half_dim_zero = img_dim_one
189                     half_dim_one = quadrant_dim_zero
190                     img_centre = (img_centre[1], img_centre[0])
191                     centre_temp = centre_one
192                     centre_one = centre_zero
193                     centre_zero = centre_temp
194                     use_quadrants = (use_quadrants[0],
    use_quadrants[3], use_quadrants[2], use_quadrants[1])
195                 else:
196                     half_dim_zero = img_dim_zero
197                     half_dim_one = quadrant_dim_one
198 
199                 folding_class = folder(half_dim_zero, half_dim_one,
     2)
200 
201                 # Process each half of the image
```

```
202                 folding_class.process_half(raw_image[:,img_centre
    [1]:],\
203                         use_quadrants[0], use_quadrants[3])
204                 folding_class.process_half(np.fliplr(raw_image[:, :
    img_centre[1] + centre_one]),\
205                         use_quadrants[1], use_quadrants[2])
206 
207             folding_class.finalise_image()
208 
209             return folding_class.folded_image, folding_class.
    fold_segments
210 
211         ##############################
212         if apply_detector_mask == True:
213             #Apply mask if required
214             masked_image = apply_mask(raw_image)
215             return folding_function(masked_image, img_centre,
    symmetry_axis, use_quadrants)
216 
217         return folding_function(raw_image, img_centre,
    symmetry_axis, use_quadrants)
218 
219     def invert_image(self, folded_image):
220         if self.method == 'basex':
221             inverted_image = abel.basex.basex_transform(
    folded_image, direction=self.direction, **self.transform_options
    )
222         elif self.method == 'hansen-law':
223             inverted_image = abel.hansenlaw.hansenlaw_transform(
    folded_image, direction=self.direction, **self.transform_options
    )
224         elif self.method == 'three_point':
225             inverted_image = abel.dasch.three_point_transform(
    folded_image, direction=self.direction, **self.transform_options
    )
226         #Add more inversion methods in as required
227 
228         return inverted_image
229 
230     def reconstruct_image(self, image, fold_segs):
231         #Deal with the case of a two segment and four segment image
     separately
232         if fold_segs == 2:
233             #Need an image one under twice as wide as the half. One
     less as the
234             #0 column is treated as the central column
235             reconstructed_image = np.zeros([image.shape[0], image.
    shape[1]*2-1])
236 
237             #Assign the image to reconstructed image
238             reconstructed_image[:,image.shape[1]-1:] = image
239             reconstructed_image[:,:image.shape[1]] = np.fliplr(
    image)
240 
241         else:
```

```
242             #Want a square result. Minus one required as described
    above
243             quadrant_dim = np.max(image.shape)
244             reconstructed_image = np.zeros([quadrant_dim*2-1,
    quadrant_dim*2-1])
245 
246             #Assign the image to the reconstructed image
247             reconstructed_image[quadrant_dim-1:quadrant_dim-1+image
    .shape[0],\
248                     quadrant_dim-1:quadrant_dim-1+image.shape[1]] =
     image
249 
250             reconstructed_image[quadrant_dim-image.shape[0]:
    quadrant_dim,\
251                     quadrant_dim-1:quadrant_dim-1+image.shape[1]] =
     np.flipud(image)
252 
253             reconstructed_image[quadrant_dim-1:quadrant_dim-1+image
    .shape[0],\
254                     quadrant_dim-image.shape[1]:quadrant_dim] = np.
    fliplr(image)
255 
256             reconstructed_image[quadrant_dim-image.shape[0]:
    quadrant_dim,\
257                     quadrant_dim-image.shape[1]:quadrant_dim] = np.
    fliplr(np.flipud(image))
258 
259         return reconstructed_image
260 
261     def __call__(self, raw_image, img_centre, *, symmetry_axis
    =(0,1),use_quadrants=(True,True,True,True),\
262     apply_detector_mask=False, mask_centre=(162,162), mask_radius
    =162):
263 
264         folded_image, fold_segments = self.fold_image(raw_image,
    img_centre, symmetry_axis,use_quadrants,\
265         apply_detector_mask, mask_centre, mask_radius)
266 
267         inverted_image = self.invert_image(folded_image)
268         reconstructed_image = self.reconstruct_image(inverted_image
    , fold_segments)
269 
270         try:
271             dr = self.transform_options['dr']
272         except KeyError:
273             dr = 1.0
274 
275         #Get the radial distribution
276         radius, radial_intensity = abel.tools.vmi.\
277         angular_integration(reconstructed_image, dr=dr)
278 
279         self.inverted_image = reconstructed_image
280         self.radius = radius
281         self.radial_intensity = radial_intensity
282 
283 
```

```
284
285 # angular_integration function has been taken from the PyAbel
    package, and
286 # modified so that the correct Jacobian is used.
287
288 def angular_integration(IM, origin=None, Jacobian=True, dr=1, dt=
    None):
289     r"""Angular integration of the image.
290
291     Returns the one-dimensional intensity profile as a function of
    the
292     radial coordinate.
293
294     Note: the use of Jacobian=True applies the correct Jacobian for
     the
295     integration of a 3D object in spherical coordinates. Jacobian =
     True
296     is always passed to abel.tools.polar.reproject_image_into_polar
    , as
297     this is the required jacobian for a transform into polar
    coordinates.
298
299     Parameters
300     ----------
301     IM : 2D numpy.array
302         The data image.
303
304     origin : tuple
305         Image center coordinate relative to *bottom-left* corner
306         defaults to ``rows//2, cols//2``.
307
308     Jacobian : boolean
309         Include :math:`r\sin\theta` in the angular sum (integration
    ).
310         Also, ``Jacobian=True`` is passed to
311         :func:`abel.tools.polar.reproject_image_into_polar`,
312         which includes another value of ``r``, thus providing the
    appropriate
313         total Jacobian of :math:`r^2\sin\theta`.
314
315     dr : float
316         Radial coordinate grid spacing, in pixels (default 1). `dr
    =0.5` may
317         reduce pixel granularity of the speed profile.
318
319     dt : float
320         Theta coordinate grid spacing in radians.
321         if ``dt=None``, dt will be set such that the number of
    theta values
322         is equal to the height of the image (which should typically
     ensure
323         good sampling.)
324
325     Returns
326     ------
327     r : 1D numpy.array
```

```
328         radial coordinates
329
330     speeds : 1D numpy.array
331         Integrated intensity array (vs radius).
332
333      """
334
335     polarIM, R, T = abel.tools.polar.reproject_image_into_polar(
336         IM, origin, Jacobian=True, dr=dr, dt=dt)
337
338     dt = T[0, 1] - T[0, 0]
339
340     if Jacobian:  # x r sin(theta)
341         polarIM = polarIM * R * np.abs(np.sin(T))
342
343     speeds = np.trapz(polarIM, axis=1, dx=dt)
344
345     n = speeds.shape[0]
346
347     return R[:n, 0], speeds   # limit radial coordinates range to
    match speed
```

D.4 TOF-TOF covariance

The code used to generate the TOF-TOF covariance maps presented in this thesis. The user must first provide the range of PImMS timebins to be used in the analysis, the number of processes to start, and the 'split points', which dictate how the acquisition cycles are split between the processes. To give an example, if a PImMS file had 300,000 acquisition cycles, the number of processes was set equal to three, and the split point array was set to [0, 100000, 200000], three processes would be started, each processing 100,000 frames. The covariance matrix is calculated as discussed in section 3.4.2, before the result is displayed, and the TOF-TOF covariance map and TOF are saved as tab-delimited text files.

```
1  import numpy as np
2  import imgread
3  import matplotlib.pyplot as plt
4  import multiprocessing as mp
5  from sys import exit
6
7  if __name__ == '__main__':
8      min_tof = 1340
9      max_tof = 1540
10
11     no_proc = 3
12     split_points = [0,1500000,3000000]
13
14 def multiproc_caller(input_file_path, min_tof=0, max_tof=4095,
    no_proc=1, split_points=[0]):
15     def new_process(frames_to_skip, frames_to_proc):
16         #Start reading the pump file
17         p_parent_pipe, p_child_pipe = mp.Pipe()
18         p = mp.Process(target=tof_tof_covariance().run_calculation
    ,\
```

```
19          args=(input_file_path, min_tof, max_tof, frames_to_skip,
    frames_to_proc, p_child_pipe,))
20          p.start()
21          return p, p_parent_pipe
22
23      #Make sure there are sufficient split points
24      if len(split_points) < no_proc:
25          no_proc = len(split_points)
26
27      #Limit the number of processes to three
28      if no_proc > 3:
29          no_proc = 3
30
31      process_dict = {}
32      pipe_dict = {}
33
34      for i in range(no_proc-1):
35          process_dict[i], pipe_dict[i] = new_process(split_points[i
    ], split_points[i+1] - split_points[i])
36
37      covariance_class = tof_tof_covariance()
38      covariance_class.run_calculation(input_file_path, min_tof,
    max_tof, split_points[no_proc-1])
39
40      for out_pipe in pipe_dict.values():
41          data_dict = out_pipe.recv()
42          out_pipe.close()
43          covariance_class.tof += data_dict['total_tof']
44          covariance_class.XY_term += data_dict['XY_term']
45          covariance_class.no_frames += data_dict['no_frames']
46          covariance_class.no_frames_w_signal += data_dict['
    no_frames_w_signal']
47
48      for proc in process_dict.values():
49          proc.join()
50
51      return covariance_class
52
53
54  class tof_tof_covariance():
55      def __init__(self):
56          pass
57
58      def run_calculation(self, input_file_path, min_tof=0, max_tof
    =4095, frames_to_skip=0, frames_to_proc=-1, return_pipe=-1):
59          #Point to the file and set up the file-reading generator
60          input_file = imgread.pimms(input_file_path, frames_to_skip,
     frames_to_proc)
61          pimms_data_gen = input_file.read_pimms_file()
62
63          #Initialise all the required variables
64          tof_bins = np.arange(min_tof, max_tof+1)
65          frame_tof = np.zeros([len(tof_bins),1])
66          total_tof = np.zeros([len(tof_bins),1])
67          XY_term = np.zeros([len(tof_bins),len(tof_bins)])
68          no_frames = 0
```

```
69          no_frames_w_signal = 0
70
71          try:
72              while True:
73                  #Get the frame data
74                  frame_data = next(pimms_data_gen)
75                  #Reset frame_tof to zero
76                  frame_tof.fill(0)
77                  #Find the mask for the tof region of interest
78                  mask = np.isin(frame_data[:,2], tof_bins)
79                  #Find the unique elements in that region and count
    them
80                  unique_elements, counts_elements = np.unique(
    frame_data[mask,2], return_counts=True)
81                  #Catch any empty arrays
82                  if unique_elements.size == 0:
83                      no_frames += 1
84                      continue
85                  #Change the timecodes to match the array indices
86                  unique_elements -= min_tof
87                  #Set the frame tof equal to this, and add the frame
     tof to the total tof
88                  frame_tof[unique_elements,0] = counts_elements
89                  total_tof = np.add(total_tof, frame_tof)
90                  #Add to the XY term
91                  XY_term += np.matmul(frame_tof, frame_tof.transpose
    ())
92                  no_frames += 1
93                  no_frames_w_signal += 1
94          except ValueError:
95              pass
96          except StopIteration:
97              pass
98
99          if return_pipe != -1:
100             return_pipe.send(dict(total_tof=total_tof, XY_term=
    XY_term,\
101             no_frames=no_frames, no_frames_w_signal=
    no_frames_w_signal))
102             return_pipe.close()
103         else:
104             #Add the appropriate variables to the class
105             self.tof = total_tof
106             self.XY_term = XY_term
107             self.no_frames = no_frames
108             self.no_frames_w_signal = no_frames_w_signal
109
110
111     def produce_covariance_map(self, use_frames_w_o_signal = True,
    covar_sum_zero = False):
112         #Options allow you to either use only the frames with
    signal in the region of
113         #interest or all the frames, and make the sum of the
    covariance map equal to 0
114         #
115         #Set the divisor for when calculating means
```

```
116         if use_frames_w_o_signal == True:
117             divisor = self.no_frames
118         else:
119             divisor = self.no_frames_w_signal
120 
121         #Divide the XY term and the total tof (equivalent to X and
    Y) by no_frames
122         #Gives <XY>, <X> and <Y>
123         XY_term = np.divide(self.XY_term, divisor)
124         total_tof = np.divide(self.tof, divisor)
125 
126         #Multiply the <X> and <Y> terms
127         X_Y_term = np.matmul(total_tof, total_tof.transpose())
128 
129         #Evaluate <XY> - <X><Y>
130         if covar_sum_zero == False:
131             covariance_map = np.subtract(XY_term, X_Y_term)
132         else:
133             #Scale the <XY> term to have the same sum as the <X><Y>
     term
134             XY_sum = np.sum(XY_term)
135             X_Y_sum = np.sum(X_Y_term)
136             covariance_map = np.subtract(np.multiply(XY_term,
    X_Y_sum / XY_sum), X_Y_term)
137 
138         #Apply Bessel's correction
139         covariance_map *= np.divide(divisor, divisor - 1)
140 
141         #Add covariance_map to the class
142         self.covariance_map = covariance_map
143 
144         return covariance_map
145 
146     def mass_calibration(self):
147         pass
148 
149     def save_map(self):
150         output_path = filedialog.asksaveasfilename(title='Set file
    name',\
151         filetypes = (("Tab delimited files","*.dat"),("All files","
    *.*")),\
152         defaultextension = 'dat')
153 
154         if output_path == '':
155             return
156 
157         with open(output_path, 'w') as f:
158             np.savetxt(f, self.covariance_map, delimiter='\t')
159 
160 if __name__ == '__main__':
161 
162     import tkinter
163     from tkinter import filedialog
164 
165     #Get rid of root from tkinter
166     root = tkinter.Tk()
```

```
167     root.withdraw()
168 
169     #Choose file to open
170     input_file_path = filedialog.askopenfilename(title = "Select
        file",\
171     filetypes = (("PImMS files","*.bin"),("All files","*.*")))
172 
173     if input_file_path == '':
174         exit()
175 
176     covar_calculator = multiproc_caller(input_file_path, min_tof,
        max_tof, no_proc=no_proc, split_points=split_points)
177 
178     print(f'No frames: {covar_calculator.no_frames} (of which {
        covar_calculator.no_frames_w_signal} frames contained signal)')
179 
180     cov_map = covar_calculator.produce_covariance_map(True, False)
181     plt.figure()
182     plt.imshow(cov_map, origin='lower',cmap='viridis',
        interpolation='nearest', vmax=cov_map.max()/100, vmin=cov_map.
        min()/100)#, vmin=-0.00025)
183     plt.colorbar()
184 
185     plt.figure()
186     plt.plot(covar_calculator.tof)
187 
188     plt.show()
189 
190     np.savetxt(input_file_path[:-4] + '_tof-tof_cov_map.dat',
        cov_map, delimiter='\t')
191     np.savetxt(input_file_path[:-4] + '_tof.dat', covar_calculator.
        tof, delimiter='\t', fmt='%d')
```